Mapping UV Radiation in the East Antarctic Sea Ice Zone

by

Jane Higgins, B.I.S., B.Ant.Studies (Hons).

Submitted in fulfilment of the requirements
for the degree of
Doctor of Philosophy

Institute for Marine and Antarctic Studies
University of Tasmania

February, 2011

Declaration

This thesis contains no material which has been accepted for the award of any other degree or diploma in any tertiary institution and, to the best of my knowledge and belief, contains no material previously published or written by another person, except where due reference is made in the text of the thesis.

……..

(Jane Higgins)

Authority of access

This thesis may be made available for loan and limited copying in accordance with the Copyright Act 1968.

……..

(Jane Higgins)

University of Tasmania
February, 2011

Abstract

Ozone depletion has been a well-researched phenomenon since its discovery in the early 1980s. It is now scientifically accepted that if all other factors (cloudiness, turbidity, surface albedo, etc.) remain the same, decreases in stratospheric ozone concentrations provoke an increase in ultraviolet B (UVB) radiation (in the wavelength range 280-325 nm) at the Earth's surface. Experimental evidence also shows that exposure to UVB radiation can decrease algal productivity, and cause damage to various forms of aquatic larvae and other organisms. Biologically-effective levels of solar UV radiation penetrate water columns well, especially in the clear waters found in the Antarctic pack ice zone. To determine the relationship (if any) between increased biologically-weighted UV doses and damage to various Antarctic organisms, scientists need to know the magnitude of these increases, not only at the surface but throughout the ice and the water column.

This research initially produced surface maps of levels of cloudy-sky erythemal UV, derived from satellite data, for the East Antarctic marginal ice zone (split into four regions for ease of presentation) for the years 1996-2005. Case studies of the relationships between levels of cloudy-sky erythemal UV (at the surface of the sea ice and ocean) and ozone, sea ice concentration and the cloud modification factor are presented by way of various analyses for a selection of sub-areas within the four regions. These analyses show that the levels of erythemal UV in the sub-areas are strongly affected by levels of ozone and by sea ice concentration. The results also indicate that the Shackleton and Amery regions are more affected by lower levels of ozone associated with the Antarctic ozone hole than the Mertz and Dalton regions. Trend analyses for the nine-year study period indicated significant trends for erythemal UV, sea ice concentration and ozone for some of the selected sub-areas. The austral spring of 2001 stood out as a period of unusually high erythemal UV values.

To create maps of cloudy-sky erythemal UV radiation, the radiative transfer model UVSPEC was employed to develop a look-up table (LUT) of levels of erythemal UV radiation for various combinations of ozone, solar zenith angle and surface UV albedo. IDL software was then written to estimate a value of clear-sky erythemal UV at the Earth's surface, using the erythemal UV LUT, for each 5 x 5 km pixel of an Advanced Very High Resolution Radiometer (AVHRR) Polar Pathfinder image for each day that AVHRR irradiance and TOMS ozone data were available for the temporal coverage of the project. The main confounding issue in the determination of erythemal UV radiation at the Earth's surface is the cloud cover, as this can vary not just on a daily basis but also throughout a day. The amount of cloud in a pixel was taken into account by multiplying clear-sky erythemal UV by a cloud modification factor based on the classification of AVHRR images using an expert system.

A subsequent undertaking used the ASPeCt sea ice and snow thickness dataset to produce maps of erythemal UV values at predetermined depths within the sea ice and the water column.

Field work completed during the SIPEX voyage to the East Antarctic sea ice zone in 2007 allowed the estimation of UVB attenuation coefficients for ice and snow – these values were used, along with a known UVB attenuation coefficient for water, when determining sub-surface erythemal UV values.

Initially, the erythemal UV values were calculated at 5, 10, 15 and 20 m in the water column. To take into consideration the fact that phytoplankton do not necessarily remain at a specific depth, average erythemal UV values over the upper 5, 10, 15 and 20 m of the water column were also calculated. Erythemal UV values at the top of the sea ice (beneath the snow cover), mid-way through the ice, at the bottom of the ice and at a fixed depth of 20 cm within the ice were calculated specifically for sea ice algae research. The erythemal UV values at the bottom of the ice were used to further calculate erythemal UV in the water column at the re-established depths beneath the ice (taking into account the draft of the sea ice). The sea ice concentration was incorporated into the calculations to determine pixel-averaged values of erythemal UV at 5, 10, 15 and 20 m depth.

A final step was to use spectral biological weighting functions to develop a set of non-linear conversions between erythemal UV dose rate and more biologically-relevant dose rates. Including these aspects in the model allowed the erythemal UV values in the water column to be converted to a phytoplankton-specific dose rate, and the estimated erythemal UV values within a slab of sea ice to be converted to a sea-ice-algae-specific dose rate.

The logistical problems of undertaking *in situ* research in Antarctica require alternative methods such as satellite remote sensing and radiative transfer modelling. This project has used satellite data and a radiative transfer model (RTM) to create maps of erythemal UV values for the study area. Further research will be required to assess (either from *in situ* measurements of primary production or with the use of remote sensing of ocean colour) how significant the effects of increased levels of erythemal UV are on the primary production of the Southern Ocean.

Acknowledgements

The completion of this project would not have been possible but for the assistance, encouragement, support and 'whip-cracking' from/by many people. This has been one of the most challenging endeavours that I have taken on during my life, and at times, when I have faltered and almost been tempted to 'throw the towel in', someone has been there to give me a nudge in the right direction again. Now that I have completed the thesis, I feel deep gratitude to those who were there to encourage me to keep going, as I am now feeling a sense of great satisfaction for having completed it at the age of sixty. Another part of me is extremely pleased to be able to contribute to ongoing research in the area of ozone depletion and UVB radiation as all the data from my project will be incorporated into the Australian Antarctic Data Centre's database for use by other researchers in the field.

Sincere thanks go to my primary supervisor, Dr. Kelvin Michael for the many, many hours he spent devising new ways to manipulate data files, explaining unfamiliar concepts, advising me on ways to surmount the odd problem that arose, all the reading and editing of drafts, and generally getting me over the finish line. I am also indebted to him for his assistance in coding and training me in the intricacies of IDL. I truly appreciate his support, patience and refreshing sense of humour.

I am also grateful to my research supervisor, Dr. Rob Massom and co-supervisor, Dr. Jan Lieser for sharing their expertise and knowledge and dedicating so much time to reading and editing drafts. Through all this, they were also extremely supportive, helpful and kept me laughing. Thanks must also go to the Graduate Research Coordinator, Dr. Julia Jabour for being so supportive in times of need.

I will be forever thankful to Dr. Michael for the opportunity to undertake research in the East Antarctic sea ice zone, on the ARISE voyage in 2003 and the SIPEX voyage in 2007. It was a wonderful experience, not just because of the spectacular scenery and the great camaraderie that develops during voyages, but sharing in everyone else's research, networking with scientists from other countries, learning new skills and gaining knowledge were well worth the few moments of 'mal de mer' and slopped soup! Many thanks to all those who participated in these two voyages; scientists, crew and especially the technical support staff onboard the RSV *Aurora Australis* who overcame a technical problem for our team.

Back on campus, there are too many people who have helped and supported me throughout my candidature to name. I have developed some lovely friendships with other students who have started, completed and gone during my candidature but will remain part of the positive PhD experience. Janie and Rachael deserve a special mention because they became, and still remain, close friends of mine.

Staff members have always been willing to share their expertise to make the PhD journey easier and thus more pleasant. Ben Joseph is an outstanding example – he has the patience of Job and was never stumped when asked for a solution to an IT problem. Thank you Ben and all the IT personnel who make 'it' all happen without any of us having to lift a finger.

Finally, I would like to thank my husband, John for his unconditional love and support during this 'marathon'. Likewise, for my children, Rhett and Alice, and their respective partners, Jacqui and Chris – thank you for your love and support and I am looking forward to being a more 'accessible' mother and Nanny to Laila, Madeline, Jordan and Wesley.

Sincere thanks are extended to Dr. Ted Scambos (US NSIDC, University of Colorado) for his excellent help in procuring the AVHRR Polar Pathfinder data that are central to this thesis; also to Dr Tony Worby (Australian Antarctic Division and ACE CRC) for supplying the ASPeCt data; and to Dr. Richard McKenzie (National Institute of Water and Atmospheric Research, Lauder) for assistance in clarifying aspects of his published work.

Table of Contents:

List of Figures: xi
List of Tables: xviii
List of Acronyms and Abbreviations: xx
1. INTRODUCTION 1
2. ANTARCTICA 5
2.1 Southern Ocean 5
2.2 Sea ice and snow 6
2.3 Biological processes in Antarctica 9
2.3.1 Effects of increased UVB on organisms 11
2.3.1.1 Phytoplankton 14
2.3.1.2 Sea ice algae 17
2.3.1.3 Antarctic Krill 18
2.3.1.4 Other organisms 20
2.3.2 Biological Weighting Functions 23
2.3.2.1 BWFs – Historical background 23
2.3.2.2 Research – UVR, PAR and BWFs 24
2.3.3 Interactions between UVB radiation and other stressors 26
2.3.4 Consequences of decreased uptake of carbon 27
3. FACTORS AFFECTING LEVELS OF UVB 29
3.1 Ozone 29
3.1.1 Techniques and records of atmospheric ozone measurements 32
3.1.2 How ozone depletion happens 35
3.1.3 Other anthropogenically induced ozone depletion 37
3.1.4 Natural causes of variation in levels of ozone 38
3.1.4.1 Solar radiation 40
3.1.4.2 Volcanic eruptions 41
3.1.4.3 Inter-annual temperature and dynamical changes 42
3.1.4.4 Quasi-biennial oscillation (QBO) 43
3.1.4.5 Downflux of NO_x 43
3.1.4.6 Solar Proton Events 44
3.1.4.7 Other factors 45
3.1.5 Montreal Protocol 45
3.1.6 Development of the ozone hole 48
3.1.7 Recovery from ozone depletion 50
3.1.8 The effects of climate change 54
3.2 Parameters used in modelling ultraviolet radiation 56
3.2.1 Solar Zenith Angle 57
3.2.2 Earth-Sun Distance 57

3.2.3 Atmospheric Aerosols 57
3.2.4 Surface Albedo 60
3.2.5 Cloud Amount 62
3.2.5.1 The effect of cloud on incoming radiation 63
3.2.5.2 Cloud detection 64
3.2.5.3 Quantifying the effect of clouds on levels of UV radiation 65
3.2.5.4 Cloud Modification Factor 66
3.2.5.5 Problems associated with cloudiness in Antarctica 67
4. MODELLING OF RADIATIVE TRANSFER 69
4.1 Background 69
4.2 Examples of Radiative Transfer Models 72
4.2.1 Lubin *et al*. (1998) 72
4.2.2 Pubu and Li (2003) 72
4.2.3 Sabziparvar *et al.* (1999) 73
4.2.4 Herman *et al*. (1999) 73
4.2.5 Verdebout (2000) 73
4.2.6 SIDES algorithm (2003) 74
4.2.7 UVSPEC/libRadtran (1994) 74
4.3 Modelling of UV radiation over inhomogeneous surfaces 75
5. DATA 76
5.1 Satellite data – general 76
5.2 AVHRR irradiance data 77
5.3 Ozone data 80
5.3.1 Errors and accuracy of TOMS ozone data 82
5.4 Sea ice data 86
5.5 Surface UV Data 90
6. SIPEX VOYAGE 92
6.1 Penetration of UV through ice 92
6.2 Penetration of UV through snow 93
6.3 Site description and data acquisition (SIPEX) 93
6.4 Equipment 94
6.5 Data collection 96
6.6 Data analysis 101
6.7 Results 102
7. METHODS 107
7.1 Development of LUT of solar zenith angles 107
7.2 The Radiative Transfer Model (UVSPEC) 108
7.3 Development of LUT of values of erythemal UV 109
7.4 Steps in processing AVHRR PPF images 112

7.4.1 Ozone data for each pixel 113
7.4.2 Albedo of each pixel 113
7.4.3 Determining daily clear-sky erythemal UV at the water/ice surface 117
7.4.4 Choice of cloud algorithm 118
7.4.5 Estimating cloud-affected erythemal UV at the water/ice surface 121
7.5 UV mapping requirements for Antarctic Biologists 122
7.6 Developing 'maps' of monthly averages 124
8. RESULTS 127
8.1 Daily maps of surface cloud-affected erythemal UV 127
8.2 Validation using *in situ* data 129
8.2.1 Using station data 129
8.2.2 Using underway ship data 137
8.3 Maps of surface erythemal UV 139
8.3.1 Visual assessment of regional parameter maps 139
8.3.1.1 Amery and Shackleton 139
8.3.1.2 Dalton and Mertz 140
8.3.2 Case study sub-areas 144
8.3.2.1 Amery No. 1 145
8.3.2.2 Amery No. 3 145
8.3.2.3 Dalton No. 1 145
8.3.2.4 Dalton No. 4 145
8.3.2.5 Mertz No. 1 146
8.3.2.6 Mertz No. 2 146
8.3.2.7 Shackleton No. 4 146
8.3.3 Assessment of relationships between parameters 147
8.3.3.1 Amery and Shackleton 147
8.3.3.2 Dalton and Mertz 153
8.3.3.3 Comparison of erythemal UV values for sub-areas 154
8.3.4 Case studies – discussion 155
8.3.4.1 Assessment of plots of parameters 1996-2005 155
8.3.4.2 Amery No. 1 156
8.3.4.3 Amery No. 3 159
8.3.4.4 Dalton No. 1 161
8.3.4.5 Dalton No. 4 163
8.3.4.6 Mertz No. 1 163
8.3.4.7 Mertz No. 2 164
8.3.4.8 Shackleton No. 4 164
8.3.5 Seasonal analysis 166
8.3.6 Trend analysis 170
9. SUB-SURFACE MAPS 177
9.1 Estimating erythemal UV within sea ice and water column 178
9.1.1 Estimating erythemal UV in the water column 180

9.1.2 Estimating erythemal UV throughout sea ice/snow 183
9.1.3 Erythemal UV in the water column beneath sea ice/snow..... 190
9.2 Biological dose rates 193
9.2.1 Mathematical formulation of BWFs 194
9.2.2 Developing maps of biological dose rates 198
9.2.3 Temporal variation of biological dose rates 203
9.2.4 Summary of the results of mapping biological dose rates 209
10. CONCLUSION AND FUTURE RESEARCH 211
10.1 Conclusions..... 211
10.2 Future research..... 215
References:..... 220

List of Figures:

Figure 2.1: Forcing parameters that determine thickness distribution and physical characteristics of sea ice and snow cover (Figure 19 in Worby *et al.* 1998). 7

Figure 2.2: Schematic showing trophodynamic interactions in marine ecosystems and their effect on atmospheric gases that influence global climate (Figure 20.6, page 747 in Davidson 2006). 10

Figure 2.3: Map of Antarctica displaying relevant geographic features for this study. (The map was created using the m_map high resolution coastline in Matlab, which did not include the Antarctic ice shelves). 23

Figure 3.1: Ozone is present throughout the lower atmosphere (troposphere and stratosphere). Most ozone resides in the stratospheric 'ozone layer' above Earth's surface (between15 and 35 kms) (from http://www.esrl.noaa.gov/csd/assessments/ozone/2006/twentyquestions.html). ... 30

Figure 3.2: The area of the ozone hole (ozone levels are less than or equal to 220 DU) over the South Pole, 1999-2008. The ozone data used in this analysis is the combination of GOME (Global Ozone Monitoring Spectrometer) and SCIAMACHY (Scanning, Imaging and Absorption Spectrometer for Atmospheric Cartography). Credits: Royal Netherlands Meteorological Institute (KNMI) and European Space Agency (ESA) (2008). 32

Figure 3.3: Primary sources of chlorine entering the stratosphere in the early 1990s (NOAA Aeronomy Lab 2004). 35

Figure 3.4: Variation of ozone amount with altitude in the atmosphere and simplified cycle of reactions in which chlorine destroys ozone (NOAA 2005). 36

Figure 3.5: Percentage total ozone changes in the 65° S to 65° N latitude range for TOMS version 7 relative to the 1979 TOMS value (represented by stars). Also shown are percentage total ozone changes for the simulation which included chlorine and bromine increases, solar UV flux variations, SSA burden variations, SPEs and GCRs from the GSFC 2-D model, all relative to the 1979 simulation A value (see Jackman *et al*. (1996b) for details). 40

Figure 3.6: Ozone-destroying chemicals ('effective stratospheric chlorine') would have increased steadily ('no protocol' black line) if the Montreal Protocol and later agreements (coloured lines as marked) limiting CFCs and other chemicals had not been adopted (Welch 2010). Data for this figure compiled from the British Antarctic Survey, NASA, ESA, WDCRSA, Environment Canada, UNEP, NOAA, ESEPA and other sources as stated and credited. 2010 delineates between actual and modelled values of effective stratospheric chlorine 46

Figure 3.7: Stratospheric 'chlorine' from the world-wide use of major ozone depleting substances. Solid lines are data collected at Cape Grim, Tasmania; dashed lines are model calculations based on past and future emissions of ozone depleting substances (Montzka and Fraser 2003). Source: CSIRO Atmospheric Research, January 2005 (Beer *et al.* 2006). 48

Figure 3.8: Minimum air temperatures in the polar lower stratosphere (NOAA Aeronomy Lab 2004). 53

Figure 5.1: Box Flow Chart showing surface type from passive microwave data (Fowler *et al.* 2000). 79

Figure 5.2: Sample of TOMS ozone data from McPeters, *et al.* (1998). 81

Figure 5.3: Plot of percent difference in erythemal UV values for ozone values, X and (X + 10) DU. 85

Figure 5.4: Sea ice thickness data (metres) for (a) spring, (b) summer, (c) autumn and (d) winter (as extracted from the ASPeCt database (SCAR Antarctic Sea Ice Processes and Climate (ASPeCt) program 2008) 88

Figure 5.5: Sea ice thickness data (metres) for the average of spring, summer and autumn data (Figure 5.4) (SCAR Antarctic Sea Ice Processes and Climate (ASPeCt) program 2008). 89

Figure 6.1: a. Top of PUV-2500 instrument and b. PUV-2500 held on the left and PUV-2510 fixed in tripod. 95

Figure 6.2: Operation of the computer at an ice station. The operator sat at the table on which the deckbox and computer were placed. The table and equipment could be shielded with the blue insulated blanket to minimise the effect of extreme cold and wind-blown snow on the operation of the computer. 97

Figure 6.3: Researchers removing snow after 'with-snow measurements' completed. The radius of the snow-free circle had to be at least twice the thickness of the ice..... 97

Figure 6.4: Operation of the 'Z' frame – pulling down on the upper arm of the frame caused the lower arm to lift into a position horizontal to the under surface of the ice. 98

Figure 6.5: Feeding the 'Z' frame through the auger hole. 98

Figure 6.6: Taking measurements under snow-free area on right. A second suite of measurements were taken under the snow-free area behind the operators of the 'Z' frame. 99

Figure 6.7: This figure represents the radiation paths for each of the measurements (i.e. ice with snow, ice without snow and ice-free water. 100

Figure 6.8: Plot of snow thickness z_S (m) vs natural log of the ice/snow transmission ratio for 320 nm. 103

Figure 6.9: Plot of estimated values of snow attenuation coefficient Ks (m^{-1}) for the 6 UV channels with upper and lower 95% confidence intervals. 104

Figure 6.10: Plot of erythemally-weighted irradiance values (nm) (as produced by libRadtran) for combinations of SZA (x-axis) (20-85°) and TOC (y-axis) (50-550 DU)..... 104

Figure 6.11: Plot of ice thickness z_I (m) vs natural log of the ice transmission T_I for 320 nm.. 105

Figure 6.12: Plot of estimated values of ice attenuation coefficient K_I (m^{-1}), with upper and lower 95% confidence intervals. 106

Figure 7.1: A sample plot of SZA for time of day (e.g. 20th February) at 70º S. The red line crosses the plot at sunrise and sunset. 107

Figure 7.2: Plot of erythemal UV for SZA varied in 5 degree increments. 111

Figure 7.3: Plot of erythemal UV irradiance (in mW m^{-2}) *vs* ozone=0-500 DU (for SZA = 22º and surface reflectance = 100%). 113

Figure 7.4: Representation of the water/ice regime used for testing albedo smoothing kernels. 116

Figure 7.5: Clear-sky erythemal enhancement as a function of distance from the ice edge. UVSPEC (TOC= 350 DU, SZA=60º). 117

Figure 7.6: Plot of Earth-Sun Distance Factor *vs* day number of year. 118

Figure 7.7: Sample plots for day no. 313, 1998 for Amery region: 120

Figure 7.8: Sample plots of monthly averages of a. noon-time erythemal UV and b. daily erythemal UV dose for July 2001 to June 2002 for Amery region (all other similar plots for other years and other regions are included in Appendix A). 125

Figure 7.9: Sample plots of monthly averages of a. ozone, b. sea ice concentration, c. albedo and d. cloud modification factor for July 2001 to June 2002 for Amery

region (all other similar plots for other years and other regions are included in Appendix A). 126

Figure 8.1: Plot created by *create_maps.pro* for day no. 265, 2001 for Amery area. Includes a. surface mask (see Figure 8.2 for colour bar), b. cloud fraction (see Figure 8.3 for colour bar), c. clear-sky erythemal UV at noon (grey scale), d. cloudy-sky erythemal UV at noon (grey scale), e. ozone (grey scale), and f. PPF surface albedo (grey scale). 128

Figure 8.2: Colour bar for plot of surface mask. 128

Figure 8.3: Colour bar for plot of cloud fraction. 128

Figure 8.4: Modelled daily noon, cloud-affected erythemal UV (using CMF2) *vs* measured erythemal UV at AAD Station Davis (n = 1655). 130

Figure 8.5: Modelled, weekly average, noon-time, clear-sky erythemal UV *vs* measured erythemal UV at Davis Station. 131

Figure 8.6: Modelled, weekly average, noon-time, cloud-affected erythemal UV (using CMF2) vs measured erythemal UV at Davis Station. 132

Figure 8.7: Modelled, weekly average, noon-time, clear-sky erythemal UV *vs* measured erythemal UV at Casey Station. 133

Figure 8.8: Modelled, weekly average, noon-time, cloud-affected erythemal UV (using CMF2) *vs* measured erythemal UV for Casey Station. 134

Figure 8.9: Modelled, weekly average, noon-time, clear-sky erythemal UV *vs* measured erythemal UV for Mawson Station. 135

Figure 8.10: Modelled, weekly average, noon-time, cloud-affected erythemal UV (using CMF2) *vs* measured erythemal UV for Mawson Station. 135

Figure 8.11: Monthly plots of ozone for Amery region, using colour bar for ozone (0-425DU). 141

Figure 8.12: Monthly plots of ozone for Shackleton region using colour bar for ozone (0-425 DU). 142

Figure 8.13: Monthly plots of sea ice concentration for Amery region using colour bar for sea ice concentration (0-100%). 143

Figure 8.14: Monthly plots of noon-time erythemal UV for Shackleton region using colour bar for noon-time erythemal UV (0-300 mW m^{-2}). 144

Figure 8.15: Positions (marked as) of the selected sub-areas in Amery region (using December sea ice concentration as a background). Dimensions of the Amery region are 341 x 283 pixels. 145

Figure 8.16: Positions of the selected sub-areas in Dalton region (using December sea ice concentration as a background). Dimensions of the Dalton region are 205 x 216 pixels. 146

Figure 8.17: Positions of the selected sub-areas in Mertz region (using December sea ice concentration as a background). Dimensions of the Mertz region are 299 x 227 pixels. 146

Figure 8.18: Position of the selected sub-area in Shackleton region (using December sea ice concentration as a background). Dimensions of the Shackleton region are 246 x 268 pixels. 147

Figure 8.19: Monthly plots of TOC for the years of the project for Amery No. 1. 149

Figure 8.20: Monthly plots of TOC for the years of the project for Shackleton No. 4. 150

Figure 8.21: Monthly plots of sea ice concentration for the years of the project for Amery No. 3. 151

Figure 8.22: Monthly plots of UVB for the years of the project for Shackleton No. 4. 151

Figure 8.23: Monthly plots of UVB for the years of the project for Shackleton No. 4. 152

Figure 8.24: Plots of CMF2 for Amery no. 1 (Left panel – all nine years, Right panel – year average plus error bars – 2 s.d.). 157

Figure 8.25: Plots of TOC for Amery no. 1 (Left panel – all nine years, Right panel – 9-year average plus error bars – 2 s.d.). 158

Figure 8.26: Plots of sea ice concentration for Amery no. 1 (Left panel – all nine years, Right panel – 9-year average plus error bars – 2 s.d.). 158

Figure 8.27: Plots of noon-time erythemal UV for Amery no. 1 (Left panel – all nine years, Right panel – 9-year average plus error bars – 2 s.d.)..... 159

Figure 8.28: Plots of TOC for Amery no. 3 (Left panel – all nine years, Right panel – 9-year average plus error bars – 2 s.d.). 160

Figure 8.29: Plots of sea ice concentration for Amery no. 3 (Left panel – all nine years, Right panel – 9-year average plus error bars – 2 s.d.). 160

Figure 8.30: Plots of noon-time erythemal UV for Amery no. 3 (Left panel – all nine years, Right panel – 9-year average plus error bars – 2 s.d.)..... 161

Figure 8.31: Plots of TOC for Dalton no. 1 (Left panel – all nine years, Right panel – 9-year average plus error bars – 2 s.d.). 162

Figure 8.32: Plots of sea ice concentration for Dalton no. 1 (Left panel – all nine years, Right panel – 9-year average plus error bars – 2 s.d.). 162

Figure 8.33: Plots of noon-time erythemal UV for Dalton no. 1 (Left panel – all nine years, Right panel – 9-year average plus error bars – 2 s.d.)..... 163

Figure 8.34: Plots of CMF2 for Shackleton no. 4 (Left panel – all nine years, Right panel – 9-year average plus error bars – 2 s.d.). 165

Figure 8.35: Plots of TOC for Shackleton no. 4 (Left panel – all nine years, Right panel – 9-year average plus error bars – 2 s.d.). 165

Figure 8.36: Plots of sea ice concentration for Shackleton no. 4 (Left panel – all nine years, Right panel – 9-year average plus error bars – 2 s.d.)..... 166

Figure 8.37: Plots of noon-time erythemal UV for Shackleton no. 4 (Left panel – all nine years, Right panel – 9-year average plus error bars – 2 s.d.)..... 166

Figure 8.38: Seasonal time series for parameters for Amery no. 1 a. noon-time erythemal UV, b. ozone, c. sea ice concentration, d. CMF2. 167

Figure 8.39: Seasonal time series for parameters for Shackleton no. 4 (a. noon erythemal UV, b. ozone, c. sea ice concentration, d. CMF2). 168

Figure 8.40: Seasonal time series for parameters for Dalton no. 1 (a. noon erythemal UV, b. ozone, c. sea ice concentration, d. CMF2). 169

Figure 8.41: Trend analysis for TOC for Amery no. 1. 171

Figure 8.42: Trend analysis for sea ice concentration for Amery no. 1. 171

Figure 8.43: Trend analysis for noon-time erythemal UV for Amery no. 1. 172

Figure 8.44: EP/TOMS corrected total ozone (Dobson Units) 176

Figure 9.1: Colour table used for plots of dose rates (ERY, DNA, BEH, PHO) (mW m^{-2})..... 180

Figure 9.2: Sample plot of surface erythemal UV (mW m^{-2}) for the Amery region for Nov 2001 (157.094, 269.479) [300]. 182

Figure 9.3: Sample plot of surface erythemal UV (mW m^{-2}) for the Amery region for Nov 2002 (89.831, 152.552) [300]. 182

Figure 9.4: Plots of erythemal UV (mW m^{-2}) in water column for Amery region, Nov 2001 at a. 5 m (31.547, 54.116), b. 10 m (7.039, 12.075), c. 15 m (1.571, 2.694) and d. 20 m (0.350, 0.601) [300]. 182

Figure 9.5: Plots of erythemal UV (mW m-2) in water column for Amery region, Nov 2002 at a. 5 m (18.040, 30.635), b. 10 m (4.025, 6.836), c.15 m (0.898, 1.525) and d. 20 m (0.200, 0.340) [300]. 182

Figure 9.6: Erythemal UV (mW m^{-2}) for Amery region Nov 2001 averaged over a. upper 5 m (73.225, 125.610), b. upper 10 m (44.782, 76.819), c. upper 15 m (31.070, 53.297) and d. upper 20 m (23.506, 40.321) of the water column [300]. 183

Figure 9.7: Erythemal UV (mW m^{-2}) for Amery region Nov 2002 averaged over a. upper 5 m (41.872, 71.108), b. upper 10 m (25.608, 43.487), c. upper 15 m (17.767, 30.172) and d. upper 20 m (13.441, 22.826) of the water column [300]. 183

Figure 9.8: Plots of sea ice thickness for: a. Amery region, b. Shackleton region, c. Dalton region and d. Mertz region derived from the ASPeCt sea ice thickness data (Worby 2008). 186

Figure 9.9: Plots of snow thickness for: a. Amery region, b. Shackleton region c. Dalton region and d. Mertz region derived from the ASPeCt sea ice thickness data (Worby 2008). 187

Figure 9.10: Sample plot of erythemal UV (mW m^{-2}) for Amery region Nov 2001 a. at top of ice under snow of z_S thickness (5.76, 73.69); b. under snow and half way through ice of z_I thickness (3.26, 73.69); c. under snow and at bottom of ice (1.68, 73.69); and d. under snow and at fixed depth of ice, i.e. 20 cm (4.00, 73.69) [300]. 188

Figure 9.11: Sample plot of erythemal UV (mW m^{-2}) for Amery region Nov 2002 a. at top of ice under snow of z_S thickness (2.93, 43.56); b. under snow and half way through ice of thickness z_i (1.65, 35.80); c. under snow and at bottom of ice (0.87, 35.80); and d. under snow and at fixed depth of ice, i.e. 20 cm (2.04, 35.80) [300]. 188

Figure 9.12: A sample plot of surface erythemal UV (mW m^{-2}) for Shackleton region Nov 2000 (104.22, 163.69) [300]. 188

Figure 9.13: A sample plot of erythemal UV (mW m^{-2}) for Shackleton region Nov 2000 a. at top of ice under snow of z_S thickness (0.40, 39.78); b. under snow and half way through ice of thickness z_i (0.18, 33.52); c. under snow and at bottom of ice (0.08, 28.25) and d. under snow and at fixed depth of ice, i.e. 20 cm (0.28, 28.25) [300]. 188

Figure 9.14: Sample plot of surface erythemal UV (mW m^{-2}) for the Mertz region Nov 2000 (82.318, 129.257) [300]. 189

Figure 9.15: Sample plot of erythemal UV (mW m^{-2}) for the Mertz region Nov 2000 a. at top of ice under snow of thickness z_S (1.577e-6, 39.213); b. under snow and half way through ice of thickness z_i (1.258e-09, 39.177); c. under snow and at bottom of ice (1.366e-12, 39.141); and d. under snow and at fixed depth of ice, i.e. 20 cm (8.045e-07, 39.141) [300]. 189

Figure 9.16: Sample plot of erythemal UV (mW m^{-2}) for Shackleton region Nov 2000 in the water column beneath snow and ice at: a. Z1 (0.023, 6.632), b. at Z2 (0.005, 1.480), c. at Z3 (0.001, 0.330) and d. at Z4 (0.0003, 0.074) [300] (where depths (Zx) are detailed in Table 9.4). 191

Figure 9.17: Sample plot of pixel-averaged erythemal UV (mW m^{-2}) for Shackleton region Nov 2000 beneath snow and ice at a. Z1 (0.025, 26.737), b. Z2 (0.006, 5.966), c. Z3 (0.001, 1.331) and d. Z4 (0.0003, 0.297) [300] (where depth Zx are detailed in Table 9.4). 192

Figure 9.18: The five modified BWF, erythemal (blue), DNA (red), Behrenfeld (black) and photoinhibition (pink) used for the analysis of relations between erythemal and other doses. All BWF are normalised to 1.0 at 300 nm and are unit-less (Figure 3.1 in Ali 2001). 195

Figure 9.19: Plots of the relationship for coefficients in equations 9.5, 9.6 and 9.7 *vs* ozone column (scaled by $1000)_{Y}$. 197

Figure 9.20: Plot of average ozone for November 2000 in the Shackleton region and colour bar showing the range of ozone values in DU (0.0-425.0). 199

Figure 9.21: Sample plot of surface erythemal UV (mW m^{-2}) for Shackleton region for Nov 2000 (104.219, 163.687) [300]. 200

Figure 9.22: Sample plot of surface DNA dose rate (mW m^{-2}) for Shackleton region for Nov 2000 (48.724, 116.785) [400]. 200

Figure 9.23: Sample plot of surface BEH dose rate (mW m^{-2}) for Shackleton region for Nov 2000 (288.881, 431.824) [600]. 200

Figure 9.24: Sample plot of surface PHO dose rate (mW m^{-2}) for Shackleton region for Nov 2000 (70.075, 93.585) [100]. 200

Figure 9.25: Sample plot of erythemal UV (mW m^{-2}) for Shackleton region for Nov 2000 at a. top of ice beneath snow of thickness Z_s (0.404, 39.777); b. under snow and half way through ice of thickness Z_i (0.182, 33.522); c. under snow and at bottom of ice (0.082, 28.251); and d. under snow and at fixed depth of ice, i.e. 20 cm (0.281, 28.251) [300]. 201

Figure 9.26: Sample plot of DNA dose rate (mW m^{-2}) for Shackleton region for Nov 2000 at a. top of ice beneath snow of thickness Z_s (0.032, 9.642); b. under snow and half way through ice of thickness Z_i (0.014, 7.330); c. under snow and at bottom of ice (0.006, 5.613); and d. under snow and at fixed depth of ice, i.e. 20 cm (0.022, 5.613) [400]. 201

Figure 9.27: Sample plot of BEH dose rate (mW m^{-2}) for Shackleton region for Nov 2000 a. at top of ice under snow of thickness Z_s (1.332, 108.930); b. under snow and half way through ice of thickness Z_i (0.616, 92.483); c. under snow and at bottom of ice (0.285, 78.519); and d. under snow and at fixed depth of ice, i.e. 20 cm (0.938, 78.519) [600]. 201

Figure 9.28: Sample plot of PHO dose rate (mW m^{-2}) for Shackleton region for Nov 2000 a. at top of ice under snow of thickness Z_s (1.403, 33.314); b. under snow and half way through ice of thickness Z_i (0.801, 29.585); c. under snow and at bottom of ice (0.457, 27.235); and d. under snow and at fixed depth of ice, i.e. 20 cm (1.087, 27.235) [100]. 201

Figure 9.29: Sample plot of pixel-averaged erythemal UV (mW m^{-2}) for Shackleton region for Nov 2000 beneath snow and ice at a. Z1 (0.025, 26.737); b. at Z2 (0.006, 5.966); c. at Z3 (0.001, 1.331); and d. at Z4 (0.0003, 0.297) (where Z1, Z2, Z3 and Z4 are detailed in Table 9.4) [300]. 202

Figure 9.30: Sample plot of pixel-averaged DNA dose rate (mW m^{-2}) for Shackleton region for Nov 2000 beneath snow and ice at a. Z1 (0.002, 4.801); b. at Z2 (0.0004, 0.596); c. at Z3 (9.566e-05, 0.109); and d. at Z4 (2.134e-05, 0.023) (where Z1, Z2, Z3 and Z4 are detailed in Table 9.4) [400]. 202

Figure 9.31: Sample plot of pixel-averaged BEH dose rate (mW m^{-2}) for Shackleton region for Nov 2000 beneath snow and ice at a. Z1 (0.092, 76.096); b. at Z2 (0.022, 17.888); c. at Z3 (0.005, 4.205); and d. at Z4 (0.001, 0.989) (where Z1, Z2, Z3 and Z4 are detailed in Table 9.4) [600]. 202

Figure 9.32: Sample plot of pixel-averaged PHO dose rate (mW m^{-2}) for Shackleton region for Nov 2000 beneath snow and ice at a. Z1 (0.202, 27.054); b. at Z2 (0.070,

9.305); c. at Z3 (0.025, 3.246); and d. at Z4 (0.009, 1.133) (where Z1, Z2, Z3 and Z4 are detailed in Table 9.4) [100]. 202

Figure 9.33: For sub-area no. 1 in Amery region for 2001 a. sample plot of erythemal UV and b. sample plot of erythemal UV using logarithmic scale..... 204

Figure 9.34: For sub-area no. 1 in Amery regions for 2001 a. sample plot of DNA dose rate and b. sample plot of DNA dose rate using logarithmic scale..... 205

Figure 9.35: For sub-area no. 1 in Mertz regions for 2000 a. sample plot of BEH dose rate and b. sample plot of BEH dose rate using logarithmic scale. 206

Figure 9.36: Plots of TOC for Mertz no. 1(Left panel – all nine years, Right panel – 9-year average plus error bars – 2 s.d.). 207

Figure 9.37: Plots of sea ice concentration for Mertz no. 1 (Left panel – all nine years, Right panel – 9-year average plus error bars – 2 s.d.). 207

Figure 9.38: For sub-area no. 1 in Dalton region for 1998 a. sample plot of PHO dose rate and b. sample plot of PHO dose rate using logarithmic scale. 208

Figure 9.39: Plots of TOC for Dalton no. 1 (Left panel – all nine years, Right panel – 9-year average plus error bars – 2 s.d.). 209

Figure 9.40: Plots of sea ice concentration for Dalton no. 1 (Left panel – all nine years, Right panel – 9-year average plus error bars – 2 s.d.). 209

List of Tables:

Table 3.1: Estimated source apportionment of atmospheric particulates (10^6 metric tons/year) (SMIC 1971). 58

Table 5.1: Overview table of AVHRR Polar Pathfinder (PPF) data (Fowler *et al.* 2000). 78

Table 5.2: Table of surface mask type (SMSK) cell contents. 80

Table 5.3: Table of cloud mask (CMSK) bit number values. 80

Table 5.4: Estimated errors in retrieved TOMS ozone from McPeters *et al*. (1998). 83

Table 5.5: Difference and percentage difference of erythemal UV values (mW m^{-2}) for ozone values, X and (X + 10) DU. 85

Table 6.1: Specifications of the radiometers. 95

Table 6.2: Snow and ice thickness (metres) for 7 of the 14 ice stations occupied by the SIPEX voyage. 102

Table 7.1: Example of UVSPEC input file. 109

Table 7.2: Varying parameters for creation of erythemal UV LUT. 110

Table 7.3: Difference and percent difference between erythemal UV values generated directly by UVSPEC and interpolated *by interp_uvb.pro.* 112

Table 7.4: Colour codes for plots in Figure 7.7 (CASPR is Cloud and Surface Parameter Retrieval system as described in Section 5.2). 121

Table 8.1: Results of analyses (mean bias error, mean square difference and root mean square difference) of modelled, daily, erythemal UV *vs* measurements made at Davis Station. 131

Table 8.2: Results of analyses (mean bias error, mean square difference and root mean square difference) of modelled, weekly average, noon-time erythemal UV *vs* measurements made at Davis Station. 133

Table 8.3: Results of analyses (mean bias error, mean square difference and root mean square difference) of modelled, weekly average, noon-time erythemal UV *vs* measurements made at Casey Station. 134

Table 8.4: Results of analyses (mean bias error, mean square difference and root mean square difference) of modelled, weekly average, noon-time erythemal UV *vs* measurements made at Mawson Station. 136

Table 8.5: Statistics for analyses (mean bias error, mean square difference and root mean square difference) of daily, noon-time, modelled erythemal UV *vs* measured underway data at noon. 137

Table 8.6: Statistics (mean bias error, mean square difference and root mean square difference) for comparison of sample daily, modelled, maximum erythemal UV *vs* measured, maximum, underway data on Voyage 6, 2000/01. 138

Table 8.7: Statistics (mean bias error, mean square difference and root mean square difference) for comparison of daily, modelled, maximum erythemal UV (extracted for position of the ship when maximal erythemal UV recorded) *vs* measured, maximum, underway data. 138

Table 8.8: Table of outliers (i.e. values that were outside the 2 standard deviation range) for parameters for sub-areas in Amery and Shackleton regions. 148

Table 8.9: Outliers (i.e. values that are more than 2 standard deviations greater or less than the mean) for parameters and sub-areas in Dalton and Mertz regions. 153

Table 8.10: Minimum and maximum erythemal UV values for all sub-areas. 154

Table 8.11: Statistics for lines of best fit for each of parameters, sea ice concentration, ozone and noon-time UVB for each of selected 7 sub-areas. 175

Table 9.1: Calculations of attenuation at depths of 5, 10, 15 and 20 metres in water column and averages of attenuation over upper 5, 10, 15 and 20 metres of water column (using attenuation coefficient of water, K_W = 0.3 m^{-1})..... 185

Table 9.2: Calculations of erythemal UV, (ERY_) where S=surface, TI=top of ice, MI=middle of ice, BI=bottom of ice, ID=fixed ice depth) using attenuation coefficient of snow, K_s = 11.3 m^{-1} and of ice K_i = 2.0 m^{-1}. The software can be adjusted to change the 20 cm depth to any other value. 185

Table 9.3: Snow and ice thickness statistics extracted from the interpolated ASPeCt data. . 190

Table 9.4: Calculations of erythemal UV, at 5, 10, 15 and 20 m in water column under snow/ice (using coefficient K_W = 0.3 m^{-1}, and value of ERY_BI as calculated in Table 9.2). 190

Table 9.5: Calculations of pixel averaged erythemal UV at Z1, Z2, Z3 and Z4 in water column weighted by sea ice concentration (si) (using values of erythemal UV throughout water column ERY_S * AW1 etc. (as per calculations in Table 9.1) and ERY_Z1 etc. as calculated in Table 9.4). 191

Table 9.6: Equations and coefficients relating biological dose rates to ozone. DNA denotes the Setlow dose rate, BEH is the Behrenfeld dose rate, PHO is the photoinhibition dose rate (as referenced in this section), and (_S) signifies the specified biological dose rate at the surface. 198

Table 9.7: Colour code for time series plots in following Figures 9.33-9.35 and Figure 9.38. 203

Table 9.8: Normalisation value for plot b. in the following Figures 9.33-9.35 and Figure 9.38. 203

List of Acronyms and Abbreviations:

AAD	Australian Antarctic Division
AADC	Australian Antarctic Data Centre
ACE CRC	Australian Climate and Ecosystems Cooperative Research Centre
ADEOS	ADvanced Earth Observing Satellite
AFGL	Air Force Geophysics Laboratory
AMSR-E	Advanced Microwave Scanning Radiometer-EOS
ARPANSA	Australian Radiation Protection and Nuclear Safety Agency
ASPeCt	Antarctic Sea Ice Processes and Climate
AVHRR	Advanced Very High Resolution Radiometer
BEH	Behrenfeld dose rate
BWF	Biological Weighting Function
CASPR	Cloud and Surface Parameter Retrieval
CBH	Cloud Base Height
CDOM	Chromophoric Dissolved Organic Matter
CFCs	chlorofluorocarbons
chl *a*	Chlorophyll *a*
CIE	Commission Internationale de l'Éclairage
CZCS	Coastal Zone Color Scanner
DAAC	Distributed Active Archive Centre
DISORT	Discrete Ordinate Radiative Transfer
DMS	dimethyl sulphide
DMSP	dimethylsulfoniopropionate
DNA	Deoxyribonucleic Acid, also the Setlow dose rate
DOAS	Differential Optical Absorption Spectroscopy
DOC	Dissolved Organic Carbon
DU	Dobson Unit – unit of measurement of atmospheric ozone
EASE-grid	Equal Area Scalable Earth-Grid
EESC	Effective Equivalent Stratospheric Chlorine
EM	Electro Magnetic
EMR	Electro Magnetic Radiation
ENVISAT	ENVIronmental SATellite
EPP	Energetic Particle Precipitation
EP-TOMS	TOMS on Earth Probe satellite
ERBE	Earth Radiation Budget Experiment
ERY	Erythemal dose rate
EUMETSAT	The European Organisation for the exploitation of Meteorological Satelllites

FTP	File Transfer Protocol
FURM	Full Retrieval Method
GCR	Galactic Cosmic Rays
GISMO	Graphical Interface for Subsetting, Mapping, and Ordering
GOME	Global Ozone Monitoring Experiment
GOOS	Global Ozone Observing System
GSFC	Goddard Space Flight Center
HO_x	A collective term for hydrogen oxides, specifically H, OH and HO_2
HSCT	High Speed Civil Transports
HSP	Heat Shock Proteins
ICESat	Ice, Cloud and land Elevation Satellite
IPCC	Intergovernmental Panel on Climate Change
IR	Infra Red
ISCCP	The International Satellite Cloud Climatology Project
KNMI	Royal Dutch Meteorological Institute
libRadtran	library for Radiative Transfer calculations
LSCO	Lower Stratospheric Column Ozone
LUT	Look-Up Table
MAA	Microsporine-like Amino Acid
METEOSAT	Geostationary meteorological satellites of EUMETSAT
MIPAS	Michelson Interferometer for Passive Atmospheric Sounding
MIZ	Marginal Ice Zone
MLD	Mixed Layer Depth
NASA	National Aeronautics and Space Administration
NCAR	National Center for Atmospheric Research
NCEP	National Center for Environmental Prediction
NDSC	Network for the Detection of Stratospheric Change
NOAA	National Oceanic and Atmospheric Administration
NO_x	A collective term for nitrogen oxides, specifically NO and NO_2
NSIDC	National Snow and Ice Data Center
OMI	Ozone Monitoring Instrument on board the NASA EOS Aura spacecraft
PAR	Photosynthetically Active Radiation
PHO	Photoinhibition dose rate
PPF	Polar Pathfinder
PSC	Polar Stratospheric Cloud
QBO	Quasi-Biennial Oscillation
RAF	Radiation Amplification Factor
REP	Relativistic Electron Precipitations

RTM	Radiative Transfer Model
SAGE	Stratospheric Aerosol and Gas Experiment
SAM	Southern Annular Mode
SBUV	Solar Backscatter UltraViolet Instrument
SBUV/2	Solar Backscatter Ultraviolet Version 2
SCAR	Scientific Committee on Antarctic Research
SCIAMACHY	Scanning, Imaging and Absorption Spectrometer for Atmospheric Cartography
SeaWiFS	Sea-viewing Wide Field of View Sensor
SED	Standard Erythemal Dose
SH	Southern Hemisphere
SIDES	Surface Irradiance DErived from a range of Satellite-based sensors
SIPEX	Sea Ice Physics and Ecosystem eXperiment
SIZ	Sea Ice Zone
SMMR	Scanning Multichannel Microwave Radiometer
SOE	State of the Environment
SPE	Solar Proton Event
SSM/I	Special Sensor Microwave Imager
SST	Sea Surface Temperature
SZA	Solar Zenith Angle
TIROS	Television Infrared Observation Satellite
TOA	Top of the Atmosphere
TOC	Total Ozone Column
TOMS	Total Ozone Mapping Spectrometer
TOVS	TIROS Operational Vertical Sounder
UML	Upper Mixed Layer
UNEP	United Nations Environmental Programme
USCO	Upper Stratospheric Column Ozone
UTC	Universal Coordinated Time
UV	Ultraviolet
UVA radiation/(UVAR)	Ultraviolet A radiation
UVB radiation/(UVBR)	Ultraviolet B radiation
UVC radiation/(UVCR)	Ultraviolet C radiation
UVER	Ultraviolet Erythemal Radiation
UVI	Ultraviolet Index
UVR	Ultraviolet Radiation
WMO	World Meteorological Organisation
WOUDC	World Ozone and Ultraviolet Data Centre

1. INTRODUCTION

The significance of ozone depletion over the middle, high and polar latitudes of both hemispheres is well established (Harris *et al.* 1997; World Meteorological Organization (WMO) 1999). Ozone absorbs ultraviolet B radiation, (UVB radiation, 280-325 nm), therefore UV irradiance at the Earth's surface is intimately related to stratospheric ozone – if all other factors remain the same, decreases in ozone concentrations provoke an increase in UVB radiation in the wavelength range 280-325 nm (Díaz *et al.* 2003). This inverse relationship has been proven and is well documented by many authors including Kerr and McElroy (1993), Zerefos *et al*. (1995), WMO (1999), McKenzie *et al*. (1999) and Zerefos *et al*. (2000). The UVB band represents less than 1.0% of the total energy reaching the surface of the Earth but is responsible for almost half of the photochemical effects in the aquatic and marine environments (Vincent and Roy 1993). This is of particular concern, as biologically effective levels of solar UV radiation penetrate water columns well, especially in the relatively clear waters found in the Antarctic pack ice zone (Gieskes and Kraay 1990; Karentz and Lutze 1990; Hargreaves 2003), where 'clear waters' are those with low concentrations of chromosphoric dissolved organic matter (CDOM) (Tedetti and Sempéré 2006).

The discovery of the springtime Antarctic ozone hole in the early 1980s (Farman *et al.* 1985) promoted an increased level of scientific research into the effects of enhanced levels of solar ultraviolet radiation on marine life in the Southern Ocean. The relationship between UV irradiance at the Earth's surface and ozone depletion is of critical interest in the Antarctic marginal ice zone (MIZ), where ozone depletion coincides with spring-time algal blooms (Marchant *et al.* 1991; Davidson *et al.* 1994; Davidson and Marchant 1994; Arrigo *et al.* 2008a). The marginal ice zone (MIZ) is described by Wadhams (1986) as "that part of the ice cover which is close enough to the open ocean boundary to be affected by its presence" and is generally applied to that region of the pack which is significantly affected by ocean swell. In the Antarctic this region may extend hundreds of kilometres from the ice edge, and in some regions right to the coast. The MIZ is an area of enhanced ice drift, deformation and divergence. It should be noted that the highest biologically-weighted UV doses under the Antarctic ozone hole are typically not observed in October when maximum ozone depletion occurs, but in November and early December when solar elevations are higher and low ozone values are still possible (WMO 2003). The significance of this coincidental occurrence is highlighted by experimental evidence showing that exposure to UVB radiation decreases algal productivity and causes damage to various forms of aquatic larvae and other organisms (Smith *et al.* 1992; Helbling *et al.* 1994; Vernet *et al.* 1994; Davidson 1998; Davidson and van der Heijden 2000; Davidson 2006).

Damage to DNA, proteins and lipids may result in a variety of lethal and sub-lethal effects. These effects have been reported in many organisms including viruses and bacteria (Buma *et al.* 2001a), phytoplankton and algae (Häder *et al*. 2003), amphibians and fish (Blaustein *et al.* 1998;

Hessen 2003), crops and forests (Caldwell *et al*. 1998), crustaceans (Hessen 2003) and humans (van der Leun and de Gruijl 2002). The effects of enhanced UVB radiation on organisms in aquatic habitats are of particular concern (Häder *et al.* 1995; Bancroft *et al.* 2007).

For some key organisms at the base of the Antarctic marine food chain, (e.g. juvenile Antarctic krill, *Euphausia superba*), the presence of sea ice algae is critical for survival (Nicol 2006). The sea ice supports the only significant primary production for up to nine months of the year as deep mixing, heavy ice cover and low light levels prevent the development of significant phytoplankton biomass in the underlying water column (McMinn *et al*. 2007). A decline in algal biomass and "health" caused by enhanced UVB levels could have a flow-on effect upon the krill population and subsequent higher trophic levels (i.e. predators). Resultant changes in food web structure and function may also influence biogeochemical cycles (Boyd 2002; Davidson and Belbin 2002; Day and Neale 2002), which are the complex interactions of biological, chemical and physical processes that determine the flux of material and energy within the environment (Whitehead *et al.* 2000). Global biogeochemical cycles involve the mechanisms that serve to transport and transform material within and among the terrestrial, atmospheric and oceanic pools. The effects of increased UVB radiation on one pool may provoke perturbations in the other pools (Zepp *et al.* 1995).

In situ measurements can relate phytoplankton primary production to the levels of ozone at the time the measurements were taken. However, the logistical problems of undertaking *in situ* research in Antarctica require an alternative method (such as radiative transfer modelling) of determining the relationship between ozone levels, levels of UVB radiation and primary production.

Although ozone is one of the major factors in determining surface irradiances in the UVB range, the UV reaching the ground depends on many factors. These include Earth-Sun distance, atmospheric gases and aerosols, solar zenith angle (SZA), clouds, altitude and surface albedo (Díaz *et al.* 2003) and any changes in any or all of these other factors may reduce, cancel or even reverse the expected UVB amplification caused by the ozone decline (Zerefos *et al.* 2000). Snow always occurs on ice older than a few days (R.A. Massom, pers. comm., 2010). The sea ice concentration and the probability of snow cover on the ice are included in the modelling of the levels of erythemal UV irradiance not only because of the varying albedos (McKenzie *et al.* 2003) but also because of the attenuation of UV irradiance by these media (Belzile *et al.* 2001). The main confounding issue in the determination of erythemal UV values at the Earth's surface is the cloud cover as cloud amount and type can vary not just on a daily basis but also throughout a day.

There have been many research projects that have resulted in estimates of levels of UV irradiance at the Earth's surface (see details in Chapter 4). Some of the previous attempts to determine levels of UV irradiance in Antarctica have tended to concentrate on small regions and for relatively short periods of time (Lubin *et al.* 1989b; Lubin and Frederick 1991; Lubin *et al.*

1994; Nunez *et al.* 1997; Frederick *et al.* 1998; Bernhard *et al.* 2006). Radiative transfer models have also generally been complicated and resource hungry. The primary objective of the work described in this thesis is to address the ozone/UVB relationship and develop maps of surface levels of erythemal UV for the East Antarctic sea ice zone. This differs from previous attempts to map levels of erythemal UV in that a more efficient method has been developed to derive estimates of erythemal UV and the mapping has been done for a larger region and a longer time frame. The second objective of the work is to produce maps of levels of erythemal UV at predetermined depths within the sea ice and water column, taking into account the attenuation caused by the snow, ice and water.

The third objective is to use spectral biological weighting functions to develop a set of non-linear conversions between the erythemal dose rates and more biologically relevant dose rates. Including these aspects in the modelling would allow the UV irradiance in the water column to be expressed in terms of a "phytoplankton-specific dose", and the estimated UV irradiance within a slab of sea ice to be referred to as a "sea-ice-algae-specific dose".

Chapter 2 describes the elements of the Antarctic oceanic environment, i.e. the ocean, sea ice and snow, and summarises the relevant biological processes. Chapter 3 explains the factors which affect levels of UVB radiation, with particular emphasis given to ozone and ozone depletion. Chapter 4 describes the modelling of UV radiation, providing examples of previous radiative transfer models. Chapter 5 itemises the satellite-derived and *in situ* data sets used in the estimation of the levels of erythemal UV, plus the data sets used to validate the modelled values. Chapter 6 describes the research conducted in the sea ice environment during the SIPEX voyage of September-October 2007 to East Antarctica to determine the attenuation coefficients of ice and snow. Chapter 7 describes the steps taken to develop the maps of surface erythemal UV for each of four regions within the East Antarctic sea ice zone. The decision to split the East Antarctic sea ice zone into Amery, Shackleton, Dalton and Mertz regions was based on the desire to highlight and examine regional variability and to facilitate easier data management and presentation of results. Chapter 8 describes validation of the resultant estimates of surface erythemal UV using *in situ* data collected at the Australian Antarctic research stations (Casey, Davis and Mawson) (see Figure 2.3) and onboard the RSV *Aurora Australis* on voyages to and from Antarctica. This chapter also assesses the relationships between the parameter values and resultant levels of erythemal UV for selected sub-areas within the four regions and performs trend analyses for the various parameters for the temporal coverage of the project. Chapter 9 describes the development of maps on a pixel basis of levels of erythemal UV at specified depths in the water column and averages of erythemal UV over the same depths. Maps of erythemal UV at the top of the ice (under snow), within-ice, under ice, and under ice and water, plus pixel-averaged estimates of erythemal UV are created. Biological weighting functions (for DNA by Setlow (1974), for photoinhibition by Behrenfeld (1993) and for photoinhibition by Jones and Kok (1966)) are applied to all of the

surface and sub-surface erythemal UV values to produce maps of the biologically effective dose rates. Chapter 10 includes the conclusions made as a result of the research and suggestions for possible future research.

2. ANTARCTICA

This thesis is concerned with ozone depletion and the consequential increased levels of erythemal UV that may have deleterious effects on organisms living within the open ocean and sea ice around Antarctica. This chapter gives some background information on the habitats of these organisms, and research that has shown effects of increased UVB on them.

2.1 Southern Ocean

The Southern Ocean is the largest marine ecosystem on Earth, covering an area of approximately 36 million km^2 (Priddle 1990) and bounded by the Antarctic continent (~70° S) to the south and by the Subtropical Convergence (~40°– 45° S) to the north. While the Antarctic ecosystem is almost entirely restricted to the ocean due to harsh environmental conditions that limit terrestrial life (Karentz 1991; Lubin *et al.* 1992), it is a diverse ecosystem containing many endemic species, and primary production is highly variable in space and time (Smith and Nelson 1986; Karentz 1991; Arrigo *et al.* 2008a). Lubin and Holm-Hansen (1995) describe the euphotic zone in the Southern Ocean as consisting of a light-saturated regime in the upper 25-40 metres, where there is more sunlight than phytoplankton need, and a light-limited regime at greater depths, where solar irradiance has been attenuated by the water column such that photosynthetic rates decrease with depth (Podgorny and Lubin 1998). A large area of the Southern Ocean is seasonally ice-covered – this is termed the Seasonal Sea Ice Zone (Brierley and Thomas 2002).

The Southern Ocean comprises around 20% of the area of the world ocean but is considered to play a disproportionately important role in controlling the climate of both the present day (Sarmiento *et al*. 1998) and geological past (Broecker and Henderson 1998; Moore *et al.* 2000). Moreover, this region has the greatest inventory of unused macronutrients in the world ocean (Levitus *et al*. 1993) and is the most important province for the export and burial of biogenic silica (Trèguer *et al*. 1995) and for the production of dimethyl sulphide (DMS) (Kettle *et al*. 1999). Variations in the rate of synthesis of dimethyl sulfoniopropionate (DMSP), the precursor of DMS, the utilisation rate of macronutrients, and subsequent changes in the rate of export of photosynthetically-fixed carbon in polar waters are all mediated by phytoplankton (Boyd 2002). Such variations over geological time may be key determinants of the atmospheric concentration of biogenic gases, such as carbon dioxide (CO_2) and DMS, and hence climate (Moore *et al.* 2000; Watson *et al.* 2000). The question of whether higher than usual levels of UVB due to ozone depletion will impact upon phytoplankton in the ocean and in sea ice, and cause a flow-on effect on climate needs to be answered.

2.2 Sea ice and snow

An added level of complexity to the Antarctic environment is provided by the seasonal advance and retreat of sea ice around the continent (Comiso *et al.* 1993; Moore *et al.* 2000). Massom *et al*. (1999) described the Antarctic sea ice cover as "one of the most seasonally variable geophysical parameters on the Earth's surface, and one of the most complex to interpret". Lubin and Massom (2006) include a comprehensive coverage of the sea ice phenomenon (e.g. sea ice historical records, formation processes; types; seasonal areal extent; impact and role; remote sensing and the major sensors used; and key physical parameters available from satellite data) and refer the reader to many other references for more detailed information on both satellite and *in situ* measurements of sea ice. Thomas and Dieckmann (2003), Worby *et al.* (2008a), and the ASPeCt web site (2008) include descriptions of the growth phases of sea ice, the different types of sea ice, and the mechanical and thermodynamic processes that affect the redistribution and net gain or loss of sea ice (see Figure 2.1).

The effects of sea ice on the global climate system are significantly amplified by the presence of an insulating snow cover, which is itself highly variable in thickness and properties (Massom *et al.* 2001). Details of snow thickness and snow type and their geographical and seasonal variations; snow grain size, density, and salinity; frequency of occurrence of slush; thermal conductivity, snow surface temperature, and temperature gradients within snow; and the effect of snow thickness on albedo are discussed in Massom *et al*. (2001) and Sturm and Massom (2010).

Snow also plays an important role in Antarctic sea ice formation. Snow-ice forms when the base of the snow on top of the ice is flooded by sea water and refreezes to form ice (Fichefet and Morales Maqueda 1999; Maksym and Markus 2009). This flooding is attributable to several factors. The ice cover can be loaded by the deposition of snow (or the redistribution of snow by wind), depressing the top of the ice below sea level (Lange *et al.* 1990). Alternatively, the effects of ocean heat flux melting the under-side of the ice serves to thin the ice and lower the freeboard of sea ice with a snow cover below sea level, leading to flooding (Lytle and Ackley 1996; Maksym and Jeffries 2000). Sea ice exhibits a marked transition in its fluid transport properties at a critical brine volume fraction of about 5 percent, or temperature of about -5 degrees C for salinity of 5 parts per thousand. For temperatures warmer than -5 degrees C, brine carrying heat and nutrients can move through the ice, whereas for colder temperatures the ice is impermeable. This transition plays a key role in the geophysics, biology, and remote sensing of sea ice (Golden *et al.* 1998).

In the East Antarctic region, the sea ice consists of a narrow and highly mobile band which is typically only several hundreds of kilometres wide at its maximum extent (Worby *et al*. 1998). Antarctic sea ice as a whole, covers between ~18-19 million km^2 each September-October at the end of the growth season to ~3-4 million km^2 each February-March (Gloersen *et al.* 1992). Sea ice not only varies in areal extent but also in its type and concentration (Worby 1999; Brandt *et*

al. 2005; Lubin and Massom 2006). Jacka (1987) and Allison (1989) have shown that, although the total East Antarctic ice concentration in spring is 80-100%, much of the ice is young and thin (typically less than 0.3 m). The East Antarctic pack ice is highly mobile with a mean drift speed of 0.22 m s^{-1} (Worby *et al.* 1998) but data show that this is highly variable on a daily basis. The net drift is divergent, but frequent periods of convergence cause floe deformation. The areally-averaged ice thickness within the sea ice zone may be less than 0.4 m and even in winter the majority of ice floes off East Antarctica are probably less than 1 m thick (Allison 1989).

Data from field investigations and satellites covering the period 1986-1995 were used by Worby *et al*. (1998) to develop a climatology of the sea ice conditions in the East Antarctic pack between 20º-160º E. This study shows that the characteristics of the sea ice pack in East Antarctica are largely determined by the continual passage of weather systems through the region (Worby *et al.* 1998) (see Figure 2.1). The constantly changing growth and deformation environment, coupled with high ice drift speeds (Heil and Allison 1999), result in highly variable physical properties. Such variability makes it difficult to identify regional or interannual trends in ice and snow properties in the region. Moreover, there has to date, been no regular synoptic measurement of sea ice thickness by satellite, although data from CryoSat II (launched 2010) show great potential (Wingham *et al.* 2006). A large scale snow-cover thickness on sea ice exists, derived from satellite Advanced Microwave Scanning Radiometer – EOS (AMSR-E) data, but underestimates occur in regions of rough sea ice (Worby *et al.* 2008a).

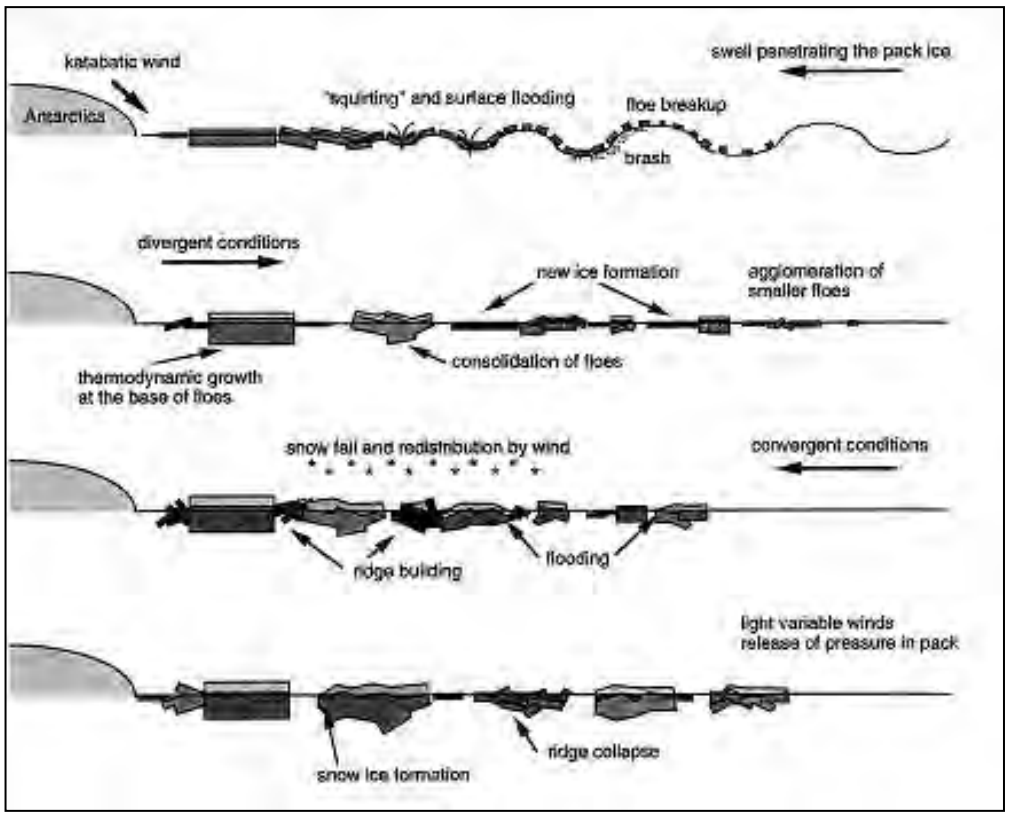

Figure 2.1: Forcing parameters that determine thickness distribution and physical characteristics of sea ice and snow cover (Figure 19 in Worby *et al.* 1998).

The ozone hole has had a profound impact on the climate of Antarctica over the last thirty years, shielding the continent from the effects of global warming (SCAR 2009). The depletion of stratospheric ozone has a cooling effect since ozone acts as a greenhouse gas. Also, in the austral spring the loss of stratospheric ozone cools the Antarctic stratosphere, thus increasing the strength of the polar vortex, then during summer and autumn the effects of the ozone hole propagate down through the atmosphere (SCAR 2009). This situation will not last, as ozone concentrations above Antarctica are expected to recover within the next century (see Section 3.1.7). There are two classic views on the possible changes in Antarctic sea ice as a result of greenhouse warming based on model predictions (Liu *et al.* 2004a). One school of thought is that the sea ice cover would decrease with warmer surface temperature. If greenhouse gas concentrations continue to rise at the current rates then temperatures across the continent will rise by several degrees and there will be about one third less sea ice by 2100 (SCAR 2009). Alternatively, the sea ice cover could increase with a warmer climate (Liu *et al.* 2004a). The latter viewpoint assumes that increased precipitation with the warmer atmosphere in the Antarctic would result in more snowfall on sea ice (which enhances the positive ice-albedo feedback) and lower salinity in the surface ocean layer (which reduces the contribution of heat from the relatively warm deep water into the surface layer) (Liu *et al.* 2004a).

Numerous studies indicate that strong, yet complex, relationships exist between large-scale (satellite-derived) anomalies in seasonal sea ice distribution, regional changes in ice season length (R.A. Massom, pers. comm., 2010) and dominant modes of atmospheric circulation such as the Southern Annular Mode (SAM), zonal wave three patterns and the high-latitude response to El Niño-Southern Oscillation (ENSO) e.g. Kwok and Comiso (2002), Fogt and Bromwich (2006), Massom *et al.* (2006), Raphael (2007), Stammerjohn *et al.* (2008) and Lefebvre and Goosse (2008). The ecological impact of these patterns on ice-dependent species has been highlighted by recent studies (e.g. Croxall *et al.* (2002), Weimerskirch *et al.* (2003), Massom *et al.* (2006) and Quetin *et al.* (2007)). Many gaps in understanding these processes still exist. To enable detection of clear trends versus interannual variability and short- to long-term cycles and decadal-scale régime shifts, there is a need for sustained consistent long-term datasets (both physical and biological combined) (R.A. Massom, pers. comm., 2010).

Antarctic sea ice provides a winter refuge for many species of phytoplankton, and these organisms are released into the open water of the marginal ice zone as the sea ice cover recedes during spring (Karentz 1991; Arrigo *et al.* 2010; Dieckmann and Hellmer 2010). Despite the presence of strong southerly/south-easterly winds throughout the winter months, sea ice concentrations (in the Ross Sea, for example) (see Figure 2.3 for map depicting this, and other geographic features) remain generally high during this time, although small areas of open water occasionally form near the ice shelf (Gloersen *et al*. 1992). This is because cold winter sea ice has sufficiently high tensile strength to resist break-up by offshore winds (Arrigo *et al.* 1998a). The hydrographic characteristics of the marginal ice zone (MIZ) make the organisms in

springtime phytoplankton blooms especially vulnerable to excess ultraviolet radiation. This is because the local decrease in salinity around the melting sea ice causes a density stratification that inhibits vertical mixing and keeps most phytoplankton in a light-saturated regime (Podgorny and Lubin 1998; Petrich and Eicken 2010).

2.3 Biological processes in Antarctica

Most of the Southern Ocean is unproductive, with average annual production rates comparable with those found in oligotrophic, tropical waters (Priddle 1990; Knox 1994; Marchant and Murphy 1994). As the sea ice melts and retreats southward during spring and summer, it generates a shallow mixed layer in and around the marginal ice zone (MIZ). The high-light and high-nutrient waters of the MIZ support 25-67% of the phytoplanktonic production in the Southern Ocean (Smith and Nelson 1986; Smith *et al.* 1992; Knox 1994). Mixed layer depths (MLD) during the times of the phytoplankton blooms may be 20 metres or less for up to 6 days (Mitchell and Holm-Hansen 1991; Veth 1991). Primary productivity of the Southern Ocean has been estimated at ~3.5 Gt of carbon per year (Marchant and Murphy 1994). There are at least 559 different species of phytoplankton inhabiting Antarctic waters (Marchant and Scott 2005) which are primarily responsible for the production of biomass in the ocean (Zepp *et al.* 2003). They are currently responsible for ~50% of global primary production (Falkowski and Raven 2007). Phytoplankton play an integral role in global climate by fixing carbon into organic matter through photosynthesis (McLain *et al*. 1993). Arrigo *et al.* (2008b) used a mechanistic three-dimensional biogeochemical model of the Ross Sea (see Figure 2.3) to show that Antarctic shelf waters are a strong sink for carbon dioxide due to high biological productivity, intense winds, high ventilation rates, and extensive winter sea ice cover. A schematic showing trophodynamic interactions in marine ecosystems is shown in Figure 2.2.

Estimates of annual primary production in the Southern Ocean have varied widely over the years as the understanding of Southern Ocean ecology has improved. Early estimates were considered biased because of a preponderance of samples collected within the high-productivity waters on the continental shelves. As more measurements were made in pelagic waters under non-bloom conditions, productivity estimates dropped. Recognition that primary production is enhanced in the MIZ led to arguments that primary production estimates should be increased again (Arrigo *et al.* 1998b).

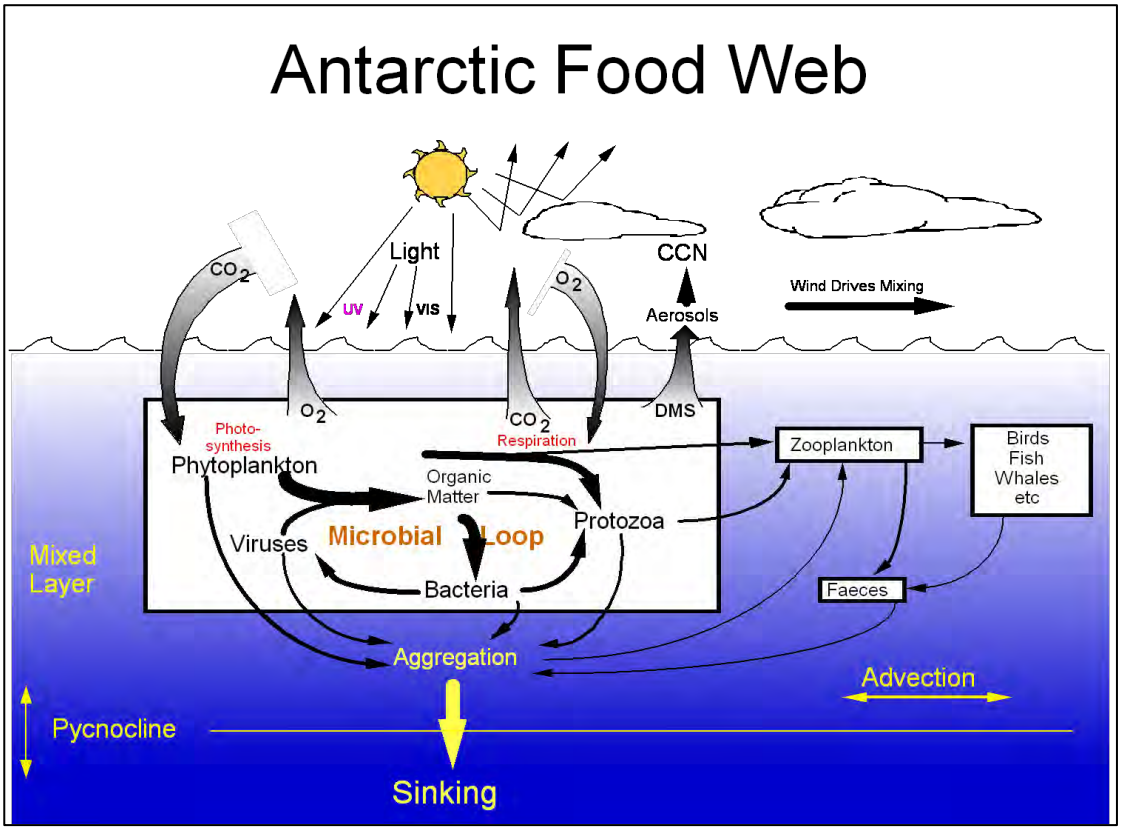

Figure 2.2: Schematic showing trophodynamic interactions in marine ecosystems and their effect on atmospheric gases that influence global climate (Figure 20.6, page 747 in Davidson 2006).

More recent research by Smith and Comiso (2008) has shown that sea ice in the Southern Ocean is a major controlling factor on phytoplankton productivity, but the relationship is modified by regional differences in atmospheric and oceanographic conditions. They used the phytoplankton biomass, photosynthetically active radiation (PAR), and cloud cover data from Sea-viewing Wide Field of View Sensor (SeaWiFS), ice concentrations data from Special Sensor Microwave Imager (SSM/I) and Advanced Microwave Scanning Radiometer-EOS (AMSR-E), sea-surface temperature data from Advanced Very High Resolution Radiometer (AVHRR), and a vertically integrated model to estimate primary productivity south of 60º S. It was found that the most productive regions of Antarctic waters were the continental shelves, and no sustained blooms occurred in waters of greater depth (>1000 m). A comparison between measured productivity and modelled productivity suggests that productivity estimates are substantially below those measured *in situ* although this will need more research to confirm these trends. A significant increase in productivity in the entire Southern Ocean during the 9-year observation period was also obvious.

Mesoscale surveys near the Antarctic Peninsula have related the abundances of Antarctic krill (*Euphausia superba*) and salps (*Salpa thompsoni*) to inter-annual variations in sea-ice extent (Loeb *et al.* 1997; Quetin *et al.* 2007). The BROKE survey (Nicol *et al.* 2000b) examined the ecosystem structure and oceanography spanning 3500 km of the East Antarctic coastline,

linking the scales of local surveys and global observations. Phytoplankton, primary productivity, Antarctic krill, whales and seabirds were concentrated where winter sea-ice extent is maximal, whereas salps were located where the sea-ice extent is minimal. The BROKE survey found enhanced biological activity south of the southern boundary of the Antarctic Circumpolar Current, rather than in association with it. They proposed that along this coastline, ocean circulation determines both the sea-ice conditions and the level of biological productivity at all trophic levels (Nicol *et al.* 2000b).

Given its negative effects (see discussion in Section 2.3.1), the increase in UVB radiation to the sea surface is a significant problem in the Antarctic marine ecosystem where during spring, the Antarctic ozone hole coincides with the proliferation of algal blooms in the sea ice and MIZ (McLain *et al.* 1993; Vincent and Roy 1993). Increased UVB as a result of ozone depletion is likely to change food web structure and function and may influence biogeochemical cycles (Davidson and Belbin 2002).

2.3.1 Effects of increased UVB on organisms

One of the main concerns of scientists with the discovery of the springtime Antarctic ozone hole in the early 1980s was that increased levels of UVB radiation penetrating ice and into the upper few metres of the water column could deleteriously affect the base of the food chain by interfering with the growth of phytoplankton. The springtime blooms coincide with the time when the Antarctic ozone hole reaches its maximum size (Arrigo 1994).

The significance of ozone depletion over the middle, high and polar latitudes of both hemispheres is well established (WMO 1995; Harris *et al.* 1997). The inverse relationship between changes in total ozone and associated changes in solar UVB (280-325 nm) at ground level has been proven and is well documented by many authors including Kerr and McElroy (1993), Zerefos *et al.* (1995), McKenzie *et al.* (1999), WMO (1999, 2003), and Zerefos *et al.* (2000). The stressful effects of solar UVR (280-400 nm) on polar phytoplankton assemblages has also been reported (Helbling *et al.* 1992; Smith *et al.* 1992; Lesser *et al.* 1996; Neale *et al.* 1998a; Neale *et al.* 1998b; Buma *et al.* 2001a). Litchman and Neale (2005) further stated that the UV-related inhibition of photosynthesis leading to decreased primary productivity on local and global scales should be quantified. All marine organisms appear to be susceptible to some degree of UV damage; however, the extent to which they are affected is highly variable and poorly understood (Bancroft *et al.* 2007).

The Antarctic marine ecosystem is very complex with diverse interactions between the different trophic levels (see Figure 2.2) making it very difficult to determine the overall effects of UVB radiation. Detrimental effects of increased UVB at the molecular and cellular levels have been clearly demonstrated for some marine organisms, but the resulting changes in community structures, ecosystems and biogeochemical cycles still remain poorly defined (Whitehead *et al.* 2000). The point was made by Vincent and Roy (1993) that continuing ozone depletion is not

likely to cause an abrupt collapse of photosynthetic production, but may result in subtle, community-level responses that could ultimately impact on higher trophic levels. Shifts in community structure may initially be more common and result in small, yet detectable, differences in ecosystem biomass (Helbling *et al.* 1992; Davidson *et al.* 1996; UNEP 2005). There are only limited data available of ambient UVB irradiances in the Antarctic (e.g. Dahlback 2002; Newsham 2003). Moreover, the existence of the relationships between ozone and UVB radiation and the effects of increased levels of UVB necessitate the continuation of research, especially in Antarctica where ozone levels are more significantly decreased compared to other latitudes (Intergovernmental Panel on Climate Change (IPCC) 1995).

The springtime increase in UV over Antarctica is primarily a temporal shift, rather than an increase in the maximum UV irradiance that ever reaches the surface. Therefore, the biological consequences of increased UVB in Antarctica do not rest entirely upon the ability of organisms to cope with UV exposure, but rather on their ability to cope with summer levels of UV occurring during spring. With the occurrence of the ozone hole, the seasonal gradient of increasing UV levels no longer exists. The fact that the full summer complement of UV can be experienced during the initial period of illumination that occurs immediately after winter darkness (Karentz 1991) is an important consideration. There is a large body of evidence to support the general consensus that UVB radiation negatively affects aquatic organisms (Buma *et al.* 2001b; UNEP 2002), e.g., measurable inhibition of phytoplankton productivity (Smith *et al.* 1992; Holm-Hansen *et al.* 1993; Vincent and Roy 1993; Prezelin *et al.* 1994; Neale *et al.* 1998b); and direct DNA damage caused by UVB (Buma *et al.* 2001a) but more research is needed to determine the adaptive responses of marine organisms in the field. Examples of questions that remain unanswered are: how much damage is sustained; how much damage can be repaired under Antarctic conditions of ozone depletion, short day lengths, and freezing ambient water temperatures; and what is the effect of higher ratios of UVB to visible wavelengths on the balance between biological damage and photo-reactivation repair (Karentz 1991).

The United Nations Environmental Program Progress Report (UNEP 2005) stated that UVB radiation elicits species-specific responses with a high degree of intra-species variation. Potential consequences of enhanced levels of exposure to UVB radiation demonstrated in recent experiments include loss of biomass (Richardson and Schoeman 2004); changes in species composition (Persaud and Williamson 2005); decrease in availability of nitrogen and other nutrients (Rothschild 1998; Zepp *et al.* 2007); and reduced uptake capacity for atmospheric carbon dioxide (Tortell 2000), resulting in the potential augmentation of global warming. Temperature changes in Antarctica can, for example, significantly affect carbon sequestration, and even small changes could affect species competition, timing of reproduction, and hatching success (UNEP 2005).

Apart from a small portion of the UVA waveband, UV irradiation is not photosynthetically active (Holzinger and Lütz 2006). Therefore UV irradiation is something to tolerate, counteract or avoid

(Larkum and Wood 1993). Life on Earth developed in the absence of a stratospheric ozone layer, with much higher UV levels than today (Garcia-Pichel 1998; Häder *et al.* 2003). Early organisms most likely possessed efficient strategies and physiological mechanisms to prevent and repair UV-induced damage (Rothschild and Mancinelli 2001; Häder *et al.* 2003). Some of the photo-protective mechanisms triggered in modern-day organisms by UV radiation include biosynthesis of UV-absorbing substances (Helbling *et al.* 1996; Riegger and Robinson 1997) and DNA repair mechanisms and enzymes that reduce photo-oxidative stress (Buma *et al.* 1997; Newman *et al.* 2000; Hoyer *et al.* 2001; He *et al.* 2002). UV radiation screening in phytoplankton and zooplankton is mediated by protective pigments (phlorotannins, melanin, mycosporine-like amino acids [MAAs], cytonemin, and carotenoids). Despite possessing various strategies to counteract UV-induced damage, protection is not perfect, and UVB radiation can still cause damage (Hoyer *et al.* 2001; He *et al.* 2002). The potential relationships between upward trends in surface UVB flux and negative impacts on human health, on terrestrial plants, and on aquatic ecosystems have been summarised, for example in Lubin and Holm-Hansen (1995), Arrigo et al. (2003a) and UNEP (2005).

Although the field and laboratory studies by Apprill and Lesser (2003) indicated that photo-inhibition under PAR exposure elicits a dynamic photo-inhibition response that does not affect primary production, they did note a UV radiation effect that resulted in chronic photo-inhibition and a decrease in primary production. These processes would be exacerbated in shallow algal populations (Laurion *et al.* 1998; Buma *et al.* 2001a) especially when local weather conditions, tides, or optical properties of the water column favoured increased UV irradiances.

Attempts have been made to estimate the loss of oceanic photosynthesis resulting from decreased ozone abundance. Reported daily losses vary from <1% to 12% of the phytoplankton carbon fixation measured under normal ozone conditions (Smith *et al.* 1992; Holm-Hansen *et al.* 1993; Arrigo 1994; Prezelin *et al.* 1994; Neale *et al.* 1998b; Arrigo *et al.* 2003a). Because current atmospheric radiative transfer models (Lubin and Jensen 1995; Lubin *et al.* 1998) can calculate fluxes of UV radiation and visible radiation as a function of ozone abundance with a high degree of accuracy, it is now possible to use numerical modelling techniques to assess the large-scale effects of stratospheric ozone depletion on oceanic primary production (Arrigo *et al.* 2003a).

A 1% decline in column ozone may correspond to a 2% increase in UV irradiance (Davidson 1998; Neale *et al.* 1998b). If the rate of change of increased exposure to UVB is greater than the ability of marine organisms to adapt, there is a greater potential for impact on marine organisms. However, the impact of increased UVB radiation on marine organisms is not precisely known. UVB radiation is strongly attenuated with depth by biotic and abiotic components of the water column, and its effects are often mediated by tolerance mechanisms (as discussed above) (Frederick and Lubin 1994).

2.3.1.1 Phytoplankton

The factors controlling the distribution of phytoplankton stocks, species composition, and their physiological status in the Southern Ocean were reviewed by Boyd (2002). The geographical isolation of the Southern Ocean has been a major barrier to collecting data to determine spatial and temporal distribution of algal stocks to enable the establishment of the environmental mode(s) of control on phytoplankton in these waters. The launch of the satellite sensors Coastal Zone Color Scanner (CZCS) and Sea-viewing Wide Field of View Sensor (SeaWiFS) made available high resolution maps of chlorophyll *a* concentration (chl *a*) which can be used to investigate the environmental forcing of the 'variegated nature' of the Southern Ocean (Comiso *et al.* 1993). Consensus is emerging on the key modes of control (iron, irradiance and silicic acid) for different oceanic basins (Boyd 2002), but more study is required to better understand the interplay of seasonal, regional and taxon factors. Boyd (2002) wrote that a synthesis of the understanding of the role of irradiance in phytoplankton processes via a mathematical model, indicated that the mixed layer depth (MLD) and light attenuation were the key determinants.

The structure of the water column thus has an important effect on primary productivity. Deep wind-mixed layers caused by strong wind forcing may prevent high productivity in the MIZ due to lack of light, but on the other hand stabilisation of the water column by ice melting may cause enhanced production during ice retreat (Veth 1991). Boyd (2002) wrote that the global circulation models predicted that climate change will have a marked effect on the waters of the Southern Ocean (Sarmiento *et al.* 1998). From such simulations, the most likely scenario – in terms of altered environmental conditions – is warming, increased stratification and alteration of the MLD. It is important to have maps of levels of UVB radiation at various depths throughout the water column, as any deleterious effects on phytoplankton will impact other organisms further up the food chain.

Despite controls instituted by the Montreal Protocol, the anthropogenic release of halocarbons into the atmosphere persists in causing effects (UNEP 2006) as demonstrated by the most severe ozone depletion on record during austral spring 2006 (see NASA press release available at www.sciencedaily.com/releases/2006/10/061019162053.htm#). A special focus has been given to the effects of these variations in UVR on phytoplankton photosynthesis in the Southern Ocean as evidenced by the inclusion of 6 chapters on the topic in an edited book on UVR in Antarctica (Weiler and Penhale 1994). These studies and numerous others (Smith and Baker 1980; Worrest *et al.* 1981; Cullen and Lesser 1991; Cullen *et al.* 1992; Smith *et al.* 1992; Behrenfeld *et al.* 1993; Holm-Hansen *et al.* 1993; Boucher and Prezelin 1996; Davidson *et al.* 1996; Neale *et al.* 1998a) have shown that photosynthesis in the Southern Ocean is inhibited by ambient and enhanced UVR. A continuing challenge is to translate such responses into estimates of the effect on productivity in the water column (reviewed in Davidson 2006; Fritz *et al.* 2008).

Results to date have shown more than 10-fold variation in the sensitivity of phytoplankton photosynthesis to UVR as measured by biological weighting functions (BWFs) (see further discussion in Sections 2.3.2 and 9.2), which translates to decreases of 16 to 30% in estimates of the daily primary productivity of lakes, estuaries and Antarctic waters (Neale *et al.* 1998a; Neale *et al.* 1998b; Neale 2001; Neale *et al.* 2001a; Arrigo *et al.* 2003a; Hiriart-Baer and Smith 2004; Litchman and Neale 2005; Fritz *et al.* 2008).

The magnitude of inhibition of phytoplankton productivity during spring is a function of:

- phytoplankton sensitivity to UVB radiation (Smith *et al.* 1992; Holm-Hansen *et al.* 1993; Neale *et al.* 1998b) – the overall effectiveness of the behavioural and physiological mechanisms developed by marine organisms to protect themselves against UV damage determines their sensitivity to UVB radiation (Arrigo *et al.* 2003a);
- their cumulative exposure to UVB as a function of ocean MLD (Sakshaug et al. 1991);
- the speed of vertical mixing (Neale *et al.* 1998b);
- the amount of non-living UVB absorbing material such as CDOM (Arrigo and Brown 1996); and
- the degree to which the UVR induced damage can be repaired by cellular processes (Holm-Hansen *et al.* 1993; Arrigo *et al.* 2003a).

McMinn *et al.* (1994) showed that the effects of increased levels of UVB on diatom assemblages in an Antarctic coastal area had been minimal in the 20 years of their study and that the compositional changes in the diatom component of the phytoplankton community in that time could not be distinguished from long-term natural variability, although there was some indication of a decline in the production of some sea-ice diatoms. Other studies (for example, Karentz and Spero (1995), Hardy *et al*. (1996) and Worrest and Häder (1997)) found evidence of negative effects on marine species caused by an increase in UVB irradiances. However, these observations suffer the inevitable difficulty in relating observed changes to UVB radiation, as it is only one of a vast array of factors that simultaneously impact the abundance and species composition of microalgae in the natural environment (Davidson 2006). In 1989 Bidigare wrote that up until that time it had been generally assumed that UV radiation does not penetrate deep enough in the water column to damage pelagic organisms. It has since been shown that biologically effective radiation can penetrate to at least 20 m in clear Antarctic water (Smith and Baker 1979; Holm-Hansen *et al.* 1989; Gieskes and Kraay 1990; Karentz and Lutze 1990; Smith *et al.* 1992; Marchant 1994; Booth and Morrow 1997), and thus has the potential to affect a substantial portion of the euphotic zone (Newman *et al.* 2003). Gieskes and Kraay (1990) wrote that UVB may penetrate to depths in excess of 50 m in Antarctic waters. Flux levels at wavelengths below 280 nm (perhaps even 290 nm) are too low to be significant or even measurable in a practical sense (Booth and Morrow 1997). It is important to note that ozone depletion does not significantly affect UVA or higher solar wavelengths and UVA attenuation in

water is lower than for UVB. Therefore, the incident and in-water ratios of UVB to UVA vary with ozone levels and depth (Karentz and Bosch 2001).

Photosynthetic inhibition is high in late spring-summer and low in winter, and the contribution of UVB and UVA to this inhibition is variable, mainly because of the differential sensitivity of phytoplankton assemblages throughout the year (Helbling *et al.* 2005). Nevertheless, the inhibition caused by UVA is generally higher than that caused by UVB. However when considering the energy received by the cells, as derived from the BWF, phytoplankton bloom assemblages are more sensitive to UVB than the pre- and post-bloom assemblages (Helbling *et al.* 2005). This is of particular significance for phytoplankton blooms exposed to higher UVB levels as a consequence of ozone depletion.

Nunez *et al*. (2006) measured the effect of ambient solar UV radiation on the biomass and species composition of phytoplankton, protozoa, bacteria and dissolved organic carbon (DOC) in natural microbial assemblages from Antarctic coastal waters. The modelling of the results showed that changes in phytoplankton biomass were primarily due to dose rate, indicating that their UV-induced mortality resulted from the equilibrium between damage and repair. There was considerable variability between individual species in their response to dose and dose rate. Changes in protozoan biomass were mainly due to dose and were likely due to community-level, trophodynamic interactions. UV radiation did not measurably affect bacterial biomass, but resulted in increasing concentrations of DOC. These results indicate that enhanced UVB radiation in Antarctic waters increases phytoplankton mortality and causes changes in the structure, function and composition of the microbial community that are likely to return more photo-assimilated carbon to the atmosphere.

Davidson (2006 and references therein) reviewed research on the effect of UV radiation on microalgae and the contribution and relevance of culture-based studies investigating UV impacts. There is abundant evidence that increased incident UVB radiation in Antarctica is damaging marine microalgae. However, there is no clear evidence of UVB-induced changes in the marine ecosystem. UVB radiation is only one of a suite of environmental stresses in the Antarctic ecosystem and relating observed changes in species composition to just one of those stresses is difficult.

It is technically complex to conduct culture experiments that simulate the effect of UVR on microalgae in nature, exemplifying the inherent problems of using cultures as an analogue for natural blooms. Given the inability to directly measure many of the effects of UVR on natural communities, culture studies have a vital role in determining the effect of UV on the marine ecosystem. Such studies, together with models of UV climatology and the biotic and abiotic marine environment, will eventually allow the determination of the effect of increases in UVR due to ozone depletion and global warming on marine microalgae, planktonic communities and the world's atmosphere (Davidson 2006).

2.3.1.2 Sea ice algae

Not only do some warm-blooded animals depend on sea ice as a platform, but the sympagic organisms living internally within the sea ice or at the ice/snow and ice/water interfaces provide a substantial part of the total primary production of the ice-covered regions of the Arctic and Antarctic (Spindler 1994). In fact sea ice algae contribute at least 20% of the primary productivity of these ice-covered areas (Legendre *et al.* 1992; McMinn *et al.* 1999).

For much of the year in the seasonally ice-covered areas of the Southern Ocean, most of the biomass and primary productivity occurs not in the water column but in the overlying sea ice cover (Lizotte 2001; Arrigo and Thomas 2004). In these regions, the sea ice supports the only significant primary production for up to nine months of the year, as deep mixing, heavy ice cover and low light levels prevent the development of significant phytoplankton biomass (McMinn *et al.* 2007). For some organisms, and juvenile Antarctic krill (*Euphausia superba*) in particular, the presence of this year-round food supply is critical for survival (Arrigo and Thomas 2004; Nicol 2006).

The fast ice near the continent is relatively transparent and transmits ~10% of UVB in October (Ryan 1992) compared with only ~0.25% in late November (Trodahl and Buckley 1989). In the fast ice close to the Antarctic coast, most of the algal biomass is concentrated in a dense band at the bottom of the ice (McMinn and Ashworth 1998). Many sea ice algae are extremely shade-adapted (Palmisano *et al.* 1985) and are thus potentially susceptible to an increase in UVB levels. Ryan and Beaglehole (1994) found that conditions of elevated UVB radiation due to ozone depletion had little effect on bottom sea ice algae. On the other hand McMinn *et al*. (1999) found that UVB radiation has a significant influence on the growth rates of shade-tolerant ice algae. Whereas it is difficult to determine the true daily dose of UV radiation received by phytoplankton in the natural marine environment, in part because they continually mix in the water column (Smith 1989), sea ice algae present a unique case, being trapped in their environment in the sea ice. There is the confounding issue that as spring advances, the algae in the bottom layers of ice will be shaded by those growing higher in the layers (Ryan 1992). In sea ice algal mats, cells closest to the top of the ice experience considerably higher irradiances and with different spectral properties from those at the bottom (SooHoo *et al.* 1987; Palmisano *et al.* 1988; McMinn *et al.* 1999). For light experiments, the irradiance selected for illumination has usually been that measured beneath the ice and thus that experienced by only the lowest-positioned algal cells. It would once again be advantageous to have levels of UVB radiation measured throughout the sea-ice environment and the maps output from this project will aid research into what effects it has on sea ice algae.

Algal communities, especially diatoms, flourish within the distinct micro-habitats created when sea ice forms and ages. The primary advantage afforded by sea ice is that it provides a platform within which sea ice algae can remain suspended in the upper ocean, where light is sufficient for net growth. Except for those areas where snow cover exceeds approximately 0.3 m, light is

usually sufficient for net photosynthesis during the spring and summer (Grossi *et al.* 1987; Arrigo *et al.* 1991; Arrigo *et al.* 2003b). Arrigo and Thomas (2004) describe a range of niches within the sea ice habitat and why various species of algae favour certain niches. The greatest fraction of sea ice micro-algae often resides in the bottom 20 cm of the ice where environmental conditions are generally stable and more favourable for growth.

Climate projections indicate that a long-term decline in Southern Ocean sea ice cover by 2100 is probable (Bracegirdle *et al.* 2008). This is likely to have a major impact on the amount of sea ice algae and thus also on the abundance of those organisms that are dependent on it (Smetacek and Nicol 2005). Algal biomass in most pack ice areas is considerably less than that which accumulates close to Antarctica on fast ice (McMinn *et al.* 2007). Fast ice algal biomass is mostly associated with bottom communities, while that in the pack ice is often also present in surface and intermediate communities (Horner 1985).

There is a growing realisation that there is a close connection between krill distribution and sea ice algal biomass (Brierley and Thomas 2002; Nicol 2006). The area of eastern Antarctica between 80-150° E which was investigated by Nicol *et al*. (2000a) during the "BROKE survey" (Baseline Research on Oceanography, Krill and Environment), is known to have a low krill biomass, and this probably reflects the low biomass and primary productivity rates within the pack ice as reported in McMinn *et al.* (2007).

2.3.1.3 Antarctic Krill

Sea ice cover limits the availability of light to the phytoplankton in the water column, but despite low light levels, significant net primary production occurs in both the sea ice and the water column in late winter (Kottmeier and Sullivan 1987). Phytoplankton production in both the water column and the sea ice increases dramatically in the spring, as the melting ice creates vertical stability in the water column. Research has shown that, as the ice edge retreats, a series of blooms follows, continuing from September until December. Increases in standing stock from these ice edge blooms extends to about 250 km from the ice edge (Smith and Nelson 1985) and are a major source of food for organisms such as Antarctic krill (*Euphausia superba*) (Smith and Nelson 1986; Nicol *et al.* 2008).

Antarctic krill are voracious consumers of phytoplankton, and at times other zooplankters, and are themselves a major prey item for higher trophic levels (Bidigare 1989). If increased UVB is having some detrimental effect on the krill population, consequential effects on both upper and lower trophic levels are likely (Newman *et al.* 1999).

The connection between krill distributions and sea ice has been highlighted by Brierley *et al.* (2002). Arrigo and Thomas (2004) stress that it is not the areal ice extent that may be important for krill, but rather the extent of the ice edge. They commented that a 25% decrease in sea ice area would in fact only equate to a 9% reduction in the overall length of the sea ice edge.

During autumn, winter and spring the role of ice and ice algae in the life history and energetics of *E. superba* may be more important than during austral summer, not only because of the increase in the extent of sea ice but because of the decrease in phytoplankton biomass in the water column (Quetin and Ross 1991). Quetin and Ross (1991) wrote that adult krill in the pack ice of the Weddell Sea (see Figure 2.3) had been observed feeding on sea ice algae on the complex under-surface of multi-year ice because there are hiding places to avoid predators and there is also enough ice algae to give them an energetic advantage. On the other hand, larvae and juvenile krill feed on ice algae in areas of annual or smooth ice (Quetin and Ross 1991).

The ability of ice algae to produce large amounts of UV-absorbing compounds such as MAAs makes them important to organisms such as krill that must obtain MAAs from their diets (Newman *et al.* 1999, 2000) for incorporation into their own tissues (Arrigo and Thomas 2004). Grazers can obtain at least ten times more MAAs per unit of chl *a* ingested by consuming sea ice algae than they can from consumption of Antarctic phytoplankton. An ice algal MAA source may be particularly important to krill during the austral spring when ozone levels are still low, sea ice algae are actively growing and the major phytoplankton blooms of the Southern Ocean have yet to develop (Arrigo and Thomas 2004). Because MAAs can be transferred from grazers to their predators (Whitehead *et al.* 2001), UV radiation photoprotectants produced by ice algae have the potential to benefit organisms at a variety of trophic levels (Arrigo and Thomas 2004).

Antarctic phytoplankton quickly acclimatise to high UV-irradiance by increasing production of MAAs in a matter of days (Helbling *et al.* 1992; Villafañe *et al.* 1995; Newman *et al.* 2000). This rapid response suggests that krill that feed on phytoplankton following a period of high UV irradiance, such as that incident on a surface bloom during spring, will consume more MAAs than krill feeding on the same species of phytoplankton shaded from UV by sea ice cover or by depth in the water column (Newman *et al.* 2000). In addition, it is commonly believed that increasing levels of UVB radiation will favour succession of UV-resistant species and alter the floristic composition of phytoplankton communities (Bothwell *et al.* 1993; Marchant 1993; Bothwell *et al.* 1994; Davidson *et al.* 1994, 1996; Davidson 1998; Davidson and Belbin 2002; Nunez *et al.* 2006; Thomson *et al.* 2008). Given that krill have such a varied diet, it can be expected that if MAA-rich species become more abundant in response to environmental UV stress, the increase in dietary availability will enhance MAA levels in consumer organisms. Therefore the accumulation of MAAs, being dependent upon the recent irradiation history of prey algae, may provide a functional mechanism whereby MAA concentrations in krill are increased by an indirect response to enhanced UVB exposure. This ‘co-acclimation’ can occur by ingesting greater amounts of MAAs synthesised by phytoplankton in response to UV exposure and/or by UV-mediated change in floristic composition to favour the presence of UV-tolerant species having a greater capacity for the production of UV-absorbing MAAs (Newman *et al.* 2000).

A characteristic attribute of *E. superba* is that they live in schools (Nicol 2003) – these schools vary in size from about 200 m in one horizontal dimension and several metres thick (Hamner 1984) to the rare "super swarm" over 12 km long (Macaulay *et al.* 1984). Juvenile krill begin to school when they reach body lengths of about 10 mm. Thereafter krill do not leave the structure of the school except to moult, mate, release eggs or forage individually on localised phytoplankton patches or ice algae (Hamner and Hamner 2000). There is no cover in the open sea and schooling is particularly advantageous against visual plankton-pickers, and it also provides excellent protection from tentaculate predators. However schooling has its disadvantages as baleen whales feed most efficiently on concentrated patches of prey, and high density of krill in schools promotes parasites and disease (Hamner and Hamner 2000). A positive aspect of schooling would be a certain amount of 'shading' from excess UVB.

2.3.1.4 Other organisms

Research efforts to evaluate the impact of increases in UVB have focussed on phytoplankton under the assumption that ecosystem effects will most likely originate through reductions in primary productivity; however, phytoplankton do not represent the only significant component in ecosystem response to elevated UVB radiation (Karentz and Bosch 2001).

Aside from a few studies that included fish (mostly larval stages) (Karentz 1991; Malloy *et al.* 1997; McClintock and Karentz 1997), there is little information available on UV responses of larger Antarctic marine animals. Fish, birds, seals and whales are physically well protected from UV-induced damage by scales, feathers, fur and thick skin layers. The only study relating to the UV-photobiology of Antarctic organisms prior to the inception of ozone depletion examined sensitivity of UV-induced corneal damage in the eyes of Antarctic birds, as compared to birds from temperate latitudes (Hemmingsen and Douglas 1970). Polar birds have higher UV thresholds for damage, attributed to their existing adaptation to the higher albedo of snow and ice that creates a high UV environment (Karentz and Bosch 2001).

Heat shock proteins (HSPs) are synthesised under stressful conditions such as exposure to elevated temperatures, contamination, free radicals, UV light or patho-physiological states resulting from parasites and/or pathogens. HSPs function to protect cells by means of modulation of protein folding. The Antarctic Peninsula region has shown strong latitudinal changes in several factors which could influence HSP levels such as variation in temperature, UV radiation and contamination and human pressure. Barbosa *et al*. (2007) studied the variation in HSP levels in several populations of three penguin species along the Antarctic Peninsula to establish a baseline for future comparisons.

The pattern of latitudinal variation found in the Adélie penguin, opposite that of the gentoo, could be related to changes of UV radiation, although nothing is known about the direct effects of UV radiation on penguins (Karentz and Bosch 2001). On the other hand, temperature decreases

from north to south, and low temperatures can increase the levels of HSPs even in homeotherms (Barbosa *et al.* 2007).

If there is an impact of ozone depletion on larger marine organisms, it is expected to occur through potential limitation of food sources. Evaluation of the UV effects on birds and mammals is confounded by the fact that there are many environmental variables that can be implicated in regulating the size and fitness of a population. The multi-year life histories of these organisms also make it especially difficult to establish cause and effect; therefore, the impact of a single environmental variable is not readily apparent (Karentz and Bosch 2001).

Antarctic bacterioplankton are adversely affected by UVB radiation exposure (Karentz and Bosch 2001). In addition, invertebrates and fish, particularly early developmental stages that reside in the plankton, are sensitive to UVB. Understanding the balance between direct biological damage and species-specific potentials for UV tolerance (protection and recovery) relative to trophic dynamics and biogeochemical cycling is a crucial factor in evaluating the overall impact of ozone depletion (Karentz and Bosch 2001).

While there have been a number of investigations of UV effects on freshwater Antarctic cyanobacteria (e.g. Vincent and Quesada 1994; Quesada *et al.* 1995; Quesada and Vincent 1997; Roos and Vincent 1998), relatively little has been reported about the impact of ozone depletion on Antarctic marine heterotrophic bacteria, although Martin *et al.* (2008) confirmed that sea ice is a productive microbial habitat. Martin *et al.* (2009) observed significantly reduced metabolic activity in sea ice bacteria exposed to hyposaline seawater combined with rapid exposure to increased UVB radiation, conditions simulating those experienced during the thaw process. Early studies show that Antarctic bacterioplankton isolates do not possess UV-screening compounds that might protect cells, but they do have capability for recovery from UV-induced damage (Karentz 1994). A primary cellular target for UVB is deoxyribonucleic acid (DNA). DNA absorbs UVB, altering the molecular structure and potentially impairing DNA function. There are several metabolic pathways that repair DNA damage and an organism can have various combinations of these repair mechanisms. Some Antarctic bacteria have photoreactivation, an enzymatic repair process that requires UVA or higher wavelength radiation (Karentz 1994; Karentz and Bosch 2001). Another repair pathway in bacteria is the “SOS” response – a post-replication DNA repair system that allows DNA replication to bypass lesions or errors in the DNA. The timing of induction of genes involved in the “SOS” response is an important factor in the level of UV-tolerance within Antarctic microbial populations (Helbling *et al.* 1995).

Research has shown that increased UVB radiation can also cause human illnesses (Smith *et al.* 1992; Caldwell *et al.* 1998; Rousseaux *et al.* 2001; Searles *et al.* 2002), which is of particular significance to the temporary population of Antarctic researchers. The Antarctic vortex is usually more pole-centred, but by spring has slightly shifted off the pole towards the Atlantic sector. The vortex air masses reach populated areas of South America on about 10-20% of all days in

October, the month of most severe ozone depletion (Karpetchko *et al.* 2005). UV measurements at Ushuaia, Argentina (54.9° S, 68.3° W) (see Figure 2.3) have revealed that the UV dose can increase by more than 50% when the vortex passes over the station as compared to typical levels (Pazmiño *et al.* 2005). Punta Arenas (at latitude 53.1° S) (see Figure 2.3) is the southernmost city in Chile, with a population of approximately 154,000. Due to its location, well within the area affected by the Antarctic ozone hole, this population may well be the first group to show health problems from environmental effects of severe ozone depletion (Casiccia *et al*. 2003). A considerable increase in the number of sunburns was reported during periods of low ozone and high ultraviolet radiation during the mid to late austral spring of 1999 (Abarca *et al*. 2002).

Exposure to UV radiation is a risk factor for all three forms of skin cancer: (i) squamous cell carcinoma (SCC), (ii) basal cell carcinoma (BCC) and (iii) cutaneous malignant melanoma (CMM) (Longstreth *et al*. 1998). Because UVB levels rise with declining ozone (other variables being equal), skin cancer rates are expected to increase worldwide. There is also a special concern for an increase in the rate of malignant melanoma in regions close to Antarctica (Longstreth *et al.* 1998; Abarca and Casiccia 2002).

Snow is not uncommon in and around Punta Arenas during spring; consequently, the already high UVB levels reported could be further increased by surface reflection, by as much as 90% (Diffey 1998), therefore reaching or surpassing levels commonly experienced by people living closer to the Equator (Abarca and Casiccia 2002). The surface-based radiometers do not accurately measure reflected or scattered radiation, therefore, people living in areas subject to high levels of reflected light can receive higher levels of UVB than what is reported by these instruments (Abarca and Casiccia 2002). There is a need to educate people regarding the harmful effects of exposure to high levels of UVB such as the use of photoprotective clothing and the application of sunscreen. A more recent approach to reduce the harmful effects of solar radiation is through the use of phytochemicals that have been found to be photoprotective in nature (Adhami *et al.* 2008).

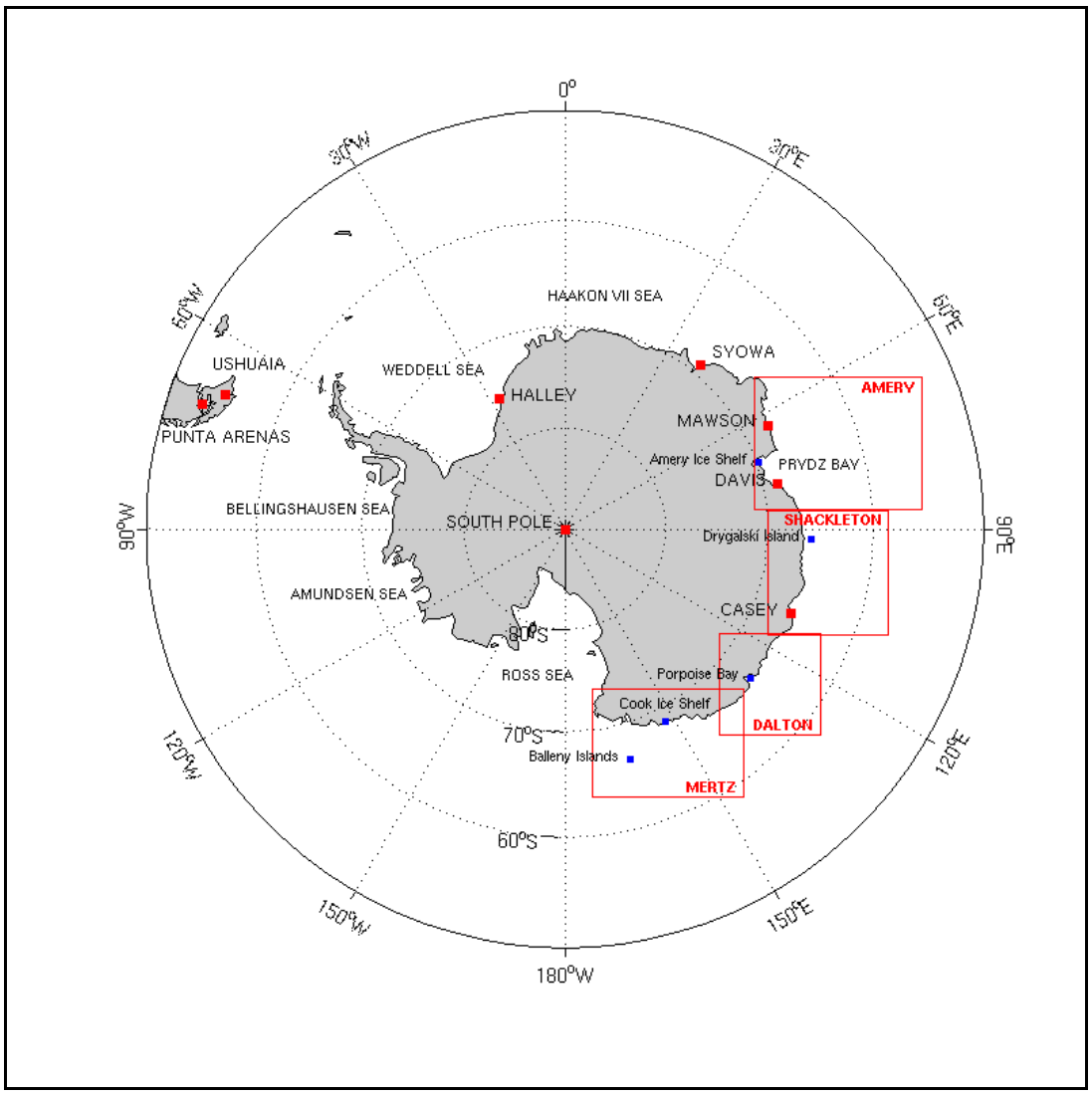

Figure 2.3: Map of Antarctica displaying relevant geographic features for this study. (The map was created using the m_map high resolution coastline in Matlab, which did not include the Antarctic ice shelves).

2.3.2 Biological Weighting Functions

2.3.2.1 BWFs – Historical background

To estimate the inhibitory effect of the changing UVB radiation on Earth's ecosystems, an understanding of its wavelength dependency is needed. The tool used for these estimations is the biological weighting function (BWF), whereby the inhibition of different wavelengths is calculated (Andreasson and Wängberg 2006). Neale (2000) includes detailed descriptions of the two types of spectral weighting functions – 'action spectra' and BWFs – their development and their use. Neale *et al*. (1998a) wrote that the choice of BWF can have an overriding influence on the prediction of the relative biological effects (Rundel 1983; Booth and Madronich 1994).

Biological effects of UVB radiation at each wavelength are extremely difficult to determine independently in nature. Action spectra (mathematical weighting functions) are therefore applied to irradiation doses from entire radiation spectra when estimates of biological effect are of interest. Applications of action spectra are optimal when limited to the organisms (or cellular components) from which they are derived. However, experimental determination of action spectra for every organism or cell component of interest is impractical. Therefore, action spectra are commonly applied to experimental irradiance conditions vastly different from the conditions in which they were originally determined (Behrenfeld *et al.* 1993). For example, Smith and Baker (1980) investigated the effects of UVR on photosynthesis in laboratories. Although the BWF obtained from these measurements has been cited often, Worrest *et al*. (1981) point out that the application of BWFs in nature is problematic, as there are a plethora of biological, physical, chemical and temporal interactions (both positive and negative) which have to be considered.

Setlow (1974) established a relation between the effects of UVR on the damage of a special target in the DNA, which is responsible for inducing skin cancer, and this work led to the development of a frequently cited action spectrum for UVR-induced DNA damage. Setlow found that the use of the erythemal weighting function for estimating changes in carcinogenic doses underestimates the actual effect. In this manner, Setlow (1974) illustrated the difficulties which occur when applying various action spectra to the same target.

2.3.2.2 Research – UVR, PAR and BWFs

UVR interacts with particles and molecules in the media through which it travels and can change the properties of these media (water and ice) during this process. Marine organisms, such as phytoplankton and sea ice algae inhabit these media and are also potentially impacted by UVR, as it has damaging effects on various biological targets. For example, the effects of UVR on human skin are obvious from sunburn, also known as the erythemal response, and is caused mainly by UVB radiation of around 290 nm (Tevini 1993). DNA also shows a strong response to UVB radiation. The chemical structure of DNA determines that the highest absorption of UVR by DNA occurs at ~260 nm (Tevini 1993). The damage of DNA in a cell results in higher mutation rates and in some cases, irreversible cell damage.

Proteins, such as enzymes, and cell membranes also respond adversely to UVB radiation and since DNA, proteins and membranes are all part of a cell, damage to any of these targets could potentially result in altered cell functions or even the destruction of the whole cell. Repair and protection mechanisms have evolved in several species; for example, excision repair, photo reactivation and post-replication repair (Tevini 1993; Davidson *et al.* 1996; Vernet 2000). Besides physiological repair at the cellular level, behavioural adaptations, such as avoidance, screening and quenching, have been developed by organisms to protect themselves against the

effects of UVR (Davidson 1998). Roy (2000) includes more details of strategies to minimise UV-induced damage.

The absolute magnitude of UVR exposure is not the sole factor responsible for damage to organisms. When the irradiance of UVB increases due to ozone depletion, there is no proportional increase in longer UVA and blue wavelengths involved in photo-reactivation and photo-repair. There is a resulting net increase in the amount of DNA damage (Sancar *et al*. 2004). The transmission in marine environments varies significantly with changes in the stability and optical properties of the water column due to seasonal variation in solar irradiation, phytoplankton blooms, or increases in dissolved organic matter (Smith *et al.* 1992; Kuhn *et al.* 2000; Lesser 2000). This variability in the attenuation of UVR has been shown to be a significant determinant of the biological effects on the planktonic life-history phases of marine organisms from a variety of taxa (Smith *et al.* 1992; Herndl *et al.* 1993; Jeffrey *et al.* 1996; Malloy *et al.* 1997; Lesser and Barry 2003). Lesser *et al.* (2006) provides a detailed explanation of the means whereby UVA and UVB damage DNA.

The ratios of UVB:UVA:PAR are important determinants of beneficial and harmful effects to organisms. For example, UVB radiation can reduce the survival rate of one species, whereas UVA radiation and PAR can support repair and survival under natural conditions (Davidson *et al.* 1996; Vernet 2000). Varying levels of UVB radiation result in a shift of the natural ratio of UVB:UVA and UVB:PAR, which is followed either by an increase or decrease of growth for a species, depending on its sensitivity to UVB radiation. Changes in the spectral balance (i.e. ratio of UVB over PAR + UVA + UVB) caused by ozone depletion can also potentially interfere with the mechanisms controlling motility in many micro-organisms, and thus their ability to avoid excessive light (Roy 2000). Since ozone has a higher attenuation for the shorter wave lengths within UVB radiation, the depletion also changes the spectra within this range (Madronich *et al*. 1998).

While laboratory research cannot exactly replicate Antarctic environmental conditions, this research is still valuable due to the great difficulties in performing *in situ* measurements (insufficient instrumentation and logistic constraints) in the Southern Ocean region. It is particularly useful to obtain information about the general effects of UVR on photosynthesis under controlled conditions, such as the light field and duration of exposure (Smith and Baker 1980; Worrest *et al.* 1981; Cullen and Lesser 1991; Cullen and Neale 1994). In more recent years, *in situ* measurements have been carried out to measure the actual influence and effects of UVR on phytoplankton photosynthesis in the field (Holm-Hansen *et al.* 1993; Boucher and Prezelin 1996; Neale *et al.* 1998a; Bracher *et al.* 1999; Neale *et al.* 2001a; Sinha and Hader 2002; Fritz *et al.* 2008)

Behrenfeld *et al*. (1993) wrote that the most commonly applied action spectra in studies of UVB radiation effects on marine phytoplankton were not derived for marine phytoplankton (see article for details of action spectra applied at the time). They also stated that three additional action

spectra had recently been reported that were more appropriate for marine phytoplankton (Cullen *et al.* 1992; Helbling *et al.* 1992; Lubin *et al.* 1992) although a wavelength-specific action spectrum for natural phytoplankton assemblages had not at that time been described.

Marine environments may experience future increases in UV radiation penetration if sea ice, which is relatively opaque and highly reflective (Lesser *et al*. 2004), decreases in spatial and temporal extent as a result of global warming (Holland *et al*. 2006). In the aquatic environment, the damaging spectrum is determined by the attenuation in the water, which is strongly dependent on the water quality, especially the content of organic matter (Piazena *et al*. 2002). It has been shown that, at least in warmer waters, microalgae repair photo damage so that damage from UVB radiation results in a photosynthesis rate in equilibrium between damage and repair (Litchman *et al*. 2002). In colder water it has been shown to repair much slower, so that the equilibrium state is never reached; instead damage accumulates and the effect depends on the UVB radiation dose. As an example, Lamare *et al*. (2007) demonstrated a slower rate of DNA repair for Antarctic sea urchin embryos when compared to non-Antarctic species. The case of equilibrium leads to a steady-state situation where the effect of UVB radiation is solely dependent on the dose rate of UVB radiation (Andreasson and Wängberg 2006).

2.3.3 Interactions between UVB radiation and other stressors

An assessment of UVB effects for polar aquatic ecosystems is complex and requires consideration of the ecosystem as a whole (Häder *et al.* 2003). In particular, climate variability has been shown to have important synergistic influences on UVB. Because the temperature is close to freezing, polar ecosystems are particularly sensitive to change, as the freeze/thaw boundary applies critical limits to subsequent environmental responses, including: air and water temperature; the timing, extent and duration of ice and snow cover; changes in surface albedo; changes in water column CDOM concentrations; and the level of solar radiation and its penetration depth. Such changes, driven by climate variability, may be more important for UVB exposure levels and spectral balance between UVB and PAR than ozone depletion. In addition, the known increases in UVB from reduction of stratospheric ozone may be augmented or reduced by changes in cloud cover related to climate variability (Häder *et al.* 2003).

It has been shown that long-term effects of UVB radiation may become manifest only in combination with other stressors (De Lange and Lürling 2003). The actual and potential effects of changes in single environmental variables are being studied intensively but the interactive effects of multiple stressors on aquatic systems (including UV radiation, climate change, temperature, precipitation, eutrophication, food web alterations, pH, toxic metals and oil contamination) have received little research attention, despite often showing enhanced damage to the system (UNEP 2005). For example, research by Hoffman *et al*. (2003) suggested that the ability to predict the effects of global change hinges on understanding interactions among environmental variables, imposing strict limits on inferences made from single-factor

experiments. Climate change can alter responses to UV through temperature-mediated effects in aquatic ecosystems, and these effects can be species specific, and are dependent on repair ability (MacFadyen *et al*. 2004). There is also emerging evidence that global warming and acid precipitation may allow increased penetration of UVB and UVA radiation into aquatic environments, predominantly through decreases in attenuation of radiation by DOC (UNEP 2005).

2.3.4 Consequences of decreased uptake of carbon

Every drop of water in the top 100 metres of the ocean contains thousands of free-floating, microscopic flora called phytoplankton. These single-celled organisms (including diatoms and other algae) inhabit three quarters of the Earth's surface, and yet they account for less than 1 per cent of the 600 billion metric tons of carbon contained within its photosynthetic biomass. This virtually invisible forest has a vital role in the planet's most critical natural cycles (Falkowski 2002).

Phytoplankton fix carbon into organic matter through the process of photosynthesis (McLain *et al.* 1993), providing the primary source of energy for higher trophic levels in the marine food web. Photosynthesis is by far the major route of entry of inorganic carbon into the organic realm (Falkowski and Rosenthal 2001). Until recently, few researchers appreciated the degree to which phytoplankton can draw the greenhouse gas, carbon dioxide out of the atmosphere and oceans – 45 to 50 billion metric tons per year of inorganic carbon are incorporated into their cells (Falkowski 2002). New satellite observations and extensive oceanographic research projects are revealing how sensitive these organisms are to changes in global temperatures, ocean circulation and nutrient availability (Falkowski 2002). Phytoplankton can further influence global climate by releasing sulphur compounds that promote cloud formation over oceanic areas (Curran and Jones 2000).

Changes in solar UV radiation can have significant effects on aquatic carbon cycling, nutrient cycling, and water-air trace gas exchange. Co-occurring climate change can influence these UV effects (Zepp *et al.* 2003). UVB accelerates the decomposition of CDOM entering the sea via terrestrial runoff, thus having important effects on oceanic carbon cycle dynamics (Zepp *et al.* 2003).

Changes in aquatic primary productivity and decomposition due to climate-related changes in circulation and nutrient supply, which occur concurrently with increased UVB exposure, have synergistic influences on the penetration of light into aquatic ecosystems. New research has confirmed that UV affects the biological availability of iron, copper and other trace metals in aquatic environments thus potentially affecting the growth of phytoplankton and other micro-organisms that are involved in carbon and nitrogen cycling. There are several instances where UVB modifies the air-sea exchange of trace gases that in turn alter atmospheric chemistry, including the carbon cycle (Zepp *et al.* 2003).

There are major feedback loops between climate change and other environmental variables and primary productivity. The primary producers are responsible for a large uptake of atmospheric carbon dioxide, part of which is sunk into the marine sediments as oceanic snow. Because of physiological differences in the substrate affinity of the carbon dioxide fixing enzymes in different organisms, changes in the partial pressure will alter autotroph diversity (Tortell 2000). With phytoplankton productivity being affected by climate change, this will simultaneously modify the degree of climate change (Beardall *et al.* 1998; Sarmiento *et al.* 1998; Louanchi and Hoppema 2000; Falkowski and Rosenthal 2001). Increasing temperatures enhance rainfall and melting of glaciers and ice shelves, augmenting the runoff of melt water, and stabilising the stratification of the water column, which in turn increases the sedimentation of particulate organic matter. Pronounced stratification decreases nutrient concentrations of coastal waters and increases UVB exposure of phytoplankton (Neale *et al.* 1998b; Arrigo *et al.* 1999).

It is clear that variations in UVR, and UVB in particular, are important to polar ecosystems. The exact mechanisms are known to some extent, but it is still a fertile area of research for biologists in the Antarctic and Southern Ocean region. The next chapter focuses on the physical factors which determine the level of UV radiation reaching the Antarctic environment.

3. FACTORS AFFECTING LEVELS OF UVB

As a consequence of ozone depletion in Antarctica, increases in erythemal UV radiation in 1998 relative to the values in the 1970s were estimated to be about 130% in spring (Madronich *et al.* 1998). This meant an increase in the ratio of UVB (280-325 nm) to both UVA (325-400 nm) and PAR (400 to 700 nm) (Frederick and Lubin 1994; Jones and Shanklin 1995; Herman *et al.* 1996; Madronich *et al.* 1998). Changes in the UVB:PAR ratios are an important indicator of the effectiveness of DNA repair processes because to be catalytically active, photolyase, which repairs UVR-induced photolesions, requires UVA and visible radiation (Lesser *et al.* 2004).

To develop a radiative transfer model which includes exact measurements of all parameters that affect levels of ultraviolet radiation would be far too resource hungry to warrant its development. In this project, it is shown that by including the total ozone column amount, the surface albedo, the SZA, the Earth-Sun distance, and estimates of cloud amount in the calculations, the resultant modelled values of UVB radiation at the Earth's surface are comparable to actual measurements made in both the sea-ice zone and at three Antarctic research stations (see Section 8.2 for validation processes). Model calculations indicate that UVB radiation increases by 5%/kilometre in altitude (Bodeker 1997) but this will not be taken into account in this project as all of the study area is at sea level. Each of the other contributing factors will now be discussed.

3.1 Ozone

The gradual formation of ozone in the Earth's atmosphere over geological time scales has resulted from interaction between the incoming solar radiation and molecular oxygen (Berkner and Marshall 1965; Dave and Halpern 1976). Ozone is continuously created and destroyed by the action of ultraviolet sunlight, so the overall amount of ozone in the global stratosphere is determined by the magnitude of these production and loss processes, and by the rate at which air is transported from regions of net production to those of net loss (Schoeberl 2002).

Approximately 90% of ozone is located in the stratosphere (Díaz *et al.* 2000), with maximum concentrations found at altitudes between 15 and 35 kilometres – the region known as the 'ozone layer' (see Figure 3.1). Although the global amount of ozone is fairly constant, the photochemical, diffusion and dynamical processes lead to rather large latitudinal and seasonal variations in the amount of ozone in an atmospheric column of unit cross-section (Dave and Halpern 1976) (see further discussion of these variations in Section 3.1.4).

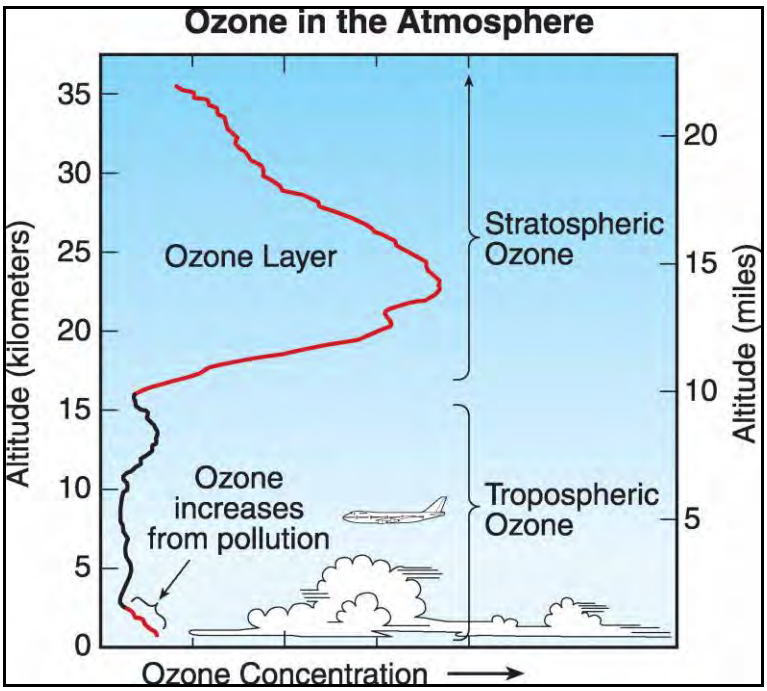

Figure 3.1: Ozone is present throughout the lower atmosphere (troposphere and stratosphere). Most ozone resides in the stratospheric 'ozone layer' above Earth's surface (between15 and 35 kms) (from http://www.esrl.noaa.gov/csd/assessments/ozone/2006/twentyquestions.html).

While ozone only represents about one millionth of the total mass of the atmosphere, it is one of the most active and important trace species in the atmosphere as it plays two critical roles (Müller *et al.* 2003). Firstly, it removes most of the biologically harmful ultraviolet radiation in the UVB range (λ = 280-325 nm) and all UVC radiation (λ< 280 nm) before the radiation reaches the surface (Dave and Halpern 1976). If all others factors (cloudiness, turbidity, etc.) remain the same, a decrease in the stratospheric ozone leads to an increase in solar radiation at the Earth's surface (Frederick and Snell 1988; Lubin *et al.* 1989a; Stamnes *et al.* 1992; Madronich *et al.* 1998; Peeters *et al.* 2000; Whitehead *et al.* 2000; Staehelin *et al.* 2001; McKenzie *et al.* 2003). This role of ozone was the reason for concern by scientists when the springtime Antarctic ozone hole was first observed by a Dobson instrument in the early 1980s (Farman *et al.* 1985). The existence of the hole was later confirmed by the Total Ozone Monitoring Spectrometer (TOMS) instrument on the NASA Nimbus 7 satellite (Stolarski *et al.* 1986; Bramstedt *et al.* 2003). When the ozone hole was over Punta Arenas, some wavelengths of UVB increased by more than 20 times compared with similar days when column ozone was normal (Casiccia *et al.* 2003). Moreover, ozone plays an essential role in determining the temperature structure and, therefore, the radiative heating/cooling balance in the atmosphere, especially so in the stratosphere (Schoeberl 2002).

Measurements of the total integrated column ozone based on ultraviolet absorption began in the first few decades of the twentieth century (e.g. Fabry and Buisson 1913; Dobson 1968; Dütsch 1974). Systematic measurements of this type have revealed that the total ozone abundances over many regions of the world have decreased markedly since about 1980, but the behaviour

seen in recent decades in the Antarctic spring lies far outside the historical variability (Solomon 1999). Conventionally, it is considered that there is an ozone hole when the ozone abundance is $\leq$ 220 Dobson Units (DU where 100 DU = 1 atm mm) in a specific location (Alvarez-Madrigal and Pérez-Peraza 2005). For example, a 60% decrease in ozone might result in 130-1900% increases in 305 nm irradiances at noon (Díaz *et al.* 2006).

In recent years, the ozone hole area has shown a larger variability than previously observed (Newman *et al.* 2006), with the year 2006 demonstrating the largest ozone hole ever and 2008 featuring the fifth largest on record (see Figure 3.2). It was shown by different studies (Kirchhoff *et al.* 1997; Cede *et al.* 2002b; Pazmiño *et al.* 2005) that the sub-polar regions of the Southern Hemisphere were affected by short periods of weak total ozone values directly linked to overpasses of the ozone hole. Pazmiño *et al.* (2008) used the UV index (UVI) together with total ozone and reflectivity (or surface albedo – see Section 3.2.4 for explanation) data from TOMS in order to characterise the UV enhancements in sub-polar regions associated with the intrusion of polar ozone-depleted air masses in the 1997-2005 period. This work showed that the sub-polar regions experience a pronounced ozone reduction with generally an enhancement of UVB radiation, depending on cloud cover conditions. For example, UVI increases larger than 80% for total ozone column (TOC) decreases larger than 45% were observed in September, October and November in the 50°– 60° S latitude band for that time period (Pazmiño *et al.* 2008).

It is well known that the main cause of the ozone depletion in Antarctica is anthropogenic activity; however, it was originally suggested that the origin of the "hole" could be explained on the basis of solar cycles or purely atmospheric dynamics (e.g. Tung *et al.* 1986). These hypotheses subsequently became inconsistent with observed features of the Antarctic ozone hole (e.g. Seinfeld and Pandis 1998). Nevertheless, according to Labitzke *et al*. (2002) and WMO (2003), recent modelling studies report increased sensitivity of lower stratospheric ozone to the solar cycle compared with earlier modelling experiments, but any effect is still too uncertain to quantify, remaining somewhat speculative (Alvarez-Madrigal and Pérez-Peraza 2005).

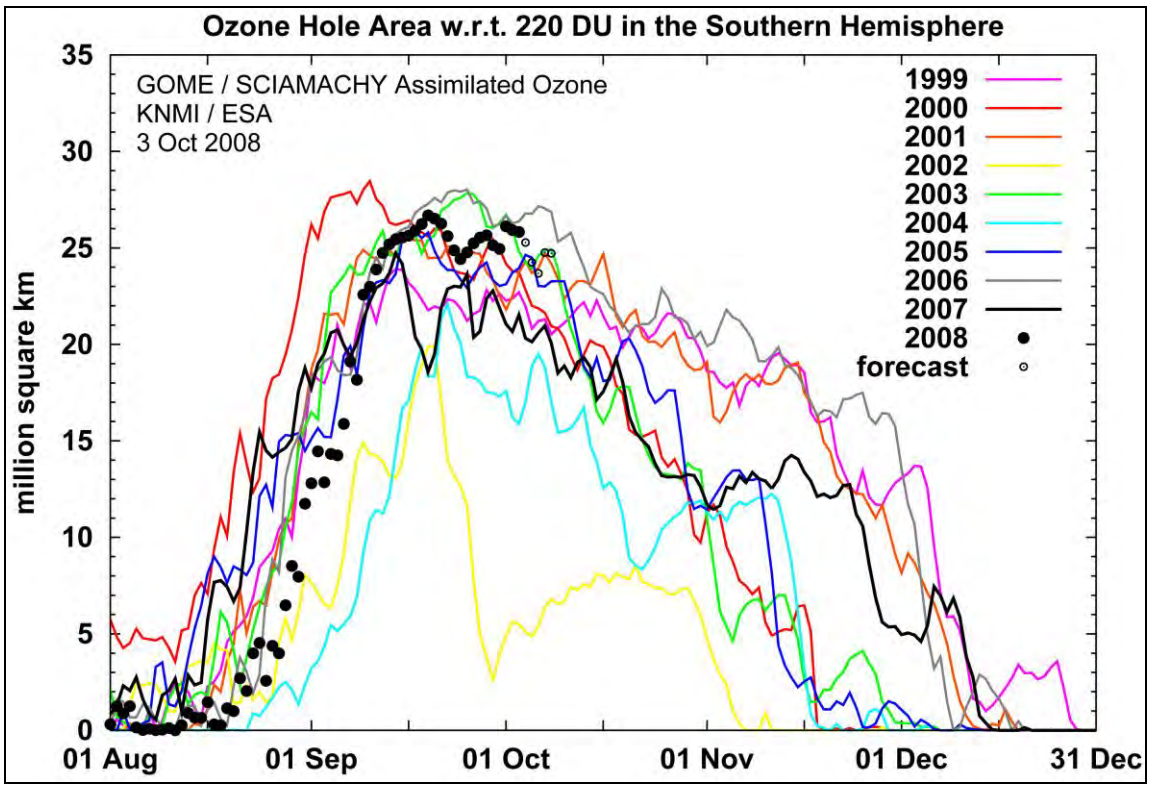

Figure 3.2: The area of the ozone hole (ozone levels are less than or equal to 220 DU) over the South Pole, 1999-2008. The ozone data used in this analysis is the combination of GOME (Global Ozone Monitoring Spectrometer) and SCIAMACHY (Scanning, Imaging and Absorption Spectrometer for Atmospheric Cartography). Credits:Royal Netherlands Meteorological Institute (KNMI) and European Space Agency (ESA) (2008).

3.1.1 Techniques and records of atmospheric ozone measurements

While scientific interest in ozone began more than a century ago, its systematic global monitoring at sites worldwide can be traced back to the International Geophysical Year in 1957-1958, when international effort helped to foster construction and year-round use of Antarctic research stations (Solomon *et al.* 2005). Among the fledgling observational records begun at that time were measurements not only of meteorological parameters, such as temperature, pressure, and wind, but also of ozone. Three stations in Antarctica have archived nearly continuous daily measurements of the total integrated ozone column since at least the 1960s: the British station at Halley (see Figure 2.3), the Japanese station at Syowa (see Figure 2.3), and the American station at the South Pole (see Figure 2.3). Records of the vertical profile of ozone as measured by balloons on a weekly or bi-monthly basis began in the 1960s at just two stations still measuring today, Syowa and the South Pole. Only the Syowa data cover the period from 1973 to 1985, making that ozonesonde record unique in its vertically-resolved coverage of the Antarctic ozone layer during a critical era in its evolution.

Global ozone monitoring is based on a data quality controlled network of ground-based measurements and satellite observations in order to make best use of the complementary

strengths of measurements from ground and space. Staehelin *et al.* (2001) summarised the principles of techniques that were developed for atmospheric ozone measurements, referring readers to WMO (1999) and Harris *et al*. (1999) for more details.

Bernhard *et al*. (2002) proposed a new algorithm to calculate total column ozone from global irradiance measurements. Bernhard *et al*. (2003) carried out a thorough uncertainty evaluation of the method and compared the resulting data set with TOMS and ground-based Dobson measurements at Barrow, Alaska. Large SZAs, although not a specific problem of the algorithm, are a principal limitation in the accuracy of any method used to calculate total ozone column from global irradiance spectra. A second important source of uncertainty is the scatter introduced by clouds, although the scatter can be significantly reduced with simple filter algorithms. To further reduce cloud-related uncertainties, ozone values could be calculated from diffuse rather than global irradiance model values whenever the direct beam of the sun is blocked (Bernhard *et al.* 2003).

Bojkov and Fioletov (1995) analysed all available total ozone data from over 150 past and present Global Ozone Observing System (GOOS) stations in order to deduce the basic global ozone characteristics both for pre-ozone-hole and during 'ozone hole' time periods. They utilised satellite (TOMS) data to estimate the longitudinal inhomogeneity of the total ozone distribution. They determined that all errors and uncertainties for the two observing systems (ground-based and TOMS) are, in general, about 1% or less. Bramstedt *et al*. (2003) investigated the drift of total ozone determined from TOMS on the Earth Probe satellite (EP-TOMS) and Global Ozone Monitoring Experiment (GOME) in comparison to ground-based measurements from Dobson and Brewer stations collected by World Ozone and Ultraviolet Data Centre (WOUDC), and they found that the overall agreement of all satellite total ozone data sets used (EP-TOMS, GOME Differential Optical Absorption Spectroscopy (GOMEDOAS), GOME Full Retrieval Method (GOMEFURM) and GOMETOMS) is generally very high, and in most cases within the uncertainty of the Dobson measurements (2%).

Ground-based instruments are easily calibrated and recalibrated, have finer spatial and temporal resolution and they do provide long and stable data records for a specified location. One of the major difficulties in using ground-based stations for estimating global ozone changes is the uneven distribution of stations and the longitudinal inhomogeneity in the total ozone field (Bojkov and Fioletov 1995). Satellite instruments provide a complete global coverage at a moderate resolution with standard sensors overcoming the limitations of sparse and non-uniform spatial coverage, and variable observation standard and quality. Over the last three decades, satellite data have been used to monitor long-term global changes in stratospheric ozone. Measurements from ground-based instruments come to the fore in ground-truthing the satellite data. Global total-ozone measurements are produced by satellite instruments like the TOMS (1978 – present) (Stolarski *et al.* 1991), the Solar Backscatter Ultraviolet Radiometer (SBUV) (SBUV – 1st November, 1978 to 21st June, 1990, SBUV/2 – 2001 ongoing) (Heath *et al.* 1975),

the TIROS Operational Vertical Sounder (TOVS) (5-day files 1978-1994, daily files 1984-1994) (Planet *et al.* 1984), and the GOME (1995 – present) (Hahne *et al.* 1993). Satellite instruments need to be validated during their complete lifetime to ensure the ongoing quality of the measured data, and to avoid long-term drifts in their data from instrumental aging effects.

Ozone maps are often hampered by missing data due to, for example, retrieval problems in the case of clouds (TOVS) or limited swath width (SBUV, GOME). In these cases only sparse data are obtained, and it is often difficult to characterise features in the ozone distribution (Levelt *et al.* 1996). Another fundamental problem with the use of data from polar orbiting satellites is that the observations are not made simultaneously. Global maps can be constructed by overlaying subsequent tracks observed at different times. However, spurious gradients due to changes in the ozone distribution in time can occur between adjacent tracks measured at different times.

Aerosols introduced by Mount Pinatubo were noted to produce errors in satellite-derived total ozone measurements (Bhartia *et al.* 1993; Harris *et al.* 1997). Radiative transfer calculations show that, except at very high SZAs, errors in total ozone derived from the aerosol-contaminated radiances are less than 2%, and vary both in magnitude and in sign with angles of observations.

Ozonesondes make *in situ* ozone measurements up to 30-35 km, while lidar and microwave instruments measure ozone vertical profiles from the ground to about 50 km. The Umkehr method also provides vertical profile data from ground-based observations by Dobson and Brewer instruments. Fioletov *et al.* (2006) used comparisons with ozonesonde, Umkehr and Stratospheric Aerosol and Gas Experiment II (SAGE II) measurements to evaluate SBUV/2 version 8 performance as well as uncertainties in the other types of ozone measurement. Fioletov *et al.* (2006) showed that sets of parallel measurements of the same parameter by two different instruments make it possible, under some basic assumptions, to estimate both the instrument uncertainties and parameter variability. They demonstrated that SBUV/2 data can be successfully used to estimate ozone variability, although the data are not completely free from some instrument or algorithm-related problems.

The downward ozone trend was predicted to cease followed by a slow recovery. In their desire to be able to determine, at the earliest possible time, when a recovery can be said to have begun, Jaross *et al.* (2003) required an understanding of the sources of uncertainty in the determination of the time-dependent calibration of each instrument as well as their inter-calibration. They estimated the uncertainties that would result when combining multiple TOMS datasets to produce a long-term column ozone record. Their investigations resulted in an uncertainty of just less than 1% per decade, close to the trend uncertainty from TOMS/N7 (the TOMS sensor on the Nimbus 7 platform) alone and to the goal for long-term ozone monitoring. The three-year data gap in TOMS data in the mid-1990s also contributes to the trend uncertainty. The re-calibrated SBUV/2 was utilised to bridge the gap between the TOMS datasets (Jaross *et al.* 2003) and this marginally reduces the uncertainty. The differing TOMS and SBUV wavelength range leads to some small differences in column ozone retrieval

algorithms, but these do not result in significant column ozone trend differences (Jaross *et al.* 2003).

Masserot *et al*. (2002) used one year (2000) of spectroradiometric data to retrieve total ozone column amount from the ratio of irradiances around 305 and 340 nm, using look-up tables based on modelled data. During cloudless days, ozone values from direct sun observations agree to within 5 DU. These ground based values compare reasonably well (to within about 4% or 12 DU) with TOMS ozone data; which is consistent with the uncertainty of both methods which is estimated as 5 DU for TOMS, and 5-7 DU for clear sky ground-based measurements.

3.1.2 How ozone depletion happens

About 18% of stratospheric chlorine comes from natural sources, such as forest fires and certain marine organisms (see Figure 3.3). The remaining 82% comes from chlorofluorocarbons (CFCs) and other chlorine-containing chemicals released as a result of anthropogenic activity (Dave and Halpern 1976; Schoeberl 2002).

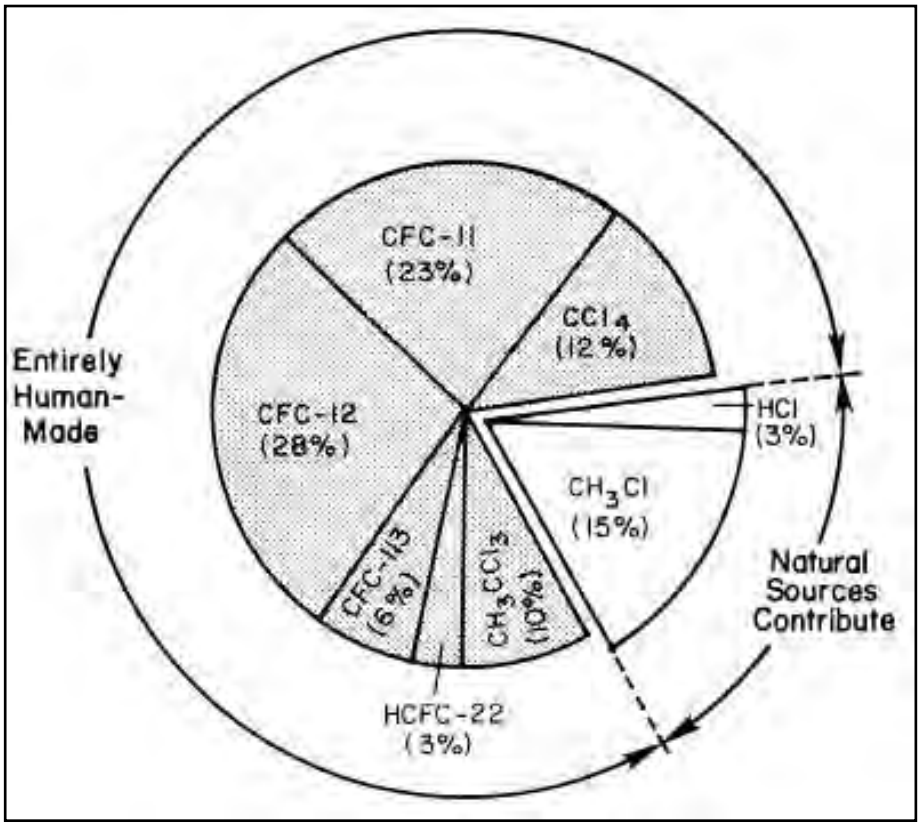

Figure 3.3: Primary sources of chlorine entering the stratosphere in the early 1990s (NOAA Aeronomy Lab 2004).

Molina and Rowland (1974) described how CFCs had been added to the environment in steadily increasing amounts over several decades as a consequence of their use as aerosol propellants, refrigerants, cleaning compounds for electronic parts and blowing agents for foam

manufacturing. CFCs have long residence times in the atmosphere (50-200 years). While they are quite stable and inert in the troposphere, they can diffuse through the troposphere to reach stratospheric altitudes (14 to 24 km) (Wofsy *et al.* 1975), where photolysis by ultraviolet radiation releases chlorine with subsequent destruction of ozone through catalytic cycles (Schoeberl 2002) (see Figure 3.4). Each chlorine atom can destroy over 100,000 ozone molecules. The catalytic reactions involving the released chlorine which destroys ozone are described by Whitehead *et al*. (2000).

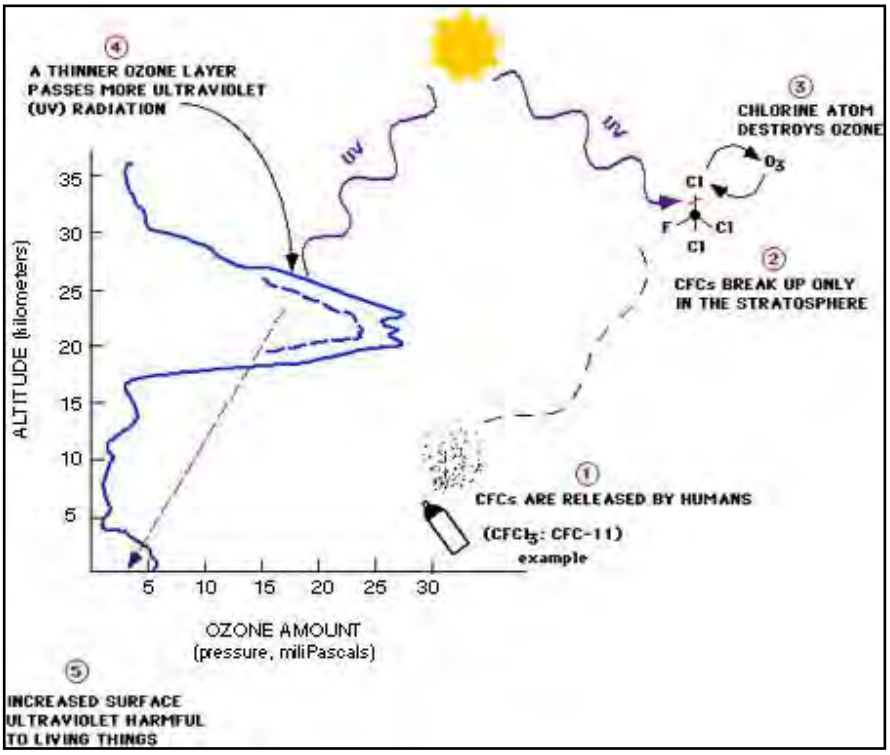

Figure 3.4: Variation of ozone amount with altitude in the atmosphere and simplified cycle of reactions in which chlorine destroys ozone (NOAA 2005).

The gas phase reactions can occur anywhere in the stratosphere; however, the rates are not fast enough to explain the large ozone hole that has regularly formed in Antarctica since the early 1980s. In the gas phase reactions, reactive chlorine species (atomic chlorine and hypochlorite) can be removed from the ozone destruction cycle and transformed into non-reactive reservoir chlorine compounds (hypochlorous acid, chlorine nitrate) (Whitehead *et al.* 2000). A rapid conversion of reservoir chlorine into reactive chlorine is necessary to explain the ozone hole over Antarctica. The mechanism for this rapid conversion was found to be provided by heterogeneous (gas-solid) reactions catalysed on the surface of polar stratospheric clouds (PSCs) (Whitehead *et al.* 2000).

The strong polar vortex that surrounds Antarctica during the winter reduces atmospheric exchange with lower latitudes and allows the build-up of stratospheric molecular chlorine and hypochlorous acid (Whitehead *et al.* 2000). With the increase of solar radiation in the spring, the

build-up of molecular chlorine and hypochlorous acid released from the gas-solid reactions is photolysed, and reactive chlorine atoms are released to drive the catalytic ozone destruction. The process continues until the PSCs dissipate later in the spring due to stratospheric warming (Whitehead *et al.* 2000). Spring also brings a weakening of the polar vortex, which allows air with higher ozone concentration to invade from lower latitudes together with the advection of air with low ozone away from Antarctica (Whitehead *et al.* 2000).

Modelling studies have shown that chlorine is the most important factor in stratospheric ozone depletion (Chipperfield and Pyle 1998). Stratospheric bromine chemistry may become more important only if the stratospheric chlorine loading decreases substantially. Since many CFCs have long lifetimes in the atmosphere, the decrease of stratospheric chlorine levels will be gradual over the next few decades, even if the production of CFCs is drastically limited (WMO 1999). The relative importance of bromine in the destruction of ozone is expected to increase in the middle of the 21st century (Stenke and Grewe 2003).

3.1.3 Other anthropogenically induced ozone depletion

The ozone layer will also be affected to some extent by the changing atmospheric abundances of several other human-influenced constituents, as well as by the changing climate of the Earth. Paradoxically, the emissions of greenhouse gases that tend to cause a temperature increase at the Earth's surface also produce a decrease in stratospheric temperatures, thereby accelerating the formation of PSCs that catalyse the CFC-ozone reactions (Vincent and Roy 1993; Lachlan-Cope *et al.* 2009). How a cooler stratosphere affects radiative balance in the rest of the atmosphere has been the subject of many detailed studies, which the IPCC re-analysed and integrated into the report, 'Climate Change 1994: Radiative Forcing of Climate Change' (IPCC 1995), which states that stratospheric ozone loss leads to a 'small but non-negligible offset to the total greenhouse forcing from carbon dioxide, nitrous oxide, methane, CFCS…'. It is ironic that the size of the negative radiative forcing from ozone loss is nearly equal to the positive radiative forcing from CFCs, the source of the stratospheric ozone loss (Schoeberl 2002). The IPCC's 'Climate Change 2007: Synthesis Report' (2007) reiterates that 'the observed pattern of tropospheric warming and stratospheric cooling is *very likely* due to the combined influences of green house gas increases and stratospheric ozone depletion'.

The prediction that increased atmospheric carbon dioxide concentrations will increase ozone depletion globally (Austin *et al.* 1992) is of concern, as the ultraviolet radiation-DMS feedbacks (see Section 3.1.8) as described in Larsen (2005) would then be expected to further amplify the greenhouse gas-driven tropospheric warming. Bouwman (1998) wrote that another anthropogenic contribution to ozone depletion may include global changes in land use and the increased emission of nitrogen dioxide, as a result of fertiliser applications.

The effects of a fleet of stratospheric aircraft (High Speed Civil Transports or HSCTs) have been a subject of considerable interest since the early 1970s (Johnston 1971). Aviation has an impact

on ozone through the release of nitrogen radicals in aircraft exhaust (Broderick 1978; Schoeberl 2002). Such a fleet would directly inject nitrogen oxides (e.g. nitric oxide and nitrogen dioxide) and water into the stratosphere as well as other compounds such as unburned hydrocarbons, carbon dioxide, carbon monoxide, sulphur dioxide and soot (Miake-Lye 1992). The sulphur in the exhaust from HSCTs could lead to the generation of numerous small particles, adding to the aerosol surface area, thus enhancing the conversion of chlorine from its reservoirs to oxides of chlorine. Jackman *et al.* (1996a) investigated this possibility by updating the work of Prather *et al.* (1990), and found a 2.5 fold increase in global ozone depletion due to the use of shuttles, but determined that the calculated impact of the launch rate of Space Shuttle and Titan 4 rockets at that time to be still quite small. They noted that the calculations did not take into consideration the effects of heterogeneous reactions on alumina particles emitted by the solid rocket boosters, which could substantially alter the results.

The other condensibles in the exhaust (water vapour and nitric acid) could impact the formation or duration of PSCs. The work by Peter *et al.* (1991) demonstrated that in an atmosphere perturbed by a fleet of 600 stratospheric aircraft flying at ~22 km altitude there is the possibility of a doubling in the occurrence of Type-I PSCs and an even stronger increase of Type-II PSCs. Considine *et al*. (1994) showed that, although overall changes in model ozone response to standard HSCT perturbation scenarios were small, there was a significant increase found in ozone sensitivity in the Southern Hemisphere spring. Transport studies show that injection of exhaust into the polar vortex is unlikely (Sparling *et al.* 1995), but there is still uncertainty about what will happen as the stratosphere cools with increasing carbon dioxide concentrations (Schoeberl 2002).

All of the chemical effects of HSCT exhaust depend on how much of the exhaust products accumulate in the stratosphere. The same is true for the exhaust of the subsonic fleet, which is released in the upper troposphere and lower stratosphere. Understanding the impact of supersonic and subsonic aircraft exhaust on the stratospheric chemical balance is complex, in that knowledge of meteorological conditions, aerosol chemistry and lower stratosphere chemistry are all required to determine the direct impact of the NO_x pollutants (Schoeberl 2002). Because a large fleet of HSCTs was not built, the problem of their exhausts lost its political relevance. In more recent times the consequences of emissions from aircraft flying in the stratosphere has been re-evaluated, and their impact on column ozone is estimated to be in the order of 1% or less (Schoeberl 2002).

3.1.4 Natural causes of variation in levels of ozone

Ziemke *et al*. (2005) examined the trends in ozone for 1979-2003 in the upper and lower atmosphere over the Pacific from combined TOMS and SBUV measurements, and discovered that for this 25-year record most ozone depletion has occurred in the lower stratosphere below ~25 km altitude. They characterised the seasonal cycle, latitude dependence and long-term

trends in ozone in three broad layers of the atmosphere: upper stratosphere, lower stratosphere and troposphere. The analyses show that seasonal variability and meridional gradients of upper stratospheric column ozone (USCO) are weak in all latitude ranges, compared to lower stratospheric column ozone (LSCO). Meridional gradients are ~3-4 times larger for those in LSCO, and are opposite in sign, compared to USCO, where USCO is seen to decrease with latitude in both hemispheres.

Much of the significant ozone decreases in the 1980s and 1990s is attributed to human activity, but natural variations also affect ozone and serve to either mitigate or enhance the decreases in ozone caused by increases in stratospheric chlorine and bromine. Jackman *et al.* (1996b) modelled stratospheric transport and photochemistry to predict ozone changes that have occurred in the past 20 years from anthropogenic chlorine and bromine emissions, solar cycle ultraviolet flux variations, the changing sulphate aerosol abundance due to several volcanic eruptions, solar proton events (SPEs), and galactic cosmic rays (GCRs) (McConnell and Jin 2008). Figure 3.5 depicts the results of modelling these aforementioned natural and anthropogenic atmospheric variations.

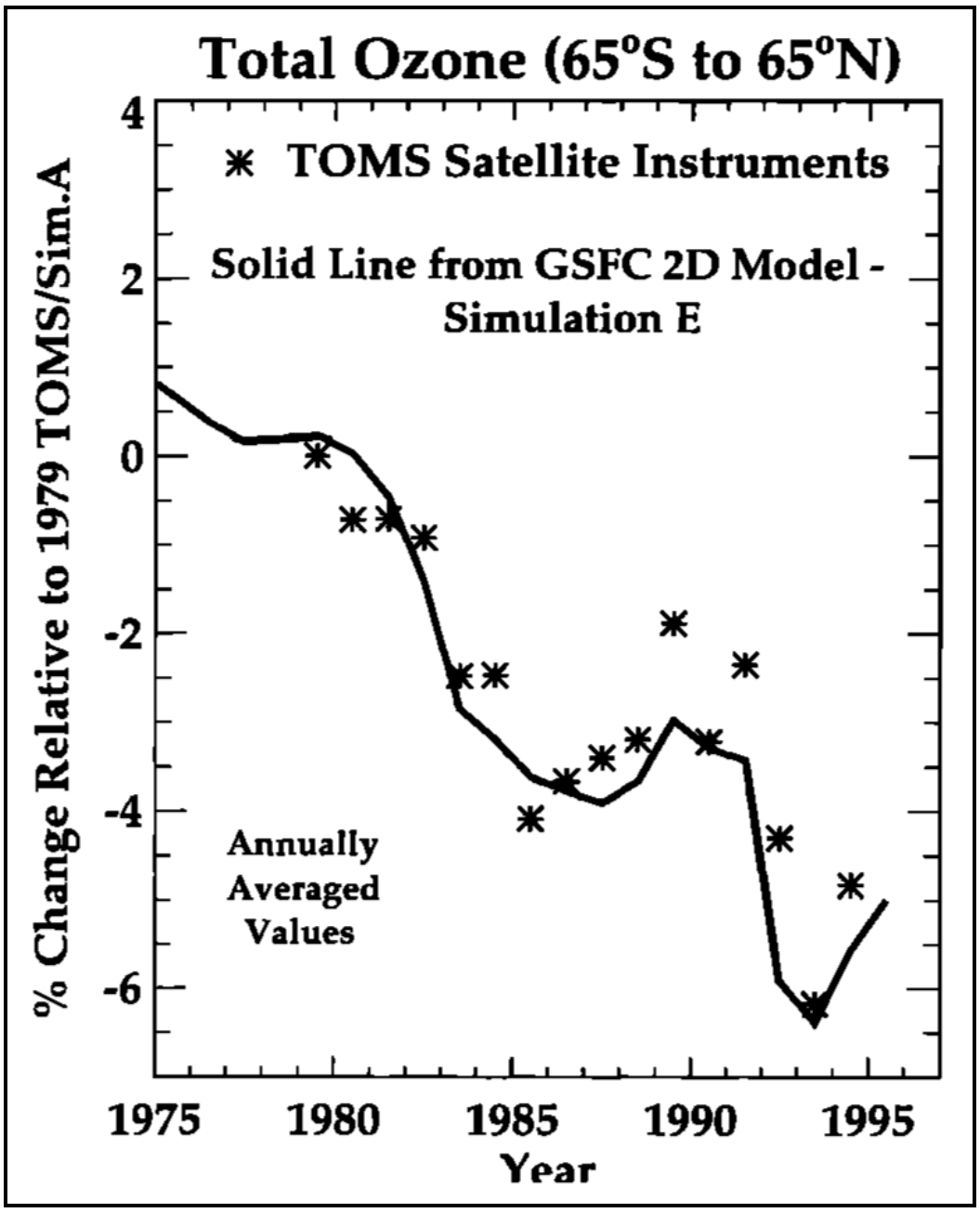

Figure 3.5: Percentage total ozone changes in the 65° S to 65° N latitude range for TOMS version 7 relative to the 1979 TOMS value (represented by stars). Also shown are percentage total ozone changes for the simulation which included chlorine and bromine increases, solar UV flux variations, SSA burden variations, SPEs and GCRs from the GSFC 2-D model, all relative to the 1979 simulation A value (see Jackman *et al*. (1996b) for details).

3.1.4.1 Solar radiation

Ozone formation is fundamentally linked to the levels of ultraviolet radiation reaching the Earth; therefore natural variations in that radiation must be understood in order to detect trends. The ultraviolet comprises only 1-2% of the total solar radiation, but it displays considerably more variation than the longer wavelength visible radiation. For example, from 1986 to 1990 the solar UV increased with the onset of the 11-year solar cycle and resulted in an increase of global total

ozone of almost 2% (Schoeberl 2002). This natural increase in ozone is comparable to the suspected anthropogenic decrease in ozone, and needs to be understood in order to totally separate the anthropogenic decrease from this natural change. Studies of total ozone trends typically subtract solar cycle and other natural changes from the total ozone record in trend resolution (Stolarski *et al.* 1991; WMO 1995; Schoeberl 2002), thus quantitative knowledge of this natural solar cycle-induced total ozone change is essential.

The research by Zerefos *et al.* (2005) showed that the amplitude of the solar activity signal in the ozone profiles, as evidenced from satellite data analysis, amounts to about 2% of the mean ozone values in the middle and upper stratosphere over most latitudes. Exceptions were seen over the high latitudes of the Southern Hemisphere and over the tropics, where there appeared to be a solar activity signal also in the lower stratosphere.

3.1.4.2 Volcanic eruptions

Inter-seasonal changes in ozone are also linked to the amount of volcanic aerosols in the stratosphere (Schoeberl 2002). For example, sulphate aerosol particles from the Mount Pinatubo eruption in June 1991 resulted in new ozone depletion in 1992 and 1993 in the 10-12 km layer, where it is too warm for PSCs to form. The volcanic aerosol also augmented depletion related to PSCs in the 12-16 km region (Hofmann *et al.* 1997). Heterogeneous reactions promoted by the increased stratospheric sulphate aerosol (SSA) surface area can convert more NO_x to nitric acid, which in turn allows more chlorine to exist in forms that actively destroy ozone (Jackman *et al.* 1996b). Modelling by Dyominov and Zadorozhny (2005) showed that the ozone depletion induced by a volcanic eruption is due to stratospheric warming and a change in the distribution of ozone-destroying gas constituents in the stratosphere. The modelling undertaken by Geller and Smyshlyaev (2002) showed that variations in solar UV radiation produce global total ozone fluctuations that are comparable to those due to volcanic eruptions and increasing concentrations of chlorine and bromine during the period 1970-2000.

Solomon *et al.* (1996) found that incorporating a realistic SSA surface area density variation significantly improved the agreement between their modelled ozone changes and those from TOMS version 6 data at northern mid-latitudes. Jackman *et al.* (1996b) followed the same approach with their modelling. It was noted, however, that the observed time-dependent fluctuations in aerosol content and sunspot number since 1979 display important similarities. Hence, depending upon the analysis technique used, the important aerosol effects demonstrated by Solomon *et al*. (1996) could be confused with solar signals in statistical studies of ozone trends. They also pointed out the need to carefully consider any process that could increase aerosol abundances in evaluations of future ozone trends. For example, subsonic and supersonic aircraft emissions can increase the stratospheric aerosol burden and deplete ozone (see Section 3.1.3).

There is considerable controversy surrounding the exact nature of the aerosol surface in the Antarctic vortex and its connection to the stratospheric sulphate layer. However, the paper by Portmann *et al*. (1996) showed that significant aerosol variations are evident in the polar regions as a result of volcanic "injections", and that these aerosols are effective at converting chlorine from reservoir species to active forms, whether they remain liquid or are transformed into frozen particles. Therefore, the central result of the research by Portmann *et al*. (1996) on volcanic aerosol modulation of the Antarctic ozone hole is likely to be robust against changes in the details of aerosol transformation within the polar vortex .

3.1.4.3 Inter-annual temperature and dynamical changes

Seasonal ozone changes are largely determined by the winter-summer changes in the stratospheric circulation. Since ozone has a lifetime of weeks to months in the lower stratosphere, the amount of ozone can vary strongly due to transport by stratospheric wind systems (Weber *et al.* 2003). Weather conditions in the stratosphere vary from year to year – therefore there is also inter-annual variability in ozone amounts (Weber *et al.* 2003).

The formation of ozone by the photolysis of molecular oxygen removes most of the light with wavelengths shorter than 200 nm. The wavelengths between 200 and 310 nm are removed by the photolysis of ozone itself. This photolysis of ozone in the stratosphere is the process by which most of the biologically damaging UVB is filtered out (Schoeberl 2002). As this filtering process occurs, the stratosphere is heated. This heating is responsible for the temperature structure of the stratosphere, where the temperature increases as the altitude increases. Without this filtering, larger amounts of UVB would reach the surface.

Huck *et al*. (2005) showed that halogen loading in the stratosphere is the primary driver of the severity of Antarctic ozone depletion, but year-to-year variability on top of this secular change is driven primarily by inter-annual variability in South Pole temperatures. These temperatures in turn are affected by mid-latitude planetary wave activity, and addition of wave activity as an explanatory variable provides the most representative model of inter-annual variability in Antarctic ozone depletion. An example of how mid-latitude planetary waves perturb the Antarctic ozone hole was the wave-induced, sudden stratospheric warming in 2002, which split the polar vortex and led to the smallest ozone hole since 1988 (Varotsos 2002; Sinnhuber *et al.* 2003).

The Southern Hemisphere Annular Mode (SAM) is a circumpolar pattern of atmospheric mass displacement in which intensity and location of the gradient of air pressure between mid-latitudes (high pressure) and the Antarctic coast (low pressure) changes in a non-periodic way over a wide range of time scales (Thompson and Solomon 2002). Over the past 50 years, the SAM became more positive, as pressure dropped around the coast of the Antarctic, and increased at mid-latitudes. Since the late 1970s, this change increased the strength of westerly winds over the Southern Ocean by 15-20%. The combination of the stronger westerly winds around the

continent, with the off-pole displacement of Antarctica, has led to a deepening of the Amundsen Sea Low (see Figure 2.3), with consequent effects on temperature and sea ice in the coastal region of West Antarctica (SCAR 2009).

The SAM changed because of the increase in greenhouse gases, and the development of the Antarctic ozone hole, the loss of stratospheric ozone having by far the greatest influence (SCAR 2009). The ozone hole occurs in the austral spring. At that time of year the loss of stratospheric ozone cools the Antarctic stratosphere, so increasing the strength of the polar vortex – a large high altitude cyclonic circulation that forms in winter in the middle and upper troposphere and stratosphere over the Southern Ocean around Antarctica (SCAR 2009). During the summer and autumn the effects of the ozone hole propagate down through the atmosphere, increasing the atmospheric circulation around Antarctica at lower levels. As a result, the greatest change in the SAM, which is indicative of surface conditions, is in the autumn (SCAR 2009).

The recovery of the ozone hole, combined with a continued increase in greenhouse gas emissions, should continue strengthening the positive phase of the SAM, but with a trend that is less rapid than seen in the last two decades (SCAR 2009). Further increases of surface winds over the Southern Ocean in the summer and autumn can thus be expected. This will lead to a continuation of the poleward shift in the Southern Ocean storm track (SCAR 2009).

3.1.4.4 Quasi-biennial oscillation (QBO)

The main temporal variations of ozone include a seasonal cycle, but there are also temporal changes related to the quasi-biennial oscillation (QBO) (Huang 1996; Randel and Wu 1996; Zerefos *et al.* 1998), the 11-year sunspot cycle and the 27-day solar rotation (Chandra and McPeters 1994; Lean *et al.* 1997; Zhou *et al.* 1997; Callis *et al.* 2000; Zhou *et al.* 2000).

Simulations show that the radiative feedback effect of the QBO through solar heating on the ozone and circulation is insignificant, contrary to the theory of Hasebe (1994). On the other hand, the radiative feedback effect through perturbations of the photolysis rates on the ozone QBO is non-negligible throughout the stratosphere (Huang 1996). The peak-to-peak amplitude of the QBO in total ozone is 8% and it was found to be associated with a 21% peak-to-peak amplitude in mean solar irradiance at 305 nm. Evidence of a pronounced QBO in UVB, supported by both observations and modelling, provides a new biorhythm for UVB-dependent ecosystems and has a wide range of implications for atmospheric chemistry (Zerefos *et al.* 1998).

3.1.4.5 Downflux of NO_x

Through dissociation and ionisation processes, energetic particle precipitation (EPP) leads to routine production of odd nitrogen in the mesosphere and thermosphere, and to sporadic production in the stratosphere when very highly energetic particles are involved (Randall *et al.*

2005). EPP also indirectly affects the stratosphere via descent of EPP-produced mesospheric NO_x to the stratosphere during polar winter and spring, where it plays a major role in ozone chemistry (Randall *et al.* 2005). The analysis of NO_x and ozone data from numerous satellite instruments suggests that EPP led to substantial production of NO_x in the upper atmosphere, beginning with the remarkable storms in late October 2003 and possibly persisting through January 2004 (Randall *et al.* 2005). Downward transport of the excess NO_x, facilitated by unique meteorological conditions in 2004 that led to an unusually strong upper stratospheric vortex from late January through March 2004, caused the enhancements.

3.1.4.6 Solar Proton Events

Changes in energetic particle flux from the Sun penetrate into the middle atmosphere, and may also drive the natural ozone variations. A series of solar flares in 1989 discharged solar particles into the Earth's polar regions and led to polar ozone depletion (Jackman *et al.* 1993). Although solar proton events (SPEs) of the magnitude of those in October 1989 occur infrequently (only two were observed in the 25 years up to 2002), they need to be understood more completely to be able to separate natural from anthropogenic effects (Schoeberl 2002). Simulations of the October 1989 SPE by Jackman *et al*. (2000) are believed to be relevant for future extremely large SPEs in the next couple of solar cycles, based on the assumption that halogen amounts in the stratosphere would decrease only very slowly over the next several decades from their levels in 2000. Jackman *et al.* (2000) predicted that those future events would probably initially decrease ozone substantially in the upper stratosphere, and then gradually impact the lower stratospheric ozone in a minor way several months to years past the events by interference with the halogen loss cycles.

The Michelson Interferometer for Passive Atmospheric Sounding (MIPAS) instrument onboard Envisat measured the abundances of NO_x and ozone in the 6-68 km altitude range in the northern and southern polar regions at the time of the large solar storms in October-November 2003. López-Puertas *et al*. (2005b) reported very high abundances of NO_x in the upper stratosphere of 180 ppbv (parts per billion by volume) just after these large solar storms. The ozone measurements showed depletion signatures associated with both HO_x ($H + OH + HO_2$) and NO_x enhancements with a smaller ozone depletion signature in Southern Hemisphere region than in Northern Hemisphere polar region.

Another paper by López-Puertas *et al*. (2005a) describes the MIPAS-observed enhancements of the NO_y components (HNO_3, N_2O_5 and $ClONO_2$) in the northern polar stratosphere after the intense SPEs October-November 2003. These species play a very important role in the processes controlling the ozone abundance. Enhancements in the above-mentioned species in the Southern Hemisphere were generally less pronounced at this time. The MIPAS data revealed a distinct, high-altitude maximum of stratospheric HNO_3 in late November 2003 in the polar upper stratosphere, and analyses suggested that particle precipitation from the intense

solar storms was responsible for this HNO_3 layer enhancement (Orsolini *et al.* 2005). Randall *et al*. (2005) concluded that detailed 3-D modelling, including explicit calculation of NO_x production in the upper atmosphere by precipitating electrons and protons over a wide range of energies, is necessary to definitively attribute, or not, the observed NO_x enhancements to the powerful solar storms of October-November 2003.

Despite all the above research, Stiller *et al*. (2005) concluded that SPEs are not a necessary precondition for pronounced long-term nitric acid enhancements in the upper stratosphere, since similar nitric acid enhancements have been found in the Antarctic winter of 2003 without any indication of a dependence on energetic particle events.

3.1.4.7 Other factors

Galactic cosmic rays (GCRs) also produce odd nitrogen and HO_x. They form odd nitrogen via dissociation of molecular nitrogen and form HO_x via complicated ion chemistry on GCR-produced ions (Jackman *et al.* 1996b). The GCR flux is anti-correlated with the sun-spot number; thus the maximum GCR flux occurs near sunspot minimum. Like the SPEs, the increased GCR production of odd nitrogen and HO_x near solar minimum generally leads to an increase of ozone in years when stratospheric chlorine levels are more than about 2.5 ppbv (i.e. since 1985), because of interference with the ozone loss caused by chlorine and bromine constituents (Jackman *et al.* 1996b).

Schoeberl (2002) noted conflicting results from research undertaken to determine the contribution of relativistic electron precipitations (REPs) to the odd nitrogen budget of the stratosphere (Callis *et al.* 1991a; Callis *et al.* 1991b; Aikan 1992). The importance of relativistic electron precipitations in regulating ozone is not well understood or characterised and further work is required to determine their importance regarding modulation of stratospheric ozone.

3.1.5 Montreal Protocol

In 1987, the recognition of the potential for chlorine and bromine to destroy stratospheric ozone led to the Montreal Protocol on Substances that Deplete the Ozone Layer, as part of the 1985 Vienna Convention for the Protection of the Ozone Layer, to reduce the global production of ozone-depleting substances (NOAA Aeronomy Lab 1999). Article 6 of the Montreal Protocol on Substances that Deplete the Ozone Layer requires periodic assessments of available scientific, environmental, technical and economic information. These assessments shall be made at least every four years (van der Leun *et al.* 1995). Subsequent to the signing of the Protocol, global observations of significant ozone depletion prompted amendments to strengthen the treaty (see Figure 3.6) (NOAA Aeronomy Lab 1999).

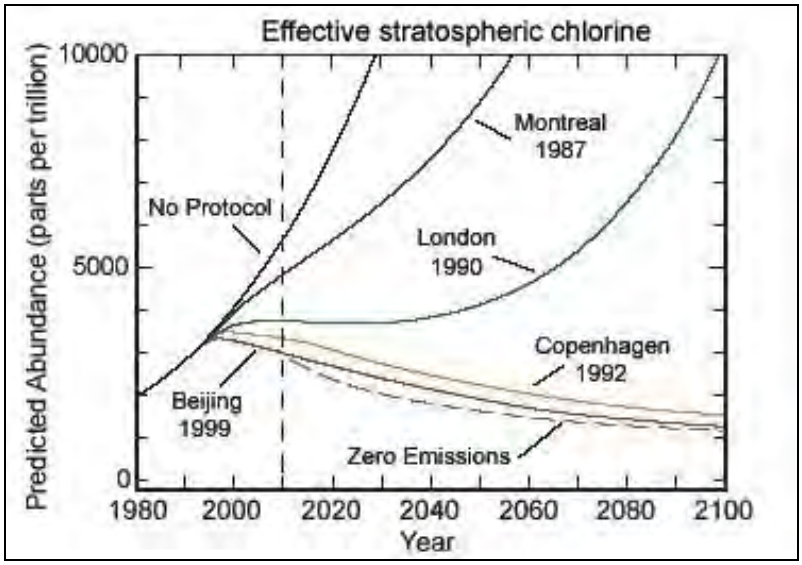

Figure 3.6: Ozone-destroying chemicals ('effective stratospheric chlorine') would have increased steadily ('no protocol' black line) if the Montreal Protocol and later agreements (coloured lines as marked) limiting CFCs and other chemicals had not been adopted (Welch 2010). Data for this figure compiled from the British Antarctic Survey, NASA, ESA, WDCRSA, Environment Canada, UNEP, NOAA, ESEPA and other sources as stated and credited. 2010 delineates between actual and modelled values of effective stratospheric chlorine

By 1994 the provisions in the Montreal Protocol and its amendments had brought about a marked decrease in production and use of ozone-depleting chemicals (van der Leun *et al.* 1995). In 1995, van der Leun *et al.* wrote that at that stage, the ozone layer was still becoming thinner and was expected to continue to thin until 1998, but would recover thereafter. The net tropospheric concentrations of chlorine- and bromine-containing compounds started to decrease in 1995 but, because three to six years are required for the mixing from the troposphere to the stratosphere, the stratospheric abundances of chlorine were just starting to reach a constant level in 1999 and were predicted to slowly decline afterwards (NOAA Aeronomy Lab 1999). Considine *et al*. (1999) presented an analysis of trends and variability in daily-averaged near-global retrievals of hydrofluoric and hydrochloric acids at 55 km, which provided evidence of highly statistically-significant slowdown in the rates of accumulation of these chemicals.

Hofmann *et al*. (1997) estimated that, if the Montreal Protocol and its amendments were adhered to, recovery of the Antarctic ozone hole may be conclusively detected from changes in the vertical profile of ozone as early as the year 2008. Any volcanic eruptions in the meantime would affect the 10-16 km region, making detection more difficult, but indicators such as depletion at 22-24 km will be immune to these effects.

As shown by Weatherhead *et al*. (1998), sudden changes in ozone data sets, such as instrumentation changes, local perturbations, or volcanic eruptions, can increase the number of years needed to detect a trend by as much as 50%. Thus, it is critical for detection of ozone recovery that monitoring stations be maintained throughout the expected recovery period. Several networks were established and are being maintained for this purpose, but it is likely that

some of these locations will detect ozone recovery sooner than others. The detection of a turnaround in total ozone would be difficult due to the natural inter-annual variation in several contributing factors (Solomon 2004; UNEP 2005) and also because of local natural variability (e.g. Brönnimann *et al.* 2004). Weatherhead *et al*. (2000) said that once detected, a turnaround in total ozone will be one of the most convincing arguments that current actions are working.

A report by UNEP (2005) stated that monitoring over several more years would be required before any increase in ozone attributable to the measures of the Montreal Protocol could be unambiguously identified. The "UNEP/WMO Scientific Assessment of Ozone Depletion: 2006" (WMO 2007), released on 18th August 2006, states that the ozone layer over the mid-latitudes (30°-60° North and South) should recover by 2049, five years later than anticipated by the previous (2002) assessment. The ozone layer over Antarctica should recover by 2065, 15 years later than once expected.

The later projected date of recovery over the mid-latitudes is primarily the result of upward revisions in the amounts of CFC-11 and CFC-12 now contained in refrigerators and other equipment, which will eventually be released, and from higher estimates of future production levels of HCFC-22 (a CFC substitute that, although much safer, still causes depletion) (see Figure 3.7). The later projected recovery of the Antarctic ozone layer is primarily due to the greater age of air in that region, which means that a return to pre-1980 levels of ozone-depleting substances will take longer (WMO 2007).

The benchmarks for the recovery dates are the pre-1980 stratospheric levels of chlorine, the chief ozone-depleting gas. Lower chlorine levels should, in principle, correlate with increased ozone levels and reduced penetration of solar ultraviolet radiation to the Earth. While recent measurements from unpolluted regions do show declines in ground-level UV radiation, climate change and other variables make it difficult to draw firm conclusions about the effectiveness of the international protocols and the future of the ozone hole (WMO/UNEP 2006).

The WMO/UNEP report (WMO 2007) concludes that a hypothetical case that goes beyond existing Protocol commitments i.e. the elimination of all emissions from production and existing equipment of CFCs, halons, HCFCs, methyl bromide, carbon tetrachloride and methyl chloroform at the end of 2006, would advance recovery at mid-latitudes by 15 years to 2034. On the other hand, a failure by governments to fully implement their commitments to phase out ozone-depleting substances under the Montreal Protocol would delay recovery beyond 2049.

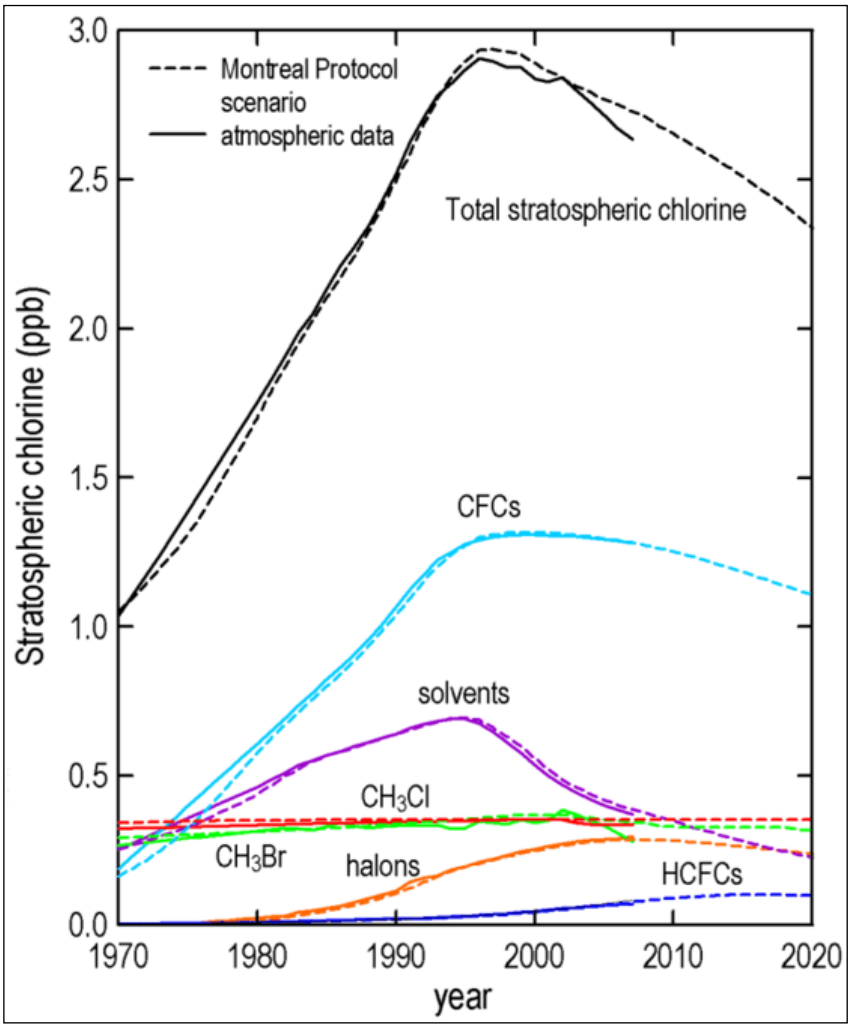

Figure 3.7: Stratospheric 'chlorine' from the world-wide use of major ozone depleting substances. Solid lines are data collected at Cape Grim, Tasmania; dashed lines are model calculations based on past and future emissions of ozone depleting substances (Montzka and Fraser 2003). Source: CSIRO Atmospheric Research, January 2005 (Beer *et al.* 2006).

3.1.6 Development of the ozone hole

In 2003, the scientific assessment by the WMO made the following points:

- That the monthly total column ozone amounts in September and October have continued to be about 40 to 50% below pre-ozone hole values, with up to a local 70% decrease for periods of a week or so;
- During the last decade, the average ozone-hole area in the spring has increased in size, but not as rapidly as during the 1980s;
- The area of the ozone hole varies from one year to another, but it is not yet possible to say whether the area of the ozone hole has maximised; and
- In recent years, the ozone hole has also persisted into early summer, increasing its impact on ultraviolet radiation.

Uchino *et al*. (1999) used both ground-based and satellite data to demonstrate that the Antarctic spring ozone decline increased rapidly toward the end of the 1980s, continued unabated through the 1990s and reached the highest values in the 1998 season. It has since equalled or surpassed that year's maximum of 25 million km^2 in 2000 (29.4 million km^2), 2003 (28 million km^2), 2005 (26.9 million km^2), 2006 (29.5 million km^2) (WMO 2006), 2007 (25 million km^2) and 2008 (27 million km^2) (European Space Agency 2008).

Results presented by Bodeker *et al.* (2002) indicated a strong increase in the ozone hole area from 1981 to 2000 without a change in either the area of the dynamical vortex or the area with temperatures below 195 K. The greater depth appeared to be due to increasing annual ozone loss within the winter vortex, rather than cumulative loss persisting from one year to the next. Lee *et al.* (2001) showed that between 60° S and 70° S equivalent latitude there is very poor mixing while the vortex core, poleward of 70° S equivalent latitude, is well-mixed. Because the mixing throughout the vortex is poor, there is a strong ozone gradient between the vortex core and edge; thus increasing depth in the core brings an ever-larger area below any fixed contour. Therefore, the ozone hole has steadily grown in area as average ozone values have fallen, even though the dynamical vortex and the region of PSC formation have not.

It has become clear that although ozone depletion over Antarctica is evident mainly in spring, the depletion process actually starts during the winter at the sunlit edge of Antarctica (Varotsos 2005). Since the mid-1990s, however, the springtime total ozone content over Antarctica has ceased to follow the negative long-term trend observed in the period 1978-1996, but instead shows no significant trend. This fact gave rise to the question of whether or not the atmosphere was on the path to 'ozone recovery' due to the implementation of the Montreal Protocol and its Amendments. Varotsos (2005) showed firstly that extreme column ozone fluctuations obey a power-law with exponents, implying that large fluctuations are more likely to occur into the ozone hole than at its edge. Secondly, for time-scales longer than one year, persistent long-range power-law correlations in the column ozone fluctuations were more pronounced during 1979-1992. However, by eliminating the long-term trend, anti-persistence (persistence) for time lags more (less) than ten days is detected for the entire data record. The latter crossover illustrates the role of planetary waves in the scaling characteristics of the spatio-temporal variability of the Antarctic ozone hole.

Although the long-term temporal evolution of the Antarctic ozone hole is related to the increase in stratospheric chlorine loading, inter-annual differences in the severity of ozone depletion are significant and may largely be accounted for by dynamic processes (Bodeker and Scourfield 1995). Planetary wave propagation is known to influence the chemical and dynamical properties of the Antarctic vortex. Waves are unable to transport trace species deep into the polar vortex, but can erode material from the edge of the vortex (Juckes and McIntyre 1987). This reduces the spatial extent of the region where heterogeneous processing can occur on the surfaces of PSCs. During the winter above 25 to 30 km, heat transport by upward-propagating planetary

waves leads to an increase in vortex temperature, limiting the altitude range for PSC formation (Schoeberl and Hartmann 1991). Finally, since 1996 the intrinsic dynamics in column ozone at the edge of Antarctica have differed; this does not hold for the Antarctic ozone hole (Varotsos 2005). The Antarctic ozone hole depends on dynamic conditions; in particular, it requires the right combination of low temperature and sunlight, which is found extensively and persistently only over Antarctica during spring. A further ingredient is the dynamical confinement of the polar air mass, so that individual air parcels can undergo severe ozone depletion. The low temperature that is characteristic of the Antarctic vortex is associated with a strong vortex, providing the necessary confinement. During the first two-thirds of September 2002, the Antarctic ozone hole developed much as it had done every austral spring since the mid-1980s. Then over a period of a few days in late September, the ozone hole was observed to split in two. A split ozone hole meant a divided vortex, and thus a stratospheric sudden warming (Shepherd *et al.* 2005).

3.1.7 Recovery from ozone depletion

Using observations of the latitude gradients in ozone, Dobson (1930) inferred the existence of a large-scale stratospheric circulation cell characterised by rising motion in the tropics, and descending motion at mid and high latitudes. Brewer (1949) reached a similar conclusion based on an analysis of measurements of water vapour. More recent studies have shown that the timescale for the overturning of this “Brewer-Dobson” circulation cell is ~5 years (Solomon 1999). Since only ~10% of the mass of the troposphere exchanges with the upper stratosphere in each 5-year period, the process will have to be repeated approximately 10 times to destroy the bulk of CFC initially released. In the case of CFC-11, this leads to a lifetime of ~50 years. For some of the other CFCs, stratospheric photo-dissociation destroys a smaller fraction of the parent compound within a single circuit through the Brewer-Dobson circulation, extending the lifetimes considerably, e.g. in the case of CFC-115 the lifetime is about 500 years (Solomon 1999). The near-insolubility of CFCs in water, and their chemically-inert character makes their destruction in the troposphere either extremely slow or non-existent (Solomon 1999).

Jucks *et al.* (1996) predicted that signs of ozone recovery would be seen first around altitudes of 40 km; however, interactions with increasing greenhouse gases, decreasing temperature, and circulation changes can mask an ozone recovery from chlorine-catalysed loss (Shindell *et al.* 1998). Shindell and Grewe (2002) showed that while CFCs dominated past ozone changes, climate change will play an increasingly important role over coming decades, and that it is important to realise that ozone recovery is not just about detection, but about detection **and** attribution. Exploiting the different spatial patterns of halogens and climate, Shindell and Grewe (2002) demonstrated a technique to isolate the halogen signature in the upper stratosphere by contrasting equatorial and mid-latitude ozone trends at 40-km altitude. This allows verification of the effectiveness of the Montreal Protocol’s limitations on substances that deplete the ozone

layer and also improves understanding of the magnitude of climate change's influence on the ozone layer.

In the early 2000s, there was some disagreement between researchers as to whether the Montreal Protocol had in fact affected ozone levels (for example Newchurch *et al.* (2003), Steinbrecht *et al.* (2004), Cunnold *et al.* (2004)). UNEP's 2004 progress report (released in 2005) states that ozone-depleting gases in the atmosphere show a downward trend (discernible in the lower stratosphere) but the WMO Antarctic Ozone Bulletin No. 5 (WMO 2005) stated that the ozone hole of 2005 ranked as the third largest ever recorded, suggesting perhaps that 20 years of pollution controls have so far had little effect.

Ozone in the lower stratosphere is sensitive to redistribution by atmospheric transport, the abundance of volcanic aerosols, and a complex set of nonlinear chemical interactions involving anthropogenic chlorine and bromine (WMO 1999, 2003; UNEP 2005). A number of studies noted a turnaround in the downward trend (Hadjinicolaou *et al.* 2005; Reinsel *et al.* 2005; Steinbrecht *et al.* 2005) that may be evidence for the beginning of an ozone recovery due to declining halogen loading (Reinsel *et al.* 2005). However, Hadjinicolaou *et al*. (2005) attributed the recent turnaround in total column ozone to effects of transport.

One year of increased total ozone, as in winter and spring 2002 in Antarctica, is not evidence of ozone recovery. In this instance, the increased Antarctic total ozone was a consequence of an unusual meteorological situation during the winter (Sinnhuber *et al.* 2003; Nishii and Nakamura 2004). Trend detection is ideally based on data collected from a uniform, well-maintained source over many years. Changes of instruments, both ground- and satellite-based prevent data collection from one continuous source (Reinsel *et al.* 2002).

Multiple satellite and ground-based observations provide consistent evidence that the thickness of Earth's protective ozone layer has stopped declining since 1997 (Yang *et al.* 2006). Regression analyses undertaken by Yang *et al*. (2006) demonstrated that the cessation of ozone depletion between 18 and 25 km is consistent with a levelling-off of stratospheric abundances of chlorine and bromine, due to the Montreal Protocol and its amendments.

Andersen *et al.* (2006) presented a comparison of trends in total column ozone from 10 2-D and 4 3-D models, and SBUV/2 satellite observations from the period 1979-2003. Trends for the past (1979-2000), the recent (1996-2003) and the future years (2000-2050) were compared. The models offer a qualitative understanding of what will happen to ozone in the coming years. Quantitatively, there is much disagreement among the models, both in terms of climatology and trends. However, the models agree that future trends are expected to be positive and less than half the magnitude of past downward trends. Based on several different statistical modelling approaches used by Reinsel *et al.* (2005), a robust feature that emerged is the substantial positive and statistically-significant estimate of change in trend in ozone for latitudes of 40° and

higher in both hemispheres, which might be interpreted as the first evidence of an early signal of a turnaround in total ozone trends.

The upper edge (20-22 km) of the ozone hole has been identified as a good place to look for reductions in ozone loss that are expected to occur as effective equivalent stratospheric chlorine (EESC) decreases (Hofmann *et al.* 1997). Measurements of the ozone mixing ratio near the top of the ozone hole in early October were higher during the years 2001-2004 than in the previous six years. The observed increases of ozone at 20-22 km in 2001-2004 were accompanied by generally higher temperatures and reduced PSC occurrence frequency, suggesting that temperature variability, possibly linked to transport changes, may be responsible for the observed ozone changes rather than a decrease in EESC (Hoppel *et al.* 2005).

The four decades of ozonesonde measurements over Antarctica, as described and inter-compared by Solomon *et al*. (2005), showed that the recent changes in ozone did not yet indicate ozone recovery linked to changing chlorine abundances, but did provide new tools to probe observations for the first such future signals. Newman *et al*. (2006) showed the following:

- the area of the ozone hole was primarily controlled by total inorganic chlorine and bromine and temperature;
- the area was no longer strongly increasing;
- the ozone hole was decreasing at a very slow rate of approximately 1% per year based upon the slow decrease of inorganic chlorine and bromine estimates; and
- the slow decrease would be masked by year-to-year variability.

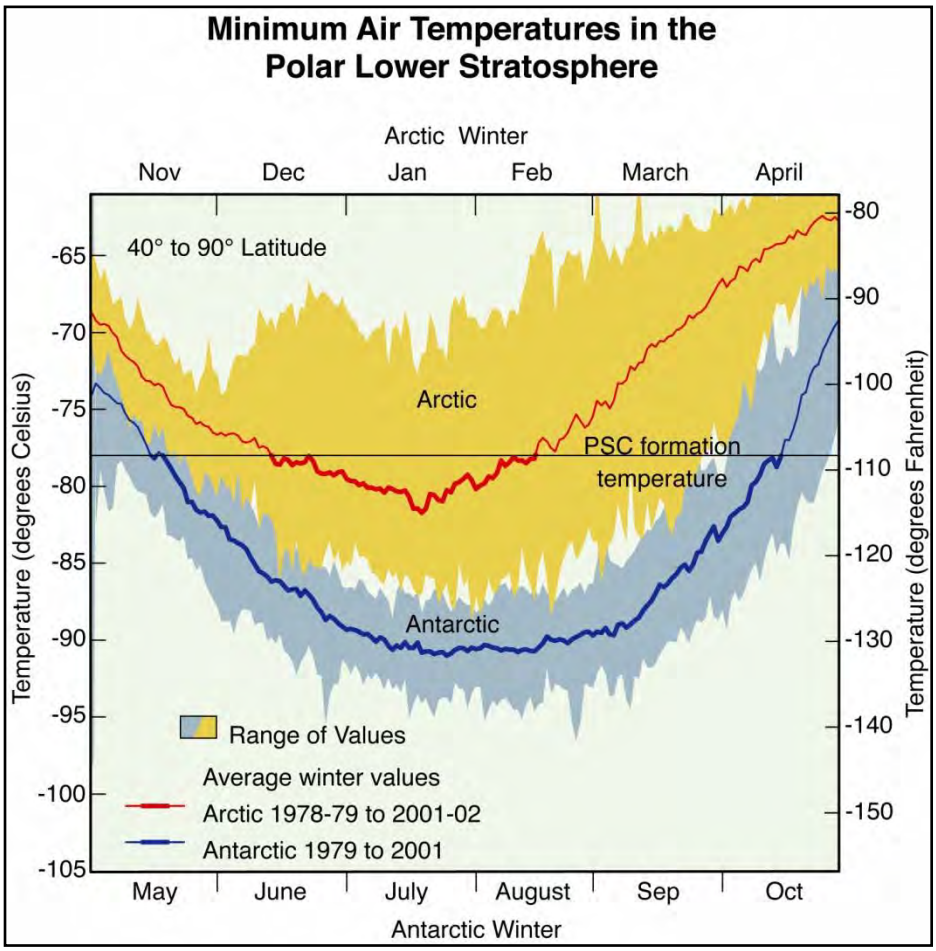

Figure 3.8: Minimum air temperatures in the polar lower stratosphere (NOAA Aeronomy Lab 2004).

PSC amounts are determined by the global average temperature of the lower and middle stratosphere (see Figure 3.8), which has reduced over the last two decades (WMO 1999). Calculations by Forster and Shine (1999) indicated that this cooling has arisen from observed increases in carbon dioxide and water and reductions in ozone. If current trends continue, a likely result would be an increased frequency of PSCs in the Antarctic vortex-edge region during the mid-21st century (Shindell *et al.* 1998), resulting in a more complete conversion of un-reactive chlorine into reactive forms, and thus more ozone loss. The modelling results by Lee *et al.* (2001) indicated that the horizontal extent of the ozone hole will not recede until after 2030 if this region cools by 4 K or more. Hence, as the amounts of halocarbons decline according to the provisions of the Montreal Protocol, it should not be expected that ozone depletion in the vortex-edge region would recover as rapidly as anticipated for the vortex core.

Making enough ozone to artificially replace even a small fraction of the global burden would be an extremely expensive proposition, and alternative schemes involving interference with chlorine chemistry have also been shown to be impractical. The reduction of global emissions and resulting gradual removal of atmospheric chlorine is the only known practical approach to future recovery of the ozone layer (Solomon 1999).

Fioletov *et al.* (2002) reported that the analyses they performed did not reveal any statistically significant positive trends indicating possible recovery of total ozone. In fact, the 2006 Antarctic ozone hole exhibited some of the strongest stratospheric ozone depletion seen in recent years, based on ozone profile measurements carried out at the South Pole. Ozone in the 12-14 km layer was nearly completely destroyed, declining from an average of 125 DU in July and August to 1.5 DU on October 6th (NOAA Earth System Research Laboratory 2006). The report by the Earth System Research Laboratory at NOAA stated that, although ozone-destroying halocarbons are decreasing in the atmosphere in response to control by the Montreal Protocol, there are still sufficient concentrations of these compounds available to completely remove ozone in a large portion of the Antarctic stratosphere. The low values of total column ozone in 2006 demonstrate the strong connection between low Antarctic stratospheric temperatures and a persistent polar vortex on the severity of the ozone depletion. These low ozone values bring home the point that the Antarctic ozone hole will continue to be an annual feature well into this century (NOAA Earth System Research Laboratory 2006).

3.1.8 The effects of climate change

Mounting evidence suggests that the Earth is experiencing a period of rapid climate change (IPCC 2007). The implications of climate change for the environment and society will depend not only on the response of the Earth system to changes in radiative forcings, but also on how humankind responds through changes in technology, economies, lifestyle and policy. Climate change, its effects, and adaptation and mitigation strategies, have been the focus of much research (e.g., Kim and Pang 2009; Shindell *et al.* 2009; Washington *et al.* 2009; Alig *et al.* 2010; Anger and Kohler 2010; Bertram 2010; Bulleri and Chapman 2010; Gowdy and Juliá 2010; Moss *et al.* 2010). There has been an increased focus on interactions between ozone depletion and climate change, which can work in both directions: ozone changes can induce changes in climate and climate change can induce changes in ozone (Rind *et al.* 2009; Shindell *et al.* 2009; Zazulie *et al.* 2010). Thus a return of ozone to its value at any particular date should not necessarily be interpreted as a recovery of ozone from the effects of ozone-depleting substances alone (Waugh *et al.* 2009). For example, it has been suggested that ozone depletion in Antarctica can influence tropospheric wind patterns in the Northern Hemisphere, both at high and mid-latitudes (Rind *et al.* 2009). Furthermore, in the 2060s, when the stratospheric halogen loading is projected to return to its 1980 values, it has been predicted by Waugh *et al.* (2009) that, outside tropical regions, column ozone will be significantly higher than in 1975-1984, due to changes in circulation resulting from increases in greenhouse gases (Andrady *et al.* 2010).

Thompson and Solomon (2002) argued that the largest and most significant trends in tropospheric circulation can be traced to trends in the lower stratospheric polar vortex, which are due largely to photochemical ozone losses. During the summer-autumn season, the trend

toward stronger circumpolar flow has contributed substantially to the observed warming over the Antarctic Peninsula and Patagonia, and to the cooling over eastern Antarctica and the Antarctic Plateau.

One of the major sources of uncertainty in predicting the impacts of climate change is in understanding how clouds will respond to, and thereby alter, radiative fluxes (Zhang *et al.* 2004; IPCC 2007; Lu and Cai 2009). These uncertainties are more significant in the polar regions, where increases in global surface temperatures are expected to be amplified (Schlesinger and Mitchell 1987). Changes in cloud cover in the polar regions can be expected to have a significant effect on sea-ice conditions (Shine and Crane 1984) and on regional ice-albedo feedback (Barry 1983). The IPCC (2001, 2007) reported that there will be a climate change-induced alteration to albedo conditions as a result of decreased sea ice and snow. Wuttke and Seckmeyer (2006) concluded that the change in albedo conditions will significantly change the radiation conditions in polar regions.

The chemical reactions responsible for stratospheric ozone depletion are extremely sensitive to temperature (WMO 1995). Greenhouse gases warm the Earth's surface but cool the stratosphere radiatively and therefore affect ozone depletion (Dameris *et al.* 1998; Shindell *et al.* 1998; Reinsel *et al.* 2002; Rosenfield *et al.* 2002; Langematz *et al.* 2003). The ozone layer will also be affected to some extent by the changing atmospheric abundances of several other human-influenced constituents, as well as by the changing climate of the Earth, making it unlikely that the ozone layer which will exist late in the 21st century will be identical to the ozone layer that existed prior to the 1980s (NOAA Aeronomy Lab 1999).

Observations suggest that stratospheric water vapour is increasing, though measurements are spatially and temporally limited. Model results suggest that the observed changes may be part of a global, long-term trend (Shindell 2001). Furthermore, the required water vapour changes cannot be accounted for by increased stratospheric production, suggesting that climate change may be altering tropospheric input. If the trend continues, it could increase future global warming and impede stratospheric ozone recovery.

There is not yet a consensus on whether the overall impact of climate change on ozone depletion will be to delay or accelerate ozone recovery (Schnadt *et al.* 2002; UNEP 2005). Some processes would result in slowing of ozone recovery (e.g. Rex *et al.* 2004), while others would result in an acceleration (e.g. Marchand *et al.* 2004). Future changes in methyl bromide and methyl chloride emissions resulting from climate change may also be important. Although the majority of methyl bromide is from natural sources, and declines in its concentration have been reported (Montzka *et al.* 2003), its future role in ozone depletion cannot yet be discounted. For example, methyl bromide emissions from rice paddies may increase appreciably with global warming (Redeker and Cicerone 2004). The finding that the ozone-depleted air exported from polar latitudes accounts for a significant portion of ozone losses at mid-latitudes (e.g. Lee *et al.* 2002) may also have negative implications for future ozone recovery at mid-latitudes.

Observational data and a modelling study have both suggested that decreases in stratospheric ozone in Antarctica have led to climatic changes both in the stratosphere and at the Earth's surface. These changes in ozone have led to increased westerly winds at latitudes 50°-60° S. This in turn, has resulted in a surface cooling in Antarctica and a warming at high latitudes outside the Antarctic continent (Gillet and Thompson 2003).

Climate change can also be mediated through UV-induced changes in DMS, a substance emitted from phytoplankton that can modify the reflectivity of the atmosphere (Toole and Siegel 2004). DMS-climate feedbacks are created by the atmospheric oxidation products of DMS reducing incident solar fluxes and sea surface temperature (SST) values, which in turn reduce phytoplankton primary production rates and biogenic DMS production (Yang and Kirst 1997; Toole and Siegel 2004). UVR doses will increase as a result of observed decreases in stratospheric ozone and the shoaling of ocean mixed layers as a result of global warming (e.g. Boyd and Doney 2002). In response, open-ocean phytoplankton communities should increase their DMS production and ventilation to the atmosphere, increasing cloud condensing nuclei, and potentially playing out a coupled global change-DMS-climate feedback (Toole and Siegel 2004).

3.2 Parameters used in modelling ultraviolet radiation

Section 3.1 discussed the parameter ozone, the depletion of which has a significant effect on levels of ultraviolet radiation. This section will now discuss other parameters which also affect UVR that are included in developing the maps of levels of UVB in this project.

Forster (1995) undertook a wide-ranging sensitivity study to show how changes to the model input parameters (surface albedo, surface pressure, aerosol, cloud and ozone) as well as the model resolution affect UV irradiances at the surface. He discovered that the magnitude and even the sign of the effect obtained by changing a single parameter depends on the values of many of the others, making it difficult to determine the consequences of, for example, a slight vertical redistribution of ozone or change in cloud height. Forster's study could not cover every conceivable input, but it attempted to show the relative importance of the different input quantities. For example, cloud properties are relatively unimportant as long as the cloud optical depth is known, whereas aerosol scattering properties and ozone and temperature profile are highly important for determination of surface UV irradiances. Background knowledge of the sensitivity study made it possible to give the uncertainties of subsequent UV irradiance calculations (Forster 1995).

Many of Forster's (1995) sensitivity studies showed strong dependence of levels of UVB on SZA and wavelength. Changes in ozone during the winter have a significantly larger effect on the UVB than they do in the summer; a 42% ozone depletion leads to 85% larger relative values of UVB in winter, but only a 42% increase in UVB during the summer. This is due to the wintertime increase in the mean SZA and a subsequent increase in the path length of light through the ozone layer in the winter.

Forster *et al.* (1995) showed that it is possible to produce UV irradiances from two totally separate sources (instrument and model) that agree relatively well with each other. Although this is no guarantee of absolute accuracy, it is a good indication of it, especially when combined with the knowledge from instrument comparisons that the instrument agrees well, in absolute terms, with other independently calibrated instruments. Instrument networks are unable to provide even nationwide high-wavelength resolution data. If a numerical model has been tested and verified, it ought to be capable of estimating UV trends, provided that ozone, cloud, and aerosol concentrations can be measured, or estimated, to a reasonable accuracy.

3.2.1 Solar Zenith Angle

The dominant factor affecting UVB radiation received at the surface is the SZA – the angle between the vertical and the centre of the solar disc (McKenzie *et al.* 2003). When the SZA is small, the light path through the atmosphere is short, and absorption is minimised. The irradiance variations with time of the day, latitude and season, result from a change in the SZA.

3.2.2 Earth-Sun Distance

As a consequence of the variation in the Earth-Sun distance, extraterrestrial radiation is 7% higher when summer solstice occurs in the Southern Hemisphere, than during the Northern Hemisphere summer solstice (Fröhlich 1987). The Earth-Sun distance varies because of the Earth's elliptical orbit, and the irradiance from the sun decreases as the square of the Earth-Sun distance.

3.2.3 Atmospheric Aerosols

Jaroslawski and Krzyścin (2005) showed that aerosol forcing on the erythemally-weighted UV at the Earth's surface is as important for the clear-sky radiation level as that due to changes in TOC, both on long-term (trend) and short-term (day-to-day) timescales. Radiation models can give a prediction of the upward and downward irradiance at any level in the atmosphere from knowledge of the scattering and absorption characteristics of the atmosphere and the extraterrestrial spectrum (Forster 1995). Details of how radiation is affected (i.e. absorbed, scattered or transmitted) by the composition and physical properties of the atmosphere are given in Chapter 1 of Lubin and Massom (2006). Absorption occurs mainly through the presence of water vapour, carbon dioxide, oxygen, ozone and nitrogen. Molecules of nitrogen, or oxygen, or particles of various composition and origins (e.g. volcanic, natural sea salt, natural dust, organics, biomass burning, soot and other anthropogenic processes) act to scatter the radiation. Non-selective scattering happens when larger particles are present in the form of cloud liquid water droplets, and ice crystals. In some locations aerosols can scatter more than 50% of UVB radiation out of the direct beam (di Sarra *et al.* 2002; McKenzie *et al.* 2003). Table 3.1 includes the sources of various components of the aerosol content of the atmosphere.

Table 3.1: Estimated source apportionment of atmospheric particulates (10^6 metric tons/year) (SMIC 1971).

Natural	
Soil and rock debris	100-500
Forest fires and slash-burning debris	3-150
Sea salt	300
Volcanic debris	25-150
Particles formed from gaseous emissions:	
Sulphate from H_2S	130-200
Ammonium salts from NH_3	80-270
Nitrate from NO_3	60-430
Hydrocarbons from plant exudations	75-200
Sub-total	773-2200
Man-made	
Particles (direct emissions)	10-90
Particles formed from gaseous emissions	
Sulphate from SO_2	130-200
Nitrate from NO_3	30-35
Hydrocarbons	15-90
Sub-total	185-415
Total	**958-2615**

The largest sources of world-wide UV-absorbing aerosols in the atmosphere are from biomass-burning and wind-borne desert dust from events that last a week or longer. Most prominent amongst other sources of UV-absorbing aerosol production are volcanic eruptions (e.g. El Chichon, Mount St. Helens, Mount Pinatubo), United States, Brazilian and Canadian forest and bush fires, and smaller desert dust injections (Tarim Basin and Takla Makan Desert in western China, Lake Eyre in central Australia and in the U.S. Southwest) (Herman *et al.* 1997).

In urban and rural locations of industrialised regions, such as eastern United States and Europe, and probably most of the populated areas in other developed countries of the Northern Hemisphere, aerosols may have reduced UVB levels significantly since the Industrial Revolution, and offset increases in UVB from stratospheric ozone depletion (Liu *et al.* 1991). However, the aerosol effect on UVB is expected to be negligible over remote oceanic areas and in the Southern Hemisphere (Shaw 1982; Liu *et al.* 1991; Kylling *et al.* 2000b).

Tsitas and Yung (1996) determined that volcanic eruptions inject large amounts of aerosol into the atmosphere, and at large SZAs scattering by these aerosols can actually increase the flux of UVB radiation reaching the surface. This phenomenon makes Antarctica during spring the most susceptible place on Earth to the scattering effect of volcanic aerosols, due to the combined effect of the ozone hole and the large SZAs characteristic of this time of year. Feister *et al.* (2002) demonstrated that the extremely low ozone values in 1992 to 1995 (following the eruption of Mount Pinatubo in 1991) substantially enhanced UVB irradiation by 3-10% in the first half of the 1990s. The larger volcanic ash particles settle out in a short period of time, but the sulphuric acid aerosols produced from the SO_2 persist for several years (Shettle 1989). It should be noted that there have been no major volcanic eruptions since Mount Pinatubo in 1991, and therefore, the above phenomenon is not relevant in the temporal context of this project.

A large number of aerosol models have been developed over the years describing the optical properties of the atmospheric aerosols and their effects on radiation (see Tables 2 and 3 in Shettle (1989) for general cases and specific environments (marine, desert and stratospheric)). The aerosols normally present in the lower stratosphere (up to about 30 km) are mostly sulphuric acid droplets.

Tanré *et al*. (1981) studied the influence of background contamination on the apparent reflectance of a target as viewed from space, as a function of the characteristics of atmospheric aerosols and the simple geometry of the target. For relatively common aerosol characteristics, the main features of the environmental effect may be accounted for by simple correction terms, which depend only upon the optical thicknesses of aerosols and the molecular scattering of the atmosphere.

Since over two-thirds of the Earth's surface is covered by oceans, the marine aerosol component, which consists largely of sea salt solution particles and sulphates from the oxidation of DMS produced by oceanic phytoplankton, is the most prevalent aerosol source (Shettle 1989). Wind and wave action in the Southern Ocean (Podgorny and Lubin 1998), and the proliferation of algal blooms, means that marine aerosols have a more significant effect on atmospheric radiation than other natural and man-made sources of aerosols (see Table 3.1).

Portmann *et al*. (1996) showed that ozone depletion in the polar regions is profoundly influenced by liquid sulphate aerosols, not just after extreme volcanic events, but during the entire period since the emergence of the Antarctic ozone hole. Higher levels of UVR may drive an increase in the conversion of dissolved DMSP to DMS in the open ocean and in leads within the sea ice (Ferek *et al.* 1995), but DMS could be less stable and have a higher photoactivity under radiation of shorter UVB wavelengths.

Marine biogenic production of DMS represents more than 90% of the oceanic flux (Toole *et al.* 2008). DMS is already discussed in Section 3.1.8 and details of distribution, sources, emission rates, concentrations, effects on the atmospheric chemistry and on the climate, of DMS and its precursor, DMSP can be found in Curran *et al.* (1998), Trevena *et al*. (2003), Lubin and Massom (2006) and Toole *et al*. (2008). The research by Curran and Jones (2000) highlighted the sea ice zone as important for DMSP and DMS production.

Antarctica is expected to have the cleanest air mass in the global atmosphere, being located in the Southern Hemisphere, away from inhabited land masses and having minimal human activities on the continent. Air circulation over Antarctica also seems to prevent the direct transport of air originating from anthropogenic sources of pollution at the lower latitudes (Di Carmine *et al.* 2005).

3.2.4 Surface Albedo

The reflectance, or albedo, of a surface is a measure of its ability to reflect incident energy, and is defined as the ratio of reflected to incident energy at a given wavelength or narrow waveband (Lubin and Massom 2006). Of all the surface types on Earth, snow and ice surfaces have the highest albedo. The albedo of sea ice depends upon the depth and state of its snow cover, the optical properties of the snow and ice, the properties and distribution of melt ponds, and the amount of open water (Grenfell and Maykut 1977; Curry *et al.* 2001; Perovich *et al.* 2002; Pirazzini 2004).

During polar summers incident solar radiation increases, and the air warms, and the ice cover evolves from a highly scattering, snow-covered medium to a darker combination of bare ice, melt ponds and leads (Perovich *et al.* 2002). Freshwater melt ponds (or puddles) are rare in Antarctica compared to the Arctic Ocean (Andreas and Ackley 1982) although seawater "deformation ponds" can cover up to 20-30% of the Antarctic sea ice surface in places, and occur up to 200 km from the ice edge (Massom *et al.* 1998b). The presence of water on the surface of the ice causes a decrease in albedo, but if the ice surface drains, the brine pockets become air bubbles, resulting in more scattering and an increase in albedo, with less light transmitted through the ice (Perovich 2003).

Degünther *et al*. (1998) used 3-D radiative transfer calculations to model the albedo effect on UV irradiance when there is a cloud-free atmosphere and surfaces with inhomogeneous albedos. It was found that such inhomogeneities have the strongest effect on UV irradiance when the albedo contrast is high, e.g. in the Antarctic sea ice zone where the albedo of ocean is ~0.02-0.08 and snow-covered ice is ~0.95 (Grenfell *et al.* 1994).

It has been shown that a large increase in estimated irradiance occurs as a snow-covered coastline is approached from the ocean (Nunez *et al.* 1997). Arola *et al*. (2003) determined that an increase in the surface albedo due to snow can enhance the clear-sky global UV irradiance by up to about 30%. This is due to multiple reflections between the snow surface and the atmosphere. Under a cloudy sky, this amplifying effect of snow becomes even stronger (Lenoble 1998; Herman *et al.* 1999; Smolskaia *et al.* 1999; Kylling *et al.* 2000a; Curry *et al.* 2001) because of the enhanced backscattering. Similar results were reported by Podgorny and Lubin (1998) and Ricchiazzi and Gautier (1998). The effect of these multiple reflections depends primarily on cloud base height, cloud optical depth, and only slightly on cloud thickness. The insolation enhancement is also a function of wavelength, being larger for ultraviolet wavelengths than for the visible. Smolskaia *et al.* (2006) determined more specifically that the albedo of an ice surface can affect the UV irradiance at the surface of the ocean some tens of kilometres away.

In most parts of the Antarctic sea ice zone, the oceanic surface flow is divergent, exposing open water in the form of leads and polynyas (Brandt *et al.* 2005). In summer the open water persists,

but in colder seasons new ice can form rapidly. In most regions and at most times, there is usually a great variety of ice types of varying thickness and snow cover, with a corresponding variety of albedo values (Brandt *et al.* 2005). The all-wave albedos of the wide variety of types of ice constituting the Antarctic pack range from 0.07 to 0.87 (see Table 1 in Brandt *et al.* 2005). For young sea ice on which snow has not yet accumulated, sunlight is reflected at the upper surface and is also scattered by air bubbles and brine pockets in the interior of the ice. The albedo is relatively low and is controlled by the size and number of air bubbles (and brine pockets) (Allison *et al.* 1993). The albedo increases gradually as the ice thickens, and then jumps significantly when it acquires even just a thin cover of snow (Allison *et al.* 1993). The frequency of synoptic storms in the Southern Ocean ensures that new ice does not remain snow-free for long. Allison *et al.* (1993) determined that young sea ice normally acquires a covering of snow within a few days after it forms, and that sea ice thicker than 15 cm always had a snow cover. However, if the ice floes are pushed apart by winds and currents to give rise to a substantial fraction of open water, the area-averaged albedo will be lowered (Brandt *et al.* 2005). Table 2 in Brandt *et al*. (2005) includes representative albedos for the various ice types and for open water in the East Antarctic sea ice zone, in spring and summer (for clear sky), for AVHRR visible channels 1 and 2. Brandt *et al.* (2005) include area-averaged albedos in Tables 4 and 5 for all seasons and for both clear-sky and cloudy-sky irradiance. These area-averaged albedos α, are obtained by combining the ice-only albedos α_i, with the ice concentrations, c_i:

$$\alpha = \alpha_i c_i + \alpha_w(1 - c_i)$$

where α_w is the albedo of open water.

Areal coverage is a more important factor for snow cover than its thickness. Initially, cold, fine-grained snow with an average thickness less than 3 cm is likely to be patchy because of wind drifting. When the average snow depth is thick enough to provide a continuous cover (about 3 cm), the albedo is determined by the snow depth and grain size, as very little sunlight reaches the ice below (Brandt *et al.* 2005). In summer the snow does not drift, but the grain sizes are larger and sunlight penetrates deeper into the snowpack, so a uniform layer of less than 3 cm qualifies as “thin” (Wiscombe and Warren 1980). The key physical properties of Antarctic snow on sea ice are detailed in Massom *et al*. (2001). Even when there is no snowfall caused by storms, “frost flowers” can form on thin nilas exposed to cold air, and their effect on albedo is similar to that of a thin snow layer (Perovich and Richter-Menge 1994).

Since the concentration of snow impurities is very low in Antarctica (Kumai 1976; Warren and Clarke 1990) and remote sea ice areas (Warren and Clarke 1986), the snow aging effect on albedo related to snow impurities in these areas would be weaker than that determined in the study by Aoki *et al.* (2003). Of secondary importance for snow albedo are the SZA (albedo increasing as the sun lowers) and cloud cover (total albedo increasing as cloud thickness increases) (Wiscombe and Warren 1980; Warren 1982).

Although a thick snow cover appears near opaque, its albedo is still likely to be affected by the thickness of the underlying sea ice (Brandt et al., 2005). Sufficiently thin sea ice can be pushed below the sea surface by a heavy snow load (due to gravity) so that sea-water can percolate upwards through the sea ice into the lower part of the snow-layer, and create a slushy layer at the snow/ice interface, which can eventually re-freeze and form so-called snow-ice (see Section 2.2) (Grenfell *et al.* 1994; Massom *et al.* 2001).

The values obtained by Grenfell *et al.* (1994) for the ground-based measurements of snow albedo are not directly applicable for satellite UV methods. Typically such a surface measurement concerns a small unbroken homogeneous area, whereas the footprint of a space-borne instrument is much larger, inhomogeneous and often only partly covered by snow (Arola *et al.* 2003). Therefore, the high albedo values measured by Blumthaler and Ambach (1988b), Grenfell *et al*. (1994), Feister and Grewe (1995), Wuttke *et al*. (2006) and Meinander *et al.* (2008) are only rarely representative of the ground surface areas within a satellite instrument field of view.

In developing a climatology of UVR over Argentina, Luccini *et al.* (2006) used the UV albedo from the TOMS monthly climatology (Herman and Celarier 1997), which is determined from an average of the smallest albedo values at each point, and this is appropriate for zones and seasons without large variations. Cede *et al.* (2004) determined that in regions with a large variability in albedo, it is more appropriate to use a climatology of "mean" albedo.

Satellites can provide temporally repetitive coverage and spatially continuous data in the polar regions that are not easily accessible for ground-based measurements (Zhou and Li 2003). A direct comparison between the satellite-derived and available *in situ* measurements is generally difficult when the surface is very heterogeneous. Comparison of satellite sensor data with *in situ* measurements over pack ice in polar seas is even more difficult for two reasons. Firstly, the pack ice in polar seas is a dynamic surface, which undergoes constant motion and deformation, and thus no 'permanent' ground data exist. Secondly, sea ice is very heterogeneous and a satellite pixel generally covers more than one ice type, and different types of ice have distinctive reflectivity (Zhou and Li 2003).

Changing temperatures as a result of climate change could alter the albedo of the Antarctic Ocean in several ways: change in ice margin position, change in ice concentration within the pack, change in the mix of ice types and change in snow cover, snow depth, or snow wetness (Brandt *et al.* 2005).

3.2.5 Cloud Amount

Highly energetic weather systems in the Southern Ocean bring extensive cloud cover over Antarctic waters year-round (Lubin and Massom 2006), making a maritime, cloud-free satellite image a rarity. The mean annual cloudiness in coastal regions of Antarctica near 60° S is about

80-90% (as a result of frontal activity) (Láska *et al.* 2009). Near 70° S, surface observations show a total cloud cover of about 45-50% with little variability throughout the year, and only a small decrease during the winter months (King and Turner 1997). Clear skies are more common over central Antarctica than on the coast, with research by Mahesh *et al*. (2005) showing clouds to be present over the Antarctic plateau 40% of the time.

3.2.5.1 The effect of cloud on incoming radiation

The persistent cloud cover in the Antarctic coastal areas has significant effects on the properties of the light arriving at the sea surface, including UVB radiation. In fact, variations in cloud cover have more of an effect on the amount of this radiation reaching the surface of the Earth than do variations in ozone (Gautier *et al.* 1994; Blumthaler *et al.* 1996; Kylling *et al.* 2000a). Because clouds are formed by small water droplets or ice crystals, radiation is scattered when passing through them, generally resulting in extinction or diminished transmissivity of the atmosphere. Under some circumstances clouds can increase UV radiation at the Earth's surface. Light clouds scattered over a blue sky make little difference to UV intensity (for less than four octas, the effect of cloud is negligible (Alados-Arboledas *et al.* 2003)), unless directly covering the Sun; while complete light cloud cover reduces terrestrial UV to about one half of that from a clear sky. In Antarctica, Ambach (1974) determined that the presence of polar stratus clouds and a highly reflecting surface can result in higher incoming shortwave radiation in the presence of clouds than for clear skies – this was coined the "radiation paradox".

Radiative and meteorological measurements were collected during a cruise from Australia to Antarctica in austral summer 2000 (Wendler *et al.* 2004). On average, the amount of fractional cloud cover was high (81%), reducing the incoming solar radiation. When a highly reflecting surface was present (total snow-covered, undisturbed ice pack with an albedo of 81%), the incoming global radiation under overcast conditions was 85% higher than for a water surface, due to multiple reflections (Wendler *et al.* 2004). A preliminary study by Sabburg *et al.* (2003) investigated spectral UV irradiances to determine the UV wavelength ranges that undergo enhancement in the irradiances due to cloud. The data suggested that on average, cloud enhancements in the UVB are influenced by increases in irradiance below 306 nm, and generally all higher wavelengths contribute, on average, similar enhancements.

Cloud transmission depends partly on wavelength (Blumthaler and Ambach 1988a; Frederick and Steele 1995; Seckmeyer *et al.* 1996; Frederick and Erlick 1997). A larger fraction of radiation is backscattered by molecules beneath a cloud layer at shorter wavelengths (where Rayleigh scattering is stronger), and some of this is then reflected by the cloud base back toward the ground. A cloud, thereby, preferentially reinforces ground level radiation at short wavelengths (Bordewijk *et al.* 1995; Frederick and Erlick 1997). The magnitude of the reduction in UV irradiances by clouds is highly variable, depending on cloud amount and coverage, cloud cell morphology, particle size distributions and phase (water droplets and ice crystals), and

possible in-cloud absorbers (especially tropospheric ozone) (Madronich *et al.* 1998). Because of the high spatial and temporal variability of clouds, no single value can be given for their effects on surface UV levels, and this impacts on the ability to detect long-term trends in the UV intensities reaching the Earth's surface (Madronich *et al.* 1998). At shorter wavelengths in the UVB range, long photon path lengths in clouds can increase absorption by tropospheric ozone, resulting in a sharp decrease in effective transmission (Frederick and Lubin 1988; Mayer *et al.* 1998)

Sabburg and Wong (2000) studied the frequency, magnitude and sky properties associated with UVB enhancement, from which they attempted to explain the physical mechanism for this enhancement. Chen *et al.* (2004) analysed both ship-borne measurements of UVB and computed values of UVB using a radiative transfer model (RTM). The ratio of the measured dose to that computed for clear-sky conditions was defined as transmittance. It was found that attenuation is almost independent of SZA; transmission is reduced by 7.7% if the cloud cover is increased by one octa; and the average transmittance of the UVB doses is 0.4, indicating that clouds played an important role in reducing the UV radiation. Calbó *et al.* (2005) determined that the variability that clouds induce on UV radiation is particularly significant when short timescales are involved.

3.2.5.2 Cloud detection

When observing sea ice and snow conditions, all channels of the AVHRR sensor are limited to cloud-free conditions, because none of the frequencies can penetrate cloud. Further problems are caused by the frequent isothermal conditions or temperature inversions common in polar regions (Rabindra *et al.* 1992). At mid-IR (infra red) wavelengths, temperature inversions in the lower troposphere can render temperature discrimination between the surface and cloud top ineffective (Lubin and Massom 2006). Regular observation of surface properties can only be done at wavelengths where clouds are nearly transparent, i.e. in parts of the microwave.

Various methods have been developed to detect the surface of pixels in a satellite image which are obscured by clouds. The difficulty in this process, is that cloud signatures differ depending on their height, their temperature, whether they are over land or water, and from any number of variations produced by the ecosystem they cover. One approach to the problem of processing such large amounts of data is the use of expert systems – computer programs that can solve problems in a way that would be considered intelligent if done by a human, but can be performed at a much faster rate (Rabindra *et al.* 1992). Advantages of expert systems apart from their speed of processing are: permanence, multiple expertise, increased reliability and heuristic knowledge (Turban 1995).

Rabindra *et al.* (1992) applied a hybrid expert system, for which the knowledge base was derived from a set of spectral and textural features which had been shown to provide high classification accuracy in AVHRR Local Area Coverage Arctic scenes (Welch *et al.* 1992). The

hybrid expert system constructed by Rabindra *et al.* (1992) was able to classify 10 polar cloud and surface types with an overall classification accuracy of 87 ± 1%.

The ICEMAPPER analysis system developed by Williams *et al.* (2002) uses a set of rules to classify Antarctic surface types (high cloud, low cloud, open water, land ice and sea ice), and another set of rules to determine sea-ice concentrations. When tested on six AVHRR images of the East Antarctic coastline, acquired late in the 1997/1998 summer season, it successfully identified 85% of the pixels. This system was restricted to the summer season and for SZAs less than 75°. Evaluation of the system for higher SZAs indicated that the system produces higher misclassification rates, probably due to the inapplicability of the Lambertian reflectance model at these higher SZAs (Zibordi and Meloni 1991). If a surface is made of an idealised material that reflects incident radiation equally into all directions, such that the upwelling intensity is isotropic, it is known as a Lambertian surface (Lubin and Massom 2006). In nature there are very few surfaces that are true Lambertian reflectors. Changes in meteorological conditions during the year cause the misclassification rate of the system to increase if the system is used for times for which the system was not trained.

3.2.5.3 Quantifying the effect of clouds on levels of UV radiation

Typically, cloud information in polar regions is calculated from satellite measurements done once a day, while the cloudiness may change rapidly during the course of the day. This low temporal resolution of satellite data may cause differences between daily satellite- and ground-based surface UV (Arola *et al.* 2002). Matthijsen *et al.* (2000) and Williams *et al.* (2004) both reported a higher satellite-derived UV cloud transmittance with respect to that measured from the ground, particularly for large cloud cover. This difference is more noticeable when observed on daily averages than on monthly averages, given that large cloud cover percentages are more frequent for shorter time periods.

A limited number of empirically-derived cloud cover correction functions (e.g. Antoine *et al.* 1996; Antoine and Morel 1996; Davis 1996 - which are based on fractional cloud cover estimated using a two-dimensional cloud cover approximation) have been developed. It is the complex three-dimensional morphology of clouds that ultimately affects the surface irradiance (O'Hirok and Gautier 1998; Ricchiazzi and Gautier 1998; Ricchiazzi *et al.* 1998). Information on the radiative properties of actual cloud conditions (which often occur as horizontally inhomogeneous cloud fields) are thus generally poor (Schwander *et al.* 2002). Moreover, the irradiance attenuation due to clouds is often approximated using monthly or seasonally-averaged cloud cover amounts, but the large spatial and temporal variability of clouds affects marine primary production at shorter time scales, such as diurnal (Kim and Hofmann 2005).

The solar angle influence on the cloud transmission factor is rather low for SZAs greater than 30°, especially for the completely covered conditions (eight octas) (Josefsson and Landelius 2000; Alados-Arboledas *et al.* 2003). If the SZA is less than 30°, the cloud attenuation for partial

cloud cover is greater than that encountered for larger SZAs the attenuation for overcast conditions is 20% smaller than that obtained for larger SZAs. These different behaviours can be explained in terms of the reflection-enhancement under partial cloud cover conditions, an effect that is absent under overcast conditions.

3.2.5.4 Cloud Modification Factor

A common approach to modelling global irradiance for skies with discontinuous cloud is the combination of the result of a clear-sky model, with a factor to describe the cloud influence, called cloud modification factor, CMF:

$$CMF = E_{cloud} / E_{clear} \qquad (3.1)$$

where E_{cloud} is the global irradiance in the presence of clouds and E_{clear} is the global irradiance for the same atmospheric conditions but for a cloudless atmosphere (Schwander *et al.* 2002). Individual CMF values can be determined from a UV irradiance value under cloudy conditions in combination with an irradiance value for the corresponding clear-sky conditions. The irradiance for the cloudy condition is always determined by observation, while the clear-sky irradiance either is taken from measurements or is modelled. A CMF parameterisation is determined by the correlation of many measured CMF values with an appropriate description of the corresponding cloud properties. Different CMF parameterisations can be found in the literature (e.g. Bais *et al.* 1993; Blumthaler and Ambach 1994; Bodhaine *et al.* 1996; Chubarova 1998; Grant and Heisler 2000; Josefsson and Landelius 2000). The quality of the CMF parameterisation depends largely on the quality and length of the measurement time series that are analysed for the parameterisation (Schwander *et al.* 2002).

Calbo *et al*. (2005) reviewed several works that deal with the effect of clouds on UV radiation. The reviewed relationships were compared through the use of the CMF. The range of CMF values found within the reviewed papers is very large, especially in broken and overcast conditions, and owing to the broad range of sites, climates, temporal basis, UV variable concerned, instrumentation, etc. Despite the large dispersion of values, it is clear that the cloud effect on UV radiation is 15-45% lower than the cloud effect on total solar radiation. Most authors agree that difficulties in describing cloud effects on UV radiation derive basically from the large variability of cloud fields (sky condition) either in space, time, cloud type, or optical characteristics.

Calbó *et al*. (2005) determined two main shortcomings in the reviewed works. Firstly, there is limited spatial coverage in the databases used (most works are built on data from northern mid-latitudes; a few are built on other parts of the world). Secondly, most works that suggest an empirical formula to estimate CMF do not check the validity of the formula against an independent dataset. Calbó *et al.* (2005) made the following recommendations for future research, details of which can be read in the text:

- Clearly establish and accurately select the time basis for the data to be used;
- For a proper description of the yearly cycle and for having a large enough number of samples, databases should be at least one year long;
- Some limitation regarding SZA must be set in order to avoid poor cosine responses of measurement devices. In addition, rapidly changing sky conditions should be filtered out from the analyses;
- Perform accurate UV instrument maintenance and calibration; and
- Carry out suitable comparison of the cloudless model with cloudless measurements.

3.2.5.5 Problems associated with cloudiness in Antarctica

The preliminary study by McKenzie *et al.* (1998b) assessed satellite-derived fractional cloud cover as an estimator of cloud effects on UV radiation measured at Lauder, New Zealand. Although there is a good correlation between measures of cloud cover from satellite and from the ground, their correlation with surface irradiance in either the visible or UV parts of the spectrum is found to be weaker. In Antarctica, ground-based measurements of cloud cover are strictly limited, making it necessary to use satellite-derived cloud estimates as the best option available. It can be concluded that clouds are one of the major uncertainties in estimating and forecasting UV trends, since their daily, seasonal or long term variability can hide UV trends due to ozone depletion.

The influence of clouds on irradiance is strongly related to the cloud height, but only weakly related to cloud form (cumulus-type or stratus-type) (Cede *et al.* 2002a). Chen *et al*. (2004) found greater attenuation of UVB for clouds whose base lies below 300 m, with an average reduction of 65%. Clouds between 300 m and 1000 m reduced UVB doses by 56%. When conducting remote-sensing studies of cloud properties, it is fortuitous to have satellite imagery covering an intensive field program, but more often, field observations are used to develop the regionally specific radiative transfer models suitable for remote-sensing retrieval (e.g. Tsay *et al.* 1989). Cloud base height (CBH) profiles are, however, difficult to describe and analyse (Mahesh *et al.* 2001). CBH has a complex structure that varies with the coordinates of the observation point and time. Such a complexity is due to a variety of processes that take place in the marine boundary layer formed over the sea surface (Kitova *et al.* 2002). The research by Mahesh *et al*. (2005) demonstrated very little seasonal variability in CBHs, but showed that 60% of CBHs were within the lowest 400 m with the remainder ranging up to 6 km. Hutchison (2002), Kassianov *et al.* (2005) and Hutchinson *et al.* (2006) are among other researchers who have undertaken CBH research, but to date there are no CBH data for the Antarctic sea ice zone which could be included in modelling levels of UVB at the Earth's surface. In overcast conditions, physical considerations of cloud and surface reflectance suggest that the radius of influence of a given surface element is of the order of the CBH (Ricchiazzi and Gautier 1998). Presumably, surface regions that remain uniform over a horizontal scale much larger than the CBH should be well

characterised by the local surface albedo, but it is difficult to know how to weight the importance of contributions at different radii around the sensor if the snow or sea ice coverage varies on the sub-kilometre scale (Ricchiazzi and Gautier 1998)

As noted in Section 3.2.3 above, the production of DMS may increase with the increase in levels of UV radiation (Ferek *et al.* 1995). While studies have observed strong relationships between DMS flux and atmospheric properties, such as cloud condensation nuclei concentrations in certain regions (for example, Ayers and Gras 1991; Ayers *et al.* 1991; Vallina *et al.* 2006), evidence confirming a DMS-climate feedback remains elusive (Toole *et al.* 2008). A cloud optical thickness of τ =11 is typical for clouds in the Antarctic sea ice zone (Fitzpatrick *et al.* 2004), and aerosol loadings are low (Shaw 1982; Liu *et al.* 1991; Kylling *et al.* 2000b), but this status may change in the future.

4. MODELLING OF RADIATIVE TRANSFER

4.1 Background

> "The essence of 'remote sensing science', the retrieval of geophysical products from satellite data, involves the interpretation of calibrated satellite images (myriad measurements of electromagnetic radiation intensity) in terms of specific phenomena in the Earth system" (Lubin and Massom 2007).

In order to develop maps of biologically effective UV doses at various levels within the sea ice and water column, it is necessary to estimate levels of erythemal UV at the surface of these media. This first step required the use of a radiative transfer model (RTM) and satellite data (TOMS data and AVHRR irradiance data). This chapter reviews some of the RTMs available researched for this study.

The propagation of radiation through a medium is affected by absorption, emission and scattering processes. The equation of radiative transfer describes these interactions mathematically. Analytic solutions to the radiative transfer equation exist for simple cases (Chandrasekhar 1960; Paltridge and Platt 1976; Lenoble 1985; Stamnes 1986), but for more realistic media like the atmosphere, with complex multiple scattering effects due to the influences of the many thousands of trace gas absorption features, numerical methods are required. Once the atmosphere is accounted for, the algorithms for exploiting physical (e.g. sea ice) or biological (e.g. chlorophyll) spectral signatures of the surface can take many forms, and efficient computation is required to choose, evaluate, and validate the most suitable algorithm from those available. Some geophysical retrievals that are relatively straightforward at lower latitudes are much more difficult in polar regions. One example is satellite detection and classification of cloud cover, which is challenging at high latitudes because both cloud tops and snow/ice surfaces are very bright at visible/near-IR wavelengths, and, due to frequent polar temperature inversions, often have very similar temperatures as measured at mid-IR wavelengths (Lubin and Massom 2007). To reliably detect and classify clouds, it is often necessary to train an algorithm to recognise differences in texture between polar surface types (Lubin and Massom 2006, 2007). This project employs such an algorithm: namely the ICEMAPPER analysis system (Williams *et al.* 2002), developed to analyse summertime images of Antarctic surfaces, and the version of ICEMAPPER modified by Borsche (2001) used for analysing springtime images (see Section 7.4.4 for further discussion).

To determine the physiological effects of increases in UV, the irradiances need to be accurately estimated, or measured, with a spectral resolution better than 1 nm (Gardiner et al. 1993). Measuring UV at the surface to the required accuracy is difficult, requiring well-calibrated and expensive equipment (Bais *et al.* 1997), as well as a skilled operator. Measurements of the

required accuracy have only been obtained at a few locations and are therefore unable to provide reliable UV surface irradiance values, except in very well-instrumented areas [e.g. in some parts of the following regions – Antarctica (Bernhard *et al.* 2006); South America (Cede *et al.* 2002b); Barrow, Alaska (Bernhard et al. 2007); Canada (Fioletov *et al.* 2003; Tarasick *et al.* 2003); Europe (Bais *et al.* 1997; Glandorf *et al.* 2005)]. Fioletov (2004) used both ground-based and satellite estimates to develop a UV index climatology over North America. If a long enough database is available, the UV radiation climatology of averages and trends for a single location can be determined (Weatherhead *et al.* 1998). For more extensive geographical coverage, a frequently used approach to establish UV climatology consists of using a reliable radiative transfer model (RTM) to calculate the clear-sky, ground-level UV irradiance using TOMS total ozone and reflectivity data (Fioletov *et al.* 2004), and applying attenuation factors to account for cloudiness. The input parameters for the radiative transfer calculations in the UV range include the elevation of the place, total ozone column, aerosol parameters, surface UV albedo and cloud optical parameters. These input data are often obtained from satellite databases, which cover the whole planet at variable geographical resolution. RTMs can give useful predictions of surface UV irradiances from available atmospheric measurements (Luccini *et al.* 2006), and even without the input parameters, RTMs can be implemented with standard climatological atmospheric values that are representative of the meteorological conditions of a particular area (Davis 1996).

Several UV radiation global climatologies have been established in this way: Lubin *et al*. (1998) (at a geographical resolution of 2.5° latitude by 2.5° longitude), Mayer and Madronich (1998) (1° x 1.25°), Sabziparvar *et al*. (1999) (5° x 5°), Herman *et al*. (1999) (approximately 1° x 1°), and Pubu and Li (2003) (1° x 1.25°). Similar approaches have been used to generate UV maps for specific regions, e.g. Peeters *et al*. (2000) and Verdebout (2000) for Europe; Meloni *et al*. (2000) for Italy; Fioletov *et al*. (2003) for Canada; Fioletov *et al*. (2004) for United States and Canada; and Luccini *et al*. (2006) for Argentina.

RTMs are generally based on a clear-sky assumption. Stratospheric ozone and clouds are the main factors which prevent incoming UVB radiation from reaching the Earth's surface (Tsay and Stamnes 1992). The attenuation of irradiance by cloud cover has more of an effect on the surface irradiance than does any other meteorological variable. Increases in (man-made) aerosols or cloudiness may for example, counteract ozone-related trends (Mayer *et al*. 1997). Also, in high latitude regions, the strongest departure from the one-dimensional assumptions on which the RTMs are based comes from the spatial distribution of high-contrast ocean and snow-covered surfaces, which locally increase albedo effects (Smolskaia *et al.* 1999). Thus, to obtain an accurate simulation of surface irradiance, it is necessary to account for both spatial and temporal variation of cloud cover and albedo effects (Kim and Hofmann 2005).

Ozone absorption is a function of the temperature and the path of propagation through atmospheric layers that contain ozone (Lapeta *et al.* 2000). Hence, the absorption of solar UV

radiation by ozone does not only depend on the TOC, but also on the SZA, atmospheric scattering and the vertical distribution of ozone and temperature. RTMs typically use standard ozone and temperature profiles, since *in situ* measurements of ozone and temperature profiles are generally not available. Lapeta *et al*. (2000) determined that discarding the variations in the ozone profile should not be a serious shortcoming of a model.

The accuracy of the output from RTMs is limited by uncertainties in input parameters representing the atmosphere and Earth's surface. Another source of uncertainty are the approximations made to the radiative transfer calculations, which are a compromise between accuracy and available computer time. The two sources of uncertainty are related, as there is little point in computing the irradiances to high numerical precision if input parameters are poorly known (Sabziparvar *et al.* 1999).

The semi-empirical model proposed by Green, Cross and Smith (GCS) (1980) [and refined by Green and Schippnick (1981), Schippnick and Green (1982) and Green (1983)] provided an analytical representation of solar UV spectral irradiance incident at the Earth's surface for a variety of atmospheric conditions and surface albedos (Petrucci 2003). This representation was obtained by adjusting the model parameters to reproduce the results of more precise radiative transfer calculations elaborated previously by Braslau and Dave (1973), and Dave and Halpern (1976). The GCS code is able to handle the UV radiation transfer through the atmosphere without implementing any complex physical processes, making it much easier and faster than other more rigorous and sophisticated radiative transfer codes described in the literature. On the other hand it is less accurate and, whereas complex codes can be easily modified to account for newly available atmospheric data, the GCS model is heavily dependent upon accurate characterisation of the atmosphere on which it was based (Petrucci 2003). Nunez *et al*. (1997) applied the GCS model to initially develop cloud-free erythemal irradiances for a section of the Antarctic coast bounded by latitudes 59° to 64° S, and longitudes 140° to 160° E. Cloudy irradiances were then estimated using the product of the cloudless irradiances and a cloud transmittance derived from AVHRR satellite imagery.

Arola *et al*. (2002) assessed four different methods to map UV using satellite data, and determined that UV doses derived by satellite algorithms can differ significantly from ground-based measurements. Even for the algorithms showing smaller deviations, the discrepancies are not yet fully understood, showing the need for further studies. It was furthermore concluded that satellite algorithms cannot be blindly used for derivation of UV doses at the ground; they should always be accompanied by ground-truthing. Further research and development should be carried out to improve the cloud parameterisation and to further develop the treatment of albedo of snow-covered surfaces.

4.2 Examples of Radiative Transfer Models

The reliability of RTMs depends on how realistically they represent the physical atmospheric processes governing UV radiation. In the following sections an evaluation is made of some of the more relevant RTMs available. The final section (4.2.7) discusses the RTM chosen for this project.

4.2.1 Lubin *et al*. (1998)

Lubin *et al*. (1998) used a RTM adapted from a leading global climate model (NCAR Community Climate Model) to estimate effective cloud optical depth, and the spectrally-resolved RTM used for the final calculation of surface UVR flux is based on the same formulation (delta-Eddington) (Joseph *et al.* 1976; Briegleb 1992; Lubin and Massom 2006). The major approximation in their work is the global application of a plane-parallel RTM to a satellite footprint of the order of 100 km. Some cloud systems should be well represented by this model (e.g. marine stratocumulus). For other, more complicated cloud (e.g. tropical cumulonimbus cells with extended cirrus anvils) the model may not be so applicable. It was necessary to use the computationally-fast delta-Eddington formulation to complete the study in a reasonable time frame. A more sophisticated 3-dimensional radiative transfer formulation would not necessarily yield better results without accurate information about cloud geometry. Any RTM simulation of surface UVR can best be refined by regularly checking the results against simultaneous surface UVR measurements (e.g. Weihs and Webb 1997b). Lubin *et al*. (1998) showed that a satellite-based UVR mapping method based on local noon data alone can provide useful estimates of the daily dose as well as the instantaneous local noon flux.

4.2.2 Pubu and Li (2003)

Pubu and Li (2003) adopted the inversion algorithm developed by Li *et al*. (2000) to take advantage of its high efficiency and accuracy, as demonstrated by Wang *et al*. (2000) when they compared the modelled results with observation data. The algorithm of Li *et al*. (2000) consists of two equations with four input variables, namely the Top of the Atmosphere UV (TOA UV) or visible albedo, total ozone amount, SZA, and aerosol properties. Except for aerosol, the input variables are available with good accuracy (Li *et al.* 2000). Since the algorithm was derived with few assumptions and empirical parameters, it is valid in principle under any conditions. The simple inversion algorithm is found to be able to estimate surface UVB irradiance very accurately under a wide variety of conditions, when results are compared with those of extensive modelling using a detailed DISORT-based (i.e. Discrete Ordinate Radiative Transfer) RTM (Li *et al.* 2000). The modification introduced by Pubu and Li (2003) was to take into account the effect of the varying Rayleigh scattering strength on the narrowband to broadband relationship, i.e. converting TOA albedo at 360 nm to TOA mean albedo in the wavelength range from 280 to 400 nm without ozone absorption.

4.2.3 Sabziparvar *et al.* (1999)

Sabziparvar *et al*. (1999) used the Discrete Ordinate Method of Stamnes *et al*. (1988) (as modified by Forster (1995)) in conjunction with a multi-year climatology of ozone, cloud coverage, surface pressure, surface albedo, temperature and a rudimentary representation of aerosols to calculate the UV reaching the surface. The spectral resolution is 5 nm, and the assumption is made that the surface is a Lambertian reflector. The model outputs were evaluated using daily UV measurements, and found to be accurate to about ±10% for clear skies and ±20% for all-sky conditions. The researchers determined that the cloud and aerosol properties provided the largest source of uncertainty in this work.

4.2.4 Herman *et al*. (1999)

Herman *et al*. (1999) estimated daily global maps of monthly integrated UV-erythemal irradiance (290-400 nm) at the Earth's surface using the ozone amount, cloud transmittance, aerosol amounts and surface reflectivity from the solar UV radiation backscattered from the Earth's atmosphere, as measured by the TOMS and independently measured values of the extraterrestrial solar irradiance. The daily irradiance values at a given location show that short-term variability (daily to annual) in the amount of UV radiation (290-400 nm) reaching the Earth's surface is caused by: partially-reflecting cloud cover; haze and absorbing aerosols (dust and smoke); and ozone (Herman *et al.* 1999).

4.2.5 Verdebout (2000)

Verdebout (2000) developed a method for generating surface UVR over Europe, with a spatial resolution of 0.05° and potentially on a half-hour basis. The UV irradiance was obtained by interpolation in a look-up table, the entries of which were SZA, TOC, cloud liquid water thickness, near-surface horizontal visibility, surface elevation and UV albedo. Both satellite and non-satellite data were exploited to assign values to the influencing factors. The UVSPEC code (see Section 4.2.7) was used to perform the radiative transfer calculations. A preliminary step was the generation of an effective surface albedo map from a series of 10 consecutive days, using Meteosat satellite data. Meteosat is the generic name of the geostationary meteorological satellites operated by the European Organisation for the exploitation of Meteorological Satellites (EUMETSAT). It was at this point that the difficulty of distinguishing clouds from snow-covered surfaces was encountered. The UV surface albedo was assigned uniform values for land and sea/ocean, except in the presence of snow, when it was given a value proportional to the Meteosat effective albedo.

The maps of surface UV irradiance could be produced on a half-hourly basis, and used to compute the UV dose integrated for a day. All included influencing factors were found to significantly affect the surface UV irradiance in the context of the geographical temporal variability encountered in Europe.

Verdebout (2004) extended his work from 2000 to develop a climatology of daily maps of surface UV radiation over Europe for the period 1984 to 2003, with a spatial resolution of 5 km. The quality of the satellite-derived estimates was assessed at several sites in Europe and, with few exceptions, the bias of the satellite-derived erythemal daily doses with respect to the measurements was found to lie within the uncertainty of the absolute calibration of the ground instruments (±7%). Verdebout (2004) found the dispersion to be large (~30% mean RMS difference), but found it was also affected by intrinsic differences between a measurement and the area average provided by the model.

4.2.6 SIDES algorithm (2003)

The Verdebout model (2000) was used as a basis for the development of the SIDES (Surface Irradiance DErived from a range of Satellite-based sensors) algorithm (Wuttke *et al*. 2003), which calculates various types of surface UV intensities, such as biologically-weighted or unweighted UV spectra, integrated doses or irradiance at specific wavelengths. The results from SIDES deviated less than 7% from ground-based observations for wavelengths between 295 and 400 nm. In contrast, the corresponding deviations of the Joint Research Center algorithm (Verdebout 2000) escalated for shorter wavelengths, reaching 35% at 295 nm. This large deviation was due to an inaccurate interpolation procedure that was detected by spectral analysis. Thus, spectral validation was demonstrated to be an appropriate tool to detect weaknesses in such an algorithm and provide information essential for improvement.

4.2.7 UVSPEC/libRadtran (1994)

The UVSPEC radiative transfer model (Kylling 1994) calculates the radiation field in the Earth's atmosphere for a variety of atmospheric conditions. Originally it was designed to calculate spectral irradiance in the ultraviolet and visible parts of the spectrum. Over the years, UVSPEC has undergone numerous extensions and improvements, including a complete rewrite in 1997 (Mayer and Kylling 2005), since when the model package has been called libRadtran (Mayer *et al*. 2006). Probably the most important change in UVSPEC was an extension from the ultraviolet to the complete solar and thermal spectral ranges. Thus, the name UVSPEC is outdated, but has been kept for historical reasons. libRadtran refers to the complete software package of functions and programs, including data sets, tools, examples and documentation.

The UVSPEC model has been thoroughly validated and checked against both measurements and other models (Mayer *et al.* 1997; Kylling *et al.* 1998; van Weele *et al.* 2000; Hofzumahaus *et al.* 2002; Bais *et al.* 2003; Wendisch and Mayer 2003; Hofzumahaus *et al.* 2004; Mayer and Kylling 2005) allowing the user to trust the model results. UVSPEC, available at http://www.libradtran.org, has been found to perform very well when comparing its output with measurements for clear-sky cases (Mayer *et al.* 1997; Lindfors *et al.* 2003). Other researchers

who have used UVSPEC in their modelling include Kylling *et al*. (2000a), Lindfors *et al*. (2003) and Lindfors and Vuilleumier (2005).

4.3 Modelling of UV radiation over inhomogeneous surfaces

Most of the earlier RTMs (before mid-1990s) lacked the ability to include regional albedo, which is not always homogeneous in nature. Some of the more recent studies that have investigated the effect of abrupt changes in albedo include Degünther *et al*. (1998), Lenoble (1998), Pogdorny and Lubin (1998), Ricchiazzi and Gautier (1998), Mayer and Kylling (2000).

It was observed by several authors (McKenzie *et al.* 1998a; Weihs *et al.* 1999; Kylling *et al.* 2000a) that the high albedo of a snow-covered surface, especially in the UV and visible wavelengths, has a large effect on the downwelling radiation, due to multiple reflections between the ground and the scattering atmosphere. Modelled values of ultraviolet irradiance for cloudless sky showed enhancements in irradiance levels of nearly 50% at 320 nm for a snow-covered surface compared with snow-free conditions (Lenoble 1998). The enhancement is much larger when the sky is cloudy than when it is clear, because of the increased atmospheric backscattering due to clouds. A number of previous studies investigated the combined effect of surface albedo and clouds on UV irradiance (for example, McKenzie *et al*. (1998a), Kylling *et al*. (2000a) and Nichol *et al*. (2003))

Smolskaia *et al*. (2006) undertook spectral radiance and irradiance measurements in Antarctica in combination with a 3-D modelling study. They detected two effects in response to a high surface albedo. One is the alteration of the spatial distribution of sky radiance. Radiation from directions close to the horizon is more enhanced than from other directions. This effect becomes stronger with increasing wavelength. The second effect is the enhancement of irradiance due to a snow-covered surface as well as in the surroundings of the measurement site. A region as far as 50 km away from the measuring site can still significantly contribute to the enhancement of irradiance.

5. DATA

The data required for estimating levels of erythemal UVR for this project are TOC, irradiance, and sea ice and snow thickness. The following sections describe these data, from where they were sourced, and how the output from using these data sets with an RTM was validated, using *in situ* erythemal UV data collected at Antarctic stations and onboard one of the Australian Antarctic Division chartered vessels.

5.1 Satellite data – general

Earth satellite sensors are not specifically designed for polar research. However, the realisation of the central importance of polar regions in the global climate system has seen missions dedicated to polar research being launched (for example, ICESat (Ice, Cloud, land and Elevation Satellite) and CryoSat-2 (Lubin and Massom 2006) (more detail included in Section 10.2)). At the same time, most Earth remote sensors are intrinsically valuable for polar research because they are deployed in high inclination, or "polar" orbits. Because their ground tracks converge spatially at high latitudes, polar regions benefit from more frequent coverage by the sensors, and polar processes can often be studied on a greater variety of spatial and temporal scales than those at mid- and tropical latitudes (Lubin and Massom 2006).

No ideal, all-purpose, remote sensor exists, but scientists now have a choice of a range of datasets, each with its own set of inherent attributes, strengths and limitations. The choice of an optimal dataset, or datasets, for a given application depends upon the scale and nature of the problem being investigated and the satellite dataset characteristics (Lubin and Massom 2006). Undertaking surface measurements in the sea ice zone is logistically difficult and expensive, and the data acquired from *in situ* research programs are both spatially and temporally sparse. It is hard to find a geophysical research community having a greater need for satellite remote sensing than polar researchers.

Even though satellite remote sensing is a powerful research and operational tool, it will never entirely replace *in situ* measurements in the sea ice zone (Lubin and Massom 2006). The latter continue to be extremely important, both in terms of providing (i) detailed information for the calibration of satellite-derived data and (ii) key information that cannot be measured directly from space. Satellites also play an important role in transmitting information from sensor packages deployed on ice floes (Heil and Allison 1999), in the ocean (Sallée *et al.* 2010a; Sallée *et al.* 2010b) and attached to marine mammals (Roquet *et al.* 2009) and birds (Lubin and Massom 2006).

Mahesh *et al.* (2004) and Lubin and Massom (2006, 2007) describe the two basic types of remote sensing instruments (i.e. passive and active) and how they function. Over polar oceans, the most common weather condition is overcast with extensive stratus or stratocumulus. Visible

and IR imagers cannot observe the surface through clouds, but certain microwave sensors can. As a result, microwave remote sensing, both passive and active, plays an enormously important role in the study of sea ice and ice sheets (Lubin and Massom 2007).

Massom (1991) reviewed the vital contributions made by remote sensing to the modern era of polar research in the 20th century, while Lubin and Massom (2006) give a resumé of 21st century agency missions from various countries around the world. Most national polar research programs collect satellite data with their own tracking systems. The extent to which these datasets are properly catalogued and archived varies, but researchers can usually obtain satellite datasets from the various national programs in exchange for genuine collaboration (Lubin and Massom 2006).

5.2 AVHRR irradiance data

The NASA Distributed Active Archive Center (DAAC) that specialises in polar applications, is the National Snow and Ice Data Center (NSIDC), located in Boulder, Colorado. NSIDC archives an enormous variety of polar field data, and also hosts satellite data products – some of which are "pathfinder" products. These data products have been rigorously developed with proper attention to the unique remote-sensing challenges in polar regions. The long-term datasets are designed for the convenience of polar researchers – being easy to access and use. Twice-daily images in polar stereographic grids can be ordered using the GISMO tool (see Table 5.1) and are made available for download. Table 5.1 includes basic details of the AVHRR Polar Pathfinder (AVHRR PPF) dataset for the Southern Hemisphere, which was sourced for this project. Further information on the AVHRR PPF data (Fowler *et al.* 2000) can be found in documentation at http://nsidc.org/data/docs/daac/nsidc0066_avhrr_5km.gd.html.

Table 5.1: Overview table of AVHRR Polar Pathfinder (PPF) data (Fowler *et al.* 2000).

Category	Description
Data format	1-byte and 2-byte big-endian integer grid format
Spatial coverage	Extends poleward from 53.2°S latitude
Spatial resolution	5 km
Temporal coverage	From 24 July 1981 to 30 June 2005 (the dataset documentation lists dates for which data is missing – see http://nsidc.org/data/docs/daac/nsidc0066_avhrr_5km.gd.html)
Temporal resolution	Twice-daily composites approximately 0200 hours and 1400 hours for the Southern Hemisphere
Grid type and size	Equal Area Scalable Earth-Grid (EASE-Grid) projection, 1605 pixels by 1605 pixels (centred on South Pole)
Parameters	Channel 1 Top of the Atmosphere (TOA) Reflectance Channel 2 TOA Reflectance Channel 3 TOA Brightness Temperature Channel 3A TOA Reflectance Channel 3B TOA Brightness Temperature Channel 4 TOA Brightness Temperature Channel 5 TOA Brightness Temperature Clear Sky Surface Broadband Albedo Clear Sky Surface Skin Temperature Solar Zenith Angle Satellite Elevation Angle Sun-satellite Relative Azimuth Angle Surface Type Mask Cloud Mask Universal Coordinated Time (UTC) of Acquisition
Data availability	To order data use the GISMO tool, see link at http://nsidc.org/data/gismo/index.html

The key parameter employed for the modelling in this project is the 'surface type mask' from which a surface UV albedo for the pixel was derived, based on whether it was open water or sea ice, and if sea ice, at what concentration (see Section 7.4.2 for an explanation of this process). The original intention was to use the 'clear sky surface broadband albedo' provided in the PPF dataset in the modelling calculations, but this idea was discarded for the following reasons. Firstly, the difficulty associated with discriminating between cloud and ice meant that the albedo in the PPF dataset might not necessarily have been that of the surface, but of clouds within the view of the satellite sensor instead. Secondly, insufficient research was found on which to base a reliable conversion from broadband to ultraviolet albedo (see Section 7.4.2 for details). Also, on occasions there were albedo values that were greater than 100%. This not only caused concern about the veracity of the albedo parameter overall, but it meant that these pixels did not display correctly in the plots. The derivation of the surface type mask was based on Special Sensor Microwave Imager (SSM/I) passive microwave brightness temperatures, regridded from the daily-averaged SSM/I Daily Polar Gridded Brightness Temperatures dataset to the 25 km EASE-Grid (see Figure 5.1). They were first partitioned into land (including ice sheets) or ocean. Over oceans, the NASA Team Sea Ice Algorithm (Fowler *et al.* 2000) was used to generate first-year and multi-year ice concentrations. For the purpose of the cloud detection procedure, all

ocean pixels with an estimated ice concentration greater than 0% were flagged as sea ice. In some cases, atmospheric effects and wind roughening of the ocean caused false ice concentration retrievals over open ocean. Such areas appeared as incorrectly-mapped areas of sea ice in the mask; however, for cloud detection, preliminary work suggests that it is important to avoid excluding areas with less than 15% true ice cover. Areas that consist of at least 50% multi-year ice are assigned the multi-year flag. The multi-year ice estimate is subject to considerable error and uncertainty, particularly during periods when surface melt is likely (Fowler *et al.* 2000). At such times, characteristic multi-year ice emission properties are partially or completely hidden, and melt-freeze metamorphosis or other changes in the snow cover on sea ice may cause first-year ice to appear as a fraction of multi-year ice (Fowler *et al.* 2000). Since thresholds were applied to the output from ice concentration, ice type, and snow depth algorithms, slight variations in the values yield a noisy appearance in the resulting binary-flag images, particularly in spring and summer due to algorithm limitations (Fowler *et al.* 2000). Table 5.2 describes the surface mask type (SMSK) cell contents. There is further information found in the code *create_maps.pro* (Appendix A) as to how the appropriate albedos were allocated to the different ice classes.

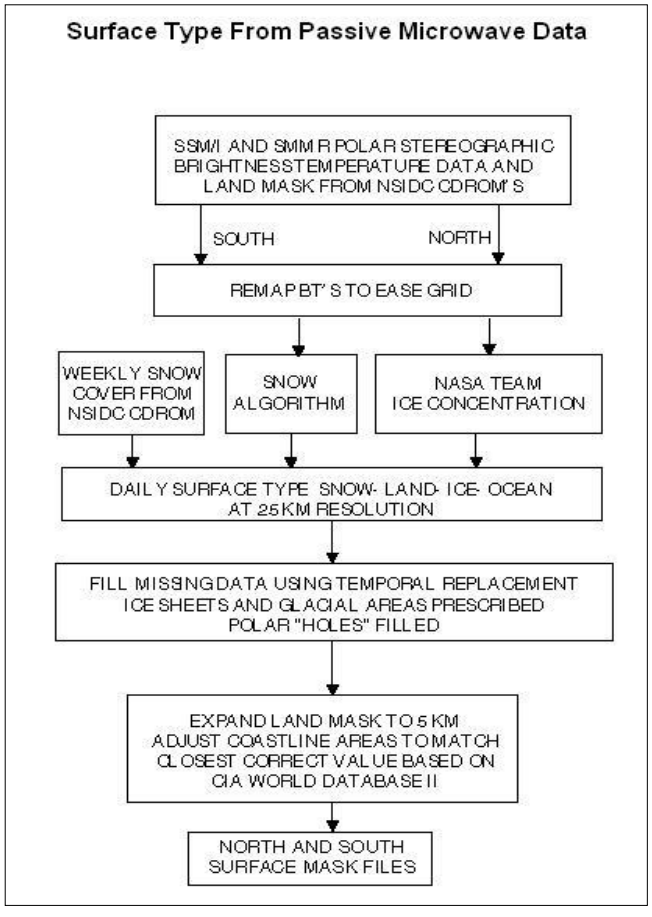

Figure 5.1: Box Flow Chart showing surface type from passive microwave data (Fowler *et al.* 2000).

Table 5.2: Table of surface mask type (SMSK) cell contents.

Surface Mask Type	
Cell Value	**Description**
10	Open water
20-29	Mostly first-year ice (range indicates total ice concentration in tens of percent; for example, a value of 20 indicates more first-year ice than multi-year ice with a total ice concentration between one and ten percent)
30-39	Mostly multi-year ice (range is same as above; however, multi-year ice is dominant)
40	Bare land
50	Snow-covered land
60	Ice sheet

For a test subset of 46 images, the plots of the 'cloud mask' provided in the PPF dataset were compared with plots of the classifications of cloud/ice by Williams *et. al* (2002) for summer and Borsche (2001) for spring. The decision was made to base the model on the latter algorithms as, on visual inspection, the surface classifications were more often close to surface types seen in plots of broadband surface albedo in the PPF dataset. Table 5.3 describes the cloud mask (CMSK) bit number values.

Table 5.3: Table of cloud mask (CMSK) bit number values.

Cloud Mask (CMSK) Version 3 Data (1994 to 2005)		
Bit number	**Description**	**Bit value**
Bit 0	The least significant bit. Cloud mask from Cloud and Surface Parameter Retrieval (CASPR) single-day algorithm (Fowler *et al.* 2000)	0 - clear
		1 - cloud
Bit 1	Cloud mask from updated CASPR multi-day algorithm	0 - clear
		1 - cloud
Bit 2	Set if no valid data are present	0 - valid data
		1 - missing data

5.3 Ozone data

The reason for undertaking this research was to determine if ozone depletion is having deleterious effects on organisms living in various niches in Antarctica. Estimates of daily total ozone column were needed in the calculations to determine levels of biologically-effective UV for the study regions.

The TOMS instrument has been successfully flown on four satellites (Nimbus-7, Meteor-3, Earth-Probe (EP), and ADEOS) for daily monitoring of regional and global distribution of atmospheric ozone, resulting in a nearly continuous, long-term record (1978-2005) of

atmospheric ozone observations. The EP-TOMS ozone data for July 1995 to December 2005 (with some missing days) were used in this project. Other satellite instruments have measured, and continue to measure, ozone, e.g. solar backscatter ultraviolet (SBUV), Global Ozone Monitoring Experiment (GOME), Scanning Imaging and Absorption Spectrometer for Atmospheric Chartography (SCIAMACHY) (Ahmad *et al.* 2004). The Ozone Monitoring Instrument (OMI) onboard the AURA spacecraft, (which was launched in July 2004) continues the TOMS record for total ozone and other atmospheric parameters related to ozone chemistry and climate (Torres *et al.* 2007).

The following is included in information on EP-TOMS available at http://nasascience.nasa.gov/missions/toms: EP-TOMS measured total ozone by observing both incoming solar energy and backscattered UV radiation at six wavelengths. 'Backscattered' radiation is solar radiation that has penetrated to the Earth's lower atmosphere, and is then scattered by air molecules and clouds back through the stratosphere to the satellite sensors. Along that path, a fraction of the UV is absorbed by ozone. By comparing the amount of backscattered radiation to observations of incoming solar energy at identical wavelengths, scientists can calculate the Earth's albedo. Changes in albedo at the selected wavelengths can be used to derive the amount of ozone above the surface (Netting 2008). TOMS on Earth Probe satellite made measurements every 8 seconds, each measurement covering 50 to 200 kilometres wide on the ground, strung along a line perpendicular to the motion of the satellite. Almost 200,000 daily measurements covered every single spot on the Earth except areas near one of the poles, where the Sun remains close to, or below the horizon during the entire 24-hour period (Netting 2008). These individual measurements vary typically between 100 and 650 DU and average about 300 DU (McPeters *et al.* 1998).

Day: 269 Sep 25, 1997 EP/TOMS STD OZONE GEN:97.269 Asc LECT: 11:19 AM
Longitudes: 288 bins centered on 179.375 W to 179.375 E (1.25 degree steps)
Latitudes : 180 bins centered on 89.5 S to 89.5 N (1.00 degree steps)
211211211211207207207207205205205205205205205205205205205205205205205205205205205205200200200
200199199199199197197197197195195195195194194194194194194194194194194194194194194194194194194
194194194194194194187187187187189189189189192192192192192192192192192192192192192192192192188
188188188188188188188188188188188188188188188188188189189189189189189189189189189189195195195
195195195195195195195195195195195197197197197200200200200198198198198199199199199201201201
201201201201201201201201201202202202202202202202202202192192192192192192192192192192192192
192192192192192192192192192192208208208208208208208208208208208208208208208208208208208208197
197197197197197197197200200200200200200200200202202202202032032032032012012012012012012012
201201201201201201201201201201201201201201201201197197197197199199199199198198198198196196196
196196196196196192192192192 lat = -89.5
217217217217217217217217209209209209203203203203202202202202202202202202202202202202202199199199
199198198198198191191191191191191191191191191191191191191191191191191191191191191191191191189
189189189189189189186186186186186186186186186187187187187187187187187187187187187187187187187
187187187187188188188188190190190190190190190190190190190190190190190190190190190190191191191
192192192192192192192192192192192193193193193193193193200200200200200200200200200200200200
200200200200200200201201201201202202202202112112112112112112112112112112112112112112112112112
211211213213213213217217217217217217217217220220220220216216216216219219219219219219219211
211211211211211211211209209209209221221221221220220220220218218218218218218218218217217217217
216216216216216214214214208208208208206206206206206206206206206206206206206206203203203198198198
198196196196196196196196196 lat = -88.5

Figure 5.2: Sample of TOMS ozone data from McPeters, *et al.* (1998).

Level 3, version 8 ozone data are archived at the Goddard Distributed Active Archive Center (DAAC) in the EOS version of Hierarchical Data Format (HDF-EOS). The individual TOMS measurements have been averaged into grid cells 1 degree of latitude by 1.25 degrees of longitude. The 180 x 288 ASCII array contains data from 90° S to 90° N, and from 180° W to 180° E. Each ozone value is a 3 digit integer, and LECT is the local equator crossing time (from http://mirador.gsfc.nasa.gov/cgi-bin/mirador/presentNavigation.pl?project=TOMS&tree=project) (see Figure 5.2).

5.3.1 Errors and accuracy of TOMS ozone data

Even though it is relatively easy to detect ozone in the atmosphere, it has proved difficult to make sufficiently precise and numerous measurements to determine changes of a few percent in a decade. Difficulties include knowing how the absolute calibrations of the instruments change with time; assessing how much variability in any set of measurements is caused by the instrument, and how much by the natural variability in the atmosphere; and interpreting comparisons of measurements made by different instruments, especially when different techniques are used (Harris *et al.* 1997).

Changes in operational satellites, recalibration of ground-based instruments, or interruptions in observation records result in data sets which may have systematic errors that change with time. These errors are usually significantly less than the ozone decline seen in recent years over middle and polar latitudes, and therefore have had limited adverse effects on the trend estimates for these regions. However, variations in global ozone are about 2-3% (WMO 1999), so a systematic error of 1%, which is typical even for the most reliable instruments, makes detection of real ozone changes on a global scale difficult. This problem has been addressed in recent years by comparing data from several sources and, if necessary, applying systematic corrections (Fioletov *et al.* 2002).

It is fortuitous that there is an ozone data source from the one instrument available for the duration of this project, which minimises the above-mentioned difficulty of multiple sources, although the problem of gaps in the data coverage persists. Because TOMS measures ozone using scattered sunlight, it is not possible to measure ozone when there is no sun (i.e. in polar regions in winter). Consequently, maps of ozone for the Antarctic will always have areas of missing data due to polar night. Data are also lost because of missing orbits and other technical problems (McPeters and Beach 1996). As an example, after failure of the ADEOS satellite on 29th June, 1997, it was decided to raise the EP/TOMS orbit to 750 km to provide more complete global coverage. This was accomplished over the period 4th December to 12th December 1997, during which time no EP/TOMS data are available. This resulted in an EP/TOMS data set of 1 ½ years of high resolution data taken at the expense of full global coverage (McPeters and Beach 1996).

At the transition between good and flagged or missing data, an "edge effect" will appear, consisting of a few pixels of apparently low ozone values. These are artefacts generated when the original data were interpolated to produce the stored image data (McPeters and Beach 1996). Another fundamental problem with the use of data from polar orbiting satellites is that the observations are not all made simultaneously. Global maps can be constructed by overlaying subsequent tracks observed at different times. However, spurious gradients due to changes in the ozone distribution in time can occur between adjacent tracks measured at different times (Levelt *et al.* 1996).

Bhartia and Wellemeyer (2009) give details of the way that the TOMS V8 total ozone algorithm was designed to remove any latitude- and seasonally-dependent biases from the data, and how the residuals are used to detect and correct errors. However, like any remote sensing technique, the aforementioned algorithm is susceptible to the following distinctly different types of errors (Bhartia and Wellemeyer 2009): forward model errors, inverse model errors and instrumental errors.

In their 'error summary', Bhartia and Wellemeyer (2009) state that all the important error sources mentioned are systematic, i.e. the errors are repeatable given the same geophysical conditions and viewing geometry. However, most errors vary in a pseudo-random manner with space and time, so they tend to average out when data are averaged or smoothed.

Table 5.4: Estimated errors in retrieved TOMS ozone from McPeters *et al*. (1998).

Source	Error (%)
Random – not applicable to long term change (typical values – may be larger in winter months or under disturbed atmospheric conditions)	
Instrument noise	0.3
Instrument characterisation	0.3
Atmospheric temperature	1.0
Retrieval error	1.0*
Tropospheric ozone	1.5
Net (Root sum of squares)	2.0
Time Invariant	
Rayleigh scattering	<0.5
Ozone absorption cross-section	<2.0**
Wavelength calibration	1.0
Radiometric calibration	<1.0
Retrieval error	<1.0
Net (Root sum of squares)	3.0
Time Dependent (over first year)	
Radiometric calibration	<0.5
Wavelength calibration	<0.25
Atmospheric temperature	0.16/K
Tropospheric ozone	0.05/percent change
* May be 5 percent or higher at very high solar zenith angles	
** Value for comparisons with non-UV instruments or UV measurements evaluated using different ozone absorption cross-sections	

There are three areas in which uncertainties can be introduced into the ozone data derived from TOMS: the accuracy and precision of the measurements; the value of the radiances calculated from the radiative transfer model; and the process of comparing the measured and calculated radiances to derive ozone values (McPeters *et al.* 1998). In each of these areas, errors of three kinds are possible: random errors, time-invariant systematic errors and time-dependent systematic errors. Table 5.4 summarises the estimated uncertainties in the retrieved EP ozone. They are organised by type of error rather than by where they originate in the ozone retrieval process. This organisation makes it clearer how the errors are to be combined to derive a total error for the retrieval.

Bhartia *et al.* (1993) examined the effect of Mount Pinatubo aerosols on total ozone measurements from backscatter ultraviolet (BUV) experiments. Radiative transfer calculations show that, except at very high SZAs, errors in total ozone derived from the aerosol-contaminated radiances are less than 2%, and vary both in magnitude and in sign with angles of observations. At SZAs greater than 75°, total ozone values may be underestimated by as much as 10% if a large concentration of aerosols is present near the ozone density peak. In subpolar latitudes, error in total ozone derived from TOMS as a function of scan angle is very sensitive to the aerosol size distribution parameters.

Email correspondence from A.R. Klekociuk (pers. comm., 2008) pointed out that there could be an instrumental effect at about the 10 DU level in the TOMS V8 data which gives a lower ozone column over ice. Cuevas *et al.* (2001) reported on the GHOST (Global Hidden Ozone Structures from TOMS) effect in a case study in the Iberian Peninsula. Over this land mass in summer, the magnitude of total ozone is 2.5% (8 DU) lower than over the surrounding seas. This phenomenon was tested by calculating what effect it would have on the output for this project as follows:

Software was written to extract a ‘slice’ of erythemal UV values from the Look-Up Table (LUT) for an ozone value, say, X DU (where X = 50, 100, 150, 200, 250, 300, 350, 400, 450, 500), then extract a slice for an ozone value (X + 10) DU. The difference and the percentage difference between each erythemal UV value in the slices were determined (Table 5.5) and plotted (Figure 5.3).

There is a stronger effect on erythemal UV values with lower ozone values. It can be assumed that TOC would not be less than 100 DU over sea ice. The percentage differences for erythemal UV values for SZA = 35° and TOC = 100 DU were extracted, and they showed that the maximum over-estimation in the erythemal UV values to be expected is 10%. Choosing a SZA of 65° and TOC of 300 DU, the maximum over-estimation in erythemal UV values is expected to be 3.5%. On this basis, the potential for the effect of GHOST-type errors in TOC values was deemed to be not highly significant.

Table 5.5: Difference and percentage difference of erythemal UV values (mW m^{-2}) for ozone values, X and (X + 10) DU.

Ozone (DU)	Max. difference	Max % difference
50	401.567	20.0875
100	140.645	11.2122
150	66.7056	7.71405
200	37.2219	5.93678
250	23.0592	4.78884
300	15.3838	4.00956
350	10.8311	3.41937
400	7.95886	3.05657
450	6.05658	2.59792
500	4.7258	2.29715

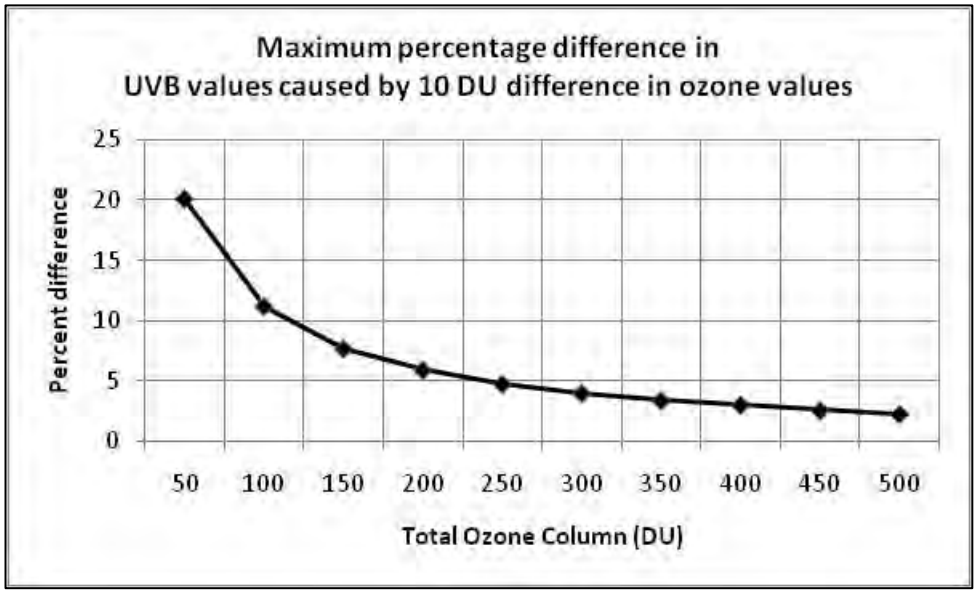

Figure 5.3: Plot of percent difference in erythemal UV values for ozone values, X and (X + 10) DU.

To determine the extent to which the real TOC differs from the satellite data over a region Lambert *et al*. (2000) undertook the following research. They compared several years of total ozone measured from space by the ERS-2 GOME, the EP-TOMS and the ADEOS TOMS with high-quality ground-based observations associated with the Network for the Detection of Stratospheric Change (NDSC), over an extended latitude range and a variety of geophysical conditions. The space- and ground-based data are found to agree within a few percent on average. However, their analysis highlights for both GOME and TOMS several sources of discrepancies. In particular for this study they were: a SZA dependence with TOMS beyond 80° SZA, and a north/south difference of TOMS with ground-based observations.

It should be noted that the quality of the EP-TOMS data for 2000 is affected by changes in the optical properties of the scanning mirror, and therefore these data should be interpreted with caution (Fioletov *et al.* 2002). Despite the above discussion of errors and inaccuracies, the fact

remains that the EP-TOMS is the best estimate of ozone that is available for inclusion in this project, which has the temporal coverage, 1996 to 2005.

5.4 Sea ice data

To determine sub-surface levels of erythemal UV within the sea ice and in the water column beneath sea ice for this project, it was necessary to include sea ice and snow thickness data. The SCAR Antarctic Sea ice Processes and Climate (ASPeCt) program made their data available for this purpose (http://www.aspect.aq). These data are also available from the Australian Antarctic Data Centre (http://www.data.aad.gov.au). The other 'sea ice data' used in this project were the sea ice concentration data that were included as the surface mask in the AVHRR Polar Pathfinder 'data packages' (explained in Section 5.2). Sea ice concentrations are generally much lower in summer than in spring, except in regions where multi-year ice prevails (e.g. West Antarctic and Weddell Sea sectors) (Brandt *et al.* 2005).

Allison *et al.* (1993) used hourly visual observations of ice characteristics made within 0.5 nautical miles of the MV *Icebird* during the first spring voyage in 1988 to verify the National Aeronautics and Space Administration (NASA) Team sea ice algorithm for the estimation of sea ice concentrations from multi-channel SSM/I satellite microwave data (Cavalieri *et al.* 1984). The two estimates were found to be in reasonable agreement between 30 and 80% concentration, but at higher concentrations the ship estimates were consistently larger than the satellite estimates. At low concentrations, the satellite estimates were larger. Some of the discrepancy between the two retrieval methods at high concentration levels may be a result of the inability of the passive microwave instrument to distinguish very thin ice from open water (Cavalieri *et al.* 1984). Massom *et al*. (1999) also found that ambiguities occur at the boundaries of some of the ice type regimes due to sensor resolution limitations and the mixing of different ice types and open water.

Researchers should be cautious when analysing and interpreting satellite passive microwave-derived ice concentrations in the ecologically-important outer pack or marginal ice zone (MIZ) (R.A. Massom, pers. comm., 2010). Sea ice within this zone typically comprises floe fragments and brash ice separated by an interstitial frazil ice and snow blend, with much of its snow cover washed away – all due to intense wave-ice interaction (Massom *et al.* 2001). These properties result in a significant underestimation in ice concentration. It is highly desirable to include additional information where possible, e.g. coincident *in situ* observations; higher-resolution satellite data that better characterise ice conditions in the MIZ, e.g. Synthetic Aperture Radar (see Chapter 5 of Lubin and Massom (2006)); and/or wind velocity data from meteorological analyses. Dr. R.A. Massom (pers. comm., 2010) directed the author to http://nsidc.org/data/docs/daac/nasateam/index.html and http://nsidc.org/data/docs/daac/bootstrap/index.html where information is available to enable the reader to evaluate the pros and cons of the NASA Bootstrap and NASA team products.

The ASPeCt data archive, published by Worby *et al.* (2008a), contains data collected from 81 voyages (21,710 observations) plus 1663 aircraft based observations over the period 1980-1995, all plotted on a coarse grid (2.5° latitude by 5.0° longitude). These routine hourly visual observations (separated by a minimum of 6 nautical miles along voyage tracks) of sea ice were accumulated by research and supply ships from several nations using a standard protocol (Worby *et al.* 2008a). These data may be biased because of the tendency for ships to locate the easiest passage through the ice, most likely to be through the areas of thinnest ice with more open water (e.g. leads, polynyas). Some of this bias can be removed by helicopter sorties taking measurements further from the ship's track. Helicopter observations can also help to overcome issues of data coverage in inaccessible areas (e.g. western Weddell and eastern Ross Seas) (Worby *et al.* 2008a) (see Figure 2.3). The ship-based observations include the ship's position, total ice concentration and an estimate of the areal coverage, thickness, floe size, topography, and snow cover characteristics of the three dominant ice thickness categories within 1 km of the ship (Worby and Allison 1999). Not all observations contain this level of information, but at a minimum the partial ice concentrations and thicknesses (or ice types) were necessary for inclusion in the data set. A simple ridge model is used to calculate the total ice thickness from the observations of level ice and surface topography, to provide a best estimate of the total ice mass, including the ridged component. The long-term mean and standard deviation of total sea ice thickness (including ridges) is reported as 0.87 $\pm$ 0.91 m, which is 40% greater than the mean level ice thickness of 0.62 m (Worby *et al.* 2008a). The data contain weighted sea ice thicknesses and snow thicknesses, but the weighting does not include the open water fraction.

Until the development of the ASPeCt dataset, no climatology of Antarctic sea ice thickness was available to modellers, who often had to use single mean averages (typically 0.5 – 1.0 m) over the majority of the Antarctic pack (e.g. Hibler and Ackley 1983), with only limited validation from field measurements (Worby *et al.* 2008a). For the purpose of this project, it would have been ideal to have sea ice thickness and snow thickness distributions for the study area at a monthly temporal resolution. After discussions with A.P. Worby (pers. comm., 2009) and other scientists, it became obvious that there is no 'perfect sea ice thickness product' available and, despite the fact that the ASPeCt dataset has significant regional and seasonal gaps (see Figure 5.4), it represents the most comprehensive dataset available.

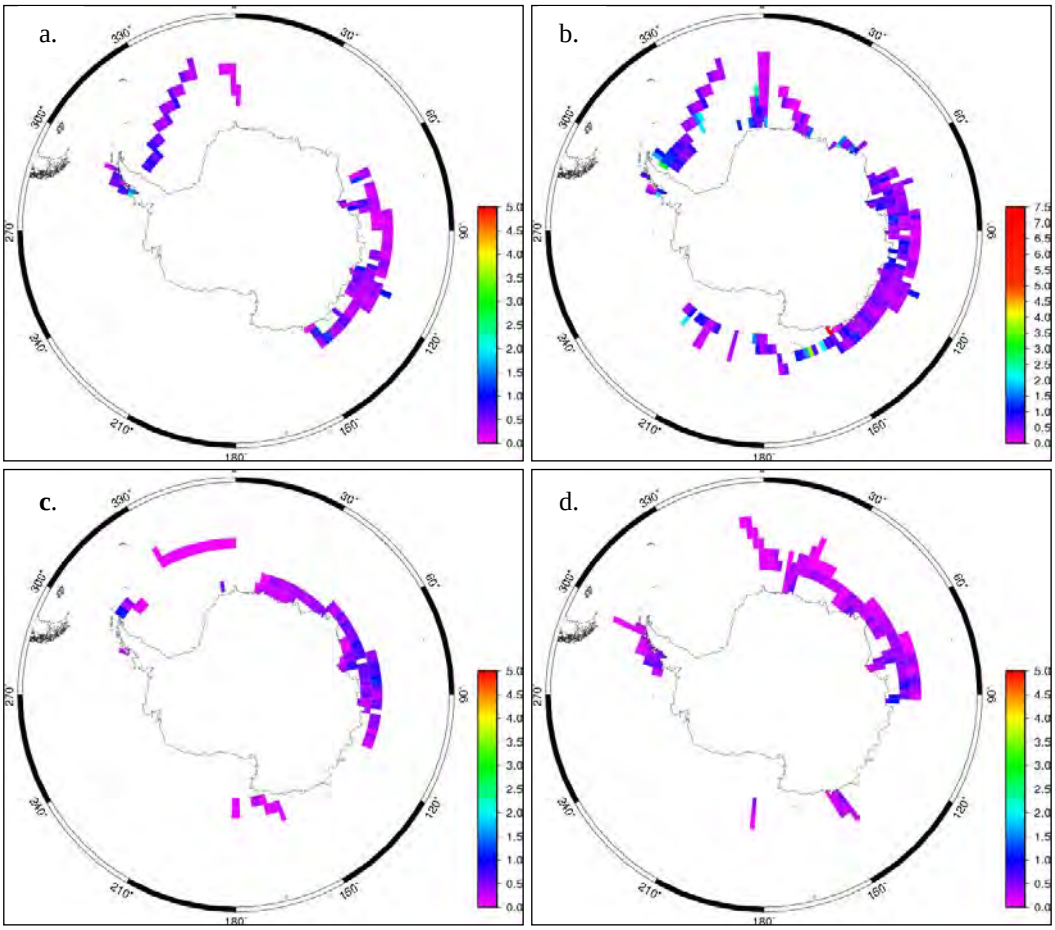

Figure 5.4: Sea ice thickness data (metres) for (a) spring, (b) summer, (c) autumn and (d) winter (as extracted from the ASPeCt database (SCAR Antarctic Sea Ice Processes and Climate (ASPeCt) program 2008)

There are fewer ships visiting Antarctica during winter, making the ASPeCt data even sparser for these months. However, there is also a lack of ozone data for parts of winter (due to the lack of sunlight), thus preventing modelling surface erythemal UV radiation for parts of the study regions. A decision was therefore made to use sea ice thickness data averaged over spring, summer and autumn for modelling the levels of erythemal UV throughout the ice and water column. The sparseness of the data for the individual seasons necessitated using an average of the three seasons (see Figure 5.5) to avoid excessive interpolation for the areas with no data.

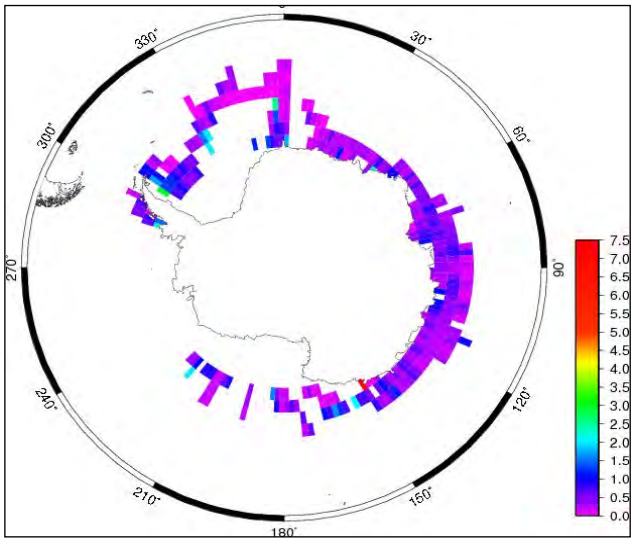

Figure 5.5: Sea ice thickness data (metres) for the average of spring, summer and autumn data (Figure 5.4) (SCAR Antarctic Sea Ice Processes and Climate (ASPeCt) program 2008).

The snow thickness data are available in the same format as above and at the same spatial and temporal coverage. A software tool, developed by A. Steer, ACE CRC (see http://sipex-server.antcrc.utas.edu.au/~adsteer/aspect.test.php) was used by the author to extract the required sea ice and snow thickness data in the following forms:

- a netCDF-compliant grid file containing mean ice/snow thickness per grid cell over the specified area;
- a text file summarising grid statistics – number of observations, mean and standard deviation per cell;
- a postscript plot of the gridded data; and
- a .png plot for showing on a results page (see examples Figures 5.4a-d).

The software tool allows the user to choose the size of the grid cell; the boundaries (latitudes and longitudes) of the required spatial coverage; the required temporal coverage (spring, summer, autumn, winter or full year); and the parameter (either sea ice thickness or snow thickness or both). Data files of sea ice or snow thickness extracted for this project include the following for each 2 x 2 degree grid cell for the region between -50° and -70° latitude and 0° and 360° longitude, and for spring, summer and autumn :

- latitude and longitude of the centre of the grid cell;
- the number of observations of sea ice /snow thickness;
- mean thickness of sea ice (z_i) and snow (z_s) in metres; and
- standard deviation.

A full description of the ASPeCt data quality control and processing can be found in Worby *et al.* (2008a).

5.5 Surface UV Data

Antarctica plays a significant role in many global environmental issues such as wind and ocean currents and world weather patterns. Using long-term monitoring of environmental and other variables, State of the Environment (SOE) Reporting provides a "snap-shot" of the status of the Antarctic environment. Trends and patterns can be detected which may be due to natural variability or anthropogenic pressures. SOE Reporting is based on environmental indicators, which are data that summarise physical, chemical, biological or socio-economic factors which best represent the key elements of the environment.

The Australian Antarctic Data Centre (AADC) has developed a web-accessible computer system called SIMR (System for Indicator Management and Reporting) that manages the indicator data, metadata, and custodian information. One of the environmental indicators is daily broad-band ultraviolet radiation observations using biologically-effective UVR detectors (Roy and Gies 2007). These data are available for Australian Antarctic research stations at Casey (66°16'54.5" S, 110°31'39.4" E), Mawson (67°36'09.7 S, 62°52'25.7" E) and Davis (68°34'35.8" S, 77 58'02.6"E) (see Figure 2.3), for which the Australian Radiation Protection and Nuclear Safety Agency (ARPANSA) is the custodian (Roy and Gies 2007).

In this project the ARPANSA data downloaded from AADC were used to validate the modelled values of erythemal UV for each of the stations for the days/years that *in situ* data are available. Data are available from AADC 23rd July 1996 to 31st May 2008. Readings are taken every ten minutes, and the total SEDs (Standard Erythemal Doses) are calculated for the day. ARPANSA uses the following detectors to make the observations:

- Detector 1 - Eppley total solar radiation pyranometer;
- Detector 2 - Eppley total UVR (TUV) radiometer - covers wavelength range 290-400 nm;
- Detector 3 - International Light UVB radiometer - covers wavelength range 290-315 nm;
- Detector 4 - Solar Light UVBiometer (SL501) - approximates Commission International de l'Éclairage (CIE) erythemal spectral effectiveness.

The fields in this dataset are Date, Time, Total Solar Radiation (counts), Gain 1, Total UVR (counts), Gain 2, UVB (counts), Gain 3, Biometer (MEDs/hour where 1 MED is 200 J/m^2 effective weighted with the CIE (1987) erythemal response) and Temperature (the temperature inside the detector). More details can be seen at the Australian Antarctic Data Centre's Catalogue of Australian Antarctic and Subantarctic Metadata website (AADC 2006).

The original data downloaded for this project were accessed from the AADC in January 2008. The following note, dated 13th June 2008, is at the bottom of the State of the Environment SIMR web page (see http://data.aad.gov.au/aadc/soe/display_indicator.cfm?soe_id=10):

"Note that the most recent Excel spreadsheet stored in the download file will be the most accurate, and should be used in preference to all other Excel spreadsheets, or .dat data". Later versions of the original data downloaded in January 2008 were obtained from Dr. Andrew

Klekociuk (Australian Antarctic Division) in November 2008, once it was confirmed by P. Gies (pers. comm., 2008) that this was the correct course of action.

Some or all of the data used for this research were obtained from the Australian Antarctic Data Centre, a part of the Australian Antarctic Division (Commonwealth of Australia). The data are described in the metadata record "Daily broad-band ultra-violet radiation observations using biologically effective UVR detectors", Roy, C. and Gies, P. (2001, updated 2008). The direct link to metadata is

http://aadc-maps.aad.gov.au/aadc/metadata/metadata_redirect.cfm?md=AMD/AU/ARPANSA_Bio.

In addition to the sensors at the mainland Antarctic stations, there is a pair of solar UV radiometers onboard the RSV *Aurora Australis*, one of the Australian Antarctic Division chartered vessels that routinely collect environmental information as they move around the Southern Ocean. Underway data typically include a number of meteorological and oceanographic parameters as well as ship parameters (such as position, heading, speed, etc). The underway UV data are processed in the same way as the station UV data and are made available through the AADC (Reeve 2008). Data collected during all voyages with useful UV data between 1999 and 2005 were obtained for use with this project.

The UV biometer (290-320 nm) monitors the biological effectiveness of UVB radiation. It is calibrated and maintained at 25° C, and data will be flagged as 'good' so long as the instrument is operated between 24- 27° C. Output units are minimum erythema dose per hour (MED/hour), where 1 MED/hour = 55.56 mW m^{-2} (P. Gies, pers. comm., 2008).

Data can typically be extracted from AADC via the Marine Science Underway Data Tool, available at http://data.aad.gov.au/aadc/marine_science/underway_extraction/. The underway UV data were used in this project to validate the modelled erythemal UV at the surface for data points in the underway UVB data file.

The parameters included in the AADC data files are date and time of collection, the position (latitude and longitude) of the ship, BIO_RAD (MED/Hr) and BIO_TEMP ($^{\circ}$C) (with an indicator of good data for the last two parameters). The time of collection of the underway data was in UTC – this was converted to local solar time, so that the UVB value for local solar noon could be chosen to compare with a modelled value for that time of day. Both station and underway data were collected using Solar Light UV Biometers (SL501). It is stated in the AADC website documentation that the resolution for this instrument is better than 0.01 MED/hour in the UV and the accuracy is $\pm$ 5% for the daily total. Notes in the voyage reports bring the reader's attention to the fact that the sensors are affected at different times by shadows, for example from the ship's superstructure or people.

6. SIPEX VOYAGE

As part of the International Polar Year (2007/2008) program, a major multi-disciplinary sea ice research program called the "Sea Ice Physics and Ecosystem eXperiment (SIPEX)" was conducted off East Antarctica, in the region 115-130° E in September-October 2007 (Worby *et al.* 2010). It is known that sea ice is closely linked to the life cycle of krill (Nicol *et al.* 2008), which play an important role in the Southern Ocean ecosystem by providing a food chain link between primary production and higher predators (Virtue *et al.* 2010). Sea ice algae make a major contribution to overall primary production, but the large scale distributions of sea ice biological and physico-chemical parameters affecting ice algal production are not well known (Dieckmann and Hellmer 2010).

Modelling levels of erythemal UV radiation that will affect organisms living in various niches in the East Antarctic Sea Ice Zone (SIZ) (for example, on the surface of the sea ice under a layer of snow, throughout the sea ice, just under the sea ice and throughout the upper 15-20 metres of the water column), requires knowledge of how much UVB radiation passes through the snow and ice. This chapter describes the research done by Dr. Kelvin Michael and the author during the SIPEX voyage onboard RSV *Aurora Australis* (V1, 2007-2008).

6.1 Penetration of UV through ice

The optical properties of sea ice are directly dependent on its intricate and highly variable structure (Perovich 2003). Sea ice exists at its salinity-determined freezing point, therefore its structure and optical properties are significantly affected by small changes in temperature. Changes in the small-scale structure of the ice, (including brine pockets, air bubbles and precipitated salt crystals) affect the scattering and absorption of sunlight in the ice (Jin *et al.* 1994; Perovich 2003). For example, the formation of air bubbles because of brine drainage results in larger albedo, and less light is transmitted. Mobley *et al.* (1998) demonstrated the process by which it is possible to begin with the physical properties of sea ice (such as the size distributions of brine pockets and air bubbles), then predict the optical absorption and scattering properties of the ice, and finally use these inherent optical properties in radiative transfer models to predict light propagation within the ice. Grenfell (1991) developed a radiative transfer model which could include the effects of biological activity in the ice as well as vertical variations in brine volume and bubble density. Absorption by algae in the ice is shown to reduce the transmitted radiation by more than a factor of 10 at certain visible wavelengths (Grenfell 1991).

Trodahl and Buckley (1989) pointed out that the spring UV enhancement will be exaggerated under the vast sea ice cover surrounding Antarctica. This conclusion was based on experiments (Buckley and Trodahl 1987b, 1987a; Trodahl *et al.* 1987; Trodahl *et al.* 1989) that demonstrated that the ice is less turbid in early spring than later in the season. This increased turbidity results

from the growth of weakly-scattering brine inclusions as the ice warms and forms the strongly-scattering air channels left near the surface as brine drains into the bulk of the ice (Buckley and Trodahl 1987a). Trodahl and Buckley (1989) demonstrated a 20-fold increase in under-ice UV radiance in early October resulting from the coincidence of the presence of the ozone hole and the period of relatively high transparency for sea ice.

6.2 Penetration of UV through snow

Hamre *et al.* (2004) calculated the transmittance of first-year Arctic sea ice with and without snow cover, using a radiative transfer code for the Coupled Atmosphere-Snow-Ice-Ocean system, based on code described by Jin *et al.* (1994). For the type of snow and ice considered in their study, a 2.5 cm thick snow layer was found to have about the same transmittance for PAR and UV radiation as a 61 cm thick ice layer. It is therefore very important to pay attention to the snow layer when calculating light transmission through the atmosphere and sea ice into polar oceans. They also noted that harmful UV radiation is removed more efficiently than PAR for snow depths greater than 3-4 centimetres. Thus algae growing under a snow cover may be protected from UV radiation, but still receive sufficient PAR for photosynthesis.

6.3 Site description and data acquisition (SIPEX)

Field data were collected in complex sea ice/open ocean environments in the East Antarctic SIZ (below 60° S) while participating in the SIPEX voyage. The aim was to determine how much ultraviolet radiation was attenuated, or lost, as it passed through the snow and ice, enabling calculation of the attenuation coefficients for the media, snow and ice. These constants are required for the calculation of sub-surface levels of UVB.

The East Antarctic sea ice zone is known as a highly dynamic and rapidly changing environment, but was perhaps even more affected than usual by strong storm systems during the SIPEX campaign (Worby *et al.* 2010). Persistent easterly winds and blizzard conditions were present during this experiment, causing extensive sea ice deformation. This was exacerbated at the boundary between the pack ice and fast ice, where a strong coastal jet influenced the drift and deformation of the ice, forming a shear zone between the two ice regimes. A combination of *in situ* and ship-based measurements characterised the ice conditions in the region, which varied considerably from west to east. The mean ice thickness was 0.99 m, based on the ASPeCt observations, but in localised areas the mean thickness was more than double that (Worby *et al.* 2010).

The voyage leaders and ship's crew were responsible for selecting siting of the fourteen ice stations taking into consideration all aspects of safety – floes too thin or showing signs of cracking; floes too close to icebergs that might move and break up the floe; heavily ridged floes and winds too strong. Very thick floes were impractical for drilling to take ice cores, gathering

krill or taking sub-ice measurements. The available floe surface at each ice station was allocated to the various research groups (e.g. biologists, glaciologists, oceanographers, UV scientists) by the voyage leaders. The priority for the UV group was a snow-covered area not yet trampled by others, with the sea ice less than a metre thick.

6.4 Equipment

The measuring system included two radiometers, PUV 2500/2510, (Biospherical Instruments Inc., San Diego, CA, USA) (Morrow *et al.* 2003) which measure radiation in several wavelengths, including UVB. The irradiance bands are 305, 313, 320, 340, 380, 395 nm and PAR (400-700 nm). One radiometer (PUV 2510), mounted on a tripod, measured the radiation coming through the atmosphere to reach the surface. The second radiometer (PUV 2500) was used to measure the sub-surface radiation. This portable radiometer package had previously been used successfully to collect profiles of irradiance in waters surrounding Heron Island (23°27' S, 151°55' E) in the Southern Great Barrier Reef, Queensland (Veal *et al.* 2009).

The PUV-2500 profiling ultraviolet radiometer (see Figures 6.1a and 6.1b and Table 6.1) is a submersible, multi-channel, profiling, ultraviolet radiometer designed to take measurements of UV irradiance and PAR to depths of 350 metres. The system has been specifically designed to measure down-welling (cosine) irradiance, pressure/depth and temperature. Incorporating a custom interference filter with a "solar blind" detector to reduce red-leakage, the 305 nm sensor is designed to respond to the region of the UVB spectrum strongly affected by atmospheric ozone concentration. The PUV-2510 is a down-welling irradiance sensor designed to radiometrically match the underwater instrument, but optimised for use in air.

The surface and underwater radiometers are connected with Kevlar-sheathed data cables to a deckbox, which both supplies power to the radiometers and handles data transfer to a laptop whilst in the field. Power is provided by rechargeable 12-V gel cell battery with AC adapter/charger. The PUV-2500 uses the Windows®-based, PROFILER® operating and data-acquisition software. This software stores collected data in a Microsoft Access® database format, which allows export to Excel® for analysis and presentation of the results. More information about the PUV 2500/2510 system is available from http://www.biospherical.com/BSI%20WWW/Products/Aquatic/puv2500.htm.

The PUV-2500 was mounted in such a way that there were extra 'legs' attached to the top to enable the operator to bring it right up to the under-surface of the sea ice without damaging the sensor (see Figures 6.1a and 6.1b). At the early ice stations, the under-ice instrument had problems assuming the desired horizontal attitude. As this was the first time the PUV system had been deployed underneath sea ice it was initially thought that irregularities in the lower surface of the ice floe were the cause. However, technical support staff onboard the RSV *Aurora Australis* assisted in determining that, when under water, the sensor in the mount had

insufficient weight to hold it in a vertical position. Adding lead weighting to the bottom of the sensor solved the problem.

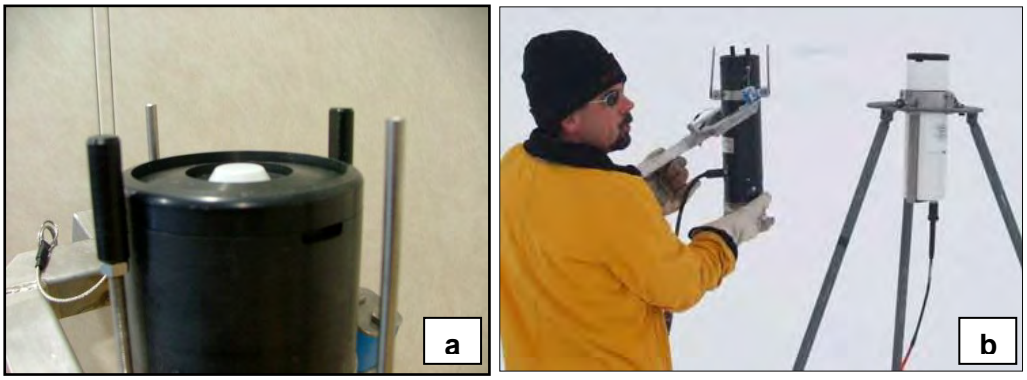

Figure 6.1: a. Top of PUV-2500 instrument and b. PUV-2500 held on the left and PUV-2510 fixed in tripod.

Table 6.1: Specifications of the radiometers.

Instrument features	**PUV-2500**	**PUV-2510**
Diameter	10.2 cm	10.2 cm
Length	40.5 cm	35.6 cm
Weight	3.2 kg in air, near neutral in sea water	3.4 kg in air
Temperature rating	-5 to 50 ºC	-10 to 50 ºC
Depth range	350 metres	N/A – surface sensor

6.5 Data collection

For each ice station, photographs were taken and the following were manually noted:

a. The ice station number;
b. Date of data collection;
c. Time (UT) that data collection commenced;
d. Weather conditions (cloud amount, sun, wind, snow, etc.), general ice and snow conditions. (More detailed information is available from meteorological records maintained on RSV *Aurora Australis*);
e. Ice thickness at the measurement site;
f. Depth of snow at the measurement site;
g. It was noted if any biology groups were working near the UV work site and if so, at what distance;
h. Access® database file number that contained the measurements of UV radiation (at 1 Hz for a minute) across wavelengths 305-395 and PAR, both at the surface and beneath the ice plus snow and then beneath ice only; and
i. Any problems encountered.

The PUV system was set up as described below (Figure 6.2 is a photograph of typical measurement site set up). The deckbox and computer (which was sitting on a heated wheat bag) were placed on a small table positioned next to the study site. The table and equipment were shielded with an insulated blanket to minimise the effect of extreme cold and wind-blown snow on the operation of the computer. When the measurement process was to be initiated, the operator of the computer was able to sit at the table and pull the insulated blanket over their head and back to prevent snow blowing in on the keyboard.

Despite these precautions, the computer failed after exposure at three ice stations. Measurements could not be made at ice station number 4. A replacement computer was sourced and assistance was obtained from the IT personnel onboard to install the PROFILER® software. There were also a further four ice stations at which the UV group did not take measurements – stations 7 and 12 were for biologists only; station 9 had very thick and deformed ice that was impenetrable by an auger; and the combination of strong wind, blowing snow and thick ice with thick snow cover at station 11 determined that it was to be a lay-day for the UV group.

Figure 6.2: Operation of the computer at an ice station. The operator sat at the table on which the deckbox and computer were placed. The table and equipment could be shielded with the blue insulated blanket to minimise the effect of extreme cold and wind-blown snow on the operation of the computer.

The PUV-2510 was set up on a tripod close to the study site (right hand side of Figure 6.1b and left hand side of Figures 6.2 and 6.3). The PUV-2500 was attached to one end of a folding 'Z' frame – a hinged metal pole (see Figure 6.5 – being fed into hole in ice). Cables connected both sensors to computer.

Figure 6.3: Researchers removing snow after 'with-snow measurements' completed. The radius of the snow-free circle had to be at least twice the thickness of the ice.

The following protocol was followed when taking measurements:

1. With the best possible site chosen (a snow-covered area not yet trampled and sea ice less than a metre thick), an auger was used to drill a 35-cm diameter hole (see Figure 6.3 – centre of photo) through which to pass the submersible sensor. At this point, the thickness of the ice plus snow was measured. It was the thickness of the ice that determined the circumference of the area from which snow should be removed after the first 'with-snow' measurements were completed. The radius of

the snow-cleared circle (with the sub-ice sensor position at the centre) was at least twice the thickness of the ice (see Figure 6.4).

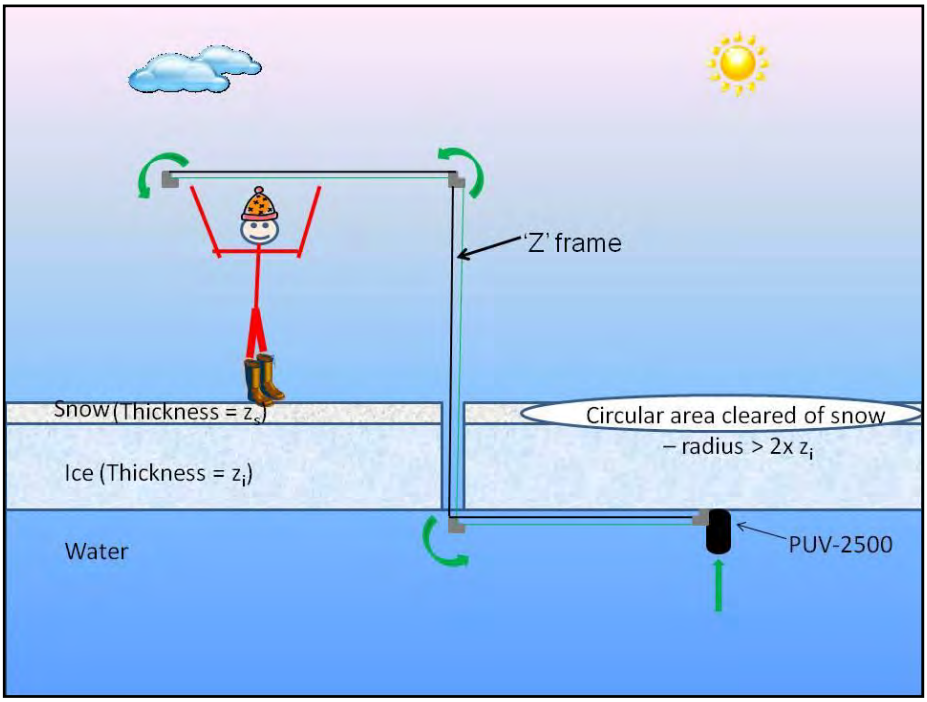

Figure 6.4: Operation of the 'Z' frame – pulling down on the upper arm of the frame caused the lower arm to lift into a position horizontal to the under surface of the ice.

2. A lightproof cap was placed over the sensors (PUV-2500 and PUV-2510) and the PROFILER® software was run for a minute to facilitate 'dark corrections'.

3. The caps were removed and the 'Z' frame, with PUV-2500 attached, was passed vertically through the hole in the ice to the point where the lower end of the middle section of the 'Z' was at the bottom edge of the hole (Figures 6.4 and 6.5).

Figure 6.5: Feeding the 'Z' frame through the auger hole.

4. The upper-most ‘arm’ of the ‘Z’ frame was levered down towards the surface of the ice (preferably by a tall second assistant! – see Figure 6.6), thus causing the ‘arm’ under the ice to be lifted into a horizontal position just under the ice via a pulley system (see Figure 6.4).

Figure 6.6: Taking measurements under snow-free area on right. A second suite of measurements were taken under the snow-free area behind the operators of the ‘Z’ frame.

5. With the sensor in place under the ice and snow (a horizontal distance of 2.4 m from the hole), the PROFILER® software was initiated and run for a minute to gather measurements of radiation passing through the ice plus snow. The sensor was then removed from the hole in the ice, a circle of the predetermined circumference was scribed in the snow, and a ‘ruler’ was inserted into the snow at a number of places (typically ~8) in this circle to determine an average snow depth for the area, which was noted in the record book at the site. The snow was then shovelled from the surface of the ice.

6. Once again the PUV-2500 sensor was inserted into the hole in the ice and positioned at the centre of the now snow-free circle. The PROFILER® software was initiated again, and run for a minute to determine levels of radiation passing through the ice only. The sensor’s equilibrium position was such that it was hanging perpendicular to the under surface of the ice, with the sensor facing up in the centre of the ‘reserved area of clean snow’ (see Figure 6.4 – bottom arm of folding frame extends to the right to the centre point of the snow-free ice). The photo in Figure 6.6 was taken at ice station number 13, where a second set of subsurface measurements were taken from the same hole, but in a different direction, under a different thickness of ice and snow.

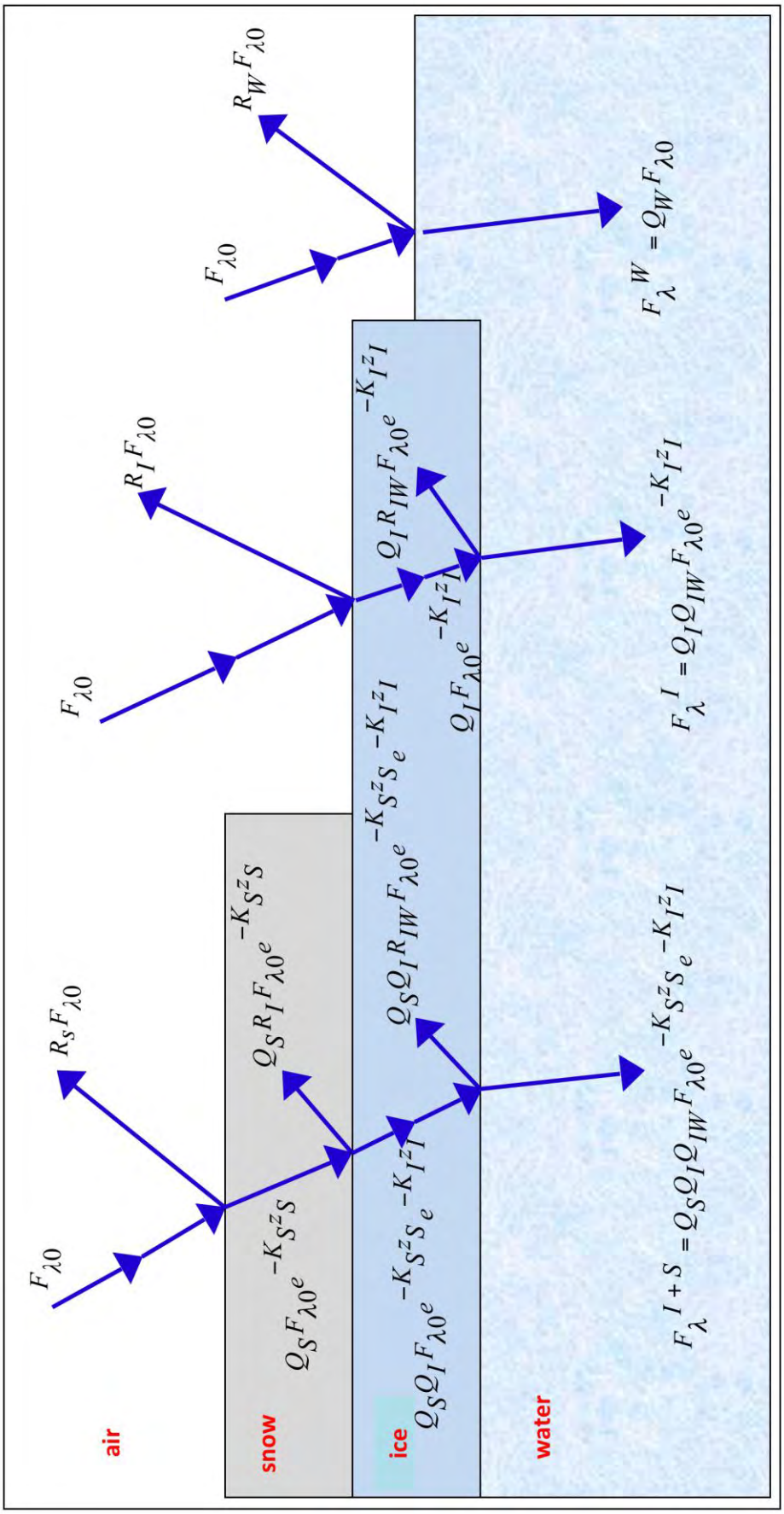

Figure 6.7: This figure represents the radiation paths for each of the measurements (i.e. ice with snow, ice without snow and ice-free water.

6.6 Data analysis

The Microsoft Access® database files collected during the measurements were exported to Excel® files on the computer for analysis and presentation of the results.

The surface irradiance is $F_{\lambda 0}$, where the subscript λ denotes the appropriate band for the PUV radiometer (305, 313, 320, 340, 380 or 395 nm, or PAR). This irradiance is modified by reflection, absorption and scattering as it passes through the snow and ice (or just through the ice) into the water. The sub-surface irradiance is F_{λ}. At each interface, there is a partial reflection (with a corresponding spectral reflection coefficient, R), so that the proportion of the irradiance which crosses the interface into the next medium is Q = 1-R. The subscripts *S* and *I* refer to snow and ice, respectively. The subscript *IW* relates to the ice-water boundary.

The field data provides a measure of the transmission ratios $\mathrm{T_{\lambda IS}} = \mathrm{F_{\lambda IS}}/\mathrm{F_{\lambda 0}}$ and $\mathrm{T_{\lambda I}} = \mathrm{F_{\lambda I}}/\mathrm{F_{\lambda 0}}$, which contain information on the attenuation of irradiance by the various effects of ice and snow. Measurements of these transmission ratios for various thicknesses of snow and ice allow the attenuation coefficients, K_S, K_I to be estimated. In so doing, it is also necessary to estimate the reflection coefficients R_S, R_I. The collection of the above-/below-ice irradiances, both with and without a snow cover, facilitates the estimation of the separate influence of snow and ice on the irradiance field.

The first step in the data processing divides the ice-snow transmission values by the ice-only transmission values. According to the equations in Figure 6.7, it follows that

$$\frac{\mathrm{T_{\lambda IS}}}{\mathrm{T_{\lambda I}}} = \mathrm{Q_S e^{-K_S z_S}}$$
$$\ln\left(\frac{T_{\lambda IS}}{T_{\lambda I}}\right) = lnQ_S - K_S z_S \qquad (6.1)$$

Therefore, measurements of the transmission ratios for various snow thicknesses (z_S) allow the snow attenuation coefficient K_S and the snow reflection coefficient R_S to be estimated from the slope and the intercept, respectively, of a plot of K_S *vs* z_S.

The second step focuses on the ice transmission, and in a similar fashion to equation 6.1, it follows that

$$T_{\lambda I} = Q_I Q_{IW} e^{-K_S z_S}$$
$$\ln(T_{\lambda I}) = ln(Q_I Q_{IW}) - K_I z_I \qquad (6.2)$$

Therefore, measurements of the ice transmission ratio for various ice thicknesses (z_I) allow the ice attenuation coefficient K_I to be estimated from the slope and the intercept of a plot of K_I *vs* z_I.

Note that the intercept of such a plot would clearly deliver information on the reflection from both upper (air-ice) and lower (ice-water) interfaces. However, as detailed in Section 9.2, it is only the snow reflectance that is of primary importance when estimating the amount of irradiance transmitted by sea ice with a snow cover.

6.7 Results

UV transmission data were collected at a subset of the total of 14 ice stations occupied by the SIPEX voyage. As Table 6.2 shows, measurements of snow and ice were each achieved at 7 of the stations.

Table 6.2: Snow and ice thickness (metres) for 7 of the 14 ice stations occupied by the SIPEX voyage.

Site	z_I (m)	z_S (m)
Ice Station 3	0.42	0.07
Ice Station 6	0.33	-
Ice Station 8b	0.37	0.05
Ice Station 10a	0.53	0.04
Ice Station 10b	0.53	0.25
Ice Station 13a	0.45	0.08
Ice Station 13b	-	0.18
Ice Station 14	0.88	0.25

The data from the SIPEX field measurements were first surface-normalised. For the seven sites with good snow transmission, graphs were created with Matlab scripts according to equation 6.1. Figure 6.8 shows a sample plot for 320 nm. This particular example led to an estimate of K_S = 11.11 m^{-1} and R_S = 0.67. Perovich (1996) found that attenuation coefficients for snow vary between 15.0 – 40.0 m^{-1} but added that these values were dependent on the wetness conditions and data source.

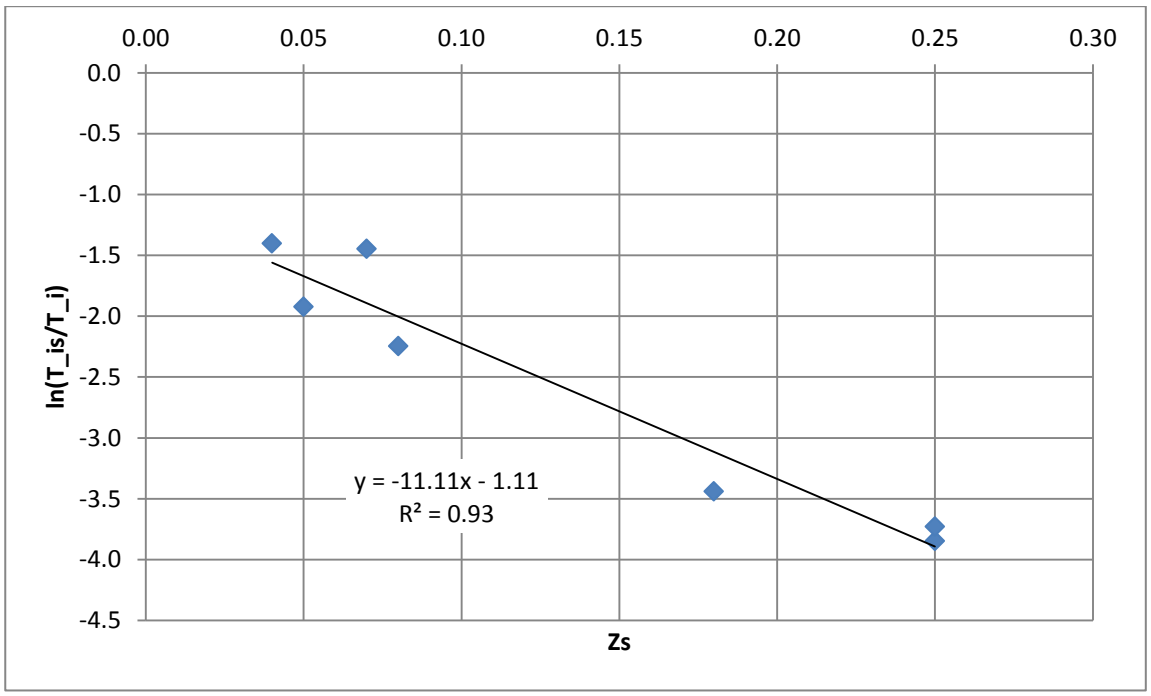

Figure 6.8: Plot of snow thickness z_S (m) vs natural log of the ice/snow transmission ratio for 320 nm.

The values of the snow reflectance across the 6 UV channels were not dissimilar, falling in the range 0.58 – 0.69. The smallest value of 0.58 was obtained for 305 nm, for which there were only 5 good data points. The range of R_S for the channels not including 305 nm was 0.66 – 0.69. Accordingly, the mean of these values (0.67) was assumed to be the wavelength-independent value of R_S for all UV channels.

The data at all UV wavelengths were reanalysed with R_S fixed at 0.67, and new fitting performed to estimate the K_S values and their 95% confidence intervals (Figure 6.9). There is some spectral variation in the K_S values across the UV channels with a gradual decrease from 12.7 m^{-1} (305 nm) to 9.8 m^{-1} (395 nm). With few data points, it is not certain that this spectral variation is real, but it is consistent with other studies of snow extinction (*eg* Fig 4 in Warren *et al.* (2006)).

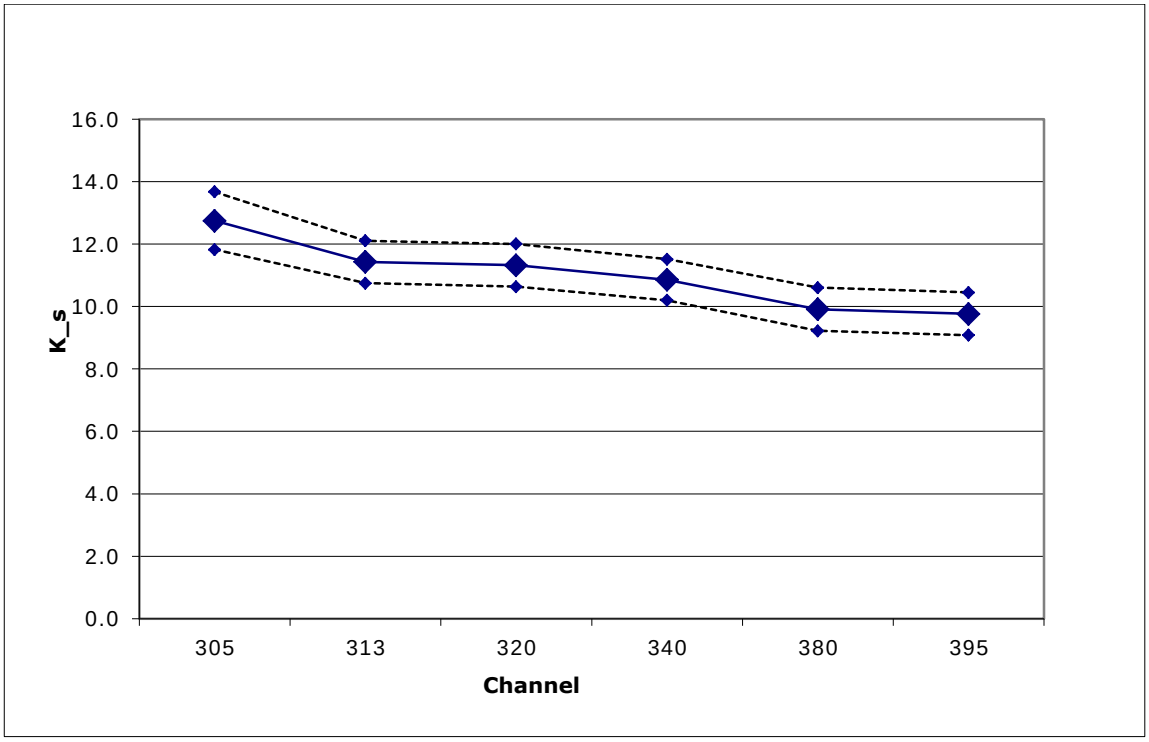

Figure 6.9: Plot of estimated values of snow attenuation coefficient Ks (m^{-1}) for the 6 UV channels with upper and lower 95% confidence intervals.

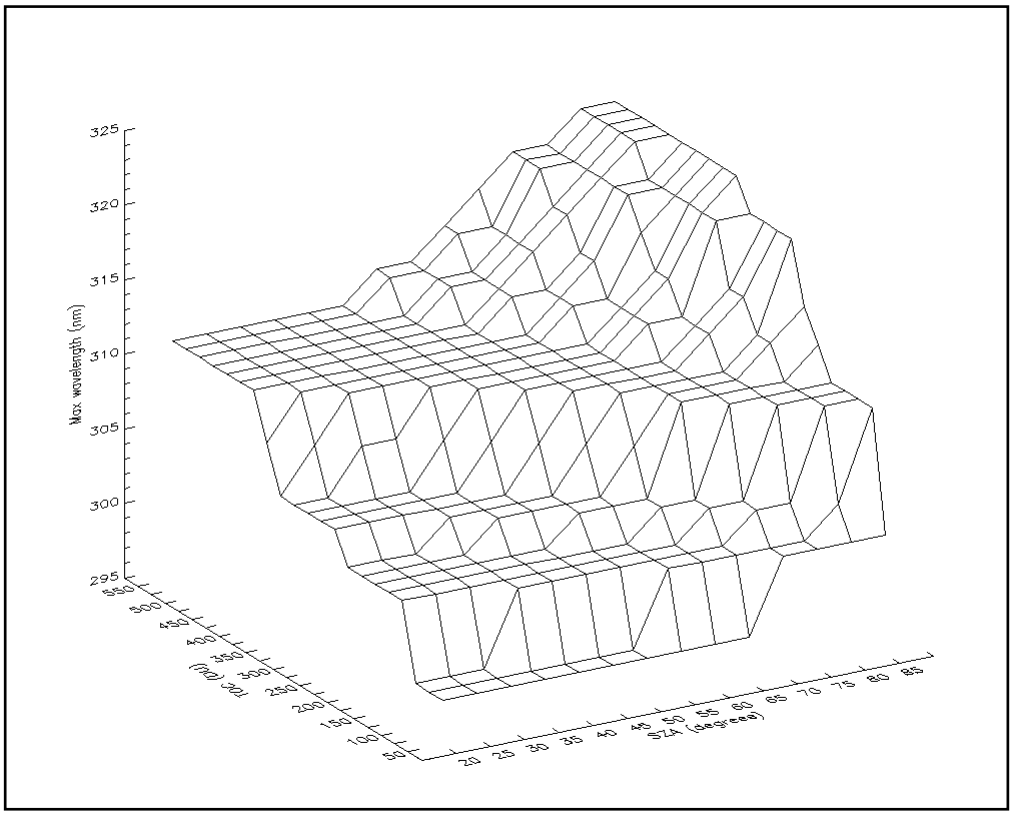

Figure 6.10: Plot of erythemally-weighted irradiance values (nm) (as produced by libRadtran) for combinations of SZA (x-axis) (20-85°) and TOC (y-axis) (50-550 DU).

An appropriate value of K_S to apply to the attenuation of the surface erythemally-weighted irradiance values developed in Chapter 8 was required. Calculations with libRadtran demonstrated that erythemal irradiance (calculated as the convolution of the surface spectral irradiance and the CIE action spectrum of McKinlay and Diffey (1987)) is dominated by wavelengths around 313 nm (see Figure 6.10), and therefore the value of K_S (namely 11.4 m^{-1}) corresponding to this channel was chosen to represent erythemal UVB radiation. This is not very different from the mean across the 6 UV channels, which is 11.0 m^{-1}.

The ice attenuation was estimated by fitting the data from the 7 ice stations identified in Table 6.2 (middle column). Again, the data were fitted with Matlab scripts to equation 6.2. Figure 6.11 shows a sample plot for 320 nm. This particular example led to an estimate of K_I = 2.05 m^{-1} and R_I = 0.33.

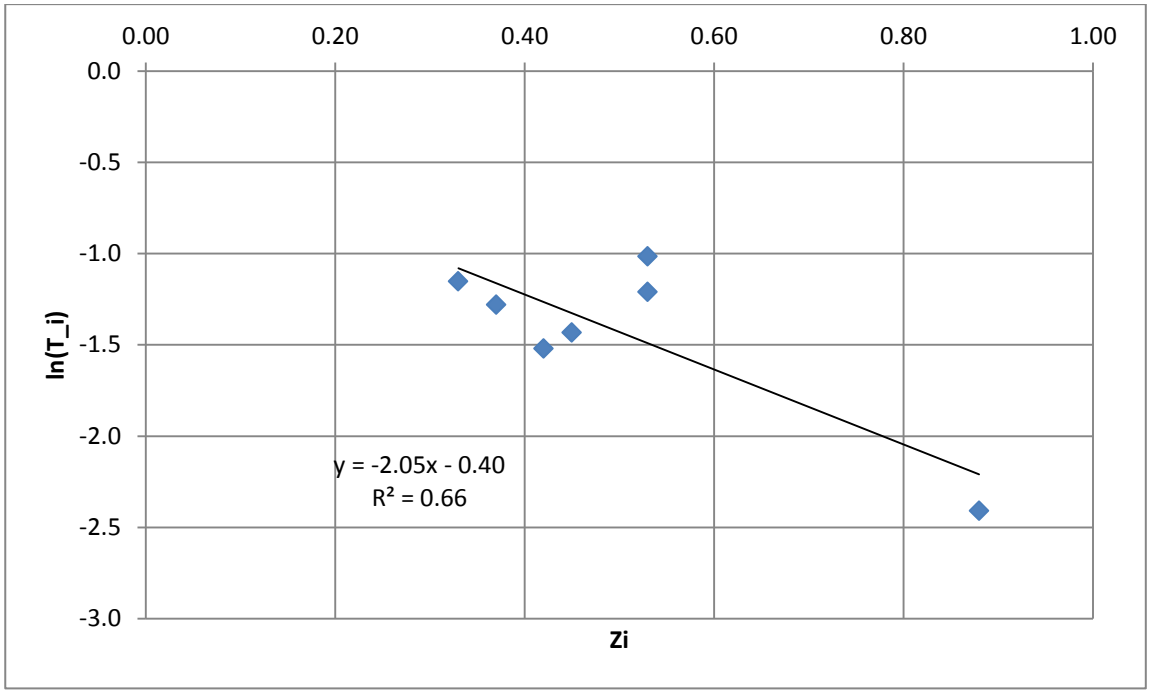

Figure 6.11: Plot of ice thickness z_I (m) vs natural log of the ice transmission T_I for 320 nm.

The values of the *y*-intercept across the 6 UV channels fell in the range 0.26 – 0.42, with a mean of 0.34. Note that in this case, as shown by equation 6.2, the intercept includes the combined effect of reflection from both the upper and lower surfaces of the sea ice. In a similar approach to that performed for the snow reflectance, a wavelength-independent value of 0.34 was assumed for this *y*-intercept for all UV channels. New fitting was performed with Matlab scripts to estimate the values of K_I and their 95% confidence intervals. Figure 6.12 depicts the values of K_I obtained, along with the upper and lower confidence limits for each of the 6 UV channels.

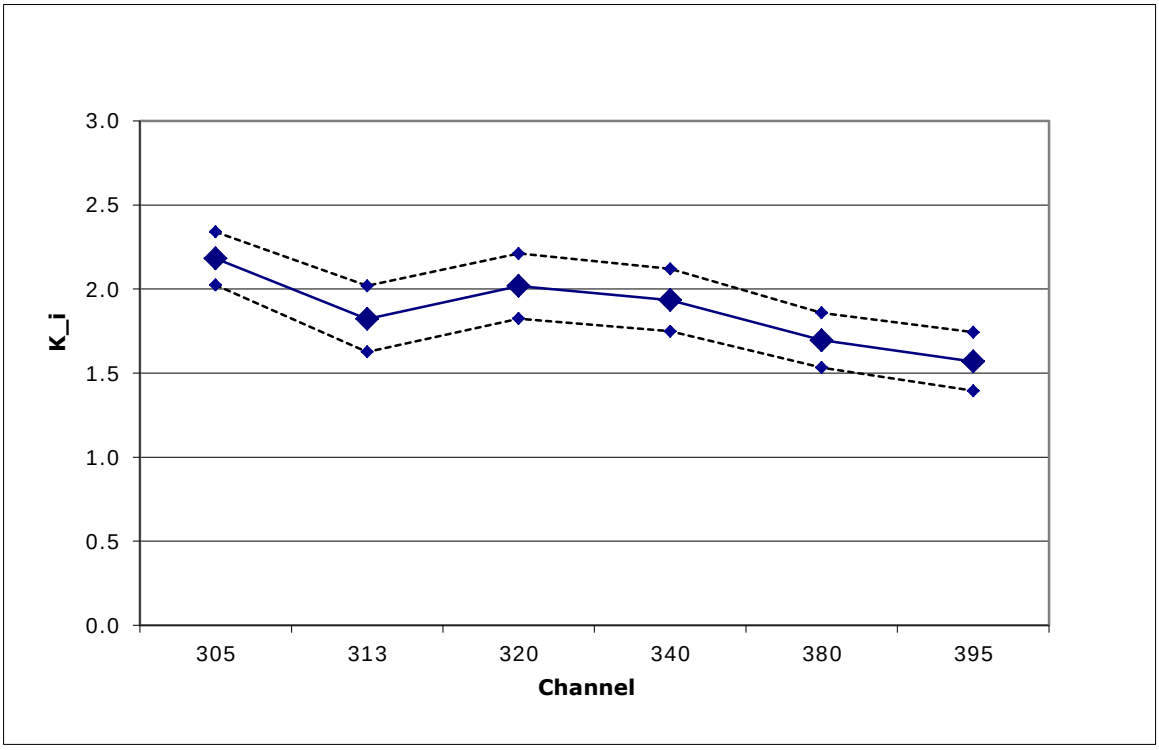

Figure 6.12: Plot of estimated values of ice attenuation coefficient K_I (m^{-1}), with upper and lower 95% confidence intervals.

There is some subtle spectral variation in the K_I values, with a general decrease from 2.18 m^{-1} (at 305 nm) to 1.57 m^{-1} (at 395 nm). Again, due to the small number of data points, it is difficult to be certain that this spectral variation is real. It is also consistent with more efficient scattering of radiation by ice at shorter wavelengths. As before, the 313-nm value of K_I = 1.82 m^{-1} is chosen as the best estimate of K_I for erythemal UVB radiation. This is again similar to the mean across the 6 UV channels, which is 1.87 m^{-1}.

7. METHODS

This chapter details how the maps of erythemal UV radiation at the surface of the sea ice and ocean were developed. The maps are within the East Antarctic sea ice zone between 55-73° S and 60-170° E. For ease of processing and presentation of results, this region was broken down into four study areas – namely; Amery (341 x 283 pixels), Shackleton (246 x 268 pixels), Dalton (205 x 216 pixels) and Mertz (299 x 227 pixels) (see Figure 2.3). Pixel size is 5 x 5 kilometres as dictated by the spatial resolution of the AVHRR PPF data.

Note that all software modules mentioned in this and subsequent chapters are included in Appendix A (CD in back of thesis). Proprietary IDL routine names are written using `courier` font and *italicised* routine names are those written specifically for this project.

7.1 Development of LUT of solar zenith angles

The purpose of developing a look-up table (LUT) of solar zenith angles (SZA) was to enable estimation of the erythemal UV for a pixel at 30-minute intervals to capture the variation in erythemal UV as a result of the changing SZA (see Figure 7.1) across a day, and particularly to pick up on the great variation in day length at high southern latitudes.

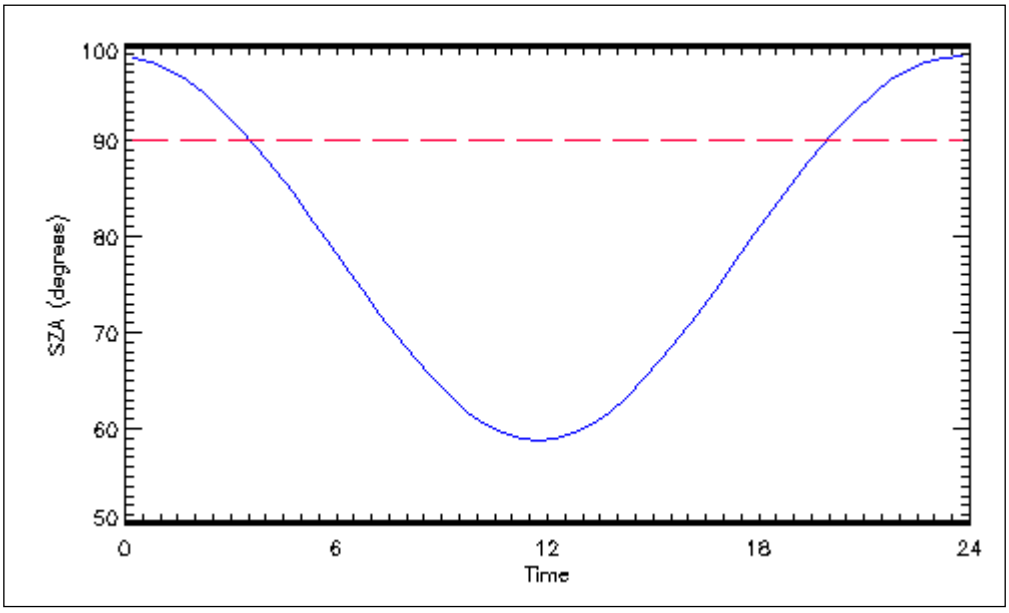

Figure 7.1: A sample plot of SZA for time of day (e.g. 20th February) at 70° S. The red line crosses the plot at sunrise and sunset.

IDL software (*mk_sza_array.pro*) was written to develop a 3-D array of SZA for each half hour of each day of the year for each 0.1 degree in latitude from -50.0 to -75.0 degrees. The 3-D array

was written to a data file (*SZA.dat)* which was then used when processing the AVHRR images (see Section 7.4).

7.2 The Radiative Transfer Model (UVSPEC)

UVSPEC was selected as the most appropriate Radiative Transfer Model (RTM) for this project. This software package has been thoroughly validated against other models and *in situ* measurements (see Section 4.2.7). UVSPEC was invoked from the command line using:

`uvspec` <input file > output file

where the input file is a free format ASCII file that contains options and corresponding parameters specified by the user. It is noted that UVSPEC is a one dimensional model which obviously cannot be used to resolve 3-D cloud fields. Section 3.2.5 details the effect of cloud on incoming radiation and the problems associated with detecting and quantifying the effects of cloud on levels of UV radiation. The option of using a 1-D model was not considered a drawback to this particular project as there are no 3-D cloud data available for Antarctica.

The syntax of input and output is described in Section 2.1 of the libRadtran documentation (Mayer *et al.* 2006). Table 7.1 is an example of a UVSPEC input file (detailed explanations of the choices for each entry are included in the `libRadtran` documentation (Mayer *et al.* 2006)). The UVSPEC input files were generated by the IDL routine, *develop_lut2* (see Appendix A) which created a LUT of erythemal UV values for each possible combination of the three parameters SZA, ozone and albedo (see Section 7.3).

Table 7.1: Example of UVSPEC input file.

Line-by-line breakdown of UVSPEC input file	Description of each item of UVSPEC input file
data_files_path data/	The location of internal UVSPEC data files is the same for each run of the software.
atmosphere_file data/atmmod/afglss.dat	Specifies the atmosphere_file (which contains profiles of pressure, temperature, air density, and concentrations of ozone, oxygen, water vapour, carbon dioxide and nitrogen dioxide). The set of six standard atmospheres (from Air Force Geophysics Laboratory) provided with libRadtran are: afglms (mid-latitude summer), afglmw (mid-latitude winter), afglss (sub-Arctic summer), afglsw (sub-Arctic winter), afglt (tropical), and afglus (US standard). The appropriate choice for this project was the AFGL sub-Arctic summer file which has a defined ozone profile. This is scaled by 'ozone_column' (see below) to set a desired ozone value.
solar_file data/solar_flux/apm_1nm	The location of the extraterrestrial spectrum is the same for each run of the software.
day_of_year 277	The day of the year (day_of_year) is an integer to correct the calculated radiation quantities for the Earth-Sun distance for the specified ordinal day. For day_of_year = 93 or 277, the Earth-Sun distance factor =1. In this instance, it was set to 277 and adjustment is made later in the processing to take into account the Earth-Sun distance effect on irradiances for other days of the year.
wvn 280.0 400.0	Wavelength range to be considered i.e. 280.0 to 400.0 nm
rte_solver disort	Choice of radiative transfer equation solver. `disort` is the standard plane-parallel algorithm by Stamnes *et al.* (1988), version 1.3.
deltam off	Turn delta-M scaling on or off – for these calculations it is turned off.
nstr 12	Number of streams used to solve the radiative transfer equation i.e. 12.
aerosol_vulcan 1	Aerosol situation above 2 km. Choose 1 = background aerosols.
aerosol_haze 4	Aerosol type in the lower 2 km of the atmosphere (as per Shettle 1989). Antarctica is expected to have the cleanest air mass in the global atmosphere (see Section 3.2.3). Air circulation over Antarctica seems to prevent the direct transport of air originating from anthropogenic sources of pollution at the lower latitudes. On this basis, and with no long-term records of measurements of atmospheric aerosols for the study area, a standard marine aerosol value was chosen.
aerosol_season 1	Specify season to get appropriate aerosol profile – selection was 1 which is spring-summer profile.
aerosol_visibility 25.0	Visibility in kilometres is set to 25.0.
sza sza[i]	ith solar zenith angle value for i = 0,70 (details in Table 7.2).
ozone_column ozone[j]	jth ozone column value for j = 0,100 (details in Table 7.2).
albedo albedo[k]	The Lambertian surface albedo, a number between 0.0 and 1.0, constant for all wavelengths. kth albedo value for k = 0, 20 (details in Table 7.2).

7.3 Development of LUT of values of erythemal UV

A look-up table, *UVB_FINAL.dat,* with ozone, albedo and SZA as the indices, was developed using the IDL program, *develop_lut2.pro* (see Appendix A). This program spawned UVSPEC

with the above-mentioned parameters increased in increments (within nested loops), and within the limits, as specified in Table 7.2. The process used to determine the sizes of the parameter increments is described below. The other parameters were permanently set as per Table 7.1.

Table 7.2: Varying parameters for creation of erythemal UV LUT.

Parameter	Limiting values	Step size
SZA	20-90 degrees	1 degree
Ozone	50-550 DU	5 DU
Albedo	0-100%	5%

The UVSPEC output included a line of the following data for each wavelength specified in the input file:

- the wavelength
- direct down beam irradiance
- diffuse down irradiance
- diffuse up irradiance
- direct contribution to mean intensity
- diffuse down contribution to mean intensity
- diffuse up contribution to mean intensity.

A call was made by *develop_lut2.pro* to an IDL function (*uvspec_ery.pro)* which performed the following:

- The UVSPEC output file was used by *uvspec_ery.pro* to calculate the following for each wavelength:
  total irradiance = (direct down) + (diffuse down) [mW m^{-2} nm^{-1}];
- Next the erythemal irradiance for each wavelength was determined by multiplying the total irradiance by the appropriate value from the CIE file containing the McKinley/Diffey action spectrum data (McKinlay and Diffey 1987);
- The erythemal UV value [mW m^{-2}] was obtained by integrating over the wavelength range (280-400 nm).

The first version of the IDL software module, *develop_lut2.pro*, took four days to run to completion with the resultant erythemal UV values stored in a 3-D array. Fine tuning the input and output required a number of runs of this first version of the program. Hardware problems (e.g. interruptions to the power supply, server problems) occasionally caused it to crash somewhere through the processing. This ultimately led to the decision to develop the LUT in 'slices' (a 2-D array of erythemal UV values for one SZA and the full ranges of TOC and albedo) to counter the longer run time and the increased chance of interruption. This was ultimately achieved after amending the first version of *develop_lut2.pro* (Appendix A) to produce 71

separate files. The individual slices were written to file and then later 'stitched' together to form the 3-D array.

The LUT therefore contains an erythemal UV value for each combination of the discrete steps in the parameters (Table 7.2). When processing the AVHRR images with software module, *create_maps.pro* (see Appendix A), a call to an IDL routine, *interp_uvb.pro*, produced interpolated erythemal UV values for between-index step values (see below for description and assessment of the interpolation process).

To determine the appropriate increments to use for each of the indices in the LUT, UVSPEC was run, holding three of the four parameters (day number, TOC, SZA and albedo) constant and changing the remaining one and plotting the results. As an example, UVSPEC was run 18 times, changing SZA by 5 degrees each time, but holding day number equal to 319, TOC equal to 300 DU and albedo equal to 0.1. The erythemal UV values output by *uvspec_ery.pro* were plotted against SZA (see Figure 7.2). From visual assessment of this plot it was decided that a smoother curve would be obtained by using an increment of one degree rather than five degrees, for building the LUT. This procedure was repeated to determine the appropriate increments of 5 DU and 5% for TOC and albedo respectively.

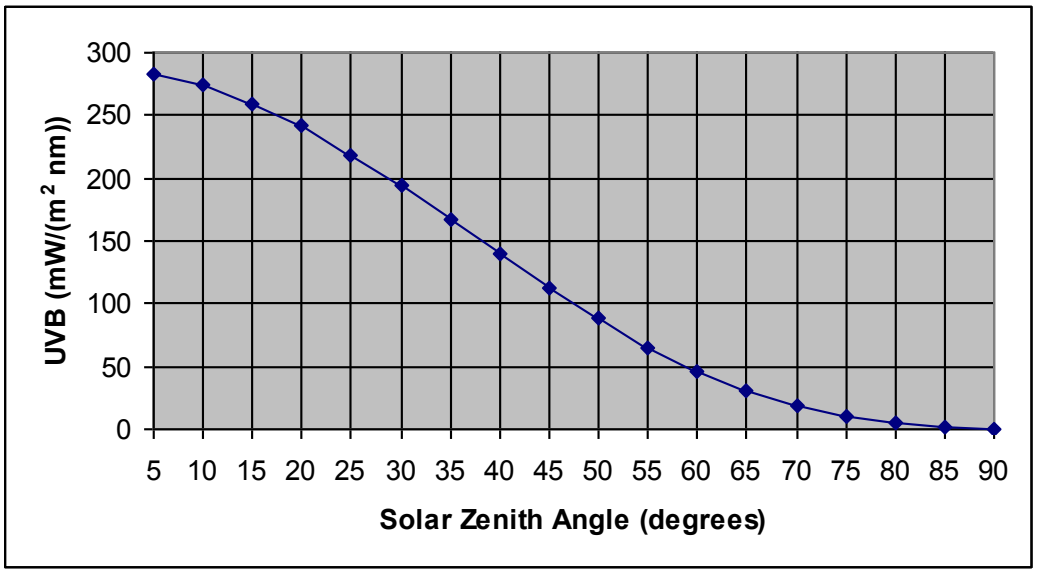

Figure 7.2: Plot of erythemal UV for SZA varied in 5 degree increments.

As mentioned above, the routine *interp_uvb.pro* was written to interpolate the erythemal UV value for a given SZA, TOC and albedo, when some or all of the parameter values fell between the specific incremental values of the LUT indices. *interp_uvb.pro* calls `findex.pro`, an IDL function written by Paul Ricchiazzi from the Institute for Computational Earth System Science, University of California, Santa Barbara (21st February 1997). The code for this routine was available via the University of Washington, Astronomy Department's link to the Earth Space

Research Group's IDL library at the University of California, Santa Barbara (http://www.astro.washington.edu/docs/idl/htmlhelp/slibrary28.html). `findex.pro` uses a binary search to compute a floating point index for a given point in a table. The resultant output was then used with the proprietary IDL function `interpolate.pro` to find the erythemal UV value for the floating point indices.

To check the accuracy of the interpolation process, software was written to compare the interpolated erythemal UV values with the erythemal UV value that resulted from running UVSPEC for the specified (see Table 7.3), between-increment parameter values. Arbitrary values were selected at the lower (L), middle (M) and upper (H) ends of the range of values for the three parameters (SZA, TOC, albedo) (see limiting values in Table 7.2) in the combinations as described in the left hand column of Table 7.3. The results of this comparison are shown in Table 7.3. The differences between the results of the two methods are negligible except when SZA is close to 90 degrees.

Table 7.3: Difference and percent difference between erythemal UV values generated directly by UVSPEC and interpolated *by interp_uvb.pro.*

Comparison of erythemal UV values – UVSPEC cf. *interp_uvb.pro*							
Index level	**SZA (degrees)**	**TOC (DU)**	**Albedo (%)**	**Erythemal UV (UVSPEC)**	**Erythemal UV (*interp_uvb.pro*)**	**Difference**	**%age diff.**
LLL	30.10	102.40	0.015	663.984	663.725	-0.259	-0.039
LLH	31.20	101.30	0.983	1097.110	1100.190	3.080	0.281
LHL	33.70	399.30	0.021	122.186	122.247	0.061	0.050
LHH	34.40	398.20	0.960	188.528	188.563	0.035	0.019
HHH	89.90	399.00	0.980	0.049	0.038	-0.011	-22.557
HLH	88.20	101.30	0.975	2.395	2.406	0.011	0.456
HLL	89.90	101.00	0.012	0.131	0.082	-0.049	-37.399
HHL	88.40	397.20	0.011	0.386	0.391	0.004	1.081
MMM	45.40	300.30	0.566	139.900	139.650	-0.250	-0.179
where	L=low	M=medium	H=high				

7.4 Steps in processing AVHRR PPF images

The software module *create_maps.pro* (see Appendix A) processed the AVHRR PPF images, pixel by pixel, via a loop that ran through the 'x' and 'y' dimensions of the specified area. The year, day of the year and area were specified in the 'run line' of *create_maps.pro*. Initially, the contents of the AVHRR PPF image (i.e. 15 parameters as listed in Table 5.1) were read into arrays for subsequent referencing in the program.

With the first test run of *create_maps.pro* using the initial erythemal UV LUT, an artefact was noticed in the resultant 'map' of erythemal UV values not explained by changes in the parameter values. Upon further investigation of the erythemal UV LUT values, anomalous 'dips' (zero values) were shown to occur randomly throughout the LUT where they should have been changing monotonically (for example, Figure 7.3).

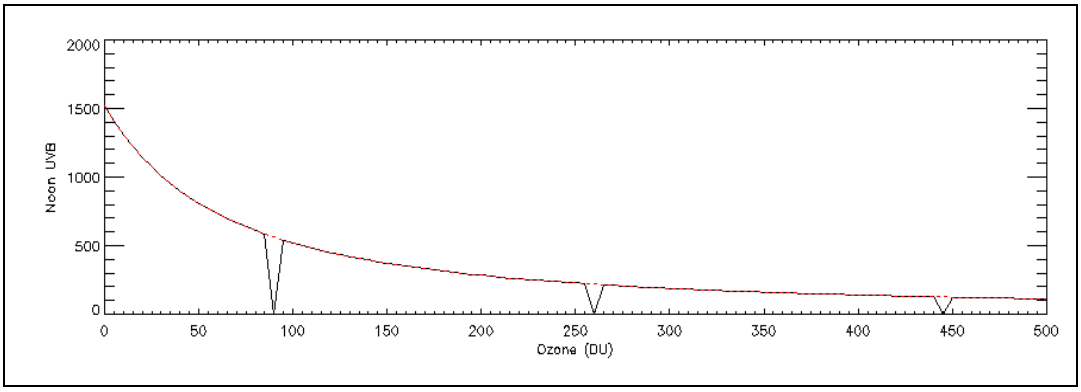

Figure 7.3: Plot of erythemal UV irradiance (in mW m^{-2}) *vs* ozone=0-500 DU (for SZA = 22º and surface reflectance = 100%).

Correspondence with the authors of libRadtran (Mayer *et al.* 2006) revealed that this was an inherent problem with the software, and not a problem with the way the LUT had been developed. B. Mayer (pers. comm., 2007) suggested some methods to rectify the problem, but with no guarantees. This would have involved a great deal of time to make changes to the input to UVSPEC, and testing the outcome prior to recreating the LUT. Instead, an IDL routine was written to check each 'slice' of the LUT, find the 'bad' data, and interpolate new values that fitted the plot. These 71 'fixed slices' were then 'stitched together' to form the complete LUT of 'good' data.

7.4.1 Ozone data for each pixel

A separate IDL routine read in the TOMS satellite data (1.0° latitude x 1.25° longitude spatial resolution) and TOC values were interpolated for each pixel in the AVHRR PPF image (5 km x 5 km spatial resolution). The interpolated ozone values were stored in an array, in preparation for processing the AVHRR PPF data for which TOC, albedo and SZA were required to estimate erythemal UV for each pixel (see Section 7.4.3).

7.4.2 Albedo of each pixel

UV albedos are often estimated, as their determination is complex especially over inhomogeneous surfaces. Global albedos may be derived from satellite measurements such as via the International Satellite Cloud Climatology Project (Rossow and Schiffer 1991; Kimes and Sellers 1993), but such albedos tend to be restricted to visible wavelengths. The UV albedo is generally slightly different from the visible albedo (Blumthaler and Ambach 1988b), and there is comparatively little information about the albedo of natural surfaces in the UV wavelength range (Weihs and Webb 1997a). By way of example, Doda and Green (1980) measured the UV reflectivity of four different kinds of surface from a plane under cloudless conditions; Eck et al. (1987) used Nimbus-7 TOMS to infer the UV surface and cloud reflectance at 370 nm). The spectral nature of the albedo of the surface of the Earth has been researched by many scientists

(e.g. Blumthaler and Ambach 1988b; Grenfell *et al.* 1994; Knap *et al.* 1999; Smolskaia *et al.* 1999; Mayer and Degunther 2000; Pubu and Li 2001; Reijmer *et al.* 2001; Smolskaia 2001; Casacchia *et al.* 2002; Perovich *et al.* 2002; Smolskaia *et al.* 2003; Pirazzini 2004; Brandt *et al.* 2005). Some of these investigations provided tables/graphs that indicated appropriate UV albedo data for a particular broadband albedo values, allowing a line of best fit to be established for the relationship between UV and broadband albedo. As mentioned in Section 5.2, with insufficient data on which to base this relationship, the decision was made to rely on the assignment of surface type from the PPF surface mask to specify the UV albedo for each pixel (see Section 5.2).

The surface mask array was used to develop an array of surface UVB albedo ('*uval*' in *create_maps.pro* code included in Appendix A) for each pixel. A pixel of open water was allocated an albedo of 7% (after Brandt *et al.* 2005) and a pixel of fast ice with snow was allocated an albedo of 91% (Grenfell and Perovich 2004; Brandt *et al.* 2005). A pixel of pack ice was allocated an albedo that was linearly interpolated between the open water albedo (7%) and the fast ice albedo (91%), according to the sea ice concentration, as indicated by the surface mask value (see Table 5.2 for explanation of surface mask type values). For example, a surface mask value of 21 indicates that there is predominantly first-year ice, total ice concentration between 10% and 19%; a surface mask value of 25 indicates predominantly first-year ice, total ice concentration between 50-59%; while a surface mask value of 33 indicates predominantly multi-year ice at 30-39% concentration, etc. The sea ice concentration at the centre of the indicated range (e.g. 15% for surface mask = 21) was used to interpolate between the open water and the fast ice albedo values – these data were written into the 'uval' array. The albedo used to choose the correct erythemal UV value from the LUT for the pixel (i.e. '*uvas*' in the *create_maps.pro* code) was the result of applying a smoothing kernel to the *'uval' array* to take into account the research by Smolskaia *et al*. (2006). The development of the kernel to best match the Smolskaia (2001) model results is explained below.

The blue plot in Figure 7.5 represents the results that Smolskaia (2001) achieved when running a 3-dimensional Monte Carlo model, UVRTIS (UV Radiative Transfer over an Inhomogeneous Surface) to determine the effect of an inhomogeneous surface albedo on UV irradiance. The following process aimed to smooth the surface albedo (water and snow-covered ice) to achieve a result as close as possible to those of Smolskaia (2001).

The proprietary IDL function `smooth.pro(albedo, X)` (where X is the number of cells over which to average) was used to average the albedo values over adjoining cells for one dimension only (for X = 3, 5, 7). UVSPEC (TOC = 350 DU, SZA = 60°) was then used to determine the erythemal UV values for each 5 km cell for the different albedo regimes. The above values for TOC and SZA were chosen to match those used by Smolskaia (2001). These erythemal UV values were then normalised by the value at the centre (i.e. where the ice met the ocean), as per the ratios from Smolskaia's Figure 5.4 (2001). Overall, averaging over 7 pixels produced the

best agreement with Smolskaia's (2001) results, but it was determined that smoothing should be done in two dimensions for a more accurate representation of the albedo edge effect.

Because of the large volume of AVHRR images to be processed, calculations needed to be kept to a minimum to aid efficiency. An IDL routine, *test_alb.pro* (see code in Appendix A) was developed for the purpose of testing various smoothing kernels to find one which was not resource-hungry but still achieved a good result. This software initially used a 7 x 7 kernel to smooth the albedo values in two dimensions (see code for arrays of albedos plus relative irradiances from the research undertaken by Smolskaia (2001)). The size of the kernel was increased by one only in each dimension, and tested by squaring and then cubing etc. the values, before incrementing the size by one again. The best match with the Smolskaia (2001) plot (sum of squares = 0.00061) was achieved using a 13 x 13 kernel (k5) (below) with the matrix values raised to the power of 5.

```
k5 =  [1,1,1,1,1,1,1,1,1,1,1,1,1]
      [1,2,2,2,2,2,2,2,2,2,2,2,1]
      [1,2,3,3,3,3,3,3,3,3,3,2,1]
      [1,2,3,4,4,4,4,4,4,4,3,2,1]
      [1,2,3,4,5,5,5,5,5,4,3,2,1]
      [1,2,3,4,5,6,6,6,5,4,3,2,1]
      [1,2,3,4,5,6,7,6,5,4,3,2,1]
      [1,2,3,4,5,6,6,6,5,4,3,2,1]
      [1,2,3,4,5,5,5,5,5,4,3,2,1]
      [1,2,3,4,4,4,4,4,4,4,3,2,1]
      [1,2,3,3,3,3,3,3,3,3,3,2,1]
      [1,2,2,2,2,2,2,2,2,2,2,2,1]
      [1,1,1,1,1,1,1,1,1,1,1,1,1]
```

The higher central value of the smoothing kernel radiating out to lesser values (i.e. one) in the perimeters of the kernel was to emphasise the greater effect of the albedo of cells closer to the central cell. The chosen smoothing kernel was tested using an array of 25 x 25 cells, half ice and half ocean as depicted in Figure 7.4. The ice edge is at the centre of the middle 5 km cell, and there are 12 cells of ice cover and 12 cells of open water on either side. The following values were assigned to the albedo for water (α_{water} = 0.05) (as used by Smolskaia 2001 after Blumthaler and Ambach (1988)), snow-covered ice ($\alpha_{snow/ice}$ = 0.855) (as measured *in situ* during field work conducted by Smolskaia *et al.* (1999), at the water/ice interface near Australian Antarctic research station Davis (hereafter Davis station)) and the central value at the ice edge ($\alpha_{central}$ = 0.5). There was slight asymmetry between the sections for ice and water of the Smolskaia (2001*)* plot. The value of the albedo in the central line was adjusted (from the average of the values for water and snow-covered ice i.e. 0.45) to 0.50 to reproduce this asymmetry and properly represent the observed smoothing.

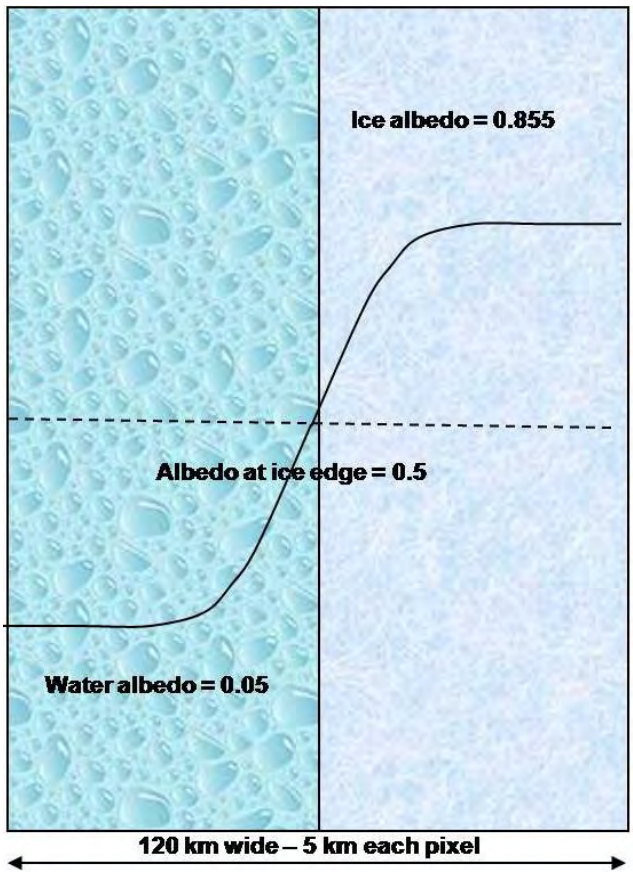

Figure 7.4: Representation of the water/ice regime used for testing albedo smoothing kernels.

The black plot in Figure 7.5 represents erythemal UV values resulting from calculations using unsmoothed albedo values when there is an abrupt change in surface albedo. The red and green curves (i.e. the results of using members of the smoothing matrix, k5, raised to the power of 4 and 5 respectively) represent the results of using just two of the many different smoothing matrices to determine which regime best matched the Smolskaia (2001) results. The code for the IDL routine *test_alb.pro* (Appendix A) includes the arrays of albedos plus relative irradiances from the research undertaken by Smolskaia (2001).

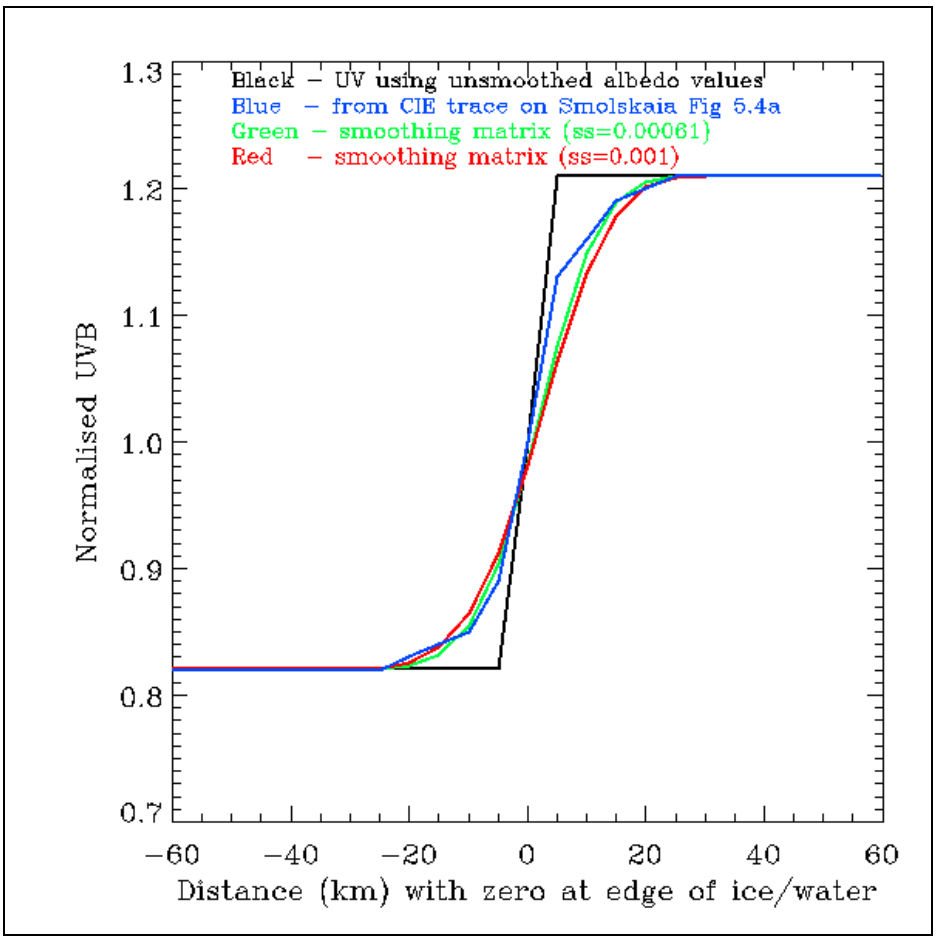

Figure 7.5: Clear-sky erythemal enhancement as a function of distance from the ice edge. UVSPEC (TOC= 350 DU, SZA=60º).

7.4.3 Determining daily clear-sky erythemal UV at the water/ice surface

At this point in the processing, the following were available for each pixel of a specified area, for each day in a year: TOC value, a smoothed albedo value (*uvas*) and an array of SZAs at half-hourly intervals across the full day obtained from the previously-created LUT (see Section 7.1 above). Using the three above-mentioned parameters as indices, estimates of clear-sky erythemal UV were interpolated from *UVB_FINAL.dat* and the data were stored in arrays. The noon-time erythemal UV value was selected as the maximum for the day, and erythemal UV dose was computed by summing the half-hourly values for the day.

The effect of the Earth-Sun distance on top-of-atmosphere solar irradiance had previously been plotted – this demonstrated a variation of ±3.5% (see Figure 7.6). If this effect was ignored, it would introduce a source of error of this magnitude. This effect was taken into account in the code of the main processing software package, *create_maps.pro* (see Appendix A) – the erythemal UV maximum and erythemal UV daily dose were multiplied by the Earth-Sun distance factor and stored in arrays.

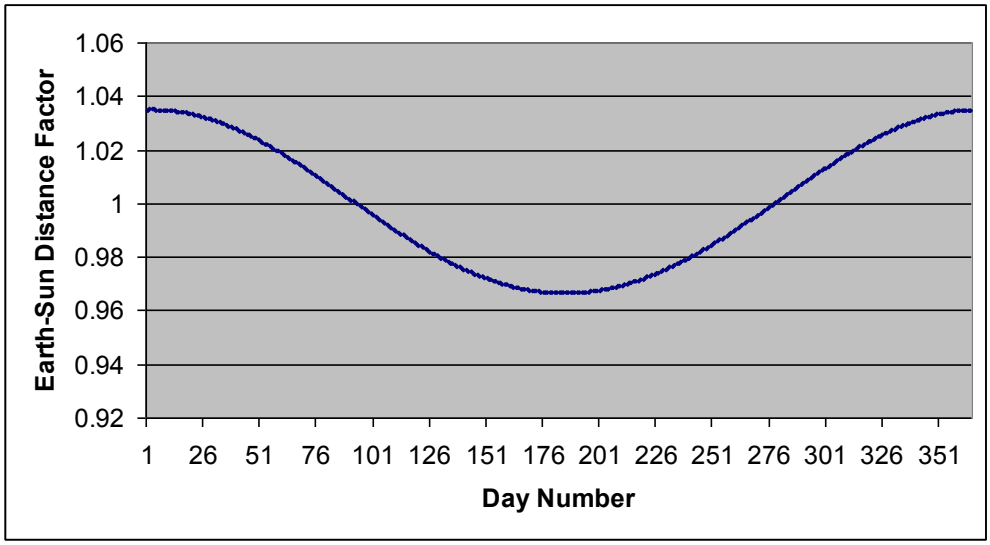

Figure 7.6: Plot of Earth-Sun Distance Factor *vs* day number of year.

7.4.4 Choice of cloud algorithm

Section 3.2.5 discussed the ways in which cloud affects levels of UVB that arrive at the surface of the Earth, and described attempts by researchers to include realistic estimates of 'cloud amount' in models of levels of UVB reaching the Earth. Sabziparvar *et al*. (1999) determined that the cloud and aerosol properties provided the largest source of uncertainty in attempts to model clear-sky and all-sky UVB irradiances. To accurately determine the effect of cloud cover on UVB levels at the surface of the sea ice, the cloud base height is needed (Kitova *et al*. 2002). There is little information on cloud base height available for the Antarctic sea ice zone, and certainly no information on the spatio-temporal variation of it for the study region and period. The AVHRR PPF dataset includes a cloud mask which only signifies the presence or absence of cloud in the pixel – there are no associated data on cloud base height, cloud type or cloud thickness. The only information available that can be included in this model is therefore the presence/absence of cloud.

ICEMAPPER (an automated satellite image analysis system) (Williams *et al.* 2002) uses one set of rules to identify areas of high cloud, low cloud, open water, land ice and sea ice, and another to determine sea ice concentration through an expert system approach. Some of the rules in *ICEMAPPER* were derived using information obtained from published and unpublished research, augmented by details given by practising meteorologists. Others were created by having an expert image interpreter analyse a set of representative AVHRR images, and processing these analyses, using a statistical package, to produce rules which closely duplicate the manual analyses. The system was tested on six AVHRR images of the East Antarctic coastline, acquired late in the 1997-1998 summer season. It successfully identified 85% of pixels selected from the images using a regular grid, as belonging to one of the five surface classes: high cloud, low cloud, open water, land ice or sea ice (Williams *et al.* 2002).

The rules of the expert system, *ICEMAPPER*, were developed for summer by Williams *et al.* (2002). These rules were included in the code of the IDL routine, *summer_cloud.pro*. The rules for spring were developed by Borsche (2001) by adjusting the *ICEMAPPER* rules (Williams *et al.* 2002), and were included in the IDL routine, *spring_cloud.pro*. The albedo and brightness temperature from the 5 AVHRR channels were read into the IDL routines, *summer_cloud.pro* and *spring_cloud.pro* to classify the pixels as water, sea ice, bare land, continental ice, high cloud, low cloud, interference and 'unclassified'. The surface mask was also used in the processing to aid in positioning the pixel over land or sea.

To determine the best method to incorporate cloud amount in the estimations of surface erythemal UV in the software, *create_maps.pro,* the following plots (see example Figure 7.7 and colour code in Table 7.4) were produced for a random selection of 45 days over the years applicable to the project:

a. plots developed using the IDL routine, *summer_cloud.pro;*
b. plots developed using the IDL routine, *spring_cloud.pro*;
c. plots of the surface albedo from the AVHRR PPF dataset;
d. plots of the AVHRR PPF surface mask; and
e. plots of the AVHRR PPF cloud mask.

The author visually compared the plots a., b. and e. above to determine which algorithm best represented cloud-affected pixels, as displayed in the plot of the surface albedo (Figure 7.7c). This process was repeated with a second independent expert. Both analyses led to the same conclusions, and consequently the decision was made to use the rules from Williams *et al*. (2002) and Borsche (2001) for summer and spring, respectively, as these classifications better matched the surface albedo plot than did the PPF cloud mask. In the absence of any rules for autumn, it was decided to use the Borsche (2001) rules for this season also, as the thermal and visible appearance of sea ice and cloud could be expected to be similar for spring and autumn.

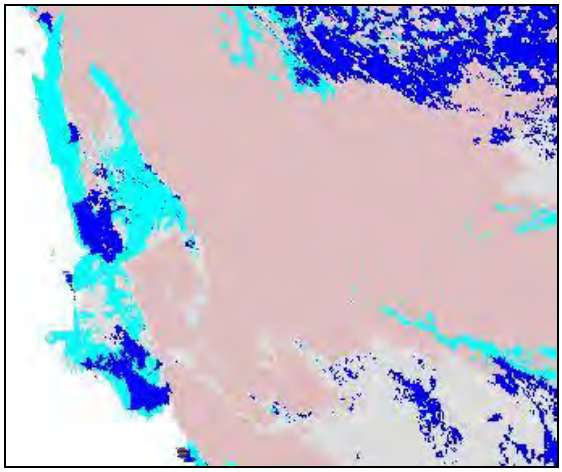

a.

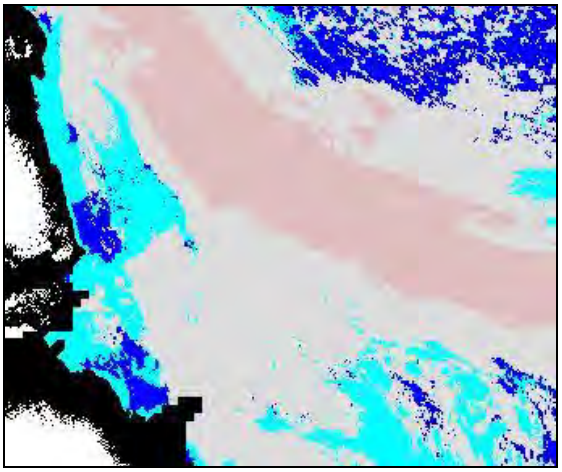

b.

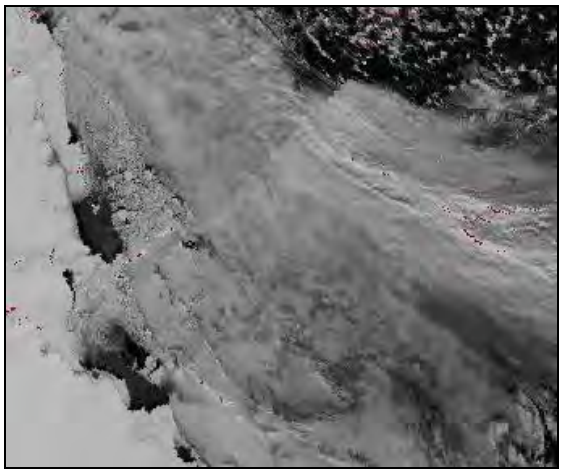

c.

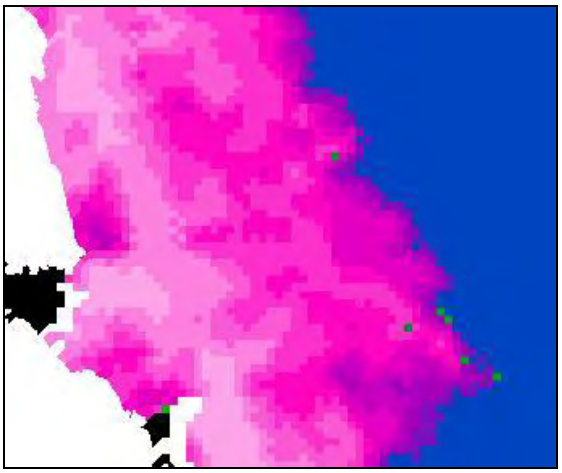

d.

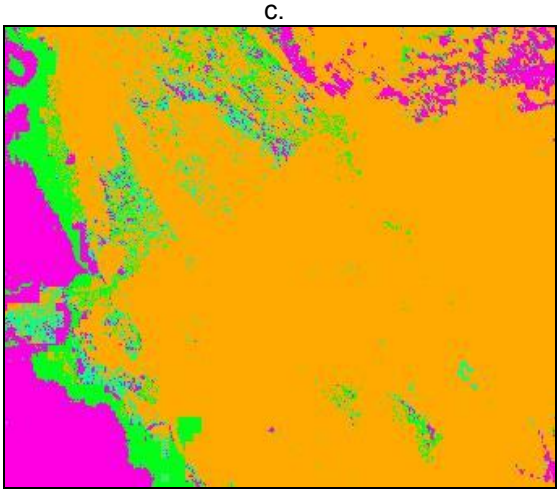

e.

Figure 7.7: Sample plots for day no. 313, 1998 for Amery region:

a. Plot produced by summer rules of Williams *et al*. (2002);
b. Plot produced by spring rules of Borsche (2001);
c. Plot of surface albedo from AVHRR PPF data set;
d. Plot of surface mask from AVHRR PPF data set;
e. Plot of cloud mask from AVHRR PPF data set.

Table 7.4: Colour codes for plots in Figure 7.7 (CASPR is Cloud and Surface Parameter Retrieval system as described in Section 5.2).

Spring and summer rules		AVHRR PPF cloud mask for version 3 data	
Open water	Blue	Both algorithms below say clear	Mauve
Sea ice	Light blue	Missing data	Red
Bare land	Dark green	CASPR multi-day says cloud	Green
Continental ice	White	CASPR single day says cloud	Blue
Low cloud	Grey	Both algorithms above say cloudy	Orange
High cloud	Pink/grey		
Interference	Red		
Not classified	Light green		

7.4.5 Estimating cloud-affected erythemal UV at the water/ice surface

Within *create_maps.pro*, the 'cloud expert system' was selected based on the day of year, and the appropriate cloud algorithm was called to develop new arrays (*imar* in *create_maps.pro code)* representing classifications of the area. No differentiation was made between first- and multi-year ice, and therefore code was included to create a new surface mask that merged these two classifications. The surface mask was then used to 'fine tune' some of the classifications of the two expert systems, i.e. Williams *et al*. (2002) and Borsche (2001). If either expert system had classified open water (as designated by the surface mask) as sea ice, it was reclassified as low cloud. If either expert system had classified sea ice (>50%) (as designated by the surface mask) as open water, it was reclassified as sea ice.

Using the array, *imar*, it was determined if cloud was present or absent for a pixel, setting the cloud fraction to one or zero accordingly. Taking into consideration a three pixel by three pixel neighbourhood, a cloud amount in tenths (with double weight for the centre pixel) was calculated using the proprietary IDL function, `smooth` that returns a copy of the original array smoothed with a boxcar average of the specified width.

Three different methods of determining the cloud modification factor (CMF) to adjust for cloud effects were used, as per the following processes:

a. Lubin and Frederick (1991) cloud modification factor (cmf = 1.0 – 0.0024*(cloud amount) – 0.0038(cloud amount)^2);
b. McMurdo cloud modification factor (cmf2 = 1.0 – (0.2*((cloud amount*0.1)$^{2.09}$)), as described in Kim and Hoffman (2005); and
c. Palmer cloud modification factor (cmf3 = 1 – (0.37*((cloud amount*0.1)$^{1.43}$)), as described in Kim and Hoffman (2005).

From preliminary runs of the software, *create_maps.pro,* three different values of cloud-affected erythemal UV values were calculated – one erythemal UV value for each of the three different cloud modification factors as above. At that stage of the processing, *in situ* measurements of erythemal UV had only been obtained for Davis Station (further *in situ* measurements were later

obtained for Australian Antarctic research station Casey (hereafter Casey Station) and Australian Antarctic research station Mawson (hereafter Mawson Station) (see Figure 2.3). These three values of cloud-affected noon-time erythemal UV were compared with *in situ* measurements for Davis Station (for the same day in the year) to determine which was the most appropriate CMF to use in this project. Section 8.2.1 details this validation process and the basis for the selection of the second cloud modification factor (CMF2). It should be noted that none of the above CMFs were developed over areas mostly covered by sea ice and ocean, as in the study area of this project, but these were the only ones available to choose from. Cloudy-sky levels of erythemal UV were then estimated by adjusting clear-sky maps of erythemal UV using CMF2.

7.5 UV mapping requirements for Antarctic Biologists

Much information has been gathered about UV-photobiology in Antarctica (see Section 2.3.1 for details and references therein); however, a definitive quantitative assessment of the effect of ozone depletion on the Antarctic ecosystem does not exist (see Section 2.3.1). So far, it is only obvious that ozone depletion has not had a catastrophic effect in the Antarctic region (Karentz and Bosch 2001). However, the long-term consequences of possible subtle shifts in species composition and trophic interactions are still uncertain (Karentz and Bosch 2001). The development of maps of levels of erythemal UV radiation at various depths throughout the water column and ice will greatly assist researchers investigating the effects of ozone depletion in Antarctica.

At the point in the data processing before the final maps of UV biological doses were developed, it was appropriate to make decisions about the following criteria to be satisfied for various fields of Antarctic research:

a. temporal coverage/resolution of the maps;
b. spatial coverage/resolution of the maps;
c. at what depths of the ocean were the maps required; and
d. at what depths within the sea ice were the maps required;

To this end, face-to-face discussions were held with a number of biologists working with the Australian Antarctic Program to determine how the end product from this project could best serve research undertaken to determine the effects (if any) of increased levels of UVB radiation on various Antarctic marine life forms.

A.T. Davidson (pers. comm., 2008) made the following points in relation to his research into phytoplankton:

a. Phytoplankton tend to concentrate in the upper 20 metres within the mixed layer depth, with the main biological effect in the top 10-15 metres, but with virtually no effect below 30 metres;

b. Maps of erythemal UV for the surface and at depths of 5, 10 and 20 metres would be most appropriate for researching the effect of UVB radiation on phytoplankton; and
c. An average value over the upper 20 metres for a mixing model would also be helpful.

S. Kawaguchi, S. Nicol and P. Virtue (pers. comms., 2008) made the following comments on Antarctic krill (*Euphausia superba*) behaviour and research:

a. The juvenile krill in spring are nektonic, i.e. they can swim against a current. They can detect UVA and swim deeper to avoid it. They cannot detect UVB but have protective pigments from their diet of phytoplankton;
b. Krill feed in the upper 20 metres under the ice in late summer;
c. Climatologies on a monthly basis at the surface, and depths of 5 and 10 metres were suggested as being useful; and
d. Krill graze under the ice in spring, and therefore levels of UVB just beneath the sea ice are needed.

A. McMinn (pers. comm., 2008) itemised the following factors that would affect research into sea ice algae:

a. Antarctic fast ice and pack ice have to be treated differently – in fast ice, most of the organisms are in the bottom few centimetres. In pack ice, the algae are distributed throughout the ice, with usually less than 20% of the organisms at the bottom; and
b. The layer of snow-ice (see Section 2.2) becomes a habitat for sea ice algae. Research would necessarily focus on the levels of UVB at the top of the ice (under the snow), the bottom of the ice and perhaps half-way through the ice.

Penguin biologist, B.C. Wienecke (pers. comm., 2008) and seal biologist, C. Southwell (pers. comm., 2008) said that because these creatures spend varying lengths of time at the surface of the ocean/ice and at greatly differing depths of the ocean, the ability to determine a relationship between levels of UVB and any resultant effects on these larger creatures would be difficult. The following points could be taken into consideration when selecting temporal/spatial resolutions of the erythemal UV maps:

a. Adélie penguins take advantage of the Antarctic summer to breed, then during February-March they are sitting on the ice moulting, potentially a time when they could be exposed to excessive UVB;
b. Monthly climatologies would be useful for research;
c. Crabeater seals (*Lobodon carcinophagus*) spend 80% of their time on the ice in the middle of day during summer, i.e. 3 hours either side of noon; and
d. Seals are thermoregulatory and haul out in the middle of the day when UVB levels are probably at their highest.

Based on the above details provided by the Antarctic biological researchers, it was decided to produce maps as follows:

a. Monthly erythemal UV climatologies;
b. At the surface of the open water / sea ice;
c. At depths of 5, 10, 15 and 20 metres within the ocean;
d. An average value over the upper 5, 10, 15 and 20 metres of water;
e. At the top of the ice but just under the layer of snow;
f. Half way through the ice;
g. At the bottom of the ice;
h. At a specific depth of ice; and
i. Pixel averaged values at these levels (5, 10, 15 and 20 metres) in the water column, including the sea ice concentration in the calculations.

The output from this project will allow scientists to extract the spatial and temporal coverage of erythemal UV data needed to further biological research previously undertaken on specific voyages through the Australian Antarctic Program (examples: V7 1997-1998 (PICCIES); V6 1998-1999 (STAY); V6 2000-2001 (KACTAS); V4 2002-2003 (KAOS); V1 2004-2005; and V3 2004-2005 (ORCKA)).

7.6 Developing 'maps' of monthly averages

For the following parameters – noon-time erythemal UV (uvnn), daily dose of erythemal UV (uvdt), albedo (albd), sea ice concentration (sicn), ozone (ozon), cloud modification factor (CMF2) and count of days of data (count) – monthly averages were computed for each region, R = Amery, Shackleton, Dalton or Mertz (i.e. A, S, D or M) for years, yyyy = 1996-2005, and for ddd = day of year. Plots of monthly averages for each of the regions (R), for every year, for each parameter are also available in Appendix A with the file naming convention '*paramRyyyy*' (see examples Figure 7.8 and Figure 7.9 and all other plots are in Appendix A) where *param* = one of the above-mentioned parameters, *R* = region (as described above) and *yyyy* = year.

Code (*time_series.pro*) was written to allow a user to enter the 'x' and 'y' coordinates of diagonally-opposite corners of a rectangle in a specified region (see Section 8.3.2). This software reads in the monthly averages for all the parameters for the region (A, D, M or S) specified in the run line. Each parameter is averaged across the 'sub-area' and a time series of the means was plotted – see discussion in Section 8.3.4.

Code (year_*ts.pro*) was written to produce plots (see Appendix A) of monthly means across the years of the project for the parameters, ozone, noon-time erythemal UV and sea ice concentration for each of the selected sub-areas. The naming convention for these plots is *mean_paramRn.jpg* where *param* = one of the parameters as described above; *R* = A, S, D or M; and *n* = number of the sub-area as described in Section 8.3.2. The IDL code, *trends.pro*,

was written to produce trend lines and the associated statistics using the least squares method. See plots and discussion in Section 8.3.6.

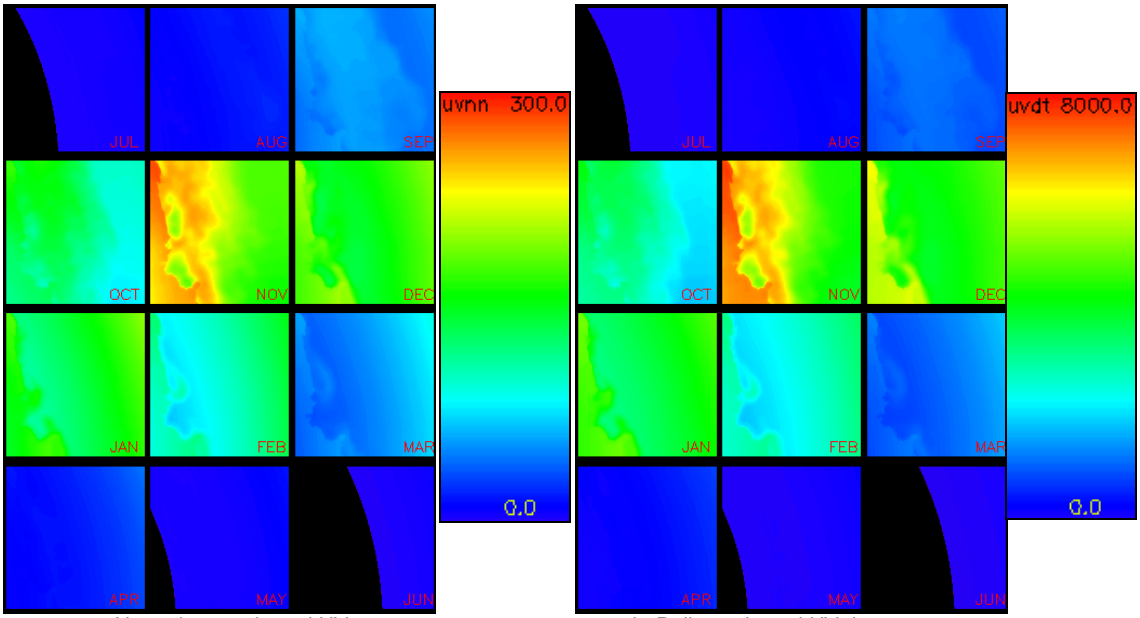

a. Noon-time erythemal UV b. Daily erythemal UV dose

Figure 7.8: Sample plots of monthly averages of a. noon-time erythemal UV and b. daily erythemal UV dose for July 2001 to June 2002 for Amery region (all other similar plots for other years and other regions are included in Appendix A).

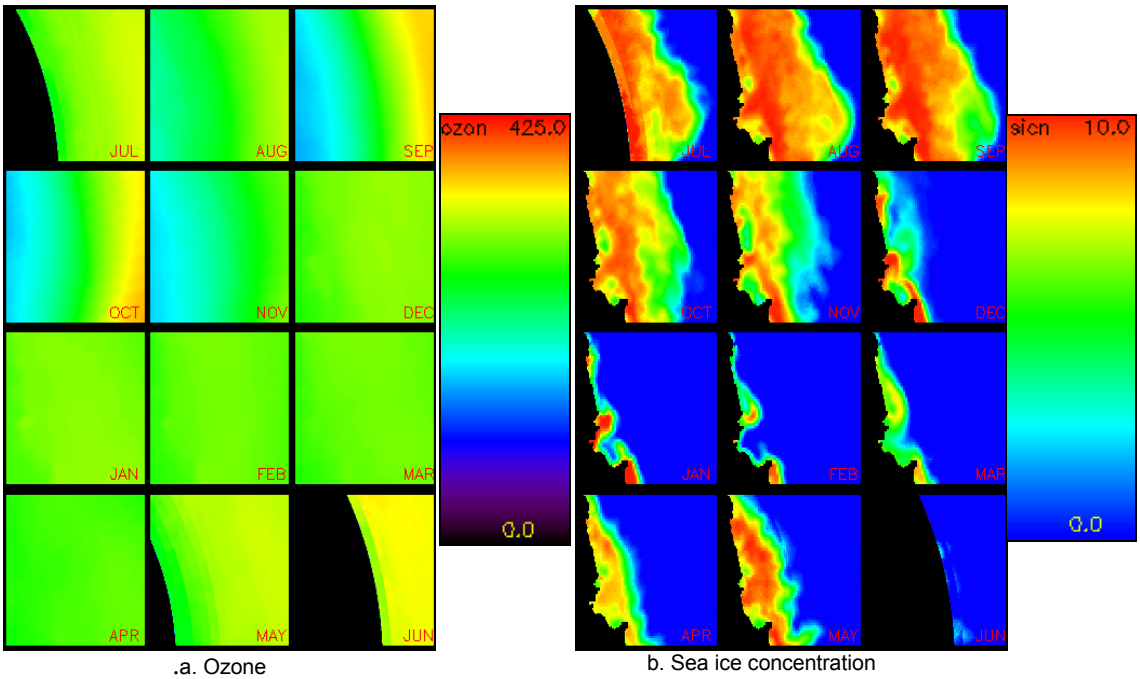

.a. Ozone

b. Sea ice concentration

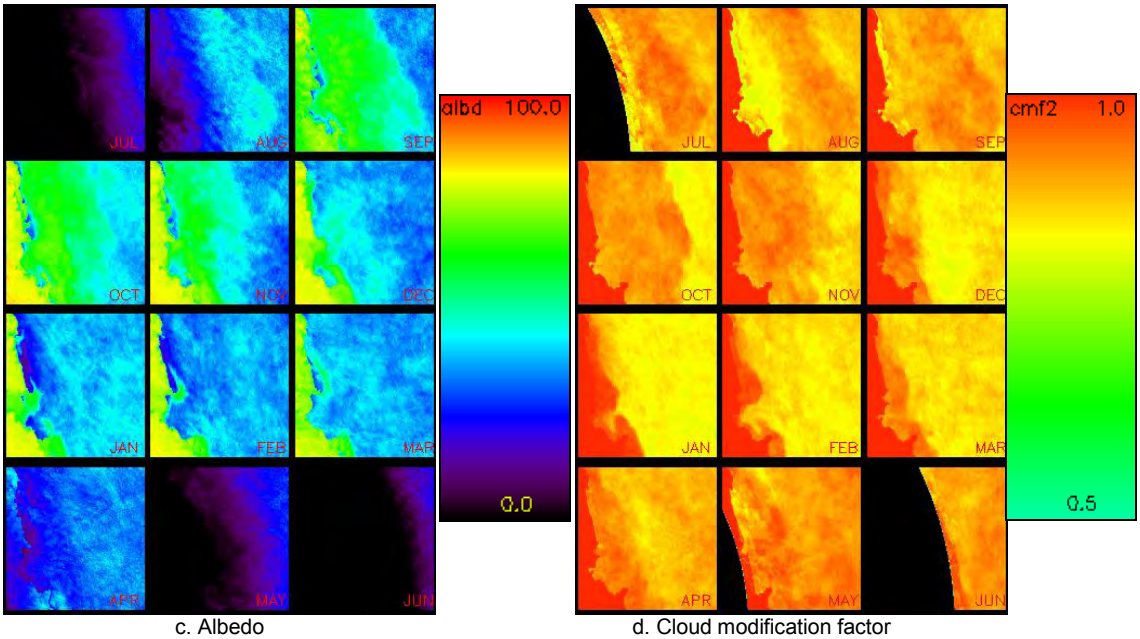

c. Albedo

d. Cloud modification factor

Figure 7.9: Sample plots of monthly averages of a. ozone, b. sea ice concentration, c. albedo and d. cloud modification factor for July 2001 to June 2002 for Amery region (all other similar plots for other years and other regions are included in Appendix A).

8. RESULTS

This chapter presents the results of the validation procedure, when the modelled values of noon-time erythemal UV are compared with *in situ* data collected at three Antarctic stations, and onboard the RSV *Aurora Australis*. Example plots of erythemal UV (noon-time and daily dose) and the parameters ozone, sea ice concentration, surface albedo, count of days where data are available and cloud modification factor are presented. Visual assessments of the plots and trend-line analyses of some case studies are also included in this chapter. Appendix A (CD in the back cover of thesis) contains the important software modules and all the plots, organised in a logical sequence with appropriate folder names.

8.1 Daily maps of surface cloud-affected erythemal UV

The IDL routine, *create_maps.pro* (see Appendix A) was run for every day that AVHRR PPF data and TOC data were available between 25th July, 1996 and 29th June, 2005 (inclusive), resulting in data files of levels of cloud-affected surface erythemal UV for each pixel of the four study areas – Amery, Shackleton, Dalton and Mertz. The data files thus created contain the following values for each pixel: clear-sky noon-time erythemal UV, clear-sky daily dose erythemal UV, the value of the cloud modification factor (CMF2), TOC, AVHRR PPF surface mask, the AVHRR PPF surface albedo, and latitude and longitude of the centre of each pixel.

For each data file there was a corresponding plot of the following, saved to disk: AVHRR PPF surface mask; the cloud fraction (as determined by the expert system for the day of the year – Williams *et al*. (2002) for summer and Borsche (2001) for spring and autumn); the clear-sky noon-time erythemal UV value; the cloudy-sky noon-time erythemal UV value; TOC (TOMS data); and AVHRR PPF albedo (see example in Figure 8.1) (see Appendix A for other examples).

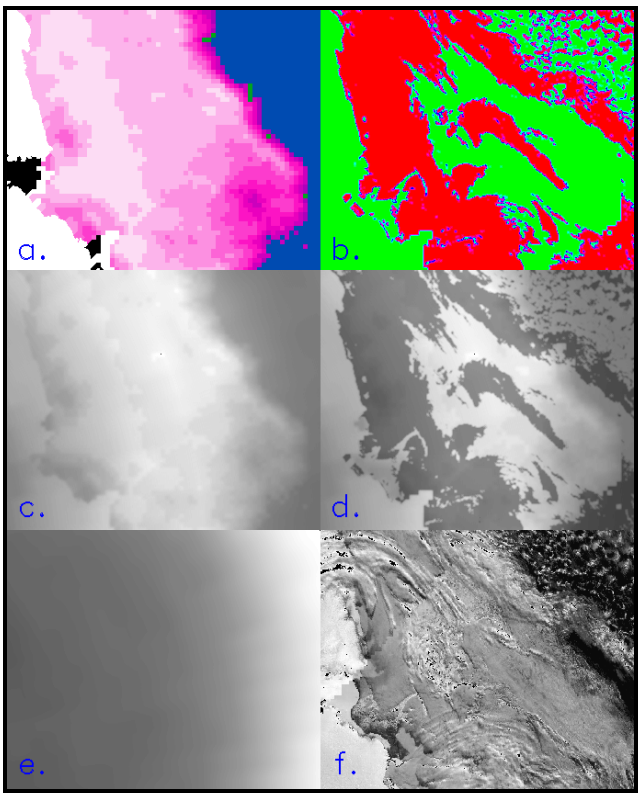

Figure 8.1: Plot created by *create_maps.pro* for day no. 265, 2001 for Amery area. Includes a. surface mask (see Figure 8.2 for colour bar), b. cloud fraction (see Figure 8.3 for colour bar), c. clear-sky erythemal UV at noon (grey scale), d. cloudy-sky erythemal UV at noon (grey scale), e. ozone (grey scale), and f. PPF surface albedo (grey scale).

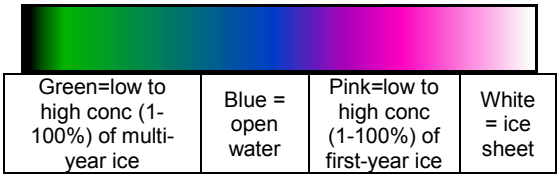

Figure 8.2: Colour bar for plot of surface mask.

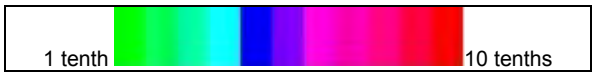

Figure 8.3: Colour bar for plot of cloud fraction.

8.2 Validation using *in situ* data

McKenzie *et al*. (2001) compared differences between satellite-derived estimates of UV and ground-based measurements at a clean air site in the Southern Hemisphere with those from more polluted sites in the Northern Hemisphere. They found that the TOMS retrievals are in good agreement with ground-based measurements at Lauder, New Zealand but they systematically overestimated the UV doses in more polluted locations. Since international inter-comparison campaigns had shown the ground-based spectroradiometers to be in agreement, McKenzie *et al.* (2001) concluded that differences in tropospheric extinctions (e.g. by ozone and aerosols) were not being adequately taken into account in the satellite retrievals of UV radiation. These findings lend tremendous support to the results from this project as the concentration of atmospheric pollutants in Antarctica is always going to be low.

Lubin *et al*. (1998) showed that a satellite-based UVR mapping method based on local noon data alone can provide useful estimates of the daily dose as well as the instantaneous local noon flux, although the research by Arola *et al.* (2002) showed that UV doses derived by satellite algorithms can differ significantly from ground-based measurements. Even for algorithms highlighting smaller deviations, the discrepancies were not fully understood (e.g., spectral effects, snow effects), showing the need for further studies. It was further concluded by Arola *et al.* (2002) that satellite algorithms cannot be blindly used for derivation of UV doses at the ground and that they should always be accompanied by ground-truthing. It is therefore expected that high-quality measurements at the ground will still be needed in future years.

More recently Tanskanen *et al.* (2007) used UV doses determined from high-quality spectral ground-based measurements to validate the daily erythemal surface UV doses derived from the Dutch-Finnish Ozone Monitoring Instrument (OMI). The validation results showed that the OMI measurements are suitable for continuation of the global satellite-derived surface UV time series using a surface UV algorithm similar to the original TOMS UV algorithm.

8.2.1 Using station data

Daily UV data measured at Davis Station between September 1997 and December 2000 was used to validate the modelled estimates of erythemal UV. The 'sample' *in situ* data was obtained from the Australian Antarctic Data Centre (AADC) (see details in Section 5.5). The data included date, day number and UVI (Ultra Violet Index). The UVI was multiplied by 25 to convert to mW m^{-2} (Gies *et al.* 2004). Modelled noon-time clear sky erythemal UV (mW m^{-2}); modelled clear-sky daily dose; the cloud modification factor; and the modelled noon-time cloud-affected erythemal UV (mW m^{-2}) (using the three different cloud modification factors) were included in the analyses. It should be noted that earlier analyses were performed using the data obtained from the AADC (n = 816). Later in the validation process, revised data were sourced

from Dr. Andrew Klekociuk (AAD) (see details in Section 5.5) on which the final analyses were based.

The data were visually assessed, and the following entries were disregarded:

a. days where there were no ozone and/or PPF data to use with the radiative transfer model to calculate an erythemal UV value for that day; and

b. days where there were no data collected (blank or zeros) at Davis Station to compare with the modelled erythemal UV value.

This left 1655 measurements and associated modelled values for validating the modelled erythemal UV values.

Assessment of the following variables was carried out:

1. modelled noon erythemal UV values (clear sky) against measured noon erythemal UV values;
2. modelled noon erythemal UV values (clear sky) against measured maximum erythemal UV values; and
3. cloud affected erythemal UV values (using the 3 cloud modification factors as described in Section 7.4.5). Figure 8.4 shows the plot of the results using cloud modification factor 2 (CMF2).

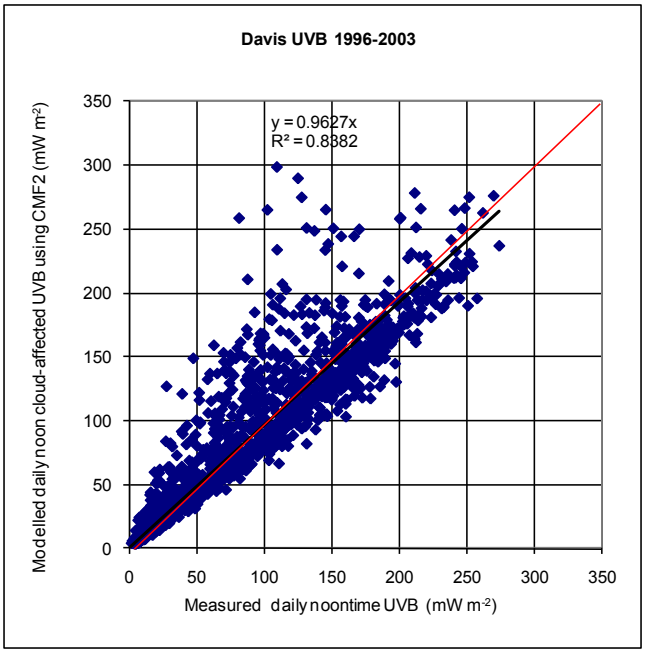

Figure 8.4: Modelled daily noon, cloud-affected erythemal UV (using CMF2) *vs* measured erythemal UV at AAD Station Davis (n = 1655).

For the daily data, CMF2 out-performed CMF1 and CMF3, both in mean bias error (MBE) and root mean square difference (RMSD) (see Table 8.1). These results were the basis for choosing the second cloud modification factor (CMF2) (see Section 7.4.5 for description of the three cloud modification factors) to develop the maps of erythemal UV.

Table 8.1: Results of analyses (mean bias error, mean square difference and root mean square difference) of modelled, daily, erythemal UV *vs* measurements made at Davis Station.

	Daily noon-time erythemal UV [mW m^{-2}] at Davis (n = 1655)			
Modelled values	Clear Noon UV	Noon using CMF1	Noon using CMF2	Noon using CMF3
MBE	-3.0	33.4	-0.2	33.5
MSD	733.0	4182.8	673.3	4169.3
RMSD	27.1	64.7	25.9	64.6

The weekly averages of the data collected at Davis Station (see plots of clear-sky and cloud-affected erythemal UV in Figures 8.5 and 8.6) were determined for all of the available erythemal UV values. These erythemal UV values included measured erythemal UV maximum, noon-time erythemal UV value and total erythemal UV, plus modelled values for clear-sky noon-time, daily clear sky total and the cloud-affected erythemal UV values using all three cloud modification factors. CMF2 still gave the best results of the three cloud modification factors (see Table 8.2).

The graphs for Davis Station data demonstrated that generally the measured erythemal UV values are higher than those estimated using the radiative transfer model. The graphs also indicated that the cloud-affected, modelled erythemal UV values were closer to the measured values than were the clear-sky, modelled values.

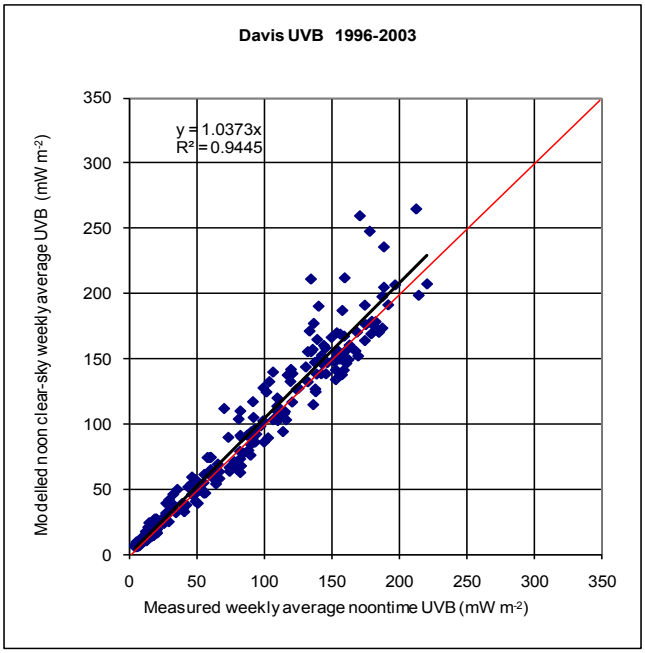

Figure 8.5: Modelled, weekly average, noon-time, clear-sky erythemal UV *vs* measured erythemal UV at Davis Station.

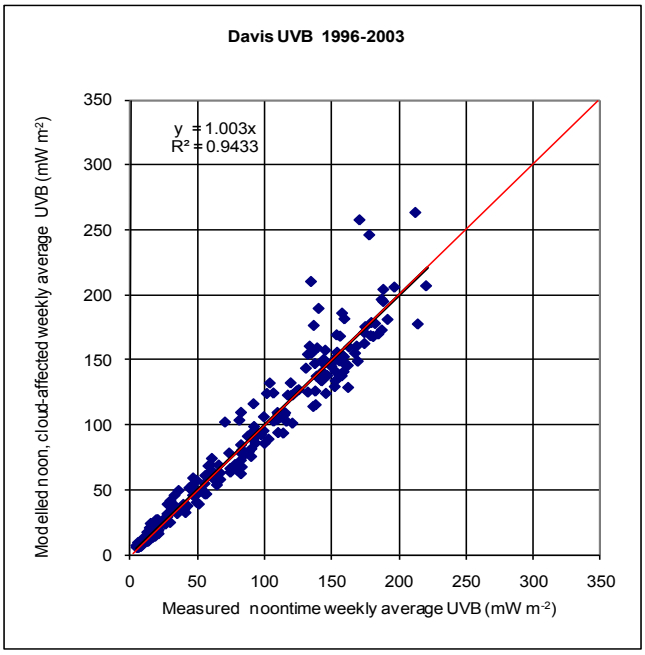

Figure 8.6: Modelled, weekly average, noon-time, cloud-affected erythemal UV (using CMF2) vs measured erythemal UV at Davis Station.

Table 8.2: Results of analyses (mean bias error, mean square difference and root mean square difference) of modelled, weekly average, noon-time erythemal UV *vs* measurements made at Davis Station.

	Weekly noon-time erythemal UV [mW m^{-2}] at Davis Station (n = 229)	
Modelled values	Clear-sky noon-time erythemal UV	Cloudy noon-time erythemal UV (using CMF2)
MBE	-3.0	-0.4
MSD	243.9	217.1
RMSD	15.6	14.7

The same data analysis was carried out for UV data collected at AAD stations, Casey and Mawson, but with less data for comparison. The results are shown in Figures 8.7-8.10 and Tables 8.3 and 8.4.

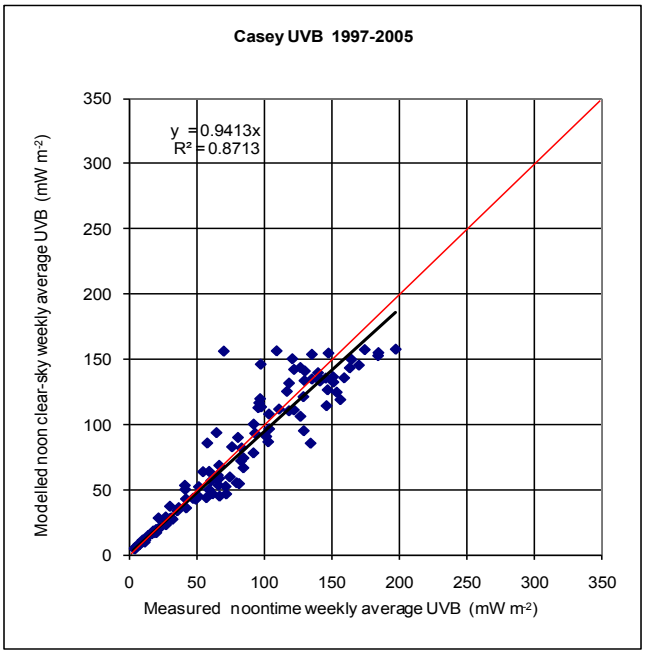

Figure 8.7: Modelled, weekly average, noon-time, clear-sky erythemal UV *vs* measured erythemal UV at Casey Station.

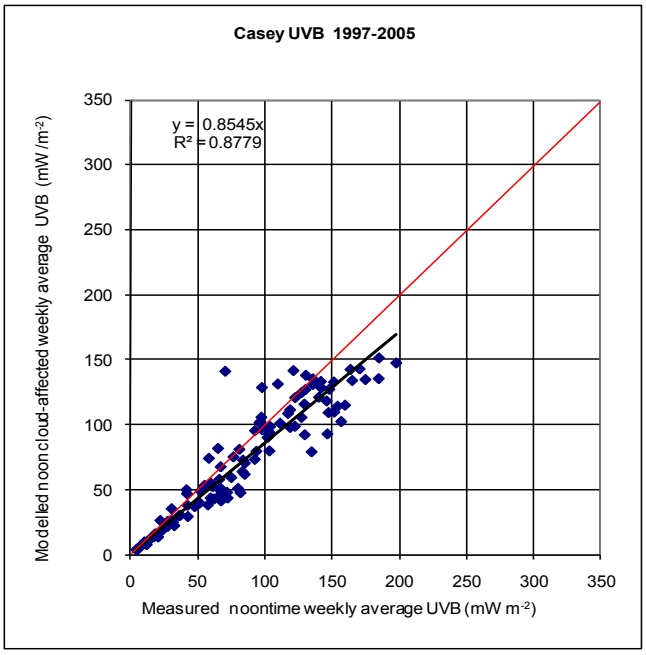

Figure 8.8: Modelled, weekly average, noon-time, cloud-affected erythemal UV (using CMF2) *vs* measured erythemal UV for Casey Station.

Table 8.3: Results of analyses (mean bias error, mean square difference and root mean square difference) of modelled, weekly average, noon-time erythemal UV *vs* measurements made at Casey Station.

	Weekly noon-time erythemal UV [mW m^{-2}] at Casey Station (n = 111)	
Modelled values	Clear-sky noon-time erythemal UV	Cloudy noon-time erythemal UV (using CMF2)
MBE	1.9	7.6
MSD	342.8	439.6
RMSD	18.5	21.0

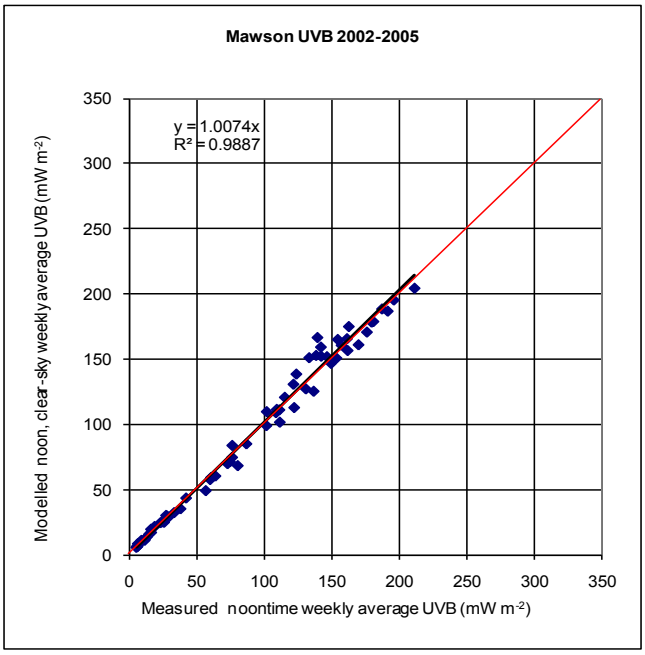

Figure 8.9: Modelled, weekly average, noon-time, clear-sky erythemal UV *vs* measured erythemal UV for Mawson Station.

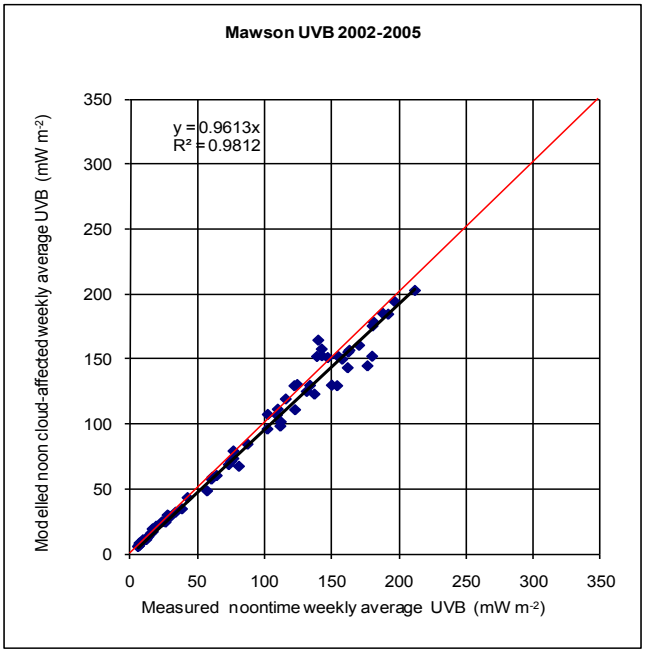

Figure 8.10: Modelled, weekly average, noon-time, cloud-affected erythemal UV (using CMF2) *vs* measured erythemal UV for Mawson Station.

Table 8.4: Results of analyses (mean bias error, mean square difference and root mean square difference) of modelled, weekly average, noon-time erythemal UV *vs* measurements made at Mawson Station.

	Weekly noon-time erythemal UV [mW m^{-2}] at Mawson Station (n = 69)	
Modelled values	Clear-sky Noon-time erythemal UV	Cloudy Noon-time erythemal UV (using CMF2)
MBE	-0.8	3.0
MSD	47.2	87.9
RMSD	6.9	9.4

The graphs for the data collected at AAD stations, Casey and Mawson (Figures 8.7 – 8.10) demonstrated that generally the measured erythemal UV values were lower than those estimated using the radiative transfer model (except for clear-sky values at Casey Station). The statistics further demonstrated that the clear-sky modelled erythemal UV values were closer to the measured erythemal UV than the cloud-affected modelled values. Even though there were fewer data points for Casey Station (n=111) and Mawson Station (n=69) than there were for Davis Station (n=229), it is beneficial to have geographic spread for the validation process. A larger dataset for Davis Station means that the data and statistics are more robust for that station.

The regression lines for clear-sky and cloud-affected weekly averages for data collected at Davis Station have coefficients of determination of approximately 0.94. Obtaining a 1-1 correspondence between measured values and those values resulting from the radiative transfer model would not be expected, when the following factors are taken into consideration:

1. Measured data are a given point on the surface of the Earth, whereas satellite data used in the RTM have a spatial resolution of 25 km x 25 km. There could be variations of surface type (and therefore albedo) within each pixel.
2. The TOMS data are available on a daily basis at approximately 100 km spatial resolution. Estimates of ozone for a particular pixel are interpolated from those (coarse) data that are available. This input parameter for the RTM is therefore only an approximation of the true value at that point.
3. The RTM is using an albedo that initially is coarse and is subsequently averaged over the surrounding pixels (taking into account the research by Smolskaia (2001)). The model does not provide the ability to take into account the variations in albedo that exist around Davis Station – the surrounding environment includes a complex mix of rock, snow and ice.

8.2.2 Using underway ship data

Underway data collected on the voyages that RSV *Aurora Austr*alis has undertaken between Australia and Antarctica are available for extraction from the Australian Antarctic Data Centre at http://data.aad.gov.au/aadc/marine_science/underway_extraction/. Data files collected between 1999 and 2005 were obtained for this project. The parameters included in these files are date and time of collection, latitude and longitude of the position of the ship, radiation measured by biometer (BIO_RAD) in MED/Hr (where MED=Minimum Erythema Dose) and temperature of biometer (BIO_TEMP) in degrees C, with an indicator of good data for the last two parameters. The time of collection of the underway data was in UTC – this was converted to local solar time, so that the erythemal UV value for local solar noon could be chosen to compare with a modelled value for that time of day. The data for the days when the ship was not within the study areas (see Figure 2.3) were deleted, leaving a total of 406 points with which to validate the modelled erythemal UV values. Table 8.5 shows the results for this set of data.

Table 8.5: Statistics for analyses (mean bias error, mean square difference and root mean square difference) of daily, noon-time, modelled erythemal UV *vs* measured underway data at noon.

	Daily noon-time erythemal UV [mW m^{-2}] (n = 406)	
Modelled values	Clear-sky Noon-time erythemal UV	Cloudy Noon-time erythemal UV (using CMF2)
MBE	36.9	-23.6
MSD	3287.4	2173.0
RMSD	57.3	46.6

Table 8.5 contains the statistics for the comparison between the erythemal UV value measured at noon and the modelled value (MBE and RMSD) for the noon position of the ship. It was expected, that as a first step, the noon and maximum values would not be that far apart, as it was noticed that most of the noon-time and maximum values were within an hour of one another, and the ship would not be expected to move far in this time. For some consecutive data points the ship registered the same latitude and longitude. This was despite the fact that even if the ship was not under power, she would still be drifting. It was decided to take the maximum erythemal UV measurement for each day, and rework the above statistics. Initially this was done for one voyage, i.e. V6 2000/01 (January – March 2001) (see Table 8.6), the statistics for which justified taking the extra time to run the software to extract the maximum erythemal UV value for all the days the ship was within the four study areas.

Table 8.7 includes the statistics for the comparison of measured maximum and modelled maximum for all the available measured, underway data. These maximum values were estimated using the position of the ship when the maximum erythemal UV was recorded. It can be seen from the tables of statistics, that calculating the maximum erythemal UV value at the

position (latitude and longitude) that the maximum erythemal UV value was measured, produces a better statistical result than that achieved when comparing it with the measured noon-time erythemal UV value.

Table 8.6: Statistics (mean bias error, mean square difference and root mean square difference) for comparison of sample daily, modelled, maximum erythemal UV *vs* measured, maximum, underway data on Voyage 6, 2000/01.

	Daily maximum erythemal UV [mW m^{-2}] for January-March 2001 (n = 55)	
Modelled values	Clear-sky maximum erythemal UV	Cloudy max erythemal UV (using CMF2)
MBE	-14.2	-2.1
MSD	1019.7	706.1
RMSD	31.9	26.6

Table 8.7: Statistics (mean bias error, mean square difference and root mean square difference) for comparison of daily, modelled, maximum erythemal UV (extracted for position of the ship when maximal erythemal UV recorded) *vs* measured, maximum, underway data.

	Daily maximum erythemal UV [mW m^{-2}] for all underway data (n = 406)	
Modelled values	Clear-sky maximum erythemal UV	Cloudy max erythemal UV (using CMF2)
MBE	-22.6	-9.3
MSD	2368.8	1705.9
RMSD	48.7	41.3

Problems associated with accuracy of erythemal UV data measured on the ship include the following:

- The UV sensors are affected at different times by shadows, e.g. from the ship's superstructure or people (from notes made under Marine Science Support Data Quality Report – V8 2000-2001);
- It cannot be guaranteed that the surface mask (as presented in the AVHRR Polar Pathfinder data), from which the albedo is estimated for a pixel, is an accurate representation of the real situation;
- The cloud mask may not accurately represent the cloud cover. The cloud mask is the 'average cloud condition' for the day, but in actual fact the cloud cover may vary throughout a day. In the Antarctic region, this method of determining cloud cover was the only option available for this research.

8.3 Maps of surface erythemal UV

In this section, maps of monthly averages of erythemal UV are presented. These were developed as described in Section 7.6 (see Appendix A for monthly plots of all parameters for 1996-2005 – naming convention is '*paramRyyyy*' where *param* = one of the parameters, i.e. . noon-time erythemal UV (uvnn), daily dose of erythemal UV (uvdt), albedo (albd), sea ice concentration (sicn), ozone (ozon), cloud modification factor (CMF2) and count of days of data (count), *R* = region and *yyyy* = year.

When reading the following sections, it should be noted that:

- there are gaps in the temporal coverage of the data (especially for June and July) in most of the sub-areas due to the lack of winter sun and sometimes due to missing satellite data; and
- it was determined that the best use of the temporal coverage of AVHRR data (July 1996 – June 2005 inclusive) was to have a 'financial year' system, whereby a 'year' would run from 1st July of the 'year' to the 30th June in the following year, thus centred on the austral, summer season. The naming convention is such, that the year given corresponds to July 1 of that year, through June 30 of the following year.

8.3.1 Visual assessment of regional parameter maps

As an initial step, a visual evaluation of the monthly parameter 'maps' (see Appendix A) and examples in Figures 8.11, 8.12, 8.13 and 8.14) resulted in the following observations for the regions.

8.3.1.1 Amery and Shackleton

For this part of the analysis, it is appropriate to discuss ozone in the Amery and Shackleton regions at the same time, because their proximity and their orientation mean that the development and dispersal of the ozone hole has similar temporal and spatial effects. Ozone depletion was more evident for the months September through November (see Appendix A and examples in Figures 8.11 and 8.12), with a smaller area affected in August. 2001 displayed lower TOC values for larger areas of the region. 2002 demonstrated higher ozone values than the nine-year average.

The maps of sea ice concentration (see Appendix A and example in Figure 8.13) demonstrate the seasonal decay and growth of sea ice with higher concentrations and greater sea ice extent in winter, and lower concentrations and reduced sea ice extent in summer. The Amery sea ice extents for January and February 2000, 2002 and 2003 were less than the nine-year average. The opening and closing of the Prydz Bay and Drygalski Island polynyas (see Figure 2.3) are evident in the maps of sea ice concentration. The Drygalski Island polynya (see Figure 2.3) opened later in the summer in 2001 than for other years.

Despite the ozone hole developing in early spring, the highest levels of erythemal UV do not occur in the sea ice zone in the Amery and Shackleton regions until between November and January, when the polar vortex has disintegrated, and allowed the lower TOC values to spread towards the coast and sea ice zone. The maps of ozone and erythemal UV (see examples, Figures 8.12 and 8.14) demonstrated that the areas of high values of erythemal UV and the low values of ozone do not necessarily 'match' spatially, although discussion about the various sub-areas in Section 8.3.4 points out that the peaks/dips in the plots of ozone for the various sub-areas often correspond to cycles of dips/peaks in the plots of erythemal UV. The fact that this 'rule' does not always apply, is because other factors (for example, cloud amount and varying albedo due to changes in sea ice concentration), as well as ozone, influence levels of erythemal UV.

8.3.1.2 Dalton and Mertz

In this section, it is appropriate to discuss the Dalton and Mertz regions at the same time, as the development and dispersal of the ozone hole has similar effects in both these regions. Ozone depletion was not as evident for the spring and early summer months, as it was in the Amery and Shackleton regions, and even when the ozone hole was present, its effect was more continental rather than over the sea ice zone (see Appendix A and Figure 8.43). 2002 had particularly high levels of TOC compared to other years and the nine-year mean.

The sea ice extent was greater for the Dalton region for August to October in 1996, 1997, 1998, 1999 and 2003 than for the other years and the nine-year average. In the Mertz region, the sea ice concentration was less for 1999 than for other years and the nine-year mean. In the Mertz and Dalton regions, both the sea ice concentration and sea ice extent were less for January to March in 2001 than for other years and the nine-year mean.

For the Mertz region, the highest erythemal UV levels occurred in December and January. The highest erythemal UV levels occurred in November to January in the Dalton region. The development of the ozone hole as presented in Figure 8.43 demonstrates how low TOC values occur earlier in the Dalton region than in the Mertz region.

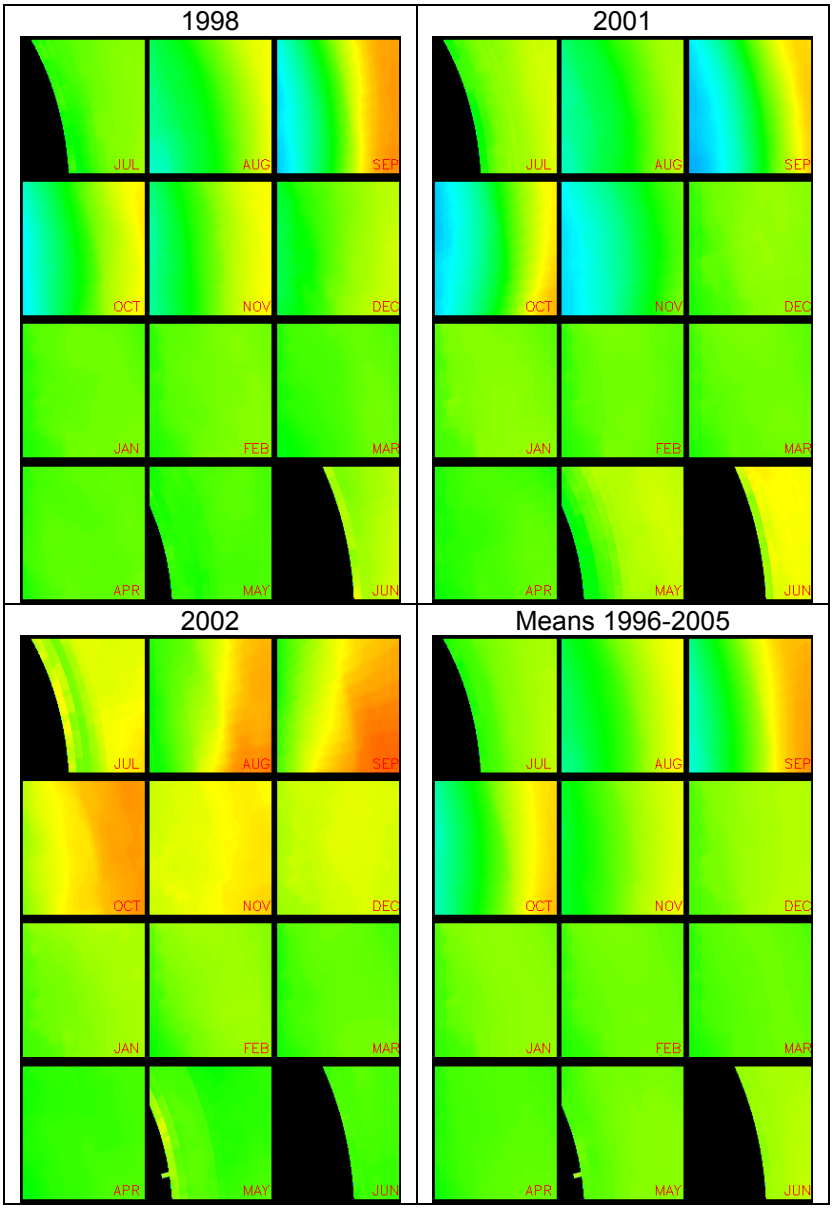

Figure 8.11: Monthly plots of ozone for Amery region, using colour bar for ozone (0-425DU).

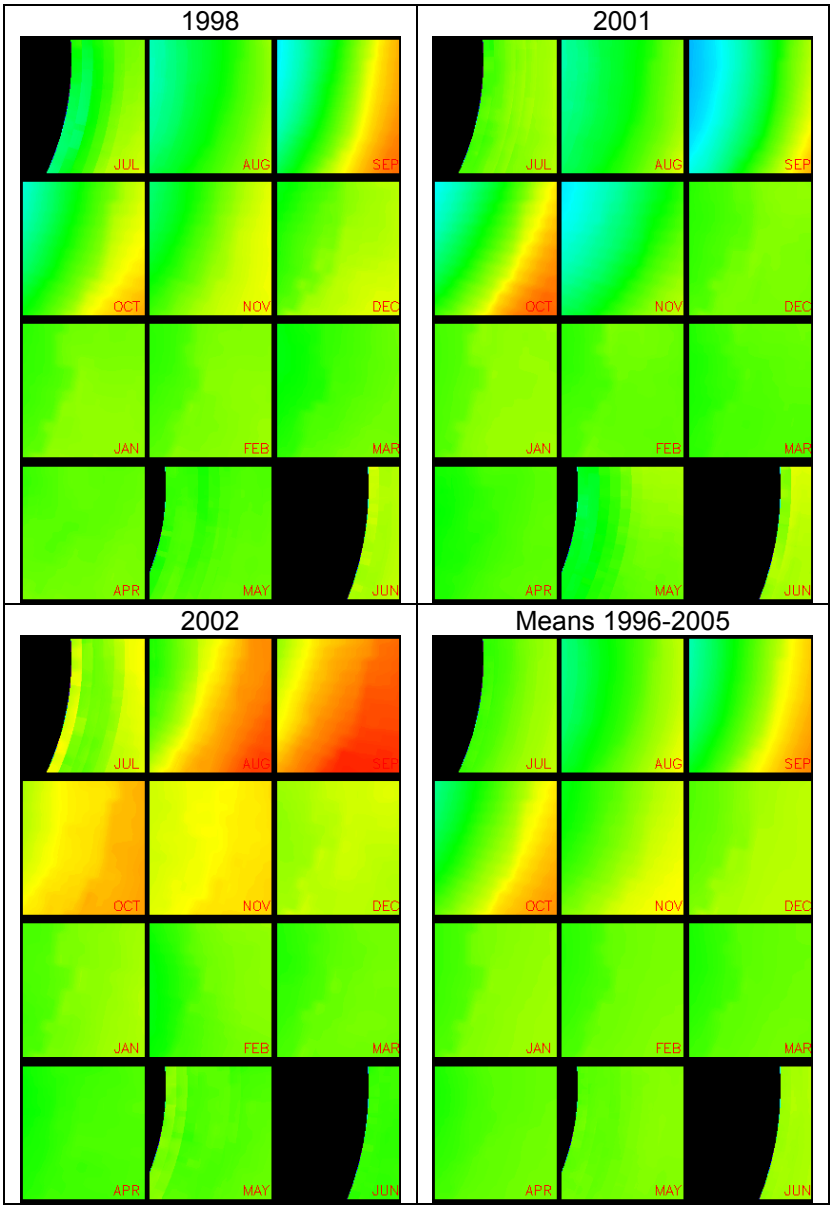

Figure 8.12: Monthly plots of ozone for Shackleton region using colour bar for ozone (0-425 DU).

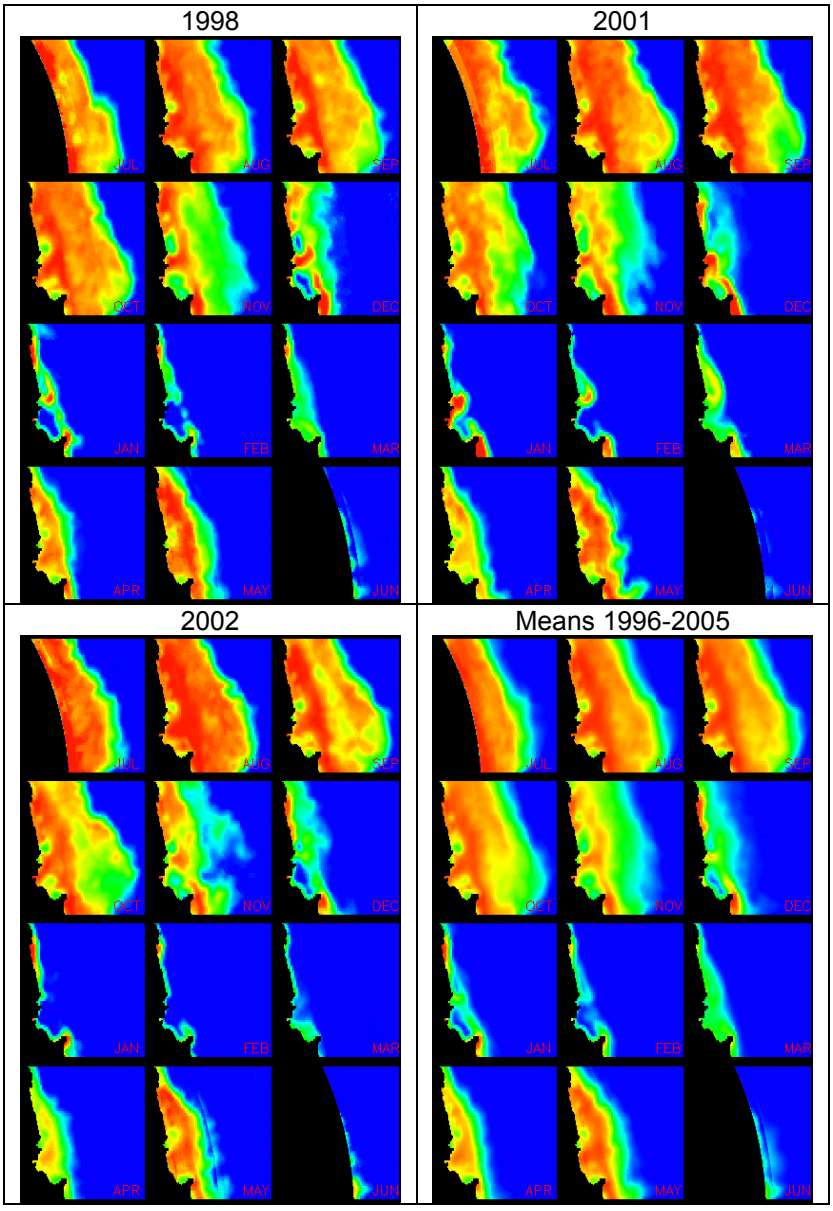

Figure 8.13: Monthly plots of sea ice concentration for Amery region using colour bar for sea ice concentration (0-100%).

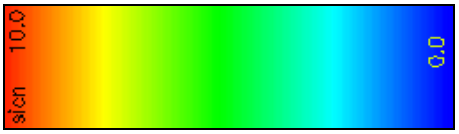

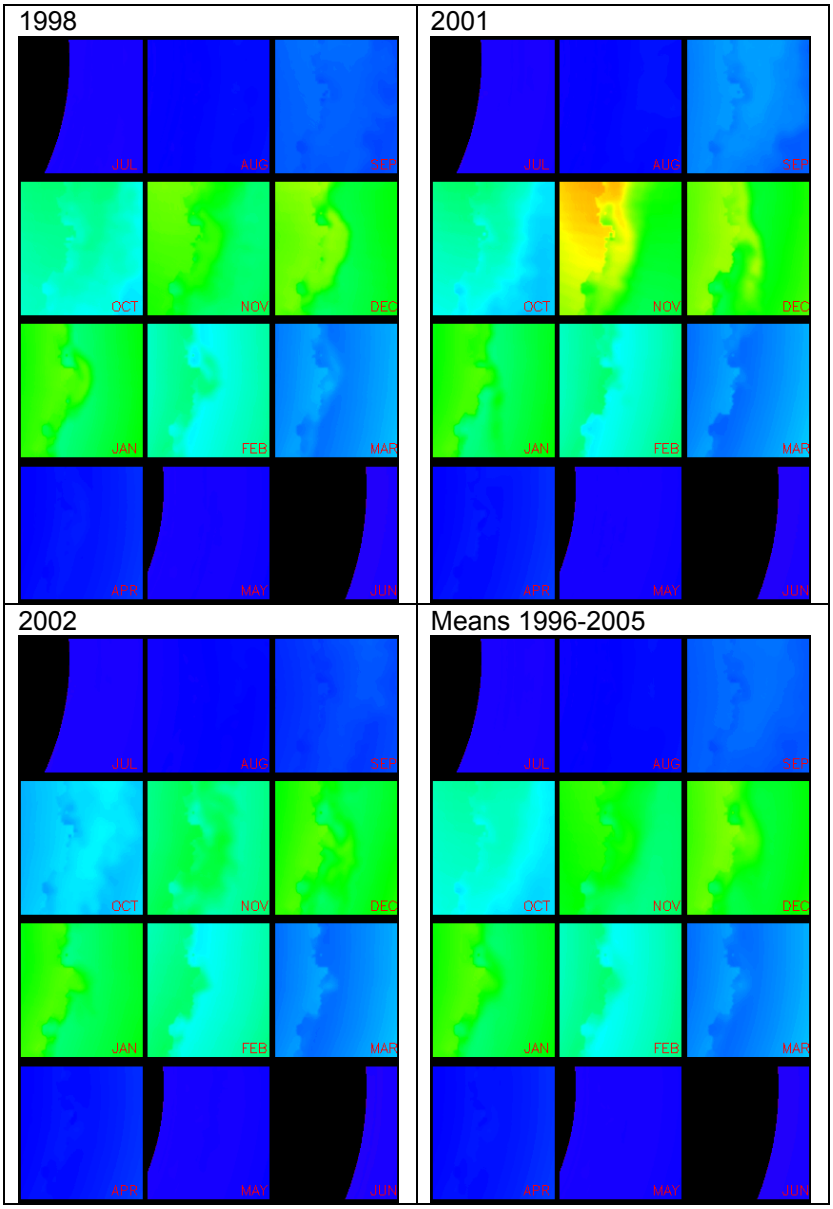

Figure 8.14: Monthly plots of noon-time erythemal UV for Shackleton region using colour bar for noon-time erythemal UV (0-300 mW m^{-2}).

8.3.2 Case study sub-areas

For a more detailed temporal evaluation of the averaging process, four sub-areas from each of the four regions (total 16 sub-areas) were selected from open ocean, marginal ice zone (MIZ), sea ice zone and polynyas. Seven of these (see details below) were chosen to demonstrate the relationships between the various parameters under different surface conditions. The numbering

of the sub-areas simply reflects their position in the original set of sixteen that were chosen to trial the software.

8.3.2.1 Amery No. 1

This sub-area (centred at -63.68º S, 82.30º E) is 5 x 5 pixels (bottom left (160, 35), top right (165, 40)), is in the MIZ off Davis Station (which is in Princess Elizabeth Land) (see Figure 2.3) (Figure 8.15, left panel). Each pixel is 5 km x 5 km.

8.3.2.2 Amery No. 3

This sub-area (centred at -67.47º S, 76.90º E), 5 x 5 pixels (bottom left (70, 70), top right (75, 75)), is in the Prydz Bay polynya (also known as Davis polynya) (see Figure 2.3) (Massom *et al.* 1998a; Barber and Massom 2007) (Figure 8.15, right panel). Barber and Massom (2007) give upwelling warm water and grounded icebergs as the formative mode for this polynya. The areal extent and location of this polynya varies greatly, indicating that it is influenced by variable synoptic forcings (Massom *et al.* 1998a).

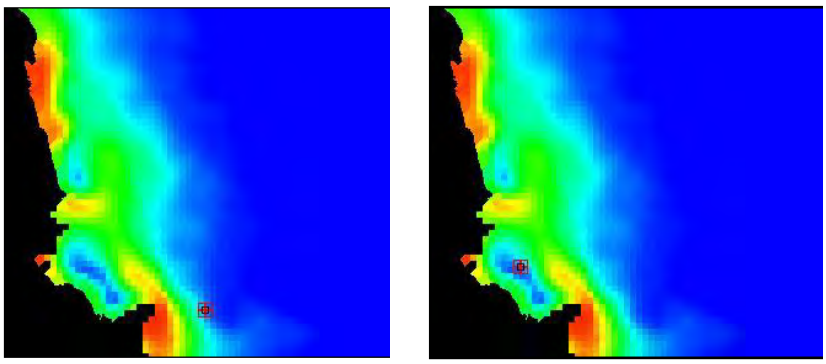

Amery No. 1 Amery No. 3

Figure 8.15: Positions (marked as) of the selected sub-areas in Amery region (using December sea ice concentration as a background). Dimensions of the Amery region are 341 x 283 pixels.

8.3.2.3 Dalton No. 1

This sub-area (centred at -64.82º S, 127.15º E) is 5 x 5 pixels (bottom left (105, 105), top right (110, 110)). It is in the SIZ off Porpoise Bay, Wilkes Land (see Figure 2.3) (Figure 8.16, left panel).

8.3.2.4 Dalton No. 4

This sub-area (centred at -54.84º S, 129.53º E) comprises 5 x 5 pixels (bottom left (190, 5), top right (195, 10)) in open water off Terre Adélie (see Figure 2.3) (Figure 8.16, right panel).

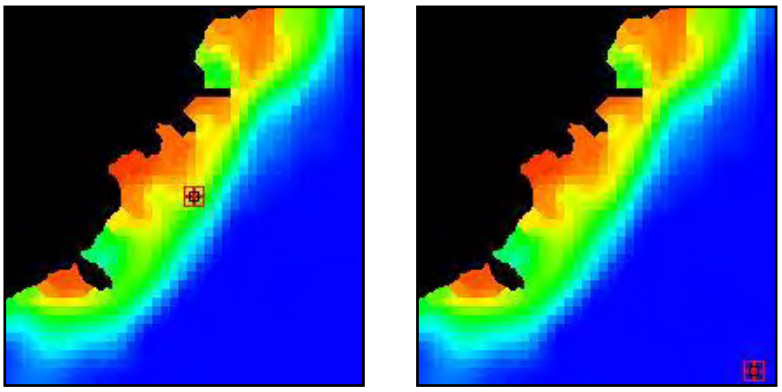

Dalton No. 1 Dalton No. 4

Figure 8.16: Positions of the selected sub-areas in Dalton region (using December sea ice concentration as a background). Dimensions of the Dalton region are 205 x 216 pixels.

8.3.2.5 Mertz No. 1

This sub-area (centred at -67.96º S, 152.27º E) is 10 x 10 pixels (bottom left (160, 140), top right (170, 150)). It is in SIZ (but very close to Cape Hudson polynya and Cook Ice Shelf) (see Figure 2.3) off George V Land (Figure 8.17, left panel).

8.3.2.6 Mertz No. 2

This sub-area (centred at -67.6º S, 160.35º E) comprises 10 x 10 pixels (bottom left (100, 105), top right (110, 115)) in SIZ between the Continent (George V Land) and the Balleny Islands (see Figure 2.3) (Figure 8.17, right panel).

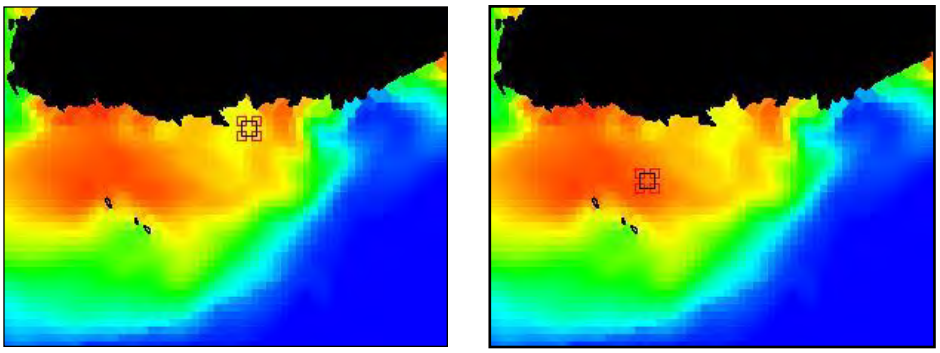

Mertz No. 1 Mertz No. 2

Figure 8.17: Positions of the selected sub-areas in Mertz region (using December sea ice concentration as a background). Dimensions of the Mertz region are 299 x 227 pixels.

8.3.2.7 Shackleton No. 4

This sub-area (centred at -65.44º S, 93.66º E) comprises 5 x 5 pixels (bottom left (95, 190), top right (100, 195)) in Drygalski Island polynya off Willhelm II Land (see Figure 2.3) (Massom *et al.* 1998a; Barber and Massom 2007) (Figure 8.18). A north-south oriented coastline, being in the

lee of off-shore islands and the presence of grounded icebergs, are all contributors to the formation of this polynya (Barber and Massom 2007).

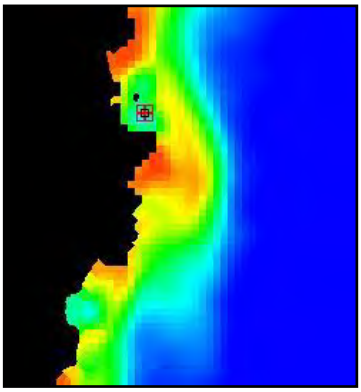

Shackleton No. 4

Figure 8.18: Position of the selected sub-area in Shackleton region (using December sea ice concentration as a background). Dimensions of the Shackleton region are 246 x 268 pixels.

8.3.3 Assessment of relationships between parameters

Plots of monthly mean values (see Appendix A and examples Figures 8.19, 8.20, 8.21 and 8.22) resulted in the following observations for the sub-areas within the regions. As in Section 8.3.1, comments will be combined for Amery plus Shackleton, and Dalton plus Mertz, because of their proximity and the similar temporal and spatial effects of the development and dispersal of the ozone hole.

8.3.3.1 Amery and Shackleton

For most months for Amery nos. 1 and 3, and Shackleton no. 4, the average TOC is approximately 300 DU (Appendix A and Figures 8.19 and 8.20). The exceptions are August and September for Shackleton no. 4 (means of 270 DU) and August to November for Amery no. 3 (means 230-270 DU). August to December have a wider spread of values either side of the mean TOC across the years (approximately ±60-80 DU), whereas other months have a spread of approximately ±10-20 DU. This is indicative of the widely varying values of TOC because of the development and subsequent dispersal of the ozone hole during spring/early summer. Outliers are values that are more than 2 standard deviations greater or less than the mean (as per Table 8.8). Outliers for various months and years can be seen in the plots of monthly TOC (see Appendix A and examples in Figures 8.19 and 8.20).

For September to November in 2001 and 2002, TOC values were extreme (although at opposite ends of the range), and even when the values were not outside the 2 standard deviation range, they were still higher/lower for 2002/2001 than values for other years – this phenomenon is demonstrated by the ozone maps (see Figures 8.11 and 8.12).

The siting of the sub-areas determines firstly, whether there is sea ice and if there is sea ice (i.e. it is not in a polynya or open water), what the average sea ice concentration will be across the months. The plots of monthly sea ice concentration (Appendix A and examples at Figures 8.13 and 8.21) show that it was indeed very variable across the years and sub-areas. The average sea ice concentration for the sub-areas in Amery and Shackleton regions for winter/early spring was approximately 80%. As already noted (Section 8.3.2.2), variable synoptic forcings can greatly influence the areal extent and location of a polynya (Massom *et al.* 1998a).

Over a year, the months July-October and April-May demonstrated less spread in sea ice concentration (approximately ±5%) (unless the sub-area was situated in a polynya) either side of the average, but other months varied by as much as ±40%. An example is May in Amery no. 1 (see Appendix A). This sub-area is in a polynya, and the wide variability is attributed to variations in meteorological conditions from year to year, which determine the opening and closing times of a polynya (Zwally *et al.* 1985) and ice production within the polynya (Massom *et al.* 1998a).

The range of erythemal UV values extends from ~3.25±0.25 mW m^{-2} in winter, to ~150±50 mW m^{-2} in summer (see Appendix A and example at Figure 8.22 and Table 8.10), with outliers (see Table 8.8) outside these ranges.

September and February in 2001 in Shackleton no. 4 were only just within the upper boundary of 2 standard deviations. The number of months for which 2001 has been noted as being 'out of the ordinary' (i.e.11) (Tables 8.8 and 8.9) indicates something exceptional about the environmental conditions for 2001 (this is discussed later in Section 8.3.4.1).

Table 8.8: Table of outliers (i.e. values that were outside the 2 standard deviation range) for parameters for sub-areas in Amery and Shackleton regions.

	Amery no.1	**Amery no. 3**	**Shackleton no. 4**
Ozone >2SD	Nil	Sep-Oct 2002	Jul-Sep 2002
Ozone <2SD	Nov 2001	Nil	Nov 2001
Sea ice conc >2SD	Apr 1997 Jan 1998	Dec 2001	Dec-Feb 2001 Jul 2002
Sea ice conc<2SD	Nov 2004	Nil	Nil
Noon erythemal UV >2SD	Dec 1998 Sep and Nov 2001 Apr 2004	Nov 2001 Apr 2004	Nov – Jan 2001
Noon erythemal UV <2SD	Nil	Oct 2002	Nil

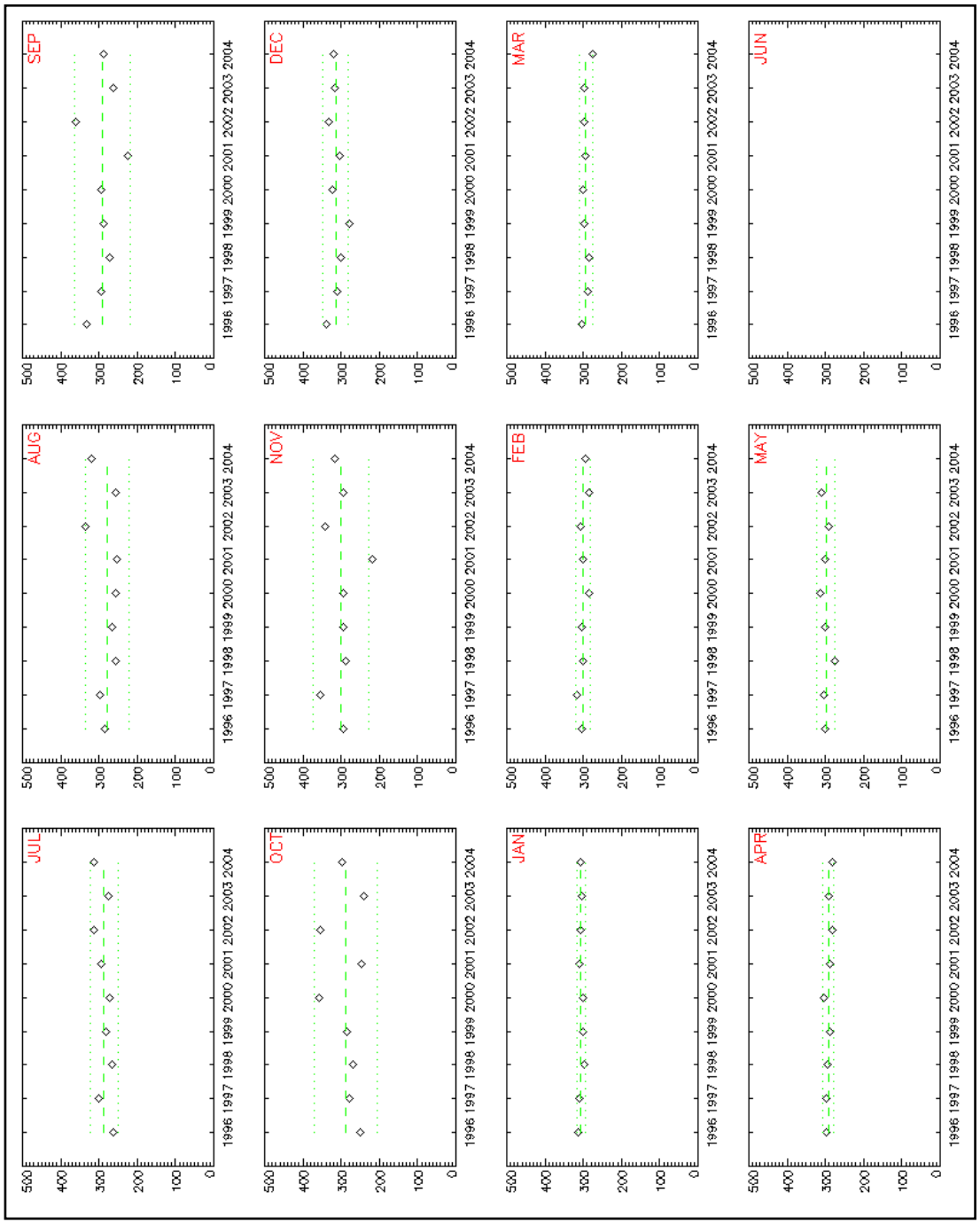

Figure 8.19: Monthly plots of TOC for the years of the project for Amery No. 1.

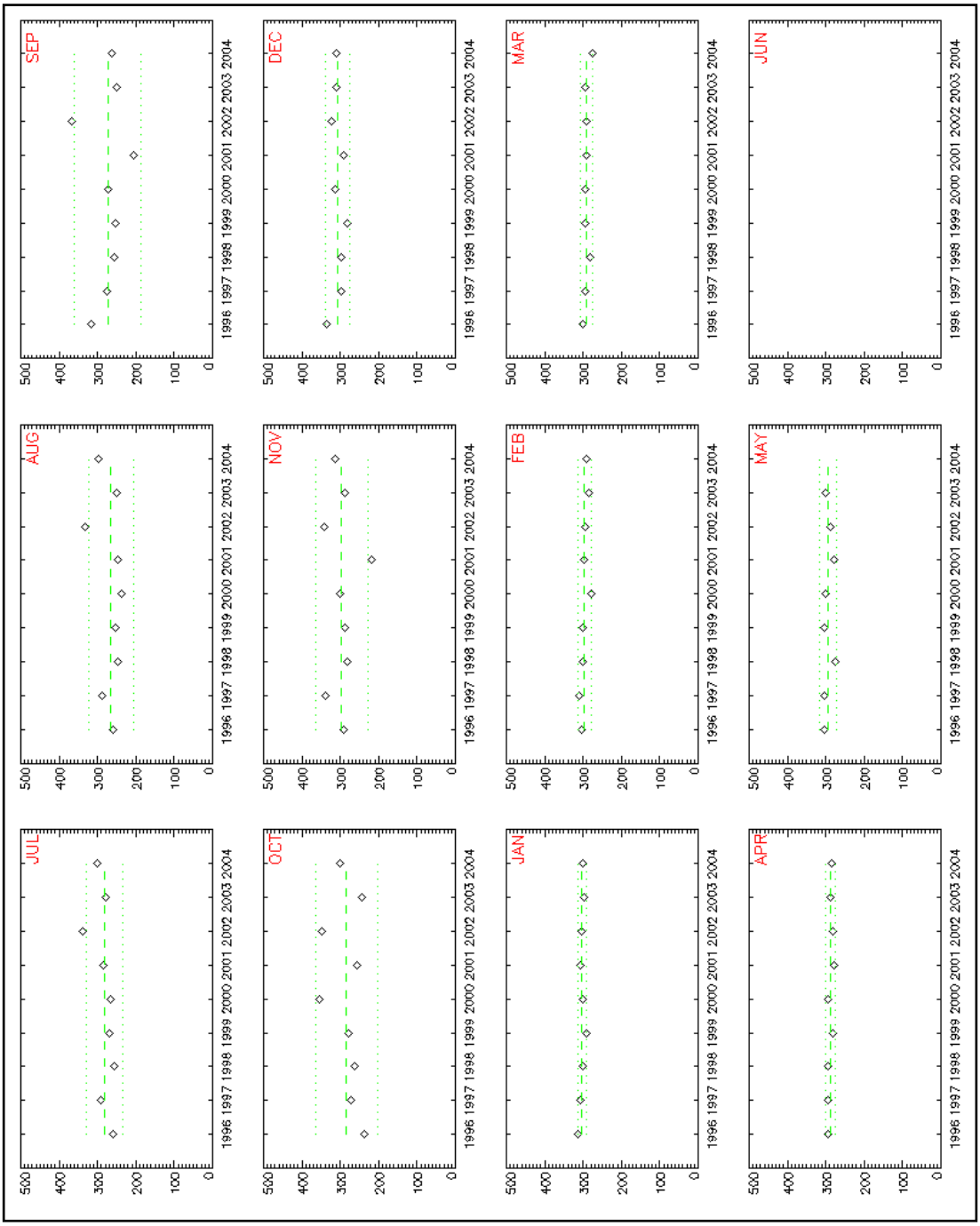

Figure 8.20: Monthly plots of TOC for the years of the project for Shackleton No. 4.

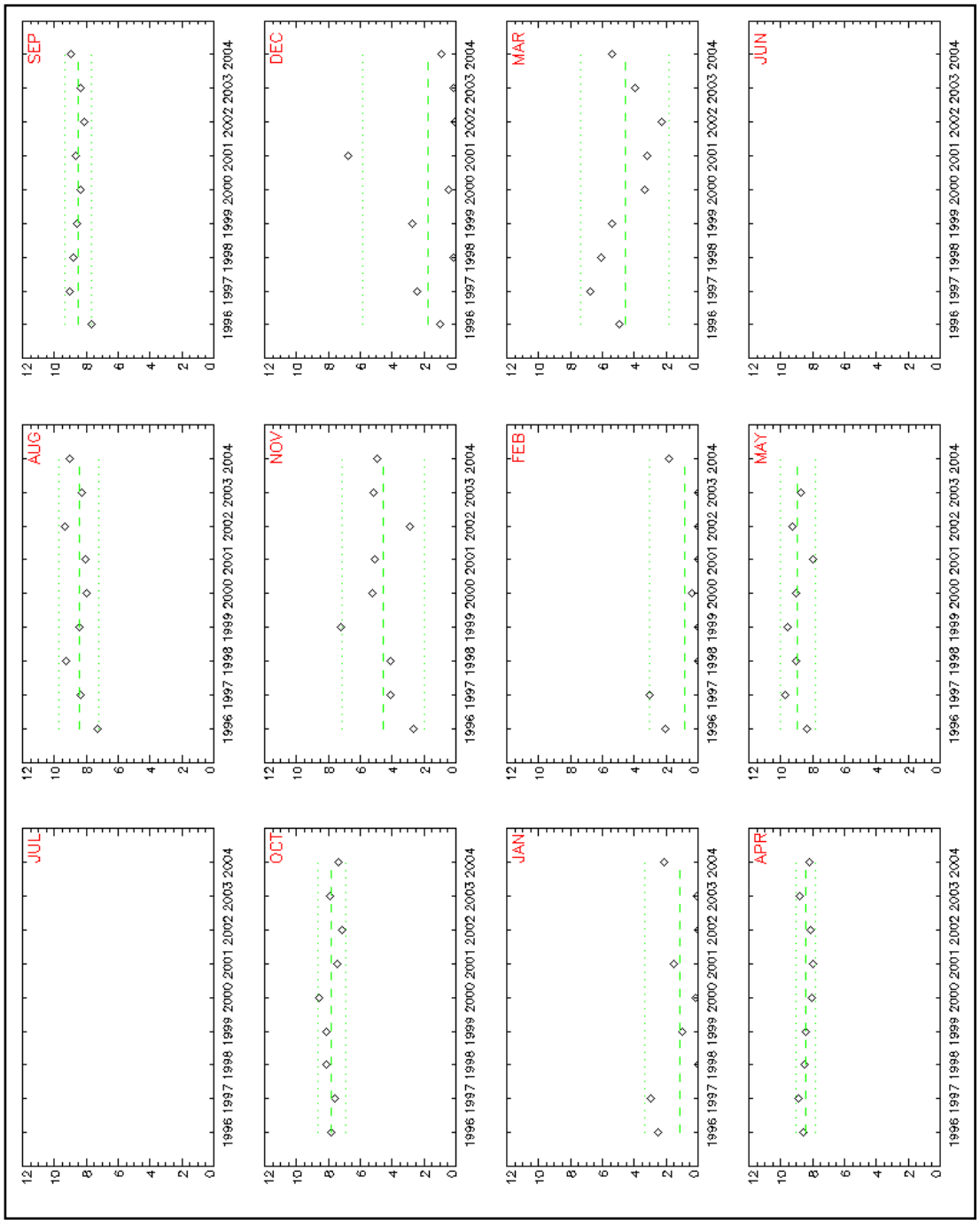

Figure 8.21: Monthly plots of sea ice concentration for the years of the project for Amery No. 3.

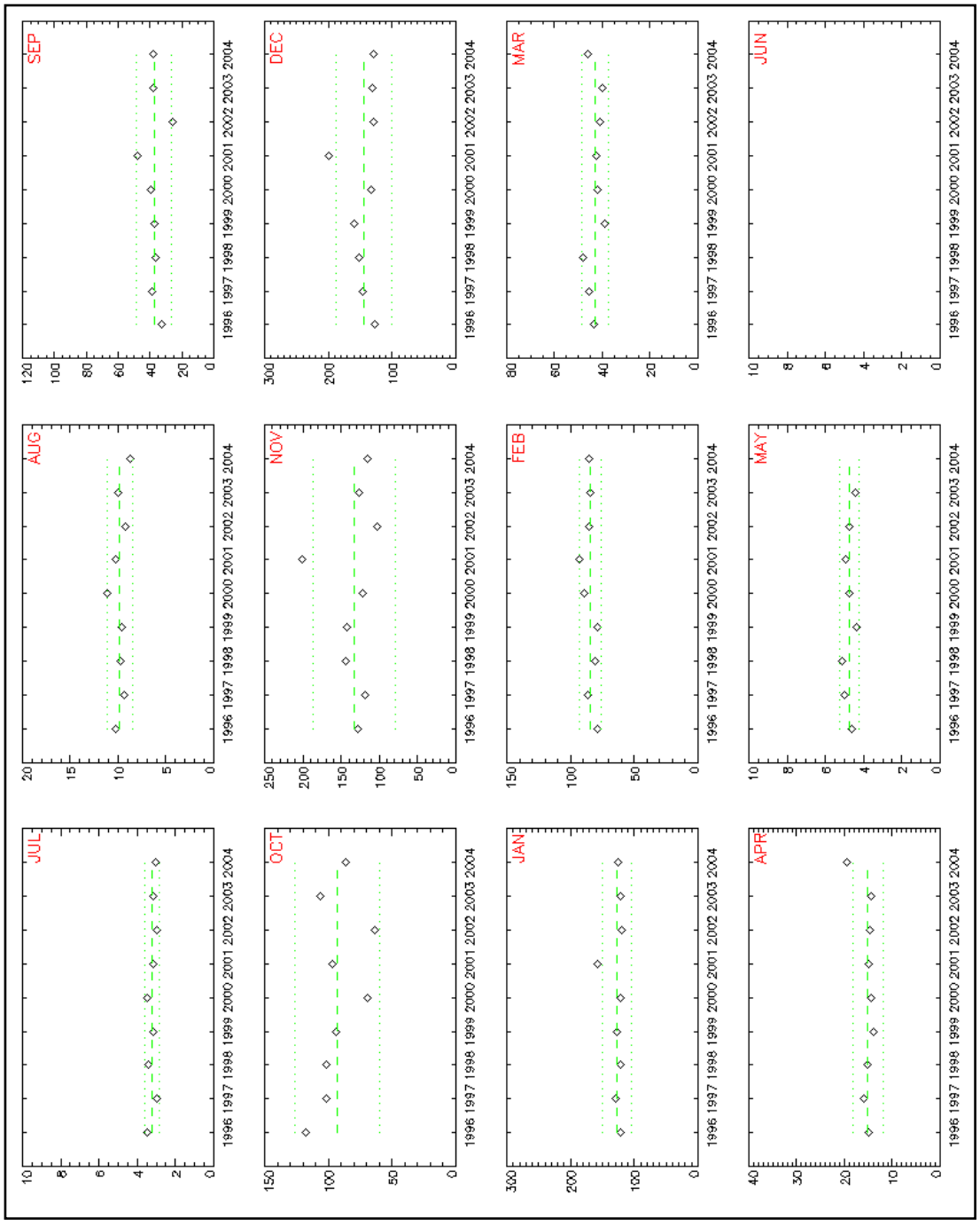

Figure 8.23: Monthly plots of UVB for the years of the project for Shackleton No. 4.

8.3.3.2 Dalton and Mertz

The Dalton and Mertz regions display similar patterns of development and dispersal of the ozone hole. As discussed in Section 8.3.1.2, ozone depletion was not as evident for the spring and early summer months as it was in the Amery and Shackleton regions, and even when the ozone hole was present, its effect was more continental rather than over the sea ice zone (see Appendix A). The plots of monthly TOC (see Appendix A) illustrate outliers (more than 2 standard deviations greater or less than the mean), as per Table 8.9.

The average sea ice concentration for Dalton no. 1, and Mertz nos. 1 and 2 is closer to 100% for the winter/early spring months, compared with the lower average of ~80% for the Amery and Shackleton sub-areas. Dalton no. 4 has no sea ice data as it is in open water, as confirmed by examination of the monthly plots of sea ice concentration for the temporal coverage of the project. Details of outliers are given in Table 8.9.

The range of erythemal UV values extends from ~3.5±0.5 mW m^{-2} in winter, to ~160±30 mW m^{-2} in summer (see plots of erythemal UV in Appendix A and minima and maxima in Table 8.10). Details of outliers are in Table 8.9.

Table 8.9: Outliers (i.e. values that are more than 2 standard deviations greater or less than the mean) for parameters and sub-areas in Dalton and Mertz regions.

	Dalton no.1	**Dalton no. 4**	**Mertz no. 1**	**Mertz no. 2**
Ozone >2SD	Dec 1998 Oct 2000 Aug-Sep 2002	Jun 1997 Jul 1998 Oct 2000 Aug-Sep 2002	Aug-Sep 2002	Aug-Sep 2002
Ozone <2SD	Jul 1998 Nov 2001	Nil	Nil	Nil
Sea ice conc >2SD	Mar 1998	Nil	Nil	Nil
Sea ice conc<2SD	Dec 2001	Nil	Nov-Dec 1999 Feb-Mar 2001	Oct-Nov 1999 Jan 2001
Noon erythemal UV >2SD	Jul 1998 Aug 2000 Apr 2004	Jul 19 Aug 2000 Apr 2004	Oct 1997 Aug 2000 May 2002 Apr 2004	Aug 2000 Apr 2004
Noon erythemal UV <2SD	Mar 2003	May 2004	Sep2002	Sep 2002

8.3.3.3 Comparison of erythemal UV values for sub-areas

Minimum and maximum erythemal UV values for all areas are given in Table 8.10. It can be seen from Table 8.10 that minimum erythemal UV values occur in the winter months for all sub-areas. The Amery sub-areas have maximal erythemal UV values in November and the Shackleton sub-area has maximal erythemal UV in December. Dalton and Mertz sub-areas have maximal values in summer.

Table 8.10: Minimum and maximum erythemal UV values for all sub-areas.

Name of sub-area	Approx. min. [mW m^{-2}]	Approx. max. [mW m^{-2}]
Amery no. 1	4.5 ± 0.5 (in July)	150 ± 50 (November)
Amery no. 3	4.0 ± 0.5 (in May)	140 ± 60 (November)
Shackleton no. 4	3.25 ± 0.25 (in July)	150 ± 40 (December)
Dalton no. 1	4.0 ± 0.5 (in July)	160 ± 30 (December)
Dalton no. 4	3.5 ± 0.5 (in June)	150 ± 10 (January)
Mertz no. 1	4.0 ± 0.25 (in May)	150 ± 40 (December)
Mertz no. 2	4.0 ± 0.5 (in May)	150 ± 25 (December)

8.3.4 Case studies – discussion

8.3.4.1 Assessment of plots of parameters 1996-2005

Another analysis to assess the monthly averaged values for the parameters, ozone, cloud modification factor, sea ice concentration and noon erythemal UV values was undertaken using the software described in Section 7.6. Time series of parameter values across the months for each year of the temporal coverage of the project, were produced for some of those sub-areas, depicted in Figures 8.15 to 8.18 in Section 8.3.2.

Some facts in relation to the plots are applicable to all sub-areas, whereas other features are unique to a particular sub-area. As an example of a general phenomenon, the plots of satellite-derived, cloud modification factor (CMF2) (example Figure 8.23) demonstrate that there is little variability across the years or across the sub-areas for this parameter. The parameter CMF2 for most months of most years demonstrated that the skies were rarely clear. Atmospheric components (aerosols, ozone, water vapour and other gases) reduce the intensity of solar radiation reaching the Earth's surface by different amounts in different spectral ranges (Piacentini *et al.* 2002). Clear sky therefore allows more radiation to reach the surface than if cloud was present. However, higher levels of UVB radiation are also possible under cloudy skies due to the "radiation paradox" (Ambach 1974), where higher levels of UVB over an ice/snow covered surface are caused by multiple reflections between the high-albedo surface and the under surface of the cloud (see Section 3.2.5). The lack of detail in the cloud data makes it difficult to have confidence in attributing any changes in levels of UVB to this parameter. It was noted by Badosa *et al.* (2007) that under cloudy conditions (which represent most of the time in many sites), very much larger errors are expected in modelling since the cloud optical parameters needed as input information are hardly ever available. This is especially true in the Antarctic environment.

The plots of ozone data (example Figure 8.24) for all sub-areas display a springtime variability in ozone that depends on the development and movement of the ozone hole and the timing of the annual break up of the polar vortex. This is demonstrated by the large error bars for springtime months on the plots of the 9-year average, whereas the months December to May are more convergent (close to 300 DU) with smaller error bars. The year 2002 has consistently higher ozone values (~320-410 DU) in early spring for all sub-areas (see Figure 8.43e), while 2000 has similarly high ozone values (~250-420 DU) late spring for all sub-areas except for those in the Amery region (360-380 DU). The ozone values for spring 2001 are consistently lower for all sub-areas except for those in the Mertz region. This is explained by Figure 8.43, which shows that the ozone hole does not extend far enough over Oates Land, George V Land and Terre Adélie (see Figure 2.3) very often to affect any of the Mertz sub-areas off the Antarctic coast with low ozone values. Figure 3.2 shows the ozone hole areas (TOC ≤ 220 DU) 1999-2008. It should be noted that despite having a mean ozone value for a particular month, daily

measurements could fluctuate considerably within that month. Stamnes *et al.* (1990) presumed that these fluctuations are caused primarily by the motion of the polar vortex. Out of those years shown, the ozone hole for 2001 is the largest and forms the earliest while the ozone hole in 2002 is the smallest – a phenomenon that is explained in Section 3.1.4.3.

Sea ice concentration typically decreases rapidly in October through to December or January (spring-time melt), and increases rapidly from February or March onwards, with a period of open water between these times depending on the site e.g. heavy sea ice does not melt enough to become open water, but it is possible in the MIZ or in a polynya (example Figure 8.25).

The plots of noon-time erythemal UV display a 'normal' curve across a year with little variability between July and September and between January and June. The relatively large error bars on the 9-year average plot depict the variability between October and December caused by the erythemal UV levels fluctuating widely for particular years (Figure 8.26, left panel) as a result of changing levels of ozone, sea ice concentration and possibly cloudiness.

In the following discussion (and in Section 8.3.1), 2001 is frequently mentioned as displaying anomalous parameter values when compared to those of other years. Massom *et al.* (2006) wrote of exceptional sea ice conditions from September 2001 to February 2002 resulting from a strongly positive atmospheric pressure anomaly in the South Atlantic, coupled with strong negative anomalies in the Bellingshausen-Amundsen and southwest Weddell Seas (see Figure 2.3). Moreover, Massom *et al*. (2004) showed that unusual atmospheric circulation conditions involving blocking-high activity in the south Tasman Sea led to strong incursion of relatively warm, moisture-laden air over the Adélie Land coast – and unusual snowfall events deep inland on the East Antarctic Ice Sheet. The abnormal sea ice conditions (and therefore abnormal erythemal UV values) noted in 2001 of this study might be attributable to the same atmospheric/meteorological conditions as those experienced for the temporal coverage of the studies by Massom *et al.* (2004, 2006).

R.A. Massom (pers. comm., 2010) noted that as a general rule, there has been a strong tendency to consider the large-scale role of sea ice mainly in terms of its areal extent, while largely neglecting other (additional) sea ice parameters and processes that may be equally, if not more important, to the ecology of krill and its prey, in addition to other key ecological assemblages. A description of events in the West Antarctic Peninsula region in October 2001, through February 2002, underlines the complexity of the system, and the potential dangers involved in equating biological activity to ice extent alone (see Massom *et al*. (2006) for details). These abnormal conditions had a profound effect on regional sea ice and ocean conditions, and thus marine ecology.

8.3.4.2 Amery No. 1

Noon-time erythemal UV for 2001 (see left panel in Figure 8.26) peaks in November at 215 mW m^{-2} – this is a higher value than any of the other 8 years. This correlates well with the ozone

value of 220 DU, and sea ice concentration of 65% for the same time that year. The cloud modification factor for November 2001 was 0.9, so this would also have driven the erythemal UV values higher. Ozone values were also low in spring 2003 but at the same time, the sea ice concentration was only 40% and CMF2 value indicated cloudier skies. These two parameter values have driven the lower erythemal UV values for 2003 than for 2001.

The plot of ozone (Figure 8.24) shows that 2001 also had a low value in September (230 DU) before it rose slightly in October, and dropped again in November to 220 DU. This is explained by the TOMS images (Figures 8.43b and 8.43c), which show the ozone hole bulging further westward towards the Haakon VII Sea (see Figure 2.3) (thus shrinking away from the Amery region) towards the end of September and into October. The ozone hole then starts to disperse allowing low ozone values to enter the Amery region again (Figure 8.43d) in November.

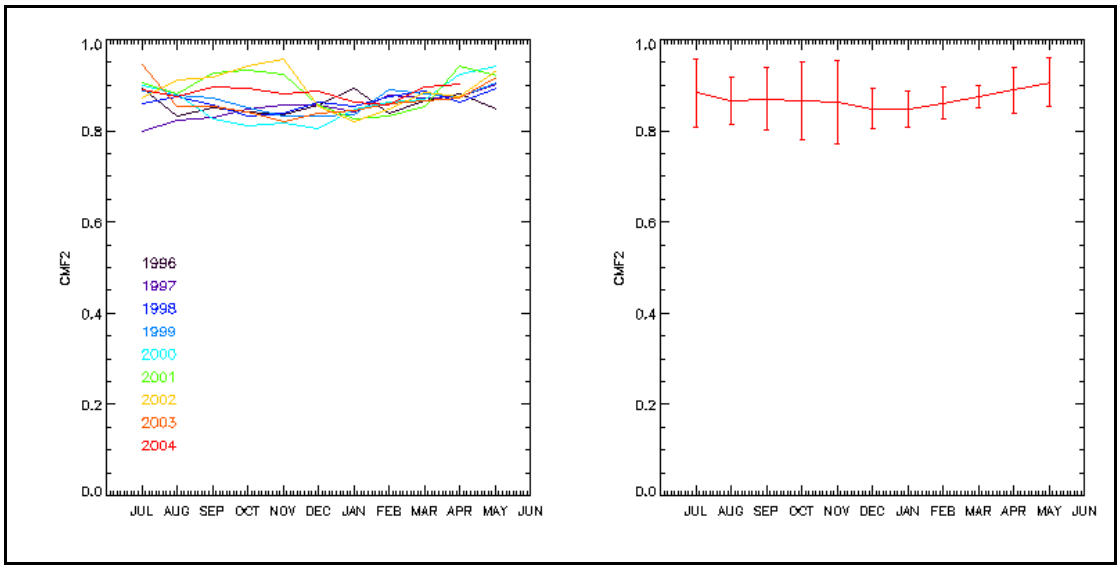

Figure 8.24: Plots of CMF2 for Amery no. 1 (Left panel – all nine years, Right panel – year average plus error bars – 2 s.d.).

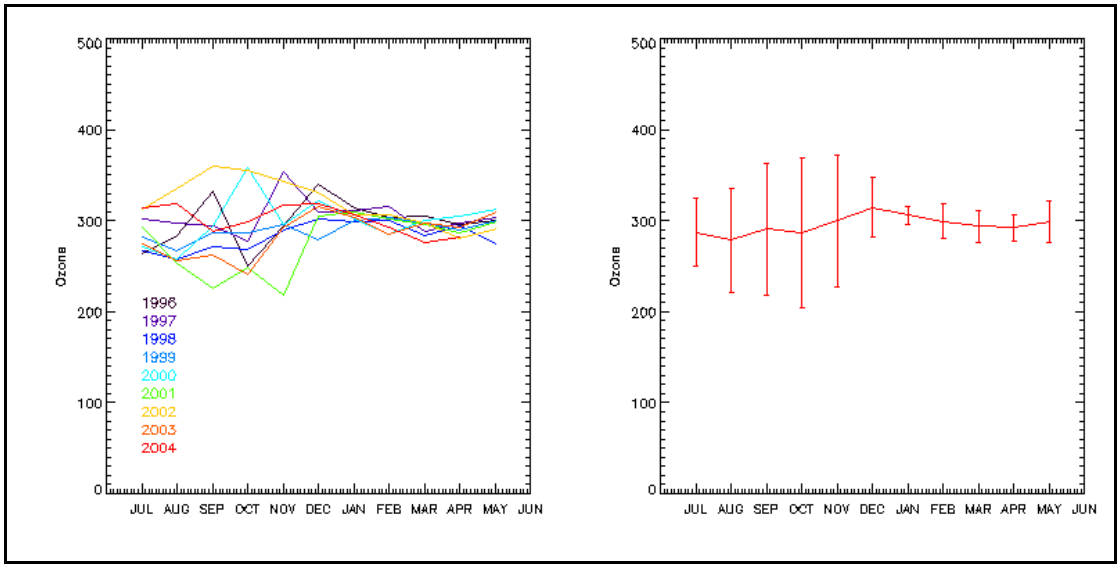

Figure 8.25: Plots of TOC for Amery no. 1 (Left panel – all nine years, Right panel – 9-year average plus error bars – 2 s.d.).

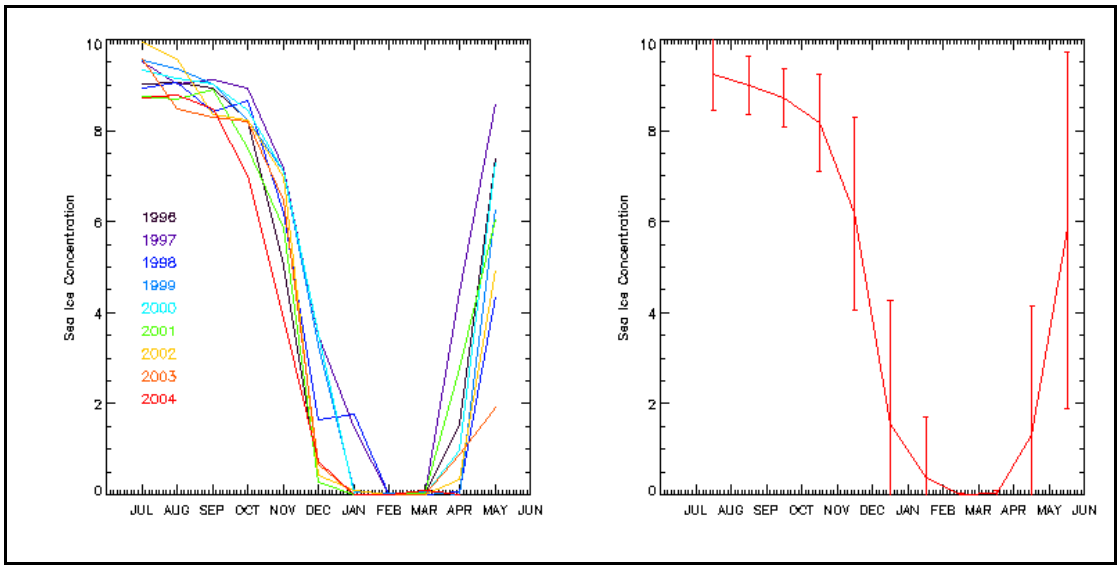

Figure 8.26: Plots of sea ice concentration for Amery no. 1 (Left panel – all nine years, Right panel – 9-year average plus error bars – 2 s.d.).

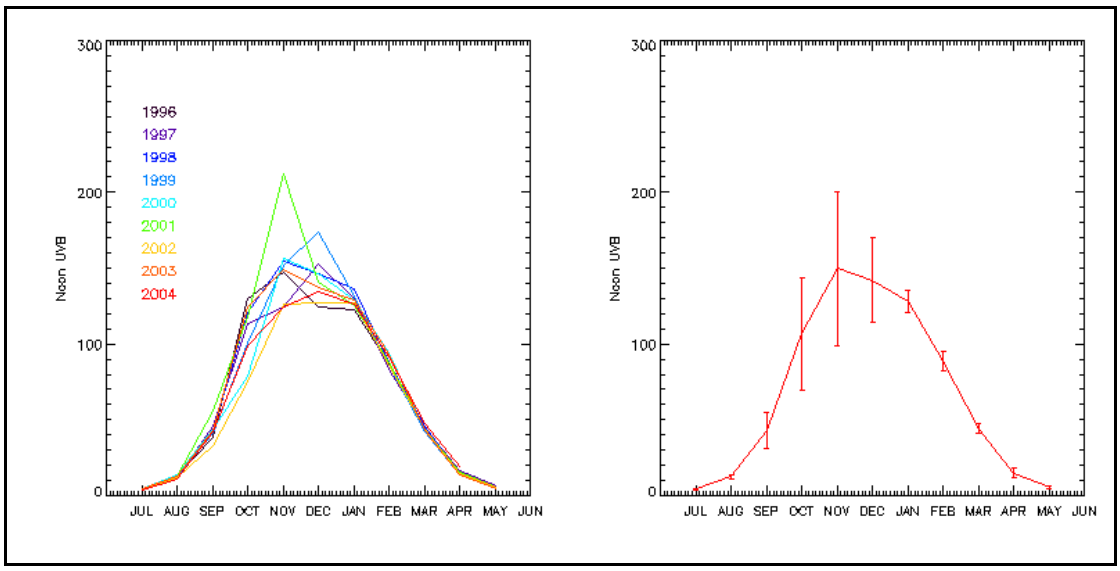

Figure 8.27: Plots of noon-time erythemal UV for Amery no. 1 (Left panel – all nine years, Right panel – 9-year average plus error bars – 2 s.d.).

8.3.4.3 Amery No. 3

Sub-area Amery No. 3 is closer to the continent, and erythemal UV levels should thus be more affected by lower values of ozone (180 DU) in September to November, 2001 (Figure 8.29), because of the positioning of the ozone hole. In spring, the ozone hole is constrained by the polar vortex and is thus 'held' in position over the Continent. As the polar vortex breaks up, the ozone hole disperses over the Antarctic coasts. The lower ozone values for spring in this sub-area are borne out by the plot of the 9-year average (Figure 8.27 – right panel) as compared to the 9-year average plot for Amery No. 1 (Figure 8.24 – right panel). August to December 2002 had unusually high ozone values (Figure 8.27 – left panel) (see explanation 8.3.4.1 above). An example of a spring 2002 TOMS image is shown in Figure 8.43e.

Amery No. 3 is in a polynya and by November 2001 the sea ice concentration had dropped to 50%, but it abnormally increased to 65% in December before continuing to decrease to the lowest value in February. This maintained a relatively high albedo for spring to early summer, which helped drive the higher erythemal UV levels for this period. The polynya was open from December to March in 2002, thus lowering the regionally-averaged albedo for that period. For 1996, 1997 and 2004, the polynya area was relatively small. The higher sea ice concentrations and the resultant higher albedo values, would have driven higher erythemal UV values for these years.

The high levels of erythemal UV in spring 2001 (Figure 8.29 – left panel) are explained by the low levels of ozone and the higher albedo due to high sea ice concentration (Figure 8.28 – left panel). Even though spring 2003 had similar low levels of ozone to those of 2001, the sea ice concentration dropped as the polynya opened up in 2003 to expose lower albedo ocean (Figure 8.28 – left panel), leading to lower erythemal UV levels (Figure 8.29 – left panel).

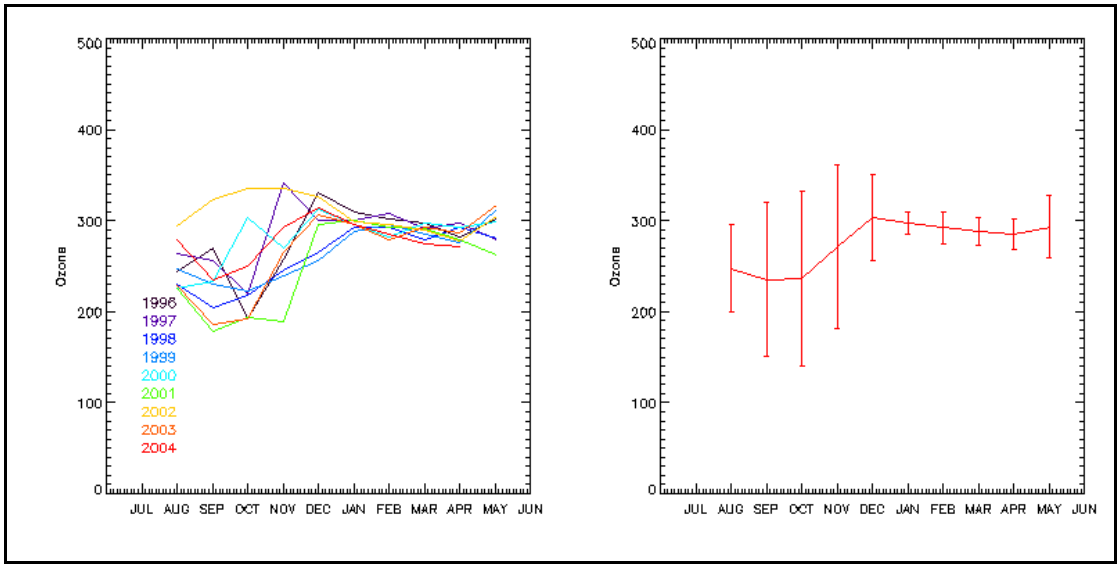

Figure 8.28: Plots of TOC for Amery no. 3 (Left panel – all nine years, Right panel – 9-year average plus error bars – 2 s.d.).

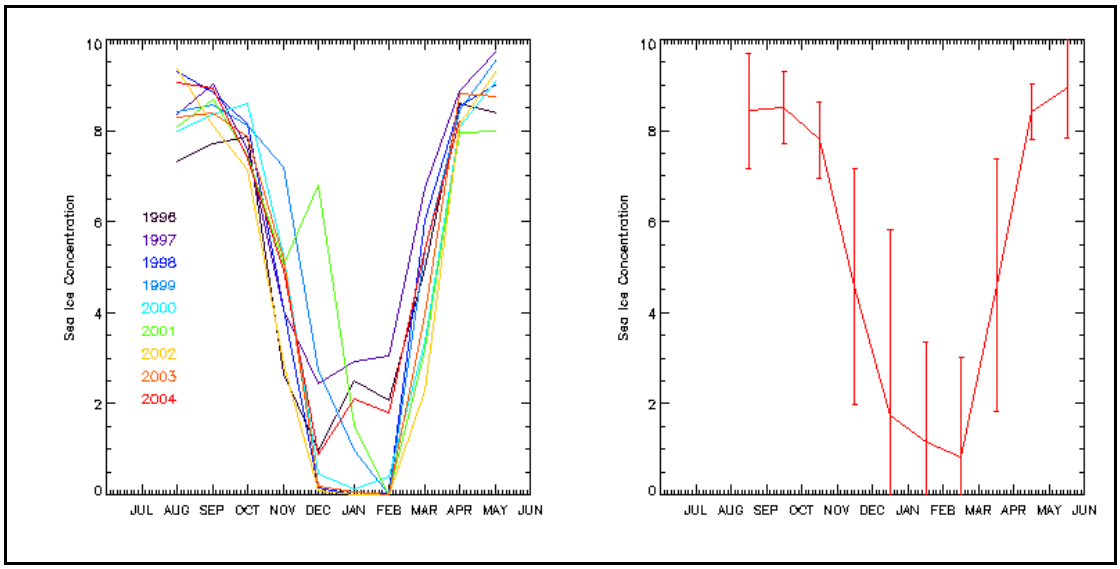

Figure 8.29: Plots of sea ice concentration for Amery no. 3 (Left panel – all nine years, Right panel – 9-year average plus error bars – 2 s.d.).

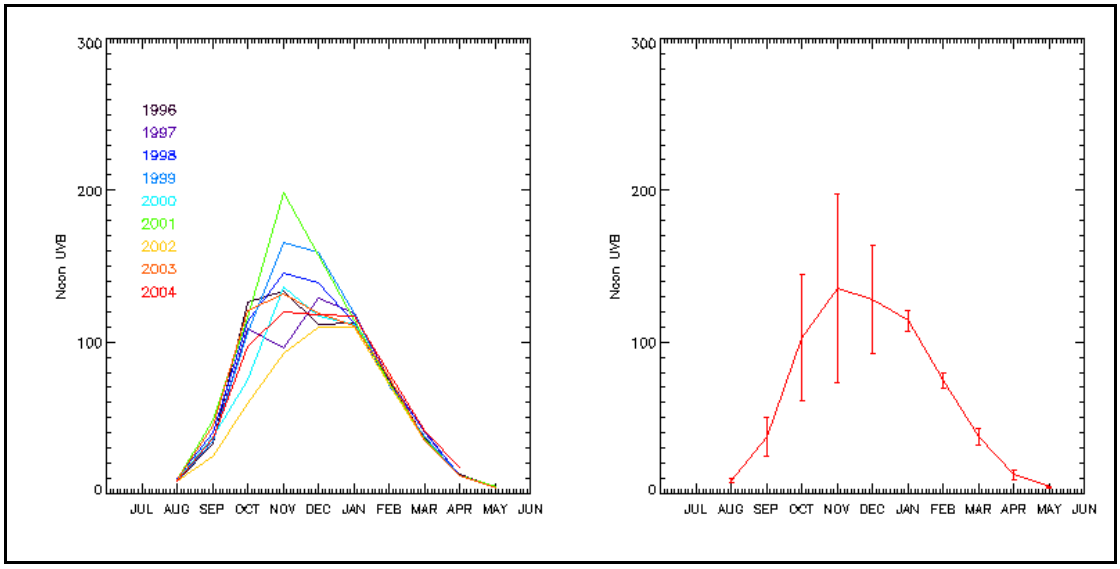

Figure 8.30: Plots of noon-time erythemal UV for Amery no. 3 (Left panel – all nine years, Right panel – 9-year average plus error bars – 2 s.d.).

8.3.4.4 Dalton No. 1

The same pattern of high-2002/low-2001 ozone values applies to this sub-area as in sub-area Amery No. 3. In this case though, the ozone values are generally higher (range 280-340 DU in the 9-year average plot, Figure 8.30, right panel) compared to those for Amery No. 3 (range 140-350 DU in the 9-year average plot, Figure 8.27, right panel). For Dalton no. 1 in 2001, the low ozone values were countered by the low albedo of the open water exposed by the reduction in sea ice concentration in summer. 2001 was the only year in which the sub-area became open water in summer, again reflecting the anomalous atmospheric circulation at that time (see Massom *et al.* 2004). The widths of the error bars in the plot of the 9-year erythemal UV average are indicative of more variability over the years in Amery No. 3 (Figure 8.29, right panel) compared to Dalton No. 1 (Figure 8.32, right panel).

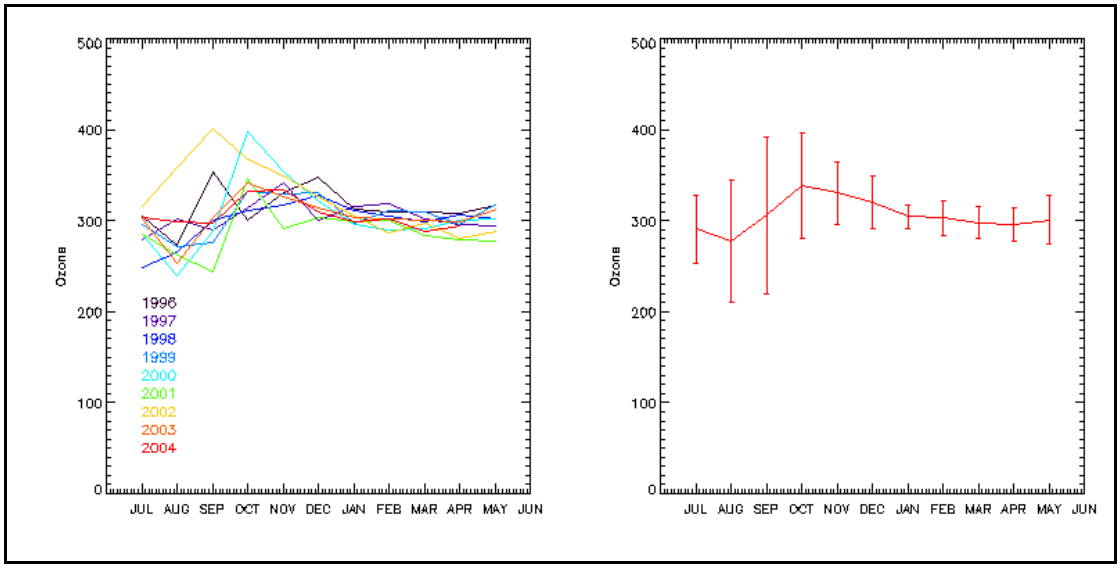

Figure 8.31: Plots of TOC for Dalton no. 1 (Left panel – all nine years, Right panel – 9-year average plus error bars – 2 s.d.).

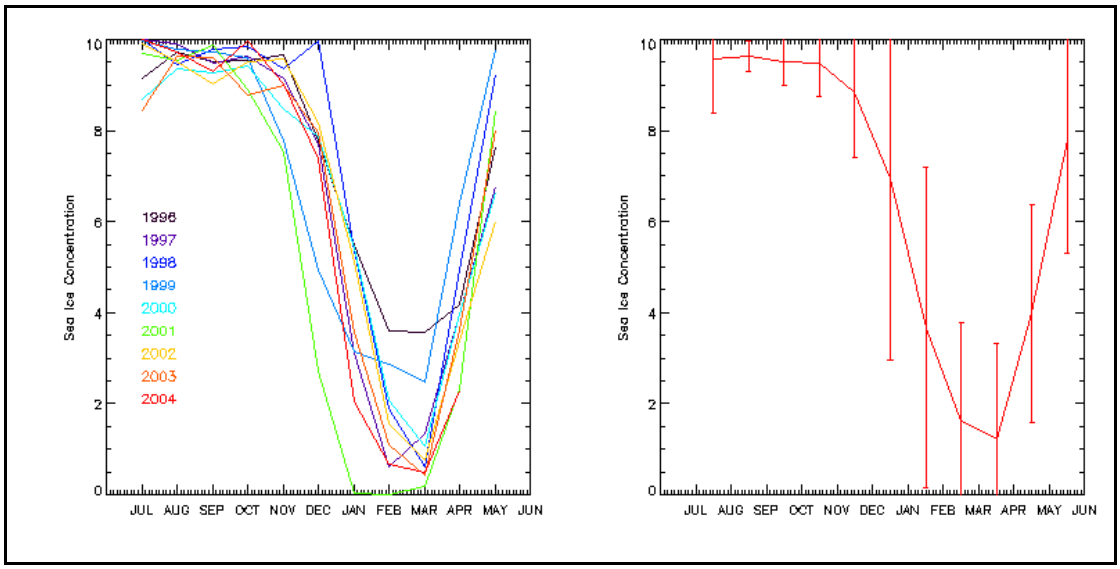

Figure 8.32: Plots of sea ice concentration for Dalton no. 1 (Left panel – all nine years, Right panel – 9-year average plus error bars – 2 s.d.).

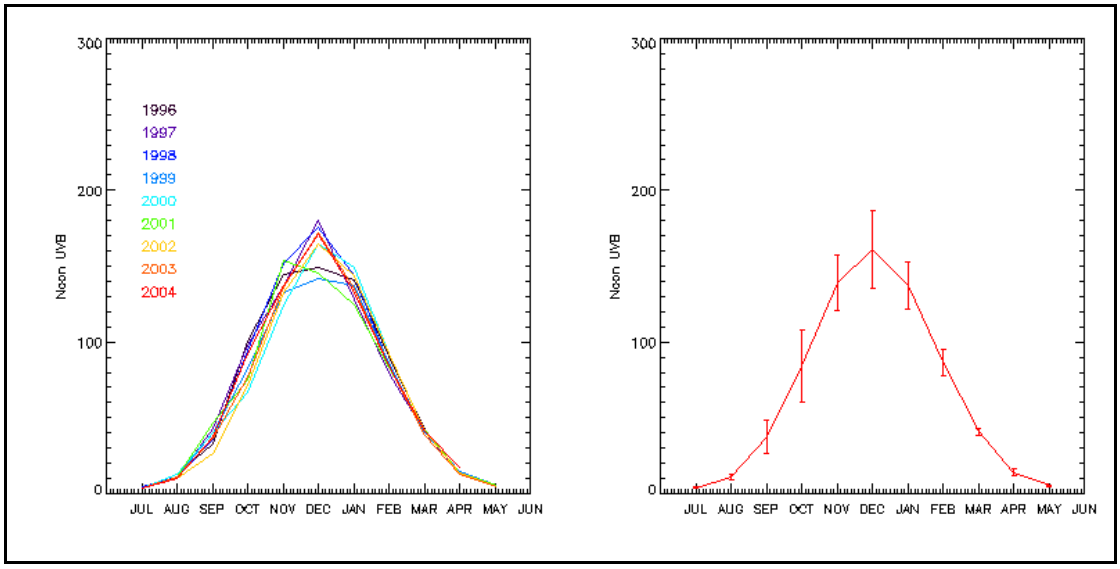

Figure 8.33: Plots of noon-time erythemal UV for Dalton no. 1 (Left panel – all nine years, Right panel – 9-year average plus error bars – 2 s.d.).

8.3.4.5 Dalton No. 4

The ozone values for this sub-area in spring are considerably higher than for any of the above sub-areas (as borne out by the plot of the 9-year averages and the fact that there are no ozone values less than 280 DU for each of the plots for the 9 years (see Appendix A)). The TOMS images (Figure 8.43) also demonstrate how the Dalton region is not affected by the ozone hole as much as the Amery region, for example.

As a consequence of the low-albedo open water environment and the high ozone values for Dalton No. 4 (Appendix A), the erythemal UV values are relatively low with little variability across the nine years (a maximum of 170 mW m^{-2} in 2004), as demonstrated by the smaller error bars for the plot of the 9-year averages (Appendix A).

8.3.4.6 Mertz No. 1

This sub-area is in the sea ice zone, and the sea ice concentration is greater than 80% for most months of all years, except for three: 1998 decreases to 55% in December, and 1999 and 2001 decrease to 30% in December and February respectively (Appendix A). The effect of a high albedo for all bar those three afore-mentioned years will push up the erythemal UV values, despite there being high ozone values. The maximum 9-year average erythemal UV is 155 ± 20 mW m^{-2}. Comparing this with a maximum erythemal UV of 140 ± 65 mW m^{-2} for sub-area Amery No. 3 (with lower ozone values and lower sea ice concentration/albedo) demonstrates the effect of the higher albedo driving the erythemal UV up despite higher ozone values. The years 2001 and 2002, which had higher ozone values in spring, also had clearer skies which would also have driven up the erythemal UV values.

8.3.4.7 Mertz No. 2

The 9-year average for Mertz 1 (Mertz 2) has a minimum ozone value of 255 DU (255 DU) and a maximum of 330 DU (340 DU). There is a large dispersal of ozone values for early spring in sub-area Mertz No. 2, as demonstrated by large error bars in the plot of 9-year averages (see Appendix A). This is a result of the high values for August to September in 2002 and October 2001 (~400 DU) and the low values (<300 DU) for the other 7 years. For the 9-year average ozone, there is a minimum of 255 DU and a maximum of 330 DU. As explained in Section 8.3.1.2, the TOMS images (Figures 8.43) demonstrate that 'ozone hole values' very rarely reach the coastline in the Mertz region during the study period.

The cloud modification factor values were very similar for sub-areas Mertz No. 1 and Mertz No. 2. This leaves the sea ice concentration as the main driving force in determining the erythemal UV values. The 9-year averages of erythemal UV show a maximum of 155 mW m^{-2} for both Mertz No. 1 and Mertz No. 2. It should be noted that the maximum erythemal UV in Mertz No. 2 occurred in December when the sea ice concentration was 95% (at that same time the sea ice concentration was 80% in Mertz No. 1). Conversely, the maximum erythemal UV for Mertz No. 1 occurred in January when 9-year average sea ice concentration is 90%, at which time the sea ice concentration was 80% in Mertz No. 2.

8.3.4.8 Shackleton No. 4

The low ozone values for spring in 2001 and the high values for spring in 2000 and 2002 give rise to the large error bars in the plot for 9-year averages (see Figure 8.34). 2001 is again the year that stands out as 'different' in all the parameters for Shackleton No. 4 sub-area. The 2001 springtime ozone values are low (Figure 8.34, left panel), and the sea ice concentration values are much higher compared to other years (Figure 8.35, left panel). These factors, along with clearer skies for spring 2001 (Figure 8.33, left panel), have resulted in the much higher levels of erythemal UV for this year (Figure 8.36, left panel), although overall, the maximum for the 9-year average plot is only 145 mW m^{-2} (see Figure 8.36, right panel).

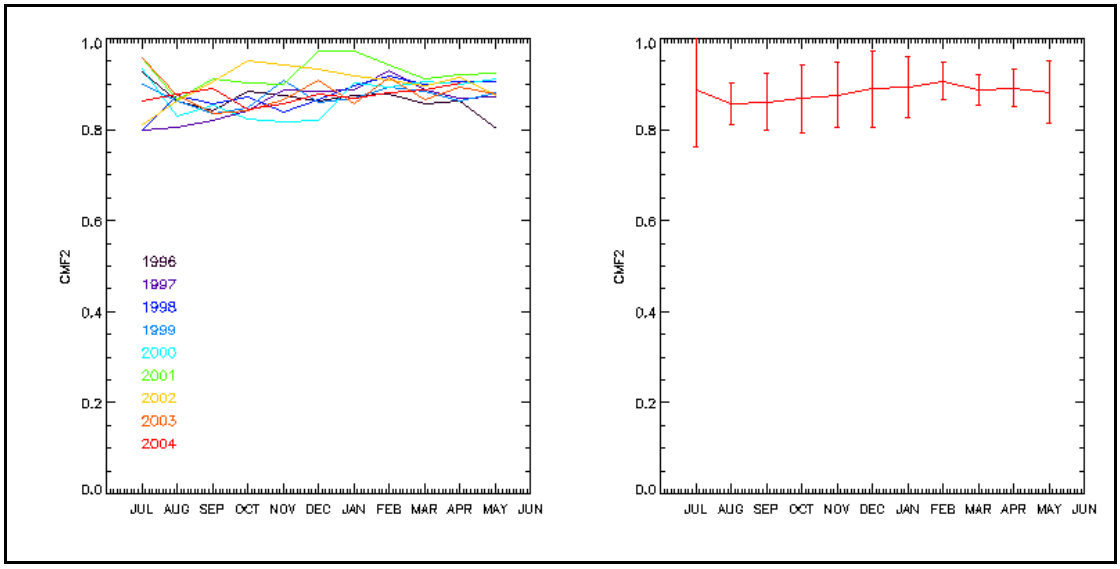

Figure 8.34: Plots of CMF2 for Shackleton no. 4 (Left panel – all nine years, Right panel – 9-year average plus error bars – 2 s.d.).

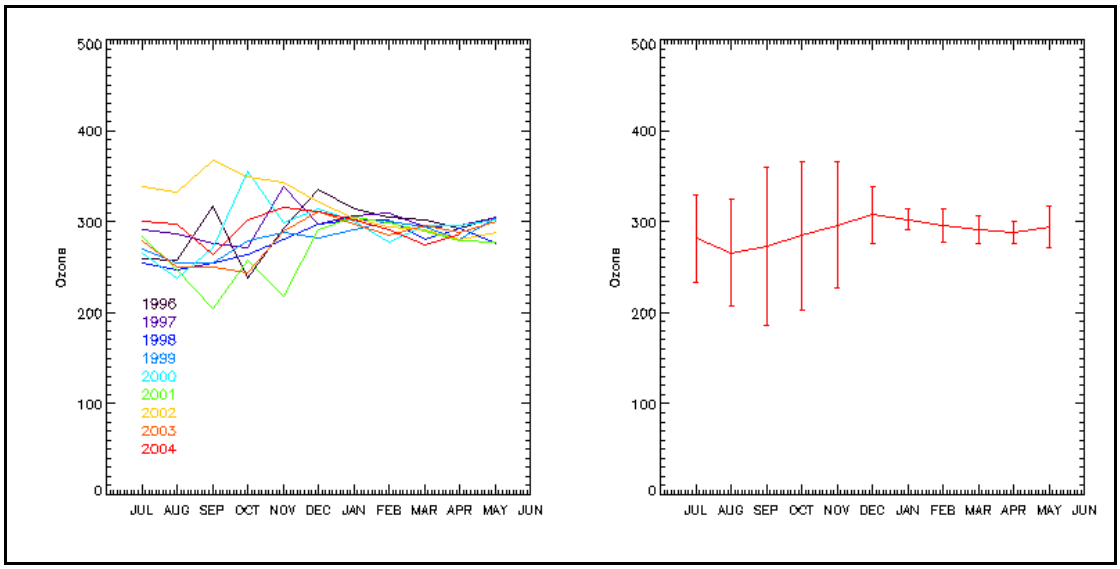

Figure 8.35: Plots of TOC for Shackleton no. 4 (Left panel – all nine years, Right panel – 9-year average plus error bars – 2 s.d.).

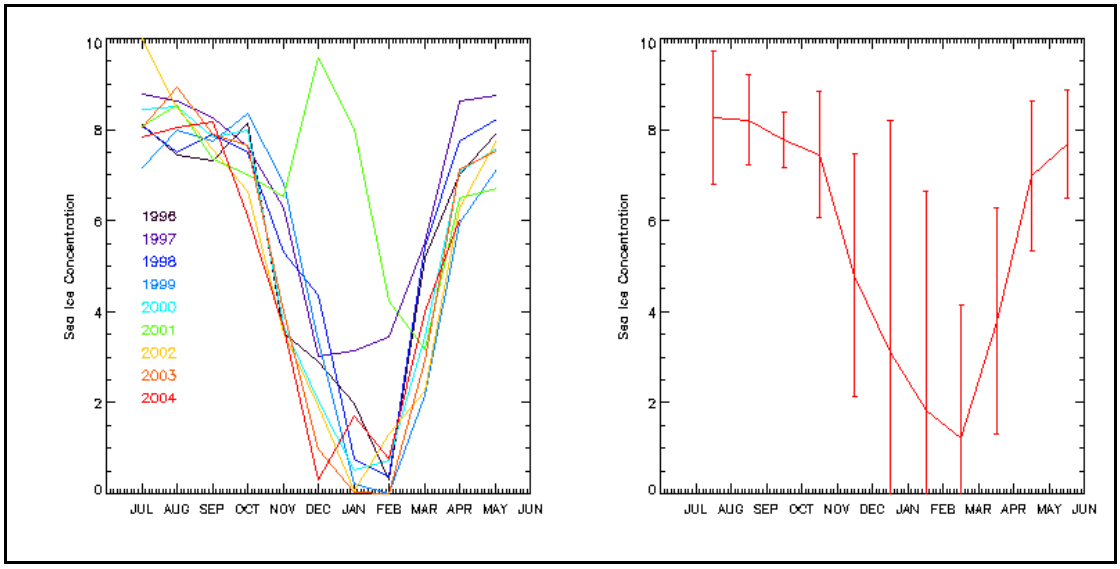

Figure 8.36: Plots of sea ice concentration for Shackleton no. 4 (Left panel – all nine years, Right panel – 9-year average plus error bars – 2 s.d.).

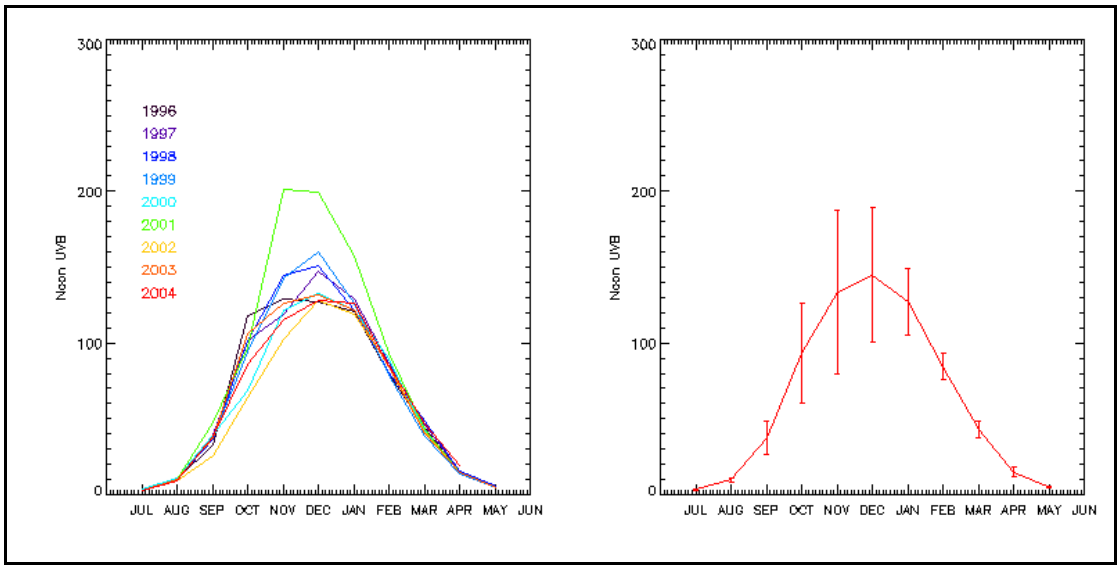

Figure 8.37: Plots of noon-time erythemal UV for Shackleton no. 4 (Left panel – all nine years, Right panel – 9-year average plus error bars – 2 s.d.).

8.3.5 Seasonal analysis

It was expected that there would be obvious patterns to the seasonal differences in the various key parameters; for example, low ozone in spring, high erythemal UV in spring, high sea ice concentration in late autumn and early spring, low sea ice concentration in summer. Means were calculated for spring, summer and autumn and these were analysed by sub-areas – see examples for Amery sub-area no. 1 (Figure 8.37), Shackleton no. 4 (Figure 8.38) and Dalton no. 1 (Figure 8.39).

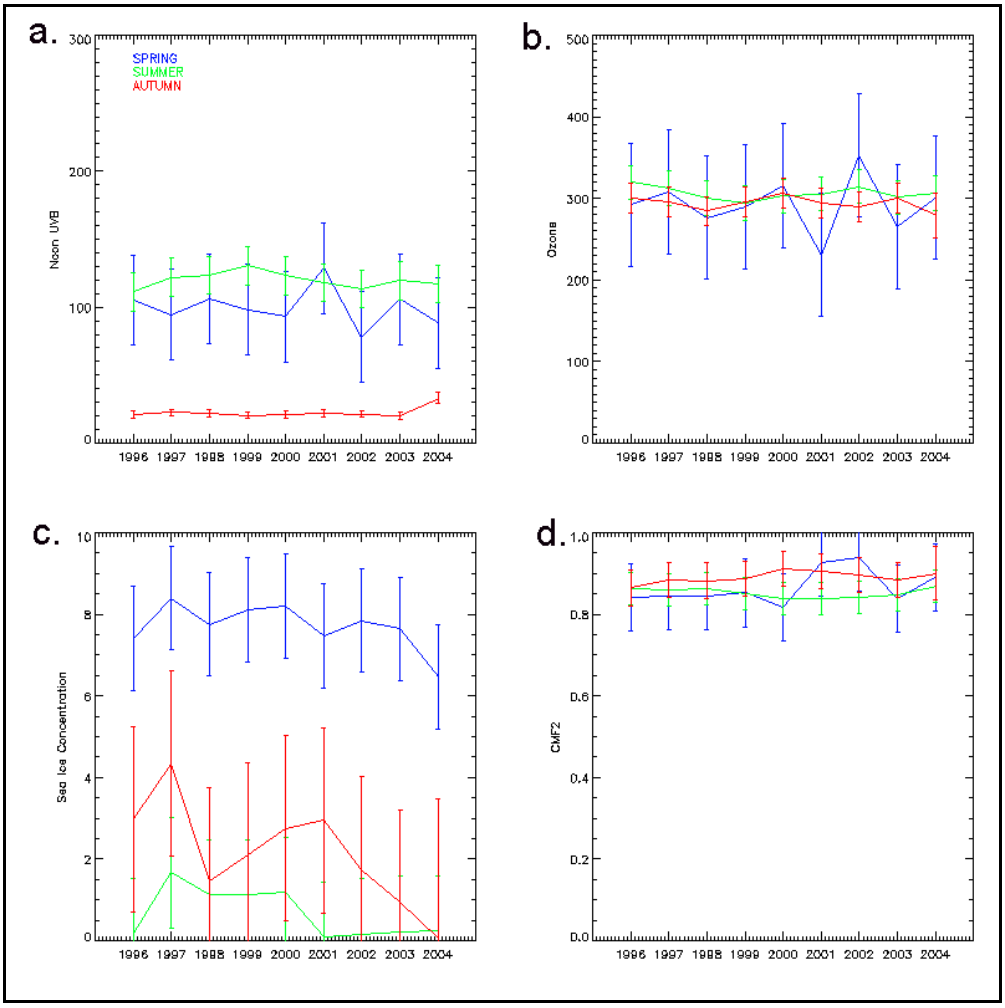

Figure 8.38: Seasonal time series for parameters for Amery no. 1 a. noon-time erythemal UV, b. ozone, c. sea ice concentration, d. CMF2.

The following points are demonstrated Figure 8.37 for sub-area Amery No. 1:

- Erythemal UV values are higher in summer than in spring (except for 2001) and both spring and summer are higher than autumn values (Figure 8.37a). Elevation in spring erythemal UV is caused by the lower TOC because of the ozone hole, and higher values occur in summer because of increased radiation. Lubin *et al.* (1989b) stated that the approach of the summer solstice during the evolution of the ozone hole implies that maximum erythemal UV does not necessarily coincide with the time of minimum ozone amount, and that any persistence of ozone depletion as the summer solstice approaches would have a major influence on the ultraviolet radiation environment of Antarctica.

- The pattern of the time series of noon-time erythemal UV for spring (Figure 8.37a) follows (in reverse) the time series plot of TOC (Figure 8.37b), i.e. in the years that have low (high) ozone, noon-time erythemal UV is high (low). This pattern is not followed by erythemal UV and ozone for the summer time series.

- There is much less variability in autumn erythemal UV values, and this is in line with the relatively constant values of ozone throughout the time series. This is in spite of the much higher sea ice concentrations for some years (e.g. 1997), which would be expected to drive the erythemal UV values higher.
- Figure 8.37b demonstrates the wider variability in TOC in spring than for the other seasons.
- Figure 8.37c shows much lower values of sea ice concentration for summer than for spring and autumn.
- There is not much variability in CMF2 (Figure 8.37d) with a maximum of ~0.95 and a minimum of ~0.8.

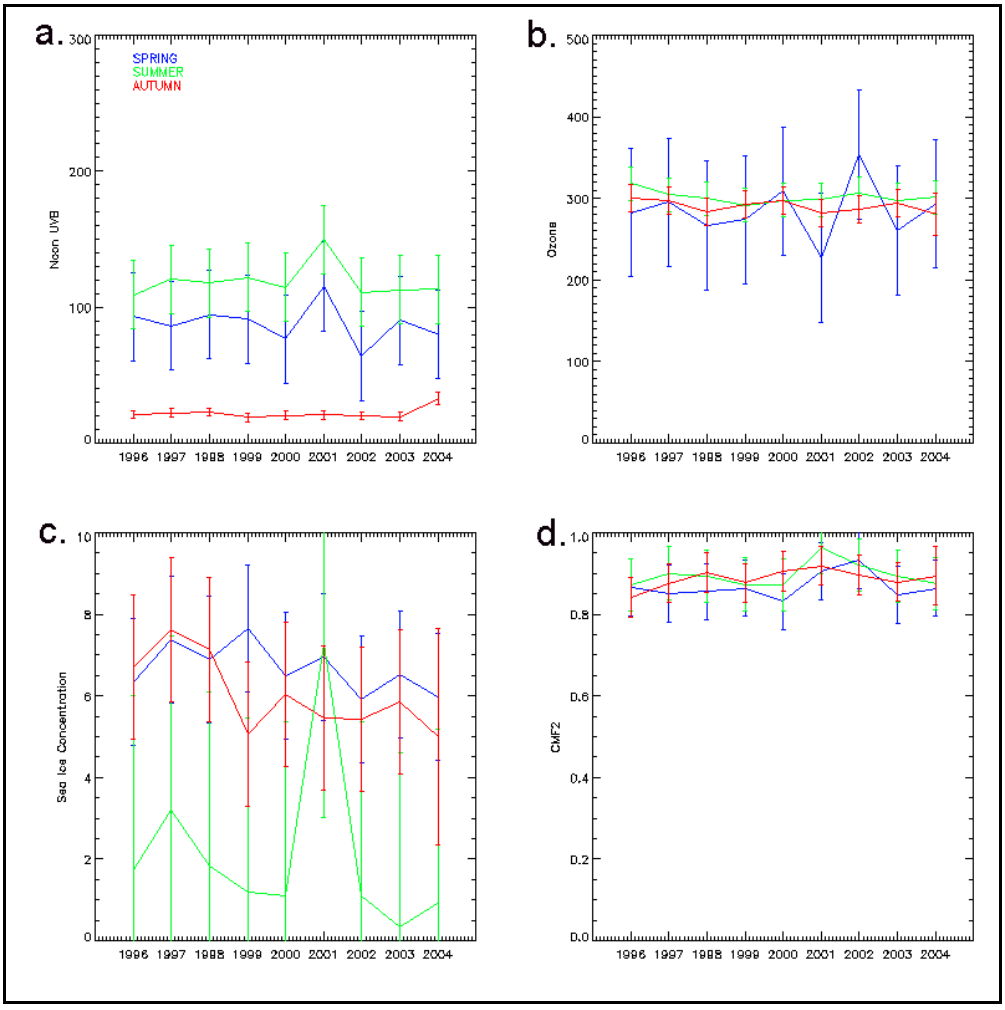

Figure 8.39: Seasonal time series for parameters for Shackleton no. 4 (a. noon erythemal UV, b. ozone, c. sea ice concentration, d. CMF2).

The following points are demonstrated by Figure 8.38 for sub-area Shackleton No. 4:

- Both spring and summer have a peak in erythemal UV in 2001, which is explained by the low ozone in spring, but for summer, it was caused by the peak in the sea ice concentration raising the albedo for the sub-area (Figure 8.38c) and a rise in CMF2 (Figure 8.38d) (i.e. clearer skies) plus increased radiation.
- The time series for sea ice concentration (Figure 8.38c) also show much lower values (except for 2001) for summer than for spring and autumn.

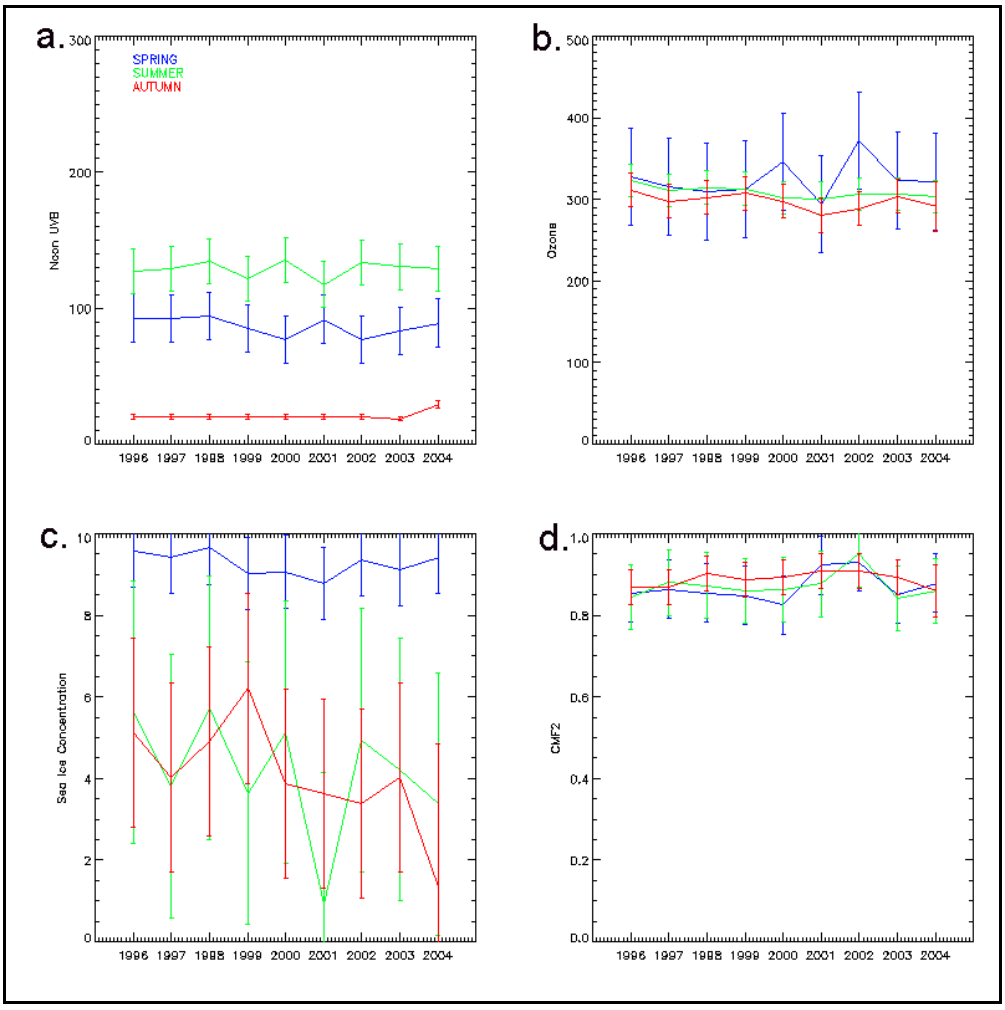

Figure 8.40: Seasonal time series for parameters for Dalton no. 1 (a. noon erythemal UV, b. ozone, c. sea ice concentration, d. CMF2).

The following points are demonstrated by Figure 8.39 for sub-area Dalton No. 1:

- This sub-area has higher TOC values for spring than for summer and autumn (Figure 8.39b). This is different to the Amery No. 1 and Amery No. 3 sub-areas, where TOC was lower for spring than the other two seasons. This is explained by Figures 8.43a, 8.43b and 8.43c, where it can be seen that the Amery region is exposed to lower values

of TOC in spring than the Dalton region – as the polar vortex breaks up, the lower ozone values spread out over the coast.

- Despite the higher values of TOC for spring, the erythemal UV values have been driven up by the high sea ice concentration of approximately 100% for the spring time series (Figure 8.39c). The summer and autumn time series display much lower values of sea ice concentration.

8.3.6 Trend analysis

The calculation of the noon-time erythemal UV for each pixel in the regions (see Figure 2.3) involved the albedo of the surface (the higher the sea ice concentration, the higher the albedo), TOC, cloud modification factor and SZA at the time. If ozone displayed a downward trend over time (while all other parameters remained constant), then it could be expected that the noon-time erythemal UV would show an upward trend. Likewise, a downward trend in sea ice concentration, and therefore a lowering of albedo, would be expected to cause a downward trend in noon-time erythemal UV, if other parameters remained unchanged. Trend estimation using the least squares method was used to determine if seasonal parameter values exhibited increasing or decreasing trends that were statistically distinguishable from random behaviour. It is acknowledged that a sequence of nine years is rather too short for the confident detection of temporal variations, but the analysis nonetheless does uncover some information on possible trends. Figures 8.40-8.42 are samples of the trend analysis plots. The plots for the other sub-areas are included in Appendix A.

Table 8.11 gives the statistics of lines of best fit (least squares method) for each of the parameters, for each of the sub-areas investigated. For six of the lines of best fit, the correlation coefficient values (as shown in bold in Table 8.11) indicate that the line explains more than 50% of the variance of the data – most of the other correlation coefficient values are less than 30%.

The trend lines for ozone demonstrated negative slopes for all seasons over the nine years for all sub-areas (~6-30 DU loss over 9 years), except for the following: positive slope for spring in Dalton No. 1, Dalton No. 4 and Mertz No. 1 and Mertz No. 2 sub-areas. This result is explained by the geographic pattern of development of the ozone hole and subsequent dispersal of the polar vortex (see Figures 8.43). The Dalton and Mertz regions are not exposed to low TOC in spring (that are common in the Amery and Shackleton regions). The break-up of the polar vortex allows lower levels of TOC to reach Dalton and Mertz regions in summer and autumn.

The trend lines for sea ice concentration demonstrated negative slopes for all seasons over the nine years for all sub-areas, except for insignificant positive slopes for spring in sub-area Amery No. 3, for summer in sub-area Mertz No. 1, and for summer and autumn in sub-area Mertz No. 2. There were no sea ice data in sub-area Dalton No. 4, as it was situated in a polynya. There

were significant decreases in sea ice concentration (~20%) for autumn in every sub-area except for Mertz No. 2.

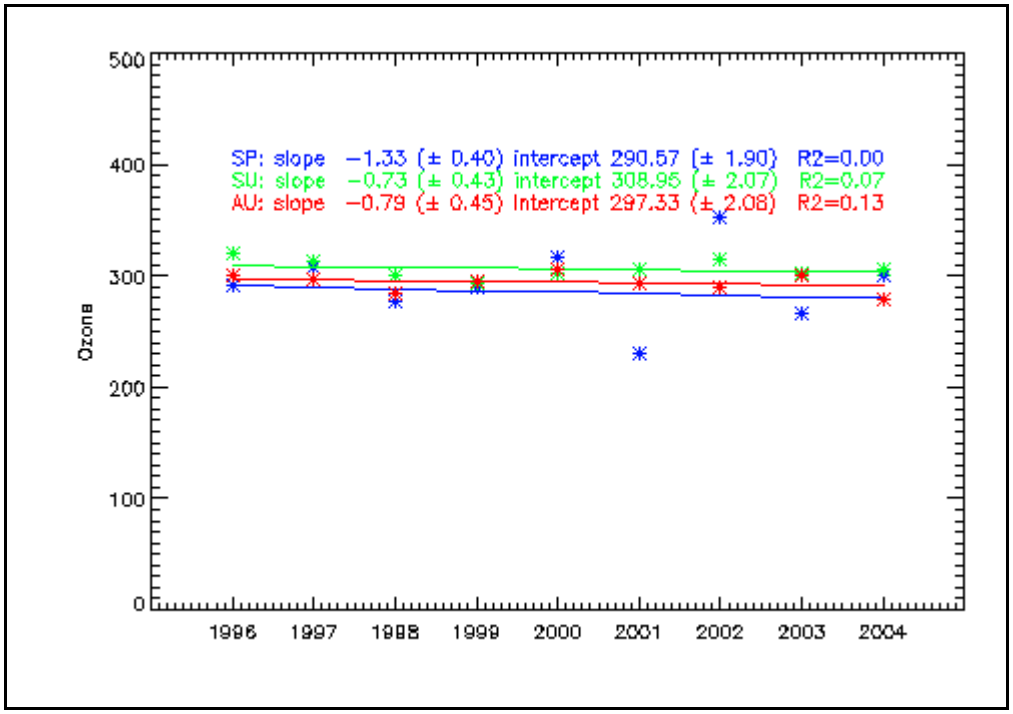

Figure 8.41: Trend analysis for TOC for Amery no. 1.

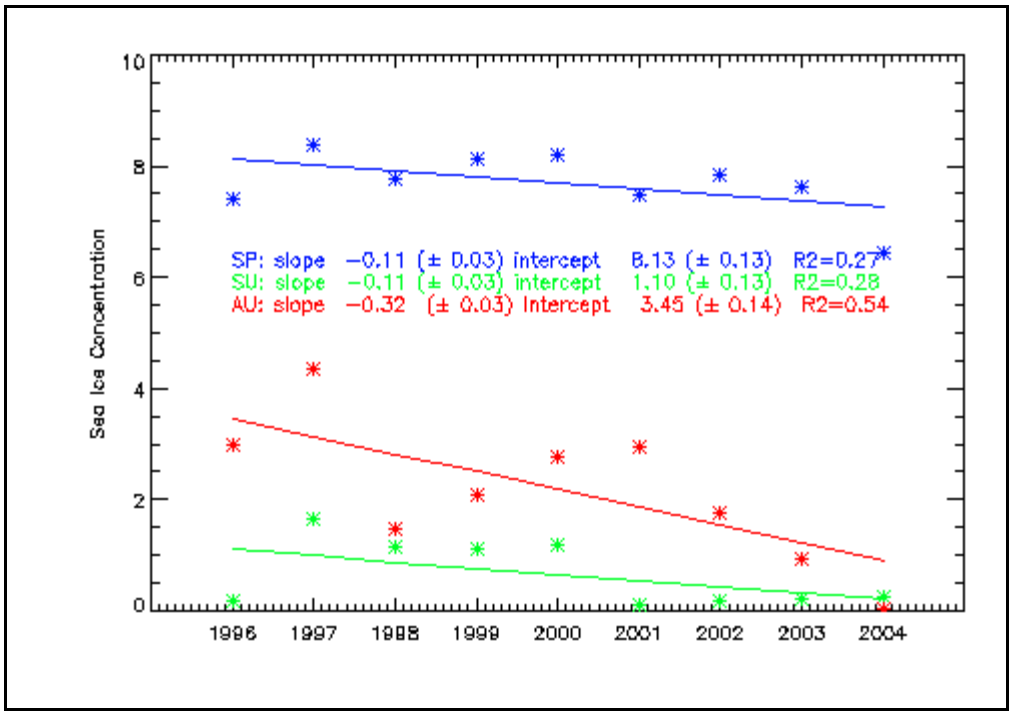

Figure 8.42: Trend analysis for sea ice concentration for Amery no. 1.

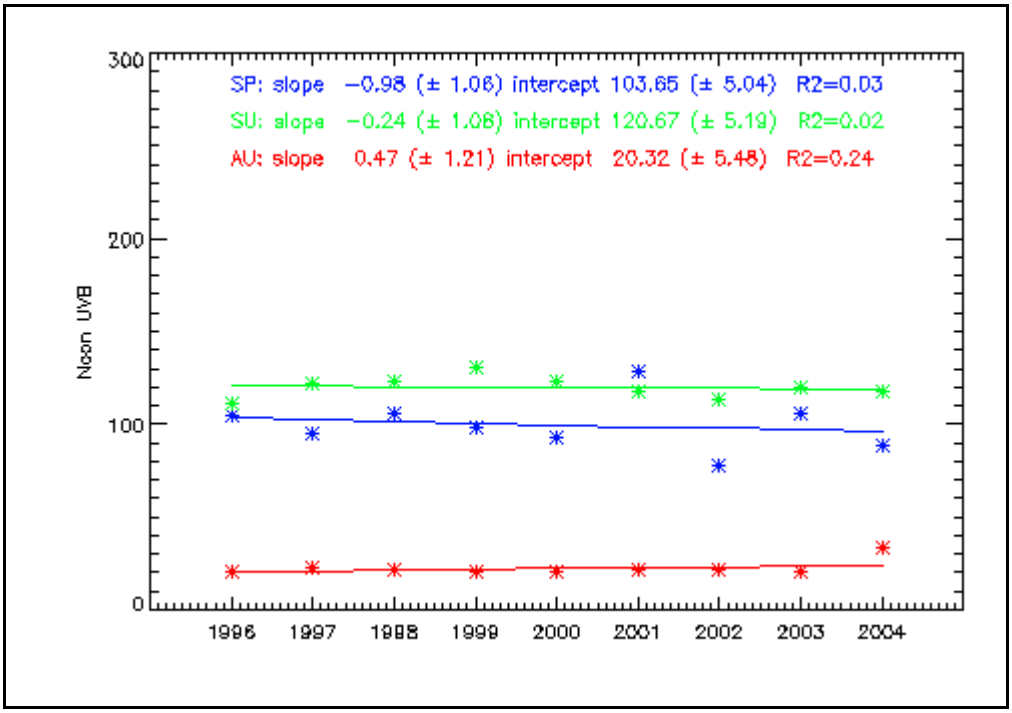

Figure 8.43: Trend analysis for noon-time erythemal UV for Amery no. 1.

Turner *et al*. (2009) suggest that while there has been a dramatic loss of Arctic sea ice, Circum-Antarctic sea ice overall has increased by a small amount (0.97% per decade) as a result of the ozone hole delaying the impact of greenhouse gas increases on the climate of the continent. The ozone hole has strengthened surface winds around Antarctica and deepened the storms in the South Pacific area of the Southern Ocean that surrounds the continent (Thompson and Solomon 2002). This resulted in greater flow of cold air over the Ross Sea (West Antarctica) leading to more ice production in this region. The satellite data reveal the variation in sea ice cover around the entire Antarctic continent. Whilst there has been a small increase in autumn sea ice extent around the coast of East Antarctica, the largest changes are observed in West Antarctica. However, statistics derived from a climate model control run suggest that the observed sea ice extent increase might still be within the range of natural climate variability (Turner *et al.* 2009). A finding of increased sea ice extent does not necessarily negate the findings of decreases in sea ice concentration for the nine years of this project. A simplistic approach would be to associate an increase in sea ice extent with an increase in sea ice concentration. This is not necessarily so, especially if the increase in sea ice extent was caused by stronger winds blowing from the Antarctic continent, causing a divergent ice cover to lower the overall regional sea ice concentration. Even if exposure of the open water led to the formation of more sea ice (in a polynya for example), it could still result in a lower sea ice concentration. There are also other factors (e.g. ocean characteristics) to be considered in the

discussion of the reasons for increases in the sea ice extent, but these are beyond the boundaries of this project (see references in Turner *et al*. (2009)).

Of the regression statistics for all of the seasons and sub-areas, only six of the trend lines for noon-time erythemal UV demonstrate significant trends. Dalton No. 1, Mertz No. 1, Mertz No. 2 and Shackleton No. 4 all had significant negative trends in spring, while Dalton No. 4 and Mertz No. 2 had significant positive trends in summer. Dalton No. 4 demonstrated a 17 DU decrease in TOC over the 9 years, and no change in sea ice concentration (in a polynya), resulting in a ~10 mW m^{-2} increase in noon-time erythemal UV. Mertz No. 2 displayed ~14 DU decrease in TOC and a 15% increase in sea ice concentration – this resulted in a ~17 mW m^{-2} increase in noon-time erythemal UV.

There were significant upward trends in ozone and significant downward trends in sea ice concentration in spring in Dalton No. 1 and Mertz No. 1, thus explaining the significant negative trend in erythemal UV for spring. Mertz No. 2 had a significant upward trend in TOC (but an insignificant downward trend in sea ice concentration), consistent with the negative springtime trend in noon-time erythemal UV. Shackleton No. 4 had an insignificant downward trend in ozone, but a significant downward trend in sea ice concentration, resulting in a negative trend in springtime erythemal UV.

The significant downward trend (~17 DU over 9 years) in TOC in summer in Dalton No. 4 has led to higher noon-time erythemal UV, as there were no sea ice changes (nil sea ice in polynya) to counter the effect of changes in ozone. In summer, Mertz No. 2 experienced a significant downward trend (5% loss over 9 years) in TOC (~14 DU) and a significant upward trend in sea ice concentration (~15% over 9 years), both contributing to the significant increase in noon-time erythemal UV (~17 mW m^{-2} increase over 9 years,).

From the trend line plots for the Amery no. 1 sub-area (Figures 8.40, 8.41 and 8.42), it is evident that there are significant negative slopes for ozone and sea ice concentration for all seasons. The slopes of the trend lines for all seasons for noon-time erythemal UV are not significant – the lower albedo surface (lower sea ice concentration) has negated the effect of lower TOC.

Weatherhead *et al.* (1998) determined that the number of years of data required to detect and estimate a given trend is highly dependent on the two major statistical factors, the autocorrelation and variance of the noise. For a typical range of values of the magnitude of variance and autocorrelation coefficient of the noise, the number of years of data needed to detect a trend of 5%/decade can vary from ~10 to >20 years (Weatherhead *et al.* 1998). Glandorf *et al.* (2005) also demonstrated that even when trends are significant, it does not mean that the trend is real when autocorrelated data are used. Given the findings of Weatherhead *et al.* (1998) and Glandorf *et al.* (2005), it is not possible to state that the data in this project demonstrated any conclusive trends.

The following notes apply to Table 8.11:

1. Statistics for intercept not included in the table;
2. Nil sea ice data for Dalton No. 4 as it is situated in a polynya;
3. SP = spring, SU = summer, AU = autumn; and
4. Slope of the sea ice concentration plots do vary, but not when expressed to 2 decimal places.

Sub-area/ Season	Ozone – line of best fit (using least squares)		Sea ice conc – line of best fit (using least squares)		Noon UVB – line of best fit (using least squares)	
	Slope (sigma error)	R^2	Slope (sigma error)	R^2	Slope (sigma error)	R^2
Amery1 (SP)	-1.33 (±0.40)	0.00	-0.11 (±0.03)	0.27	-0.98 (±1.06)	0.03
Amery1 (SU)	-0.73 (±0.43)	0.07	-0.11 (±0.03)	0.20	-0.24 (±1.08)	0.02
Amery1 (AU)	-0.79 (±0.45)	0.13	-0.32 (±0.03)	**0.54**	+ 0.47 (±1.21)	0.24
Amery3 (SP)	-0.74 (±0.33)	0.01	+0.03 (±0.03)	0.02	-1.02 (±1.06)	0.02
Amery3 (SU)	-0.38 (±0.42)	0.01	-0.13 (±0.03)	0.10	-0.32 (±1.08)	0.02
Amery3 (AU)	-0.86 (±0.48)	0.10	-0.17 (±0.03)	0.44	+ 0.39 (±1.29)	0.16
Shack4 (SP)	-0.31(±0.39)	0.01	-0.11 (±0.03)	0.27	-1.31 (±1.06)	0.06
Shack4 (SU)	-1.09(±0.42)	0.18	- 0.12 (±0.03)	0.02	+0.13 (±1.08)	0.00
Shack4 (AU)	-1.42(±0.46)	0.32	- 0.25 (±0.03)	**0.55**	+0.36 (±1.24)	0.16
Dalton1 (SP)	+1.33 (±0.44)	0.04	+0.04 (±0.03)	0.14	-1.16 (±1.06)	0.23
Dalton1 (SU)	-1.98 (±0.43)	**0.59**	-0.20 (±0.03)	0.14	+0.16 (±1.08)	0.00
Dalton1 (AU)	-2.01 (±0.47)	0.29	-0.30 (±0.03)	0.49	+0.39 (±1.23)	0.24
Dalton4 (SP)	+1.09 (± 0.50)	0.07	0.00 (±0.03)	0.00	-0.27 (±1.06)	0.14
Dalton4 (SU)	-1.93 (±0.43)	**0.57**	0.00 (±0.03)	NaN	+1.09 (±1.08)	**0.53**
Dalton4 (AU)	-1.55 (±0.43)	0.18	0.00 (±0.03)	0.06	+ 0.22 (±1.12)	0.25
Mertz1 (SP)	+3.10 (±0.42)	0.12	-0.08 (±0.03)	0.13	-1.43 (±1.06)	0.22
Mertz1 (SU)	-1.59 (±0.41)	0.42	+ 0.02 (±0.03)	0.00	+1.06 (±1.08)	0.07
Mertz1 (AU)	-3.41 (±0.50)	**0.52**	-0.19 (±0.03)	0.27	+ 0.47 (±1.31)	0.21
Mertz2 (SP)	+3.53 (±0.43)	0.15	-0.01 (±0.03)	0.01	-1.30 (±1.06)	0.25
Mertz2 (SU)	-1.55 (±0.42)	0.31	+ 0.17 (±0.03)	0.05	+1.89 (±1.08)	0.20
Mertz2 (AU)	-2.32(±0.51)	0.32	+ 0.01 (±0.03)	0.00	+0.58 (±1.30)	0.25

Table 8.11: Statistics for lines of best fit for each of parameters, sea ice concentration, ozone and noon-time UVB for each of selected 7 sub-areas.

Bold – indicates significant trend, Red – indicates a positive trend, Blue – indicates a negative trend.

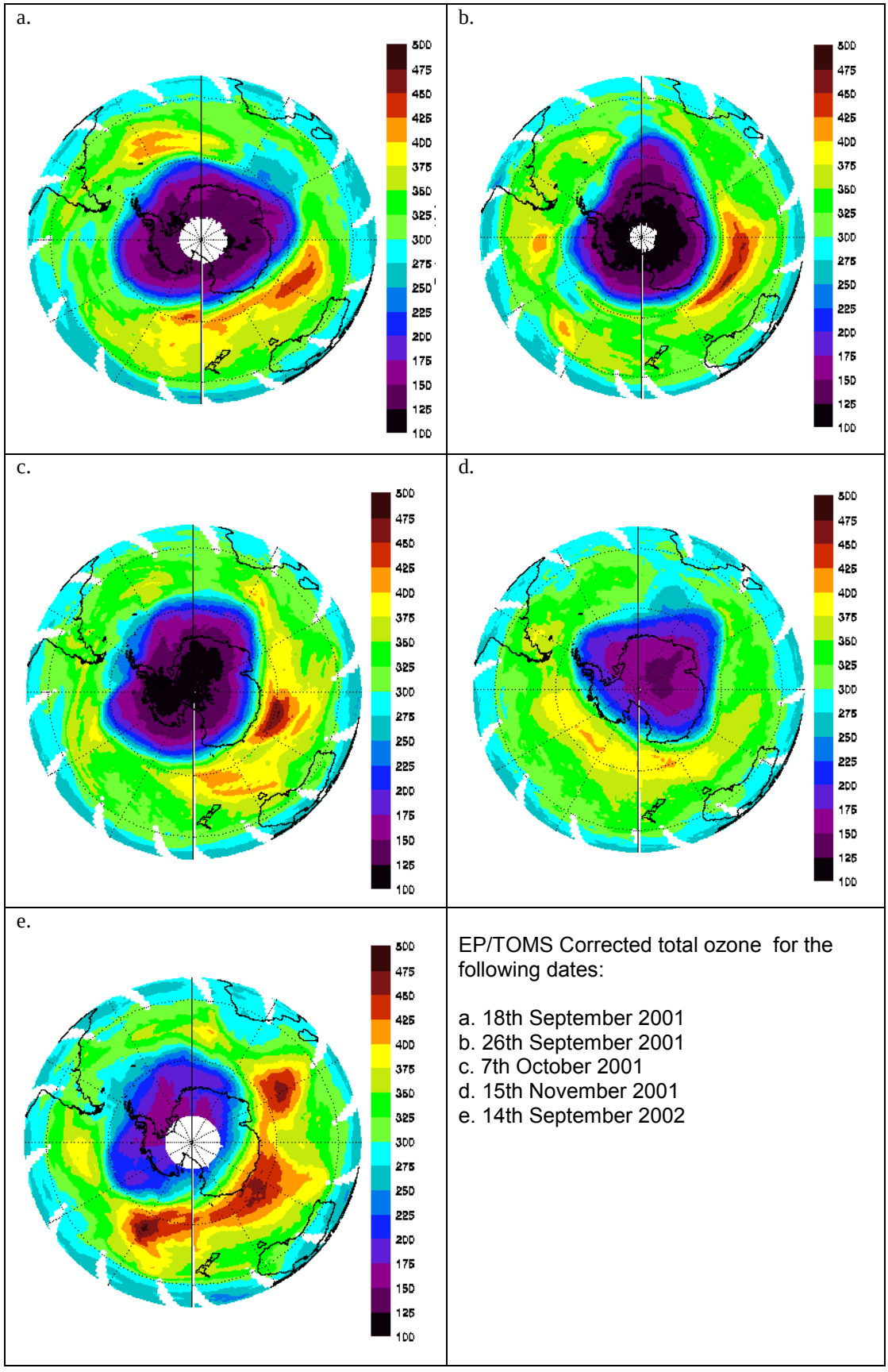

Figure 8.44: EP/TOMS corrected total ozone (Dobson Units) ftp://toms.gsfc.nasa.gov/pub/eptoms/images/spole/Y2001/.

9. SUB-SURFACE MAPS

The effects of UV radiation on living cells in the ocean are determined by its penetration into the water column, the duration of exposure and the vulnerability of planktonic organisms to UVB radiation, and their capacity to ameliorate or prevent damage (Tedetti and Sempéré 2006). This chapter describes i) the development of sub-surface levels of erythemal UV radiation (utilising the surface maps as described in Chapters 7 and 8) at various levels within sea ice and the water column; and ii) how these estimates were then converted to biologically-effective dose rates.

The transmission of UVR through the air-water interface varies with time due to changes in the incident irradiance angular distribution and to the effect of surface waves (Stramski *et al.* 1992), which both modulate the intensity at a particular depth and the amount of light reflected back into the air. As an example, calm waters reflect only about 5% of incident UV radiation, although up to 20% is reflected from choppy water (Diffey 1998). This cannot be taken into account in this project, as there are no data detailing water surface conditions for the spatial and temporal coverage – the assumption was therefore made that the water was calm.

Aquatic ecosystems differ tremendously in their transparency, thus affecting the depth of solar UV penetration (Laurion *et al*. 2000). In addition to inorganic particulate matter, dissolved and particulate organic carbon (DOC and POC) and various humic substances contribute considerably to the attenuation of short wavelength radiation (Arts *et al.* 2000). Often there is a pronounced variability and seasonal change in the transparency (Dring *et al.* 2001). Absorbing and scattering substances reduce the transparency of the water, especially in eutrophic freshwater systems and coastal areas of the oceans (Conde *et al.* 2000), while UV penetrates to greater depths in clear oceanic waters. Attempts to accurately assess the ecological impact of UVB on marine organisms must take into account the diurnal and seasonal variations in the irradiances experienced when organisms are emersed, and the moderating influence of the overlying seawater when they are submersed (Dring *et al*. 2001). Once again, these properties of the water are not known, and cannot be included in the calculations of sub-surface values of erythemal UV.

Although UVB inhibition of photosynthetic rates is substantial near the ocean surface, UVB attenuates with depth, with a 10% penetration depth at 305 nm of <10 metres (Arrigo *et al.* 2003a). The results of the study by Gieskes and Kraay (1990) indicated that the depth of ultraviolet light penetration in the Southern Ocean is so great that organisms living in the upper 20 or 30 metres may receive damaging levels. The low concentration of detritus, material that typically absorbs the most detrimental shorter wavelengths, is in this respect, an unfavourable characteristic of the Southern Ocean (Gieskes and Kraay 1990). Later research by Arrigo *et al.* (2003a) determined that there is relatively little UVB inhibition below 15 metres, depths where

primary productivity can represent a substantial fraction of the depth integrated total in the Southern Ocean (El-Sayed and Taguchi 1981). More importantly, the Antarctic ozone hole is most extensive in September–October, when sea ice coverage is near maximal, and rates of phytoplankton production are low. It is important to note, however, that in the early 2000s, ozone holes have experienced similarly reduced ozone concentrations, but have persisted for longer periods of time, and extended further north (see www.cpc.ncep.noaa.gov). Should these trends continue, phytoplankton will be exposed to increasingly intense UVR at higher solar elevations (Arrigo *et al.* 2003a).

The question "how far does UV radiation penetrate into natural waters" therefore, cannot be answered simply because it depends upon local water properties (including the properties of the air-water interface), incident irradiance conditions and definition of "penetration" (Booth and Morrow 1997). As examples, Karentz and Lutz (1990) detected biological effects of UVR at depths of 20-30 metres; Smith *et al.* (1992) reported that UVR penetrates to ecologically-significant depths in excess of 60-70 metres in Antarctic waters; research by Rasmus *et al.* (2004) showed that UVB radiation affects a 'substantial portion' of the upper mixed layer; and Lesser *et al.* (2006) reported that UVR was measured to depths of 7-10 metres at their various study sites. Finkel *et al*. (2010) stated that increased atmospheric carbon dioxide will have associated warming, and this will decrease the depth of the upper mixed layer. Because of the variance in opinion on how far UV radiation penetrates, this project calculated various biological dose rates at a selection of depths, namely 5, 10, 15 and 20 metres (see Sections 9.1.1, 9.1.3 and 9.2.2).

The penetration of UVR in the marine environment could be affected in the future by the interactions of ozone depletion and global warming. The intensity of UVR is enhanced by the decline of the stratospheric ozone layer, but also by the different chemical and dynamic effects of global warming (McKenzie *et al.* 2003; Tedetti and Sempéré 2006). In the oceanic layer, the effects of global warming could initiate a decrease in the concentration of CDOM (Häder *et al*. 2003), as well as variations in the depth and the rate of the mixing layer (Díaz *et al*. 2000; Huot *et al*. 2000).

9.1 Estimating erythemal UV within sea ice and water column

Both components of the attenuation coefficients, namely scattering and absorption, are wavelength dependent. Scattering within the three media of interest (i.e. snow, ice and water) can be assumed to be constant over the spectrum of UVR, since variations over this spectrum are negligible (Perovich 1993). The absorption inside a medium is strongly wavelength dependent, and spectral attenuation is based on the spectral absorption (Perovich 1996), but this variation of the attenuation coefficients has not been taken directly into account.

In order to estimate the transfer of radiation from the surface of the ocean/snow into the sub-surface environment, it is necessary to account for both the reflectance from the surface and the attenuation of light within the various media (snow, ice, water) (see Figure 6.7).

The (erythemally-weighted) irradiance at some depth in the water column is given by equation 9.1,

$$ERY(z) = ERY\_S * (1 - R_W) * e^{-K_W z} \quad (9.1)$$

where ERY_S is the surface irradiance, R_W is an appropriate reflection coefficient (0.1) and K_W is the erythemal attenuation coefficient for clear water (0.3 m^{-1}) (Booth and Morrow 1997; Rasmus *et al.* 2004).

The transmission into sea ice with a snow cover is treated similarly. The first step is to calculate the irradiance ERY_TI (Top of Ice) at the bottom of the snow cover with thickness, z_S, given by equation 9.2,

$$ERY\_TI = ERY\_S * (1 - R_S) * e^{-K_S z_S} \quad (9.2)$$

where the values of K_S = 11.3 m^{-1} and R_S = 0.67 were established in Section 6.7.

The irradiance beneath sea ice of thickness z_I is estimated with some simplifying assumptions. First, no account is taken of reflectance from the upper surface of the sea ice – even though the analysis of the SIPEX data in Section 6.7 suggested that the combined effect of reflectance from the upper and lower surfaces of sea ice implied a reflectance 0.34, this is not relevant to the situation where there is a snow cover on top of the sea ice. In this case, much of the radiation reflected from the upper surface of the sea ice will be scattered by the snow cover back into the sea ice. The experimental set-up on the SIPEX voyage was not able to quantify the transmission of radiation through the snow-ice interface, therefore this transmission is assumed to be unity for the purposes of estimating under-ice irradiance levels. Secondly, it is also assumed that the upward reflection of radiation from the lower surface of the sea ice is negligible. On this basis, the irradiance at the bottom of the ice ERY_BI (Bottom of Ice) with thickness z_I is given by,

$$ERY\_BI = ERY\_TI * e^{-K_I z_I} \quad (9.3)$$

where the value of K_I = 2.0 m^{-1} was established in Section 6.7. This value is consistent with other estimates and measured values in Perovich and Govoni (1991). The measurements on the SIPEX voyage did not consider any differentiation between various types of sea ice and associated crystal structure. While these physical properties certainly do affect the attenuation properties, these characteristics cannot be estimated remotely and a simple parameterisation was considered appropriate (K.J. Michael, pers. comm., 2009).

The irradiance in the water column at a distance, z metres beneath sea ice (with a snow cover) is simply calculated via the following equation

$$ERY(z) = ERY\_BI * e^{-K_W z} \quad (9.4)$$

9.1.1 Estimating erythemal UV in the water column

The attenuation values for the various depths in the water column using the coefficient of attenuation for water, K_W = 0.3 m^{-1} were calculated (see Table 9.1 and code for *uw1.pro* in Appendix A). The erythemal UV values were then calculated at 5, 10, 15 and 20 metres within the water column for each region, by multiplying the surface erythemal UV values (see Section 7.6) by the attenuation values calculated as per Table 9.1. These attenuation values are constant across all areas of ocean that are not affected by sea ice. The subsurface erythemal UV levels were calculated and associated plots of the surface and abovementioned depths in the water column were produced (see examples Figures 9.2-9.7). In this chapter ERY represents the erythemal dose rate, DNA represents the DNA dose rate, BEH represents the Behrenfeld dose rate and PHO represents the photoinhibition dose rate (see further explanation in Section 9.2.1).

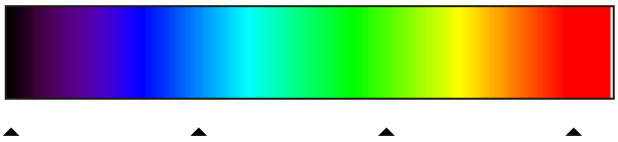

Surface-normalised	0.001	0.01	0.1	1
Grey level	0.0	80	160	240
ERY	0.3	3	30	300
DNA	0.4	4	40	400
BEH	0.6	6	60	600
PHO	0.1	1	10	100

Figure 9.1: Colour table used for plots of dose rates (ERY, DNA, BEH, PHO) (mW m^{-2}).

It should be noted that some plots appear 'flat' as displayed in this thesis, but there was always some unevenness in the values across the plots which is more obvious in versions in Appendix A. The variability in the values across the sub-areas is demonstrated by the minima and maxima displayed beneath the figures as (minimum, maximum), and the normalisation value is displayed as [normalisation value]. The units for all values are (mW m^{-2}).

Figure 9.1 presents the colour table used for display of the various dose rate values in this chapter. The "surface-normalised" scheme was used to represent ratios of the irradiance at the relevant under-water or under-ice position to the surface irradiance (and therefore plotted as an attenuation ratio). The remainder of the rows show the values applied to plot each of the four dose rates based on normalisation by an appropriate constant (selected to be larger than the

maximum value of that dose rate in the whole data set). The upper portion of the colour scale (corresponding to values of 241 and above) was not used, to avoid the appearance of similar shades of red for large values.

The sample plots (Figures 9.2-9.7) are based on the assumption that there is no sea ice present – the effect of the presence of sea ice on levels of erythemal UV in the water column is examined in Section 9.1.4. Figures 9.2 and 9.3 demonstrate the higher surface levels of erythemal UV in November 2001 than in November 2002. It can be seen from the example plots (Figures 9.4 and 9.5) that the pattern of levels of erythemal UV at the surface is transferred down through the water column but at smaller values because of the attenuation of the water.

Research undertaken by Helbling *et al*. (1994) involved exposing phytoplankton to changing irradiances, simulating the effects of moving vertically within the upper mixed layer (UML). They showed an increase in integrated carbon fixation, as compared to stationary samples, by as much as 25% on low irradiance days; however, on sunny days the fixation was lower (by up to 15%) than in stationary samples. The speed of rotation used in these experiments simulated the movement of phytoplankton cells from the surface to 17 metres depth (at which depth the irradiance at 320 nm is equal to approximately 3% of that at the surface) and back to the surface within a 6-hour period. For the purpose of estimating the effect of UVB on marine organisms in the UML, this project has included an average value over the upper 5, 10, 15 and 20 metres of water (see examples in Figure 9.6 and Figure 9.7). Recent research suggests that photodamage incurred during the high irradiance portion of the vertical mixing cycle, rather than light limitation, controls phytoplankton growth in regions of the Southern Ocean with a deep UML (Alderkamp *et al.* 2010). This concept represents a shift from the widely accepted paradigm that phytoplankton growth in the open Southern Ocean is limited by low levels of light or inadequate iron supply (Alderkamp *et al.* 2010).

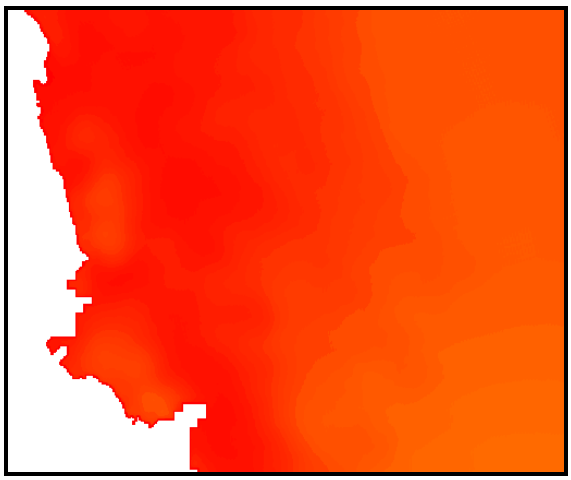

Figure 9.2: Sample plot of surface erythemal UV (mW m^{-2}) for the Amery region for Nov 2001 (157.094, 269.479) [300].

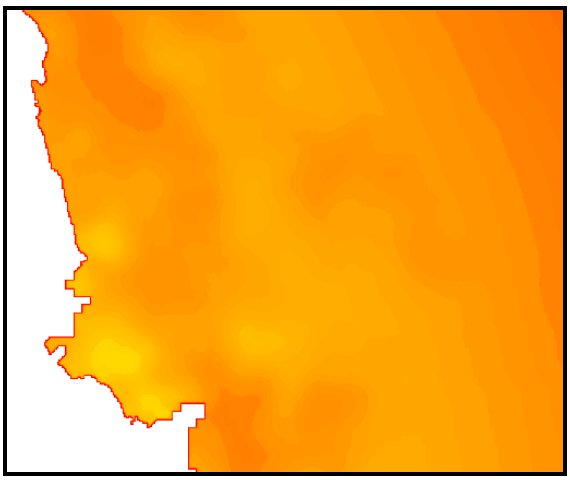

Figure 9.3: Sample plot of surface erythemal UV (mW m^{-2}) for the Amery region for Nov 2002 (89.831, 152.552) [300].

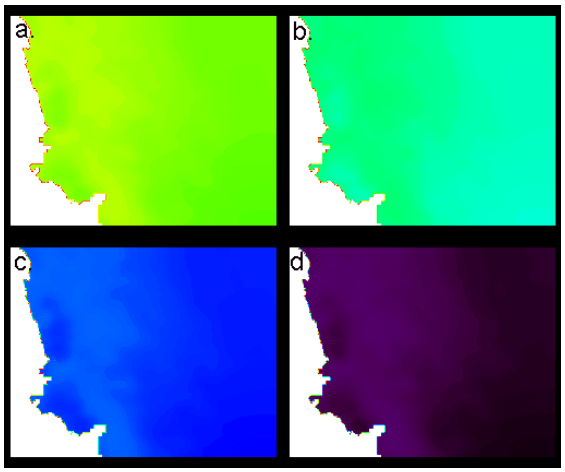

Figure 9.4: Plots of erythemal UV (mW m^{-2}) in water column for Amery region, Nov 2001 at a. 5 m (31.547, 54.116), b. 10 m (7.039, 12.075), c. 15 m (1.571, 2.694) and d. 20 m (0.350, 0.601) [300].

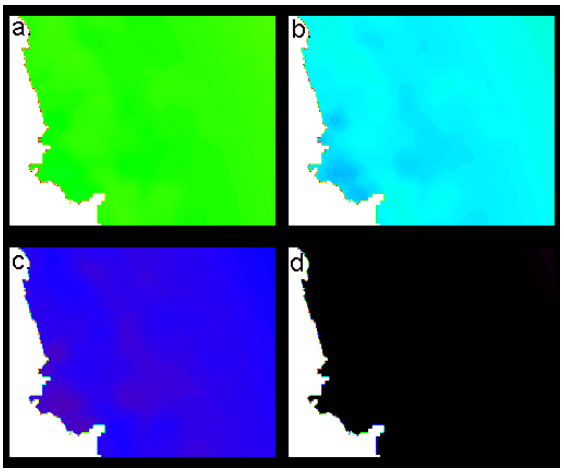

Figure 9.5: Plots of erythemal UV (mW m-2) in water column for Amery region, Nov 2002 at a. 5 m (18.040, 30.635), b. 10 m (4.025, 6.836), c.15 m (0.898, 1.525) and d. 20 m (0.200, 0.340) [300].

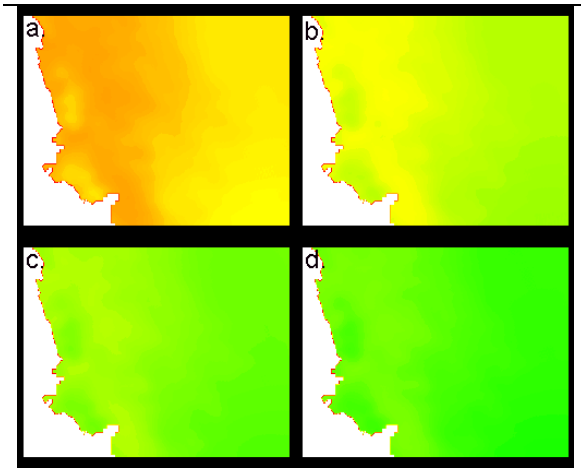

Figure 9.6: Erythemal UV (mW m^{-2}) for Amery region Nov 2001 averaged over a. upper 5 m (73.225, 125.610), b. upper 10 m (44.782, 76.819), c. upper 15 m (31.070, 53.297) and d. upper 20 m (23.506, 40.321) of the water column [300].

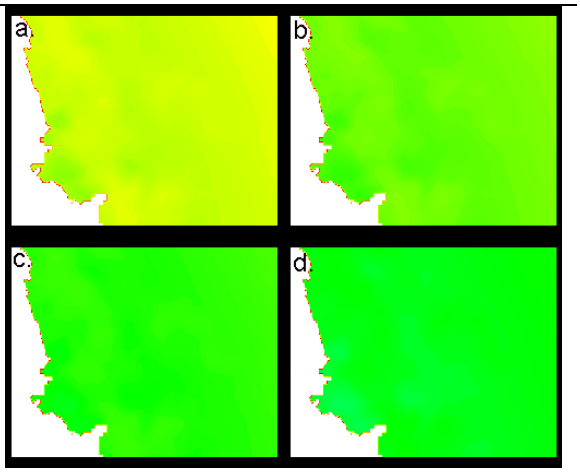

Figure 9.7: Erythemal UV (mW m^{-2}) for Amery region Nov 2002 averaged over a. upper 5 m (41.872, 71.108), b. upper 10 m (25.608, 43.487), c. upper 15 m (17.767, 30.172) and d. upper 20 m (13.441, 22.826) of the water column [300].

It is apparent from the plots of averaged erythemal UV that higher levels of erythemal UV exist in the upper 5 metre deep mixed layer (examples at Figure 9.6a and Figure 9.7a) than at 5 metres below the surface (compared with Figure 9.4a and Figure 9.5a respectively). Similarly, lower values of erythemal UV are evident at 10, 15 or 20 metres below the surface compared with higher averaged levels of erythemal UV for the 0-10 metre, 0-15 metre and 0-20 metre mixed layers. Visual assessment of the plots and comparison of the minimum and maximum values indicate that the levels of erythemal UV in the 0-15 metre mixed layer (Figures 9.6c and 9.7c are approximately equivalent to the levels of erythemal UV at the 5 metre level (Figures 9.4a and 9.5a). As mentioned above, at 17 metres depth the irradiance at 320 nm is equal to approximately 3% of that at the surface (Helbling *et al.* 1994). This is borne out by the low values of erythemal UV at the 20 metre level in Figures 9.4d and 9.5d.

9.1.2 Estimating erythemal UV throughout sea ice/snow

Prior to the development of the ASPeCt dataset (Worby 2008) (see Section 5.4 for details), there was no Antarctic sea ice thickness climatology available to modellers, who instead have often used single mean averages (typically 0.5 to 1.0 m) over the majority of the Antarctic pack (e.g. Hibler and Ackley 1983), with only limited validation from field measurements. For this project, the information about thickness of sea ice and snow in a pixel was extracted from the ASPeCt sea ice/snow thickness dataset.

It should be noted that the ASPeCt data had already been “aggregated” over autumn, summer and spring to improve its spatial coverage (see Section 5.4) and before the ASPeCt data could be integrated into the processing for this module of the project, ice thickness and snow thickness values were interpolated (using nearest neighbour) for pixels that contained no data. Figures

9.8 and 9.9 are plots of the interpolated ASPeCt sea ice and snow thickness data that gave complete spatial coverage of these parameters for the project. As ice increases in thickness, so does the snow cover (compare Figures 9.8 and 9.9). Despite the absolute accuracy of the current AMSR-E snow depth product being an issue, it still provides considerable insight into large-scale spatial patterns of snow depth variability that correspond to similar patterns in ice type and age (Sturm and Massom 2010) as demonstrated by the ASPeCt data. Erythemal UV values were calculated for the top of the ice, middle of the ice, bottom of the ice and at a fixed ice depth, using the formulae as per Table 9.2 and the attenuation coefficients for snow and ice as determined on the SIPEX voyage (see Section 6.7) (see code for *uw1.pro* in Appendix A for details). The levels of erythemal UV within and at the bottom of the ice were calculated using equation 9.1 (where ERY_S equals the surface cloud-affected erythemal UV as described in Section 7.4.5).

Table 9.1: Calculations of attenuation at depths of 5, 10, 15 and 20 metres in water column and averages of attenuation over upper 5, 10, 15 and 20 metres of water column (using attenuation coefficient of water, $K_W = 0.3\ m^{-1}$).

Attenuation at depths 5,10,15,20 m		**Attenuation averaged over depths 5,10,15,20 m**	
Formula	Attenuation value	Formula	Attenuation value
$AW1=\exp(-5.0*K_W)$	0.2213	$AM1=(1.0/(5.0*K_w))*(1-\exp(-5.0*K_w))$	0.5179
$AW2=\exp(-10.0*K_W)$	0.0498	$AM2=(1.0/(10.0*K_w))*(1-\exp(-10.0*K_w))$	0.3167
$AW3=\exp(-15.0*K_W)$	0.0111	$AM3=(1.0/(15.0*K_w))*(1-\exp(-15.0*K_w))$	0.2198
$AW4=\exp(-20.0*K_W)$	0.0025	$AM4=(1.0/(20.0*K_w))*(1-\exp(-20.0*K_w))$	0.1663

Table 9.2: Calculations of erythemal UV, (ERY_) where S=surface, TI=top of ice, MI=middle of ice, BI=bottom of ice, ID=fixed ice depth) using attenuation coefficient of snow, $K_s = 11.3\ m^{-1}$ and of ice $K_i = 2.0\ m^{-1}$. The software can be adjusted to change the 20 cm depth to any other value.

Calculations of levels of erythemal UV for various ice / snow scenarios	
Scenario	Formula
At top of ice under Z_s thickness of snow	$ERY\_TI = ERY\_S * \exp(-Z_s*K_s)$
Under snow and half way through the ice of thickness Z_i	$ERY\_MI = ERY\_TI* \exp(-0.5*Z_i*K_i)$
Under snow and at bottom of the ice of thickness Z_i	$ERY\_BI = ERY\_TI* \exp(-Z_i*K_i)$
Under snow and at fixed depth of 20 cm of ice	$ERY\_ID = ERY\_TI* \exp(-0.2*K_i)$
If ERY_ID is less than ERY_BI then they are made equal	ERY_ID = ERY_BI

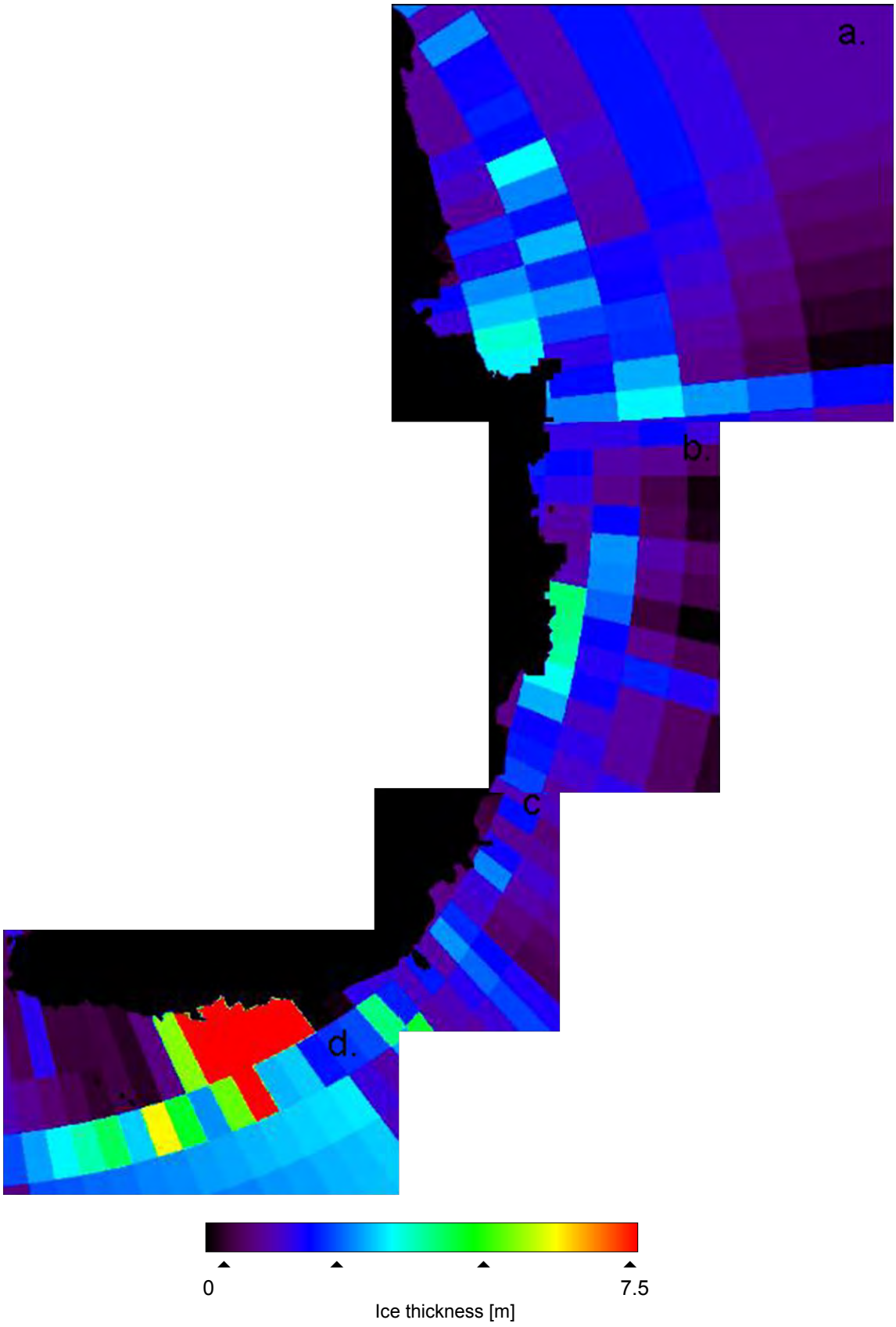

Figure 9.8: Plots of sea ice thickness for: a. Amery region, b. Shackleton region, c. Dalton region and d. Mertz region derived from the ASPeCt sea ice thickness data (Worby 2008).

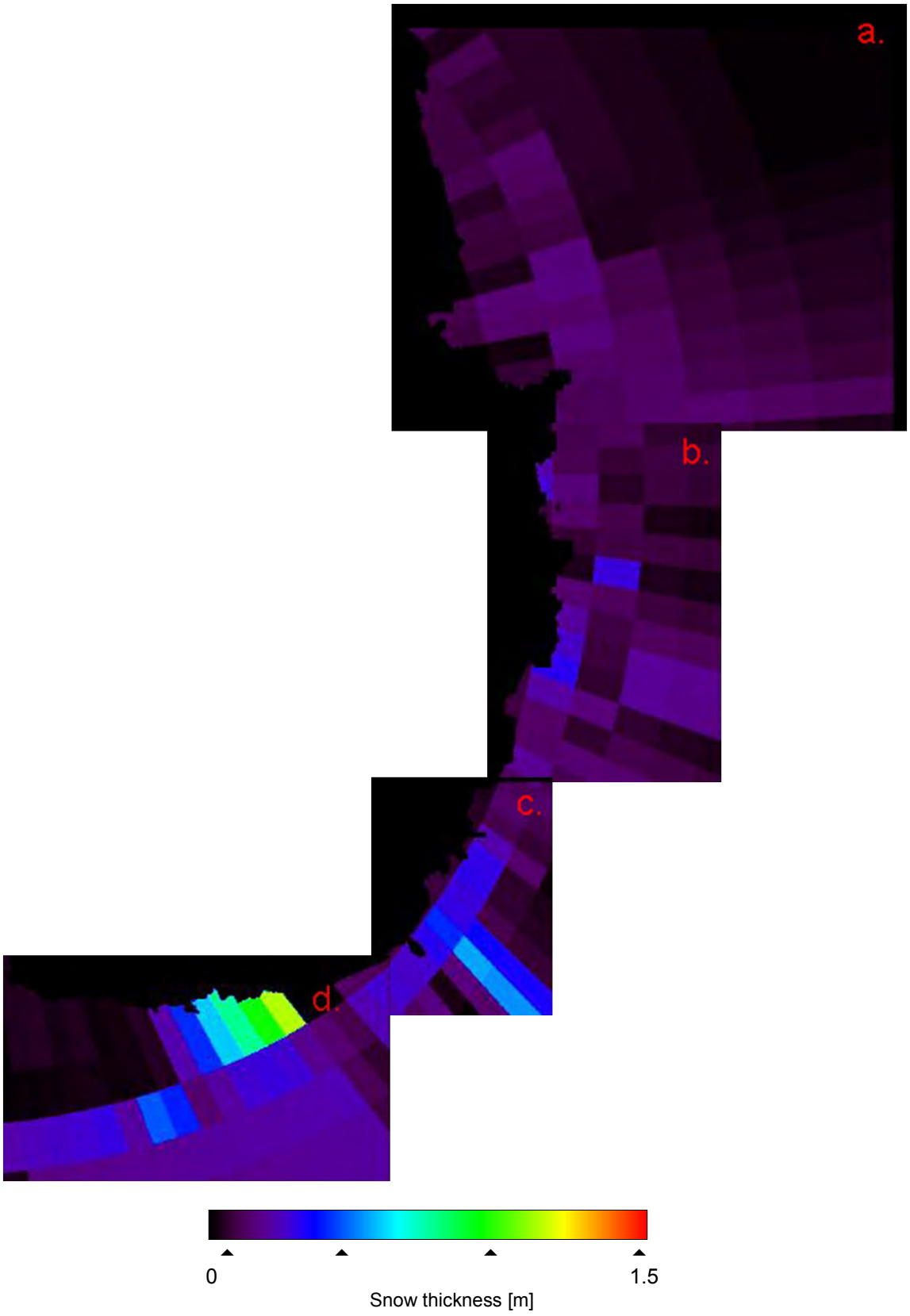

Figure 9.9: Plots of snow thickness for: a. Amery region, b. Shackleton region c. Dalton region and d. Mertz region derived from the ASPeCt sea ice thickness data (Worby 2008).

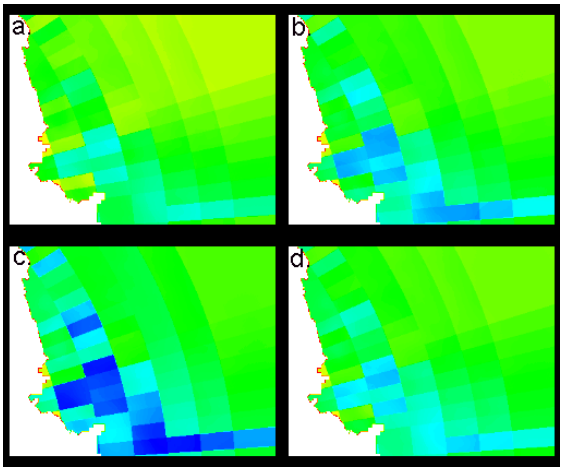

Figure 9.10: Sample plot of erythemal UV (mW m^{-2}) for Amery region Nov 2001 a. at top of ice under snow of z_S thickness (5.76, 73.69); b. under snow and half way through ice of z_I thickness (3.26, 73.69); c. under snow and at bottom of ice (1.68, 73.69); and d. under snow and at fixed depth of ice, i.e. 20 cm (4.00, 73.69) [300].

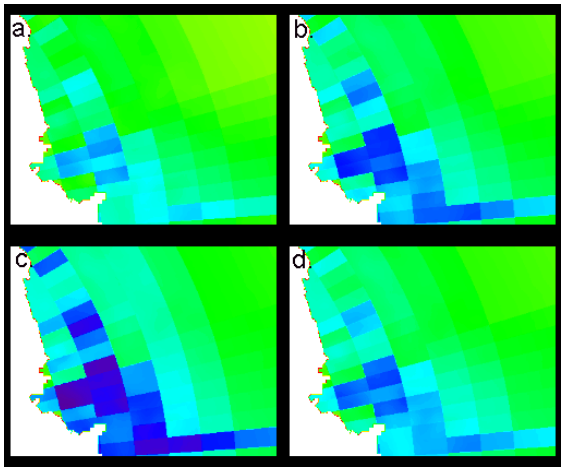

Figure 9.11: Sample plot of erythemal UV (mW m^{-2}) for Amery region Nov 2002 a. at top of ice under snow of z_S thickness (2.93, 43.56); b. under snow and half way through ice of thickness z_i (1.65, 35.80); c. under snow and at bottom of ice (0.87, 35.80); and d. under snow and at fixed depth of ice, i.e. 20 cm (2.04, 35.80) [300].

Figure 9.12: A sample plot of surface erythemal UV (mW m^{-2}) for Shackleton region Nov 2000 (104.22, 163.69) [300].

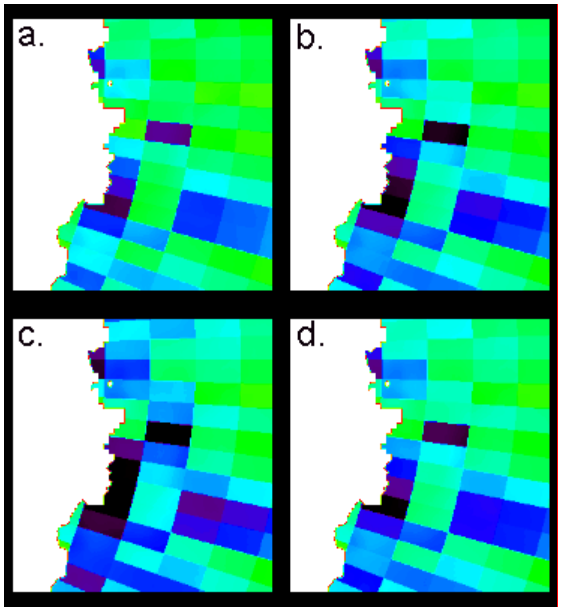

Figure 9.13: A sample plot of erythemal UV (mW m^{-2}) for Shackleton region Nov 2000 a. at top of ice under snow of z_S thickness (0.40, 39.78); b. under snow and half way through ice of thickness z_i (0.18, 33.52); c. under snow and at bottom of ice (0.08, 28.25) and d. under snow and at fixed depth of ice, i.e. 20 cm (0.28, 28.25) [300].

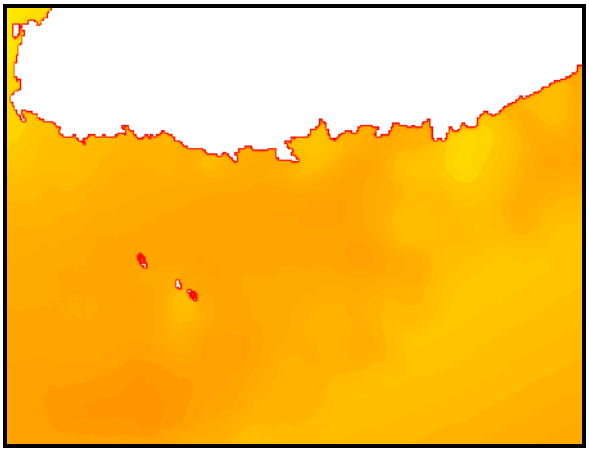

Figure 9.14: Sample plot of surface erythemal UV (mW m^{-2}) for the Mertz region Nov 2000 (82.318, 129.257) [300].

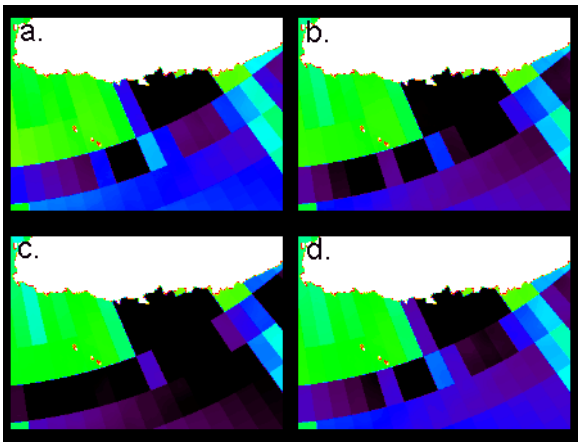

Figure 9.15: Sample plot of erythemal UV (mW m^{-2}) for the Mertz region Nov 2000 a. at top of ice under snow of thickness z_S (1.577e-6, 39.213); b. under snow and half way through ice of thickness z_i (1.258e-09, 39.177); c. under snow and at bottom of ice (1.366e-12, 39.141); and d. under snow and at fixed depth of ice, i.e. 20 cm (8.045e-07, 39.141) [300].

Sample plots of erythemal UV (Figures 9.2, 9.3 and 9.10-9.15) were inspected and compared with the plots of snow and ice thickness (Figures 9.8 and 9.9). These plots of erythemal UV at the surface, and within and beneath the ice, demonstrated the diminution of the levels of erythemal UV by the thickness of snow at the snow-ice interface – see examples, Figure 9.13a in the Shackleton Ice Shelf region and Figure 9.15a in the Cook Ice Shelf region (see Figure 2.3). This result was expected as the attenuation coefficient of snow is the highest of all three media (i.e. 11.3 m^{-1}). Examples of the combined effect of snow and ice in reducing values of erythemal UV reaching levels within the ice and at the under-surface of the ice can be seen in snow- and ice-covered pixels in Figures 9.10b, 9.10c and 9.10d; 9.11b, 9.11c and 9.11d; 9.13b, 9.13c and 9.13d; and 9.15b, 9.15c and 9.15d. Comparing Figure 9.15b (min. = 0.18 mW m^{-2}, max. = 34.01 mW m^{-2}) and Figure 9.15d (min. = 0.29 mW m^{-2}, max. = 28.18 mW m^{-2}) showed that levels of erythemal UV midway through the ice and at 20 cm within the ice cover are reasonably similar, reflecting the statistics from the interpolated ASPeCt data (Table 9.3), which showed the mean sea ice thickness to be 0.54 m over the East Antarctic sea ice zone.

Table 9.3: Snow and ice thickness statistics extracted from the interpolated ASPeCt data.

	Ice	**Snow**
Mean (m)	0.54	0.17
Standard dev.	0.55	0.03
Minimum (m)	0.001	0.009
Maximum (m)	7.5	1.5

9.1.3 Erythemal UV in the water column beneath sea ice/snow

When calculating the erythemal UV levels under the snow/ice plus 5, 10, 15 and 20 metres of water, the ice draft was approximated as z_i*0.9 (J.L. Lieser, pers. comm., 2010) (see Table 9.4 for the calculations of the four levels within the water column under the snow/ice). Comparison of Figure 9.13 and Figure 9.16 demonstrates the low levels of erythemal UV that would ultimately affect organisms living in the water column beneath a cover of ice and snow – a gradual reduction occurred with depth, resulting in very little effect at the 20 metre level (examples in Figure 9.16c, min. = 0.001 mW m^{-2}, max. = 0.329 mW m^{-2} and Figure 9.16d, min. = 0.0002 mW m^{-2}, max. = 0.073 mW m^{-2}).

Table 9.4: Calculations of erythemal UV, at 5, 10, 15 and 20 m in water column under snow/ice (using coefficient K_W = 0.3 m^{-1}, and value of ERY_BI as calculated in Table 9.2).

Scenario	**Formula**
Beneath ice / snow at 5 m depth of water (Z1=5.0 – draft where draft=Zi*0.9)	ERY_Z1 = ERY_BI*exp(-Z1*K_W)
If draft greater than 5.0 then	ERY_Z1 = ERY_BI
Beneath ice / snow at 10 m depth of water (Z2=Z1+5)	ERY_Z2 = ERY_BI * exp(-Z2* K_W)
Beneath ice / snow at 15 m depth of water (Z3=Z2+5)	ERY_Z3 = ERY_BI * exp(-Z3* K_W)
Beneath ice / snow at 20 m depth of water (Z4=Z3+5)	ERY_Z4 = ERY_BI * exp(-Z4* K_W)

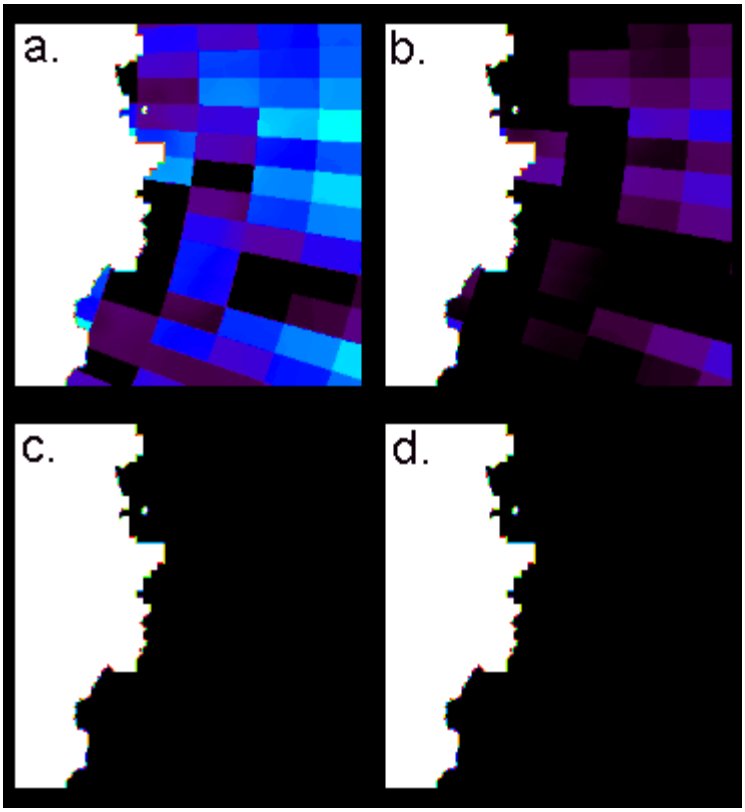

Figure 9.16: Sample plot of erythemal UV (mW m^{-2}) for Shackleton region Nov 2000 in the water column beneath snow and ice at: a. Z1 (0.023, 6.632), b. at Z2 (0.005, 1.480), c. at Z3 (0.001, 0.330) and d. at Z4 (0.0003, 0.074) [300] (where depths (Zx) are detailed in Table 9.4).

In general, a pixel will not be totally covered by sea ice, as implied in the above calculation. To examine the situation where a pixel is partially covered, the sea ice concentration was included in the calculations to arrive at pixel-averaged erythemal UV at the specified depths of 5, 10, 15 and 20 metres below the ocean or ice surface (see Table 9.5).

Table 9.5: Calculations of pixel averaged erythemal UV at Z1, Z2, Z3 and Z4 in water column weighted by sea ice concentration (si) (using values of erythemal UV throughout water column ERY_S * AW1 etc. (as per calculations in Table 9.1) and ERY_Z1 etc. as calculated in Table 9.4).

Calculations of levels of pixel-averaged erythemal UV for various scenarios in water column beneath ice / snow	
Scenario	Formula
Beneath ice / snow at 5 m depth of water	ERY_P1 = ERY_W1*(1.0-si) + ERY_Z1*(si)
Beneath ice / snow at 10 m depth of water	ERY_P2 = ERY_W2*(1.0-si) + ERY_Z2*(si)
Beneath ice / snow at 15 m depth of water	ERY_P3 = ERY_W3*(1.0-si) + ERY_Z3*(si)
Beneath ice / snow at 20 m depth of water	ERY_P4 = ERY_W4*(1.0-si) + ERY_Z4*(si)

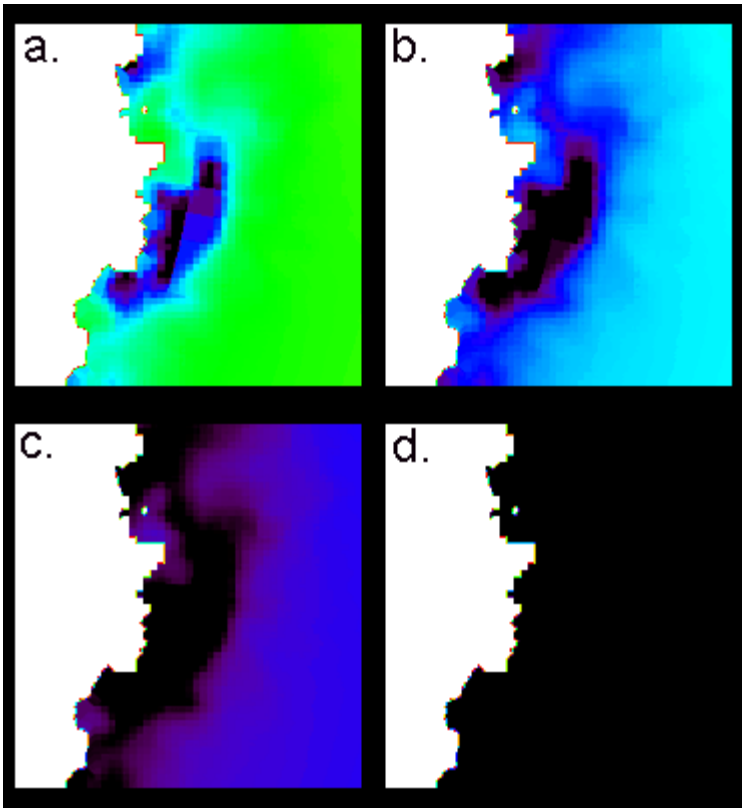

Figure 9.17: Sample plot of pixel-averaged erythemal UV (mW m^{-2}) for Shackleton region Nov 2000 beneath snow and ice at a. Z1 (0.025, 26.737), b. Z2 (0.006, 5.966), c. Z3 (0.001, 1.331) and d. Z4 (0.0003, 0.297) [300] (where depth Zx are detailed in Table 9.4).

Comparison of Figure 9.16 and Figure 9.17 demonstrates the reduction in the attenuation of the erythemal UV values when the sea ice concentration is taken into account, although at 20 metres, the levels of erythemal UV are very low (see minima and maxima erythemal UV values for the four different scenarios). The pixel-averaged values of erythemal UV in Figure 9.17a-9.17c. demonstrate the reducing effect of thick ice in the averaging process in the Shackleton Ice Shelf and West Ice Shelf regions.

9.2 Biological dose rates

The effective UV irradiance acting on a specific biological system is obtained by weighting the incoming spectral UV irradiance with its corresponding "action spectrum" (Luccini *et al.* 2006). Estimating the effects of UV is complicated by variations in sensitivity among phytoplankton and a strong spectral dependence of inhibition. In addition to differences in sensitivity, species may differ in their acclimation capabilities (Roy 2000). The finding by Fritz *et al*. (2008), that open-water phytoplankton assemblages have a slow repair capability, has important implications for modelling UVR effects on primary productivity in the surface mixed layer (e.g. Arrigo *et al.* 2003a). Polychromatic, biological weighting functions (BWFs) quantifying spectral distribution of the biological response are essential for predicting the UV effects correctly (Cullen *et al.* 1992; Neale *et al.* 2001b; Litchman and Neale 2005).

While all BWFs give greater effectiveness to shorter wavelengths of UV, the rate at which they decline with higher UV wavelengths, and how far their tails extend into these higher wavelengths, vary appreciably. This variation can lead to large differences among BWFs in their radiation amplification factor (RAF) (Day and Neale 2002). The RAF is the proportional increase in biologically-effective UV produced by a given decrease in ozone column (Booth and Madronich 1994). The differences in the wavelength dependency of UVB radiation damages depends on what indicator is measured, and what species is studied (Andreasson and Wängberg 2007).

Many BWFs for UV inhibition of phytoplankton photosynthesis have been developed in the past using solar simulators (Cullen *et al.* 1992; Neale *et al.* 1994; Neale 2000; Neale and Kieber 2000). Even though spectral responses of phytoplankton to UV are highly variable, some general patterns have emerged (Banaszak and Neale 2001). The spectral shape of BWFs in the UVB is similar to that suggested by Behrenfeld *et al.* (1993) when averaged over all assemblages for a specific region (e.g. Chesapeake Bay or Southern Ocean), but specific assemblages can diverge widely from the average (Day and Neale 2002). Work on this subject is focussing on how to better relate phytoplankton BWFs to environmental conditions (Litchman *et al.* 2002) to achieve more accurate assessments of UV effects on global aquatic primary productivity. In the meantime, an examination of UV spectral responses at some level is needed in any study purporting to estimate the effects of UVB and ozone depletion on aquatic productivity (Day and Neale 2002). Andreasson and Wängberg (2006) determined that a BWF is a good tool for comparing communities, treatments or methods, but recommended caution when taking results from artificial light with unbalanced amounts of UVA and UVB radiation and PAR to produce conclusions about field conditions.

9.2.1 Mathematical formulation of BWFs

Ali (2001) estimated the potential for UVR to impact on marine organisms by examining attenuation characteristics of water and sea ice in the Antarctic sea ice zone. Damage to marine organisms by a specified level of UV surface irradiance was considered by using BWFs to provide an appropriate biologically effective dose. The following are the BWFs included in the research by Ali (2001):

- Erythemal weighting function (D_{ERY}) by McKinley and Diffey (1987);
- Weighting function for DNA (D_{DNA}) by Setlow (1974) (from Smith and Baker (1980));
- Weighting function for photoinhibition (D_{BEH}) by Behrenfeld *et al.* (1993); and
- Weighting function for photoinhibition (D_{PHO}) by Jones and Kok (1966) (from Smith and Baker (1980)).

These BWFs were modified for the present study, using software developed by Ali (2001), which then allowed comparisons to be made between them. Datasets of UV surface irradiances were generated by the libRadtran model (Mayer *et al*. 2006) for 1st November at 65° S, at 30-minute intervals between 04:00-12:00 local time. The noon SZA on this date was 49.4813°, and the surface albedo was set to 0.80, an appropriate value for snow-covered sea ice (Perovich *et al*. 1998). The model produced the direct beam irradiance and the diffuse downward irradiance, which were added to provide the total down-welling UV irradiance. Datasets were produced for five different amounts of ozone (150, 200, 250, 300 and 350 DU).

To calculate a biologically-effective UV dose, each BWF was multiplied by the UV surface irradiance spectrum at one time, for example at 04:00 local time, and summed over the spectrum from 280-400 nm to obtain the actual dose for each weighting function at that time of the day. This calculation was repeated for each 30-minute interval for each of the five levels of ozone. Each calculated dose ($\mathcal{E}_{DNA}, \mathcal{E}_{BEH}, \mathcal{E}_{PHO}$) was plotted against the erythemal dose ($\mathcal{E}_{ERY}$). The DNA biological weighting function is heavily weighted to the smaller wavelengths (see Figure 9.18).

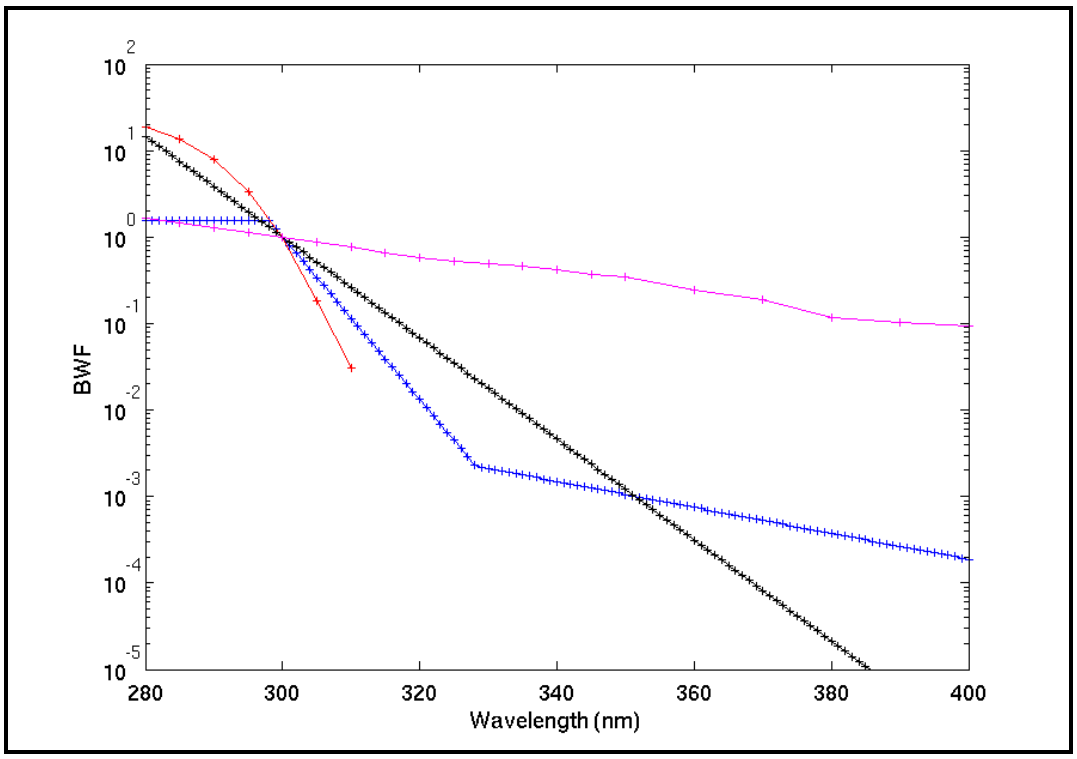

Figure 9.18: The five modified BWF, erythemal (blue), DNA (red), Behrenfeld (black) and photoinhibition (pink) used for the analysis of relations between erythemal and other doses. All BWF are normalised to 1.0 at 300 nm and are unit-less (Figure 3.1 in Ali 2001).

Based on the plots of the relations between doses, different standard IDL routines (POLYFIT, SVDFIT and COMFIT) were applied to the data to obtain *best-fit* functions for the relations between each of the three calculated doses (D_{DNA}, D_{BEH}, D_{PHO}) and the erythemal dose (D_{ERY}). The mathematical relation between D_{DNA} and D_{ERY} for all five values of ozone is described by the following set of equations:

$$D_{DNA150} = 2.80 * 10^{-1} * D_{ERY150} + 2.92 * 10^{-3} * (D_{ERY150})^2$$

$$D_{DNA200} = 1.88 * 10^{-1} * D_{ERY200} + 3.35 * 10^{-3} * (D_{ERY200})^2$$

$$D_{DNA250} = 1.31 * 10^{-1} * D_{ERY250} + 3.64 * 10^{-3} * (D_{ERY250})^2 \qquad (9.5)$$

$$D_{DNA300} = 9.27 * 10^{-2} * D_{ERY300} + 3.80 * 10^{-3} * (D_{ERY300})^2$$

$$D_{DNA350} = 6.61 * 10^{-2} * D_{ERY350} + 3.85 * 10^{-3} * (D_{ERY350})^2$$

The geometric function which describes the relation between D_{BEH} and D_{ERY} for all five values of ozone is given below:

$$\begin{aligned} D_{BEH150} &= 3.09 * (D_{ERY150})^{9.16*10\text{-}1} \\ D_{BEH200} &= 3.21 * (D_{ERY200})^{9.28*10\text{-}1} \\ D_{BEH250} &= 3.23 * (D_{ERY250})^{9.43*10\text{-}1} \\ D_{BEH300} &= 3.21 * (D_{ERY300})^{9.59*10\text{-}1} \\ D_{BEH350} &= 3.17 * (D_{ERY350})^{9.74*10\text{-}1} \end{aligned} \qquad (9.6)$$

The geometric function which describes the relation between D_{PHO} and D_{ERY} is given below:

$$\begin{aligned} D_{PHO150} &= 1.99 * (D_{ERY150})^{6.52*10\text{-}1} \\ D_{PHO200} &= 2.24 * (D_{ERY200})^{6.66*10\text{-}1} \\ D_{PHO250} &= 2.44 * (D_{ERY250})^{6.81*10\text{-}1} \\ D_{PHO300} &= 2.59 * (D_{ERY300})^{6.96*10\text{-}1} \\ D_{PHO350} &= 2.72 * (D_{ERY350})^{7.09*10\text{-}1} \end{aligned} \qquad (9.7)$$

The above equations represent the key results produced by Ali (2001).

In this study, the coefficients in each of the equations, 9.5, 9.6 and 9.7 were separately analysed against a scaled ozone column (oz = TOC/1000) to derive more versatile relationships, which permit conversion of D_{ERY} into the other dose values for any value of ozone. Figures 9.19a – 9.19f are plots of the relationship for each of D_{DNA}, D_{BEH} and D_{PHO} with D_{ERY}. From each of these plots an equation was determined, which explained the relationship between a dose rate and the ozone value.

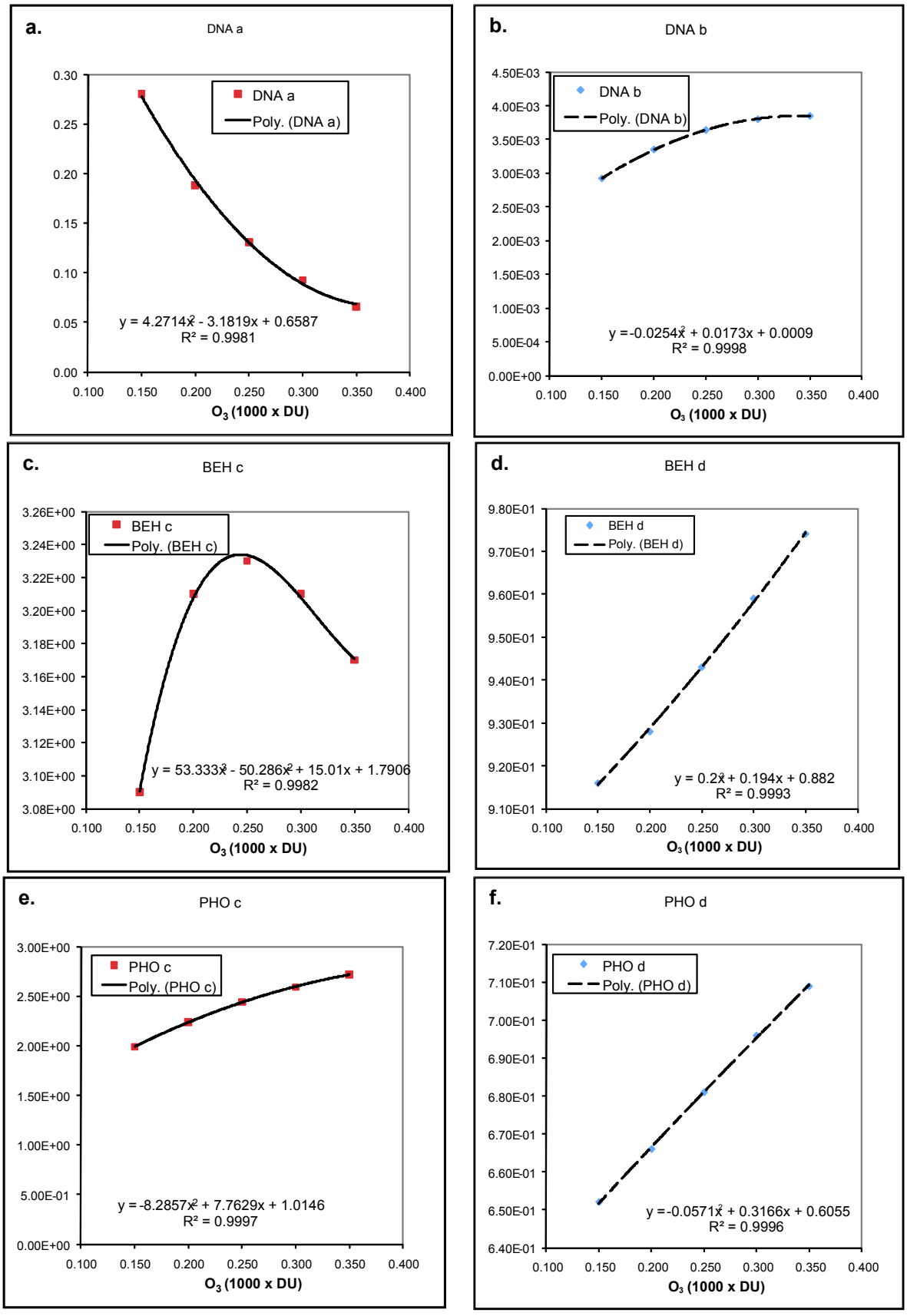

Figure 9.19: Plots of the relationship for coefficients in equations 9.5, 9.6 and 9.7 *vs* ozone column (scaled by 1000)$_Y$.

Table 9.6: Equations and coefficients relating biological dose rates to ozone. DNA denotes the Setlow dose rate, BEH is the Behrenfeld dose rate, PHO is the photoinhibition dose rate (as referenced in this section), and (_S) signifies the specified biological dose rate at the surface.

Equation relating DNA dose to ozone
DNA_S = DNAa*ERY_S + DNAb*ERY_S*ERY_S
First conversion coefficient (DNAa):
DNAa = 4.2714*oz*oz – 3.1819*oz + 0.6587
Second conversion coefficient (DNAb):
DNAb =-0.0254*oz*oz + 0.0173*oz + 0.0009
Equation relating BEH dose to ozone
BEH_S = BEHc*(ERY_S^BEHd)
First conversion coefficient (BEHc):
BEHc = 53.333*oz^3 – 50.286*oz*oz + 15.01*oz + 1.7906
Second conversion coefficient (BEHd):
BEHd = 0.200*oz*oz + 0.194*oz + 0.882
Equation relating PHO dose to ozone
PHO_S = 100*PHOc*(ERY_S^PHOd)
First conversion coefficient (PHOc):
PHOc =-8.2857*oz*oz + 7.7629*oz + 1.0146
Second conversion coefficient (PHOd):
PHOd =-0.0571*oz*oz + 0.3166*oz + 0.6055

9.2.2 Developing maps of biological dose rates

Because the other BWFs have a different action spectrum to the erythemal BWF, then the depletion of the derived doses with distance in water, snow or ice will be different from the erythemal dose. Therefore, it is extremely important to present maps of these separate BWFs for the benefit of scientists studying biological systems for which the DNA and the two different photoinhibition doses are relevant.

The relationships between dose rate and ozone value (Table 9.6) were utilised to determine the biological dose rate for a given pixel in an AVHRR image, given the erythemal UV dose and the ozone value for that time and place (see the code for *uw1.pro* in see Appendix A). The dose conversion coefficients are determined by the ozone values (see Table 9.6). For the mathematical relationship between D_{ERY} and D_{DNA}, a decrease in ozone values is accompanied by a shift of the relation towards higher values of D_{DNA}. Conversely, for the relationship between D_{ERY} and D_{BEH} (D_{PHO}), a decrease in ozone values is accompanied by a shift of the relation towards lower values of D_{BEH} (D_{PHO}). Figures 9.26 and 9.30 demonstrate how the DNA dose rate is more strongly attenuated in water and ice than erythemal UV dose rate (Figures 9.25 and 9.29). The BEH dose rate is not as strongly attenuated in water and ice (see Figures 9.27 and

9.31) and PHO dose rate is attenuated even less (see Figures 9.28 and 9.32). Plots of levels were produced for the various biological dose rates (i) at the surface; (ii) under snow and within and under ice; and (iii) under snow, ice (see examples Figures 9.25-9.28) and water (see examples Figures 9.29-32).

Levels of erythemal UV are affected not only by ozone, but also by sea ice concentration and cloud (see Section 8.3.4). Generally, sea ice concentration decreases in a northerly direction, and TOC also increases in a northerly direction during the months when ozone depletion is evident. Hence, one effect can counteract the other. This makes it difficult to visually discern the effect of low levels of TOC on biological dose rates if concurrent sea ice concentrations were high near the coast. Figure 9.20 provides an example of a plot for a month/year with ozone values which do not vary in a north-south direction. The figure shows larger values of TOC in the north-east (i.e. bottom right) corner of the plot for November than for the rest of the region. Figures 9.21-9.24 demonstrate lower levels of the biological dose rates in the same north-east corner as the high TOC than for the rest of the region.

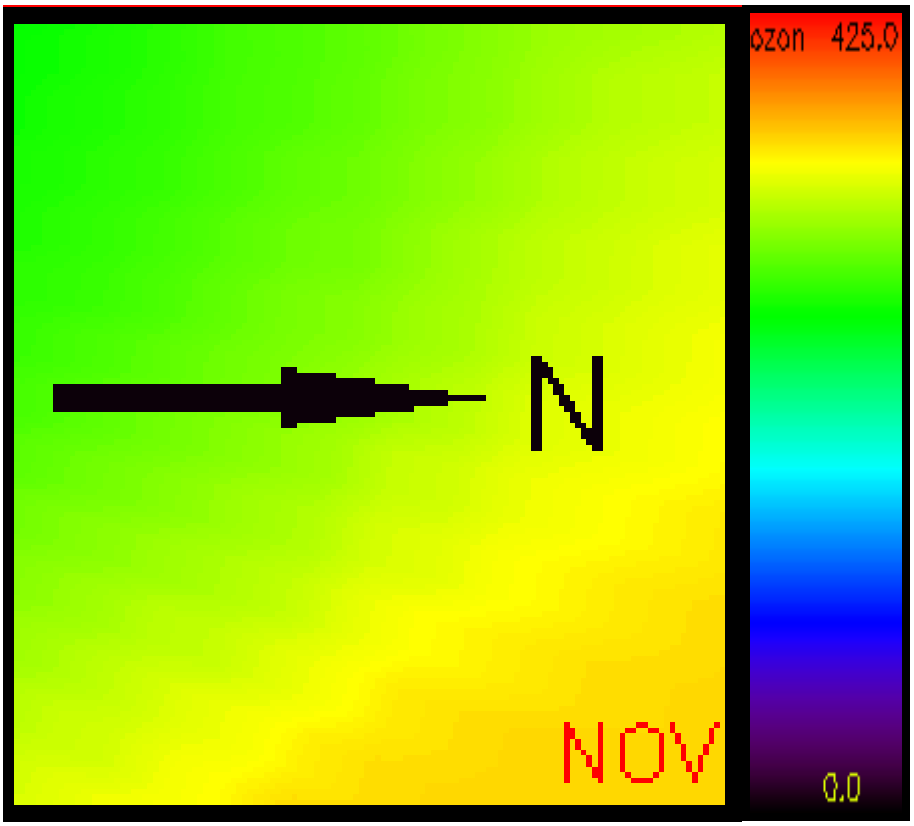

Figure 9.20: Plot of average ozone for November 2000 in the Shackleton region and colour bar showing the range of ozone values in DU (0.0-425.0).

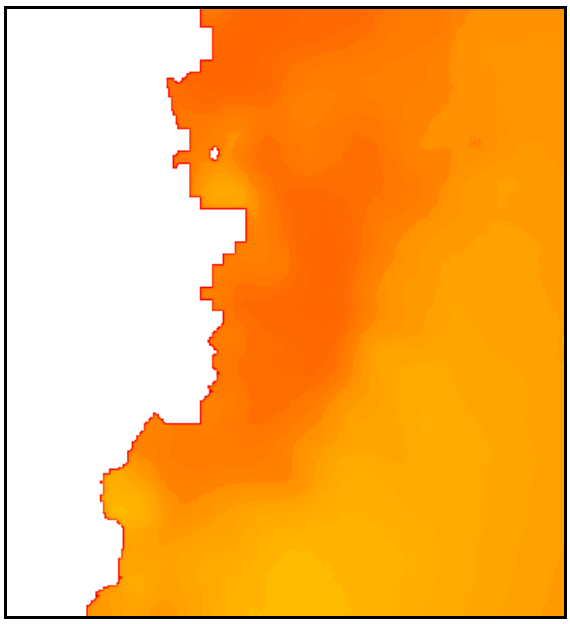

Figure 9.21: Sample plot of surface erythemal UV (mW m^{-2}) for Shackleton region for Nov 2000 (104.219, 163.687) [300].

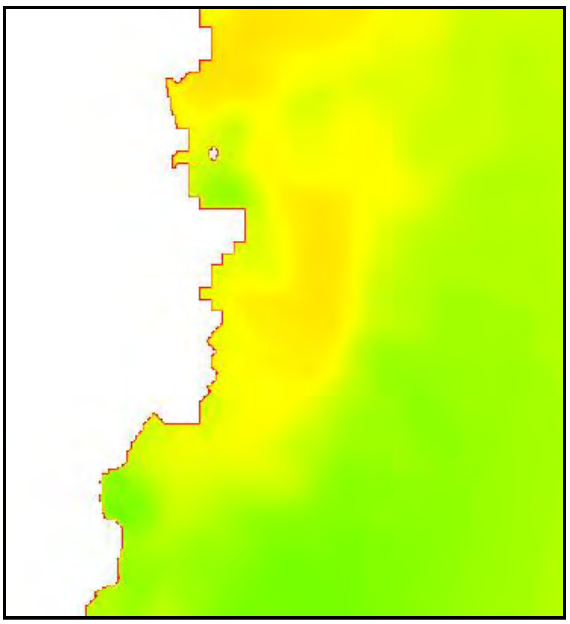

Figure 9.22: Sample plot of surface DNA dose rate (mW m^{-2}) for Shackleton region for Nov 2000 (48.724, 116.785) [400].

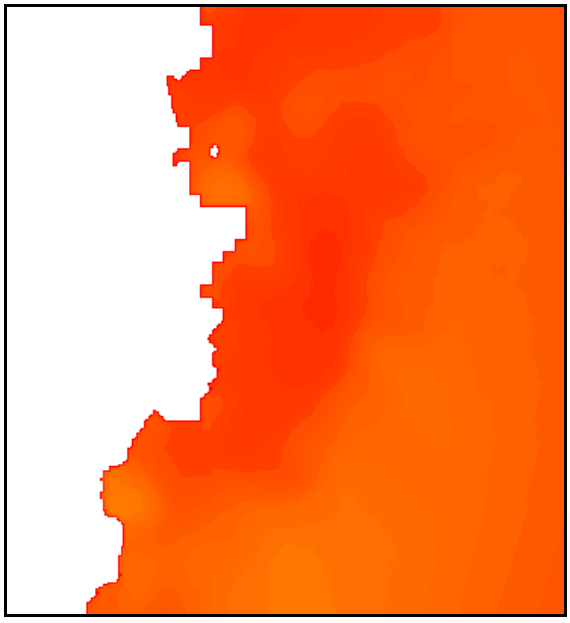

Figure 9.23: Sample plot of surface BEH dose rate (mW m^{-2}) for Shackleton region for Nov 2000 (288.881, 431.824) [600].

Figure 9.24: Sample plot of surface PHO dose rate (mW m^{-2}) for Shackleton region for Nov 2000 (70.075, 93.585) [100].

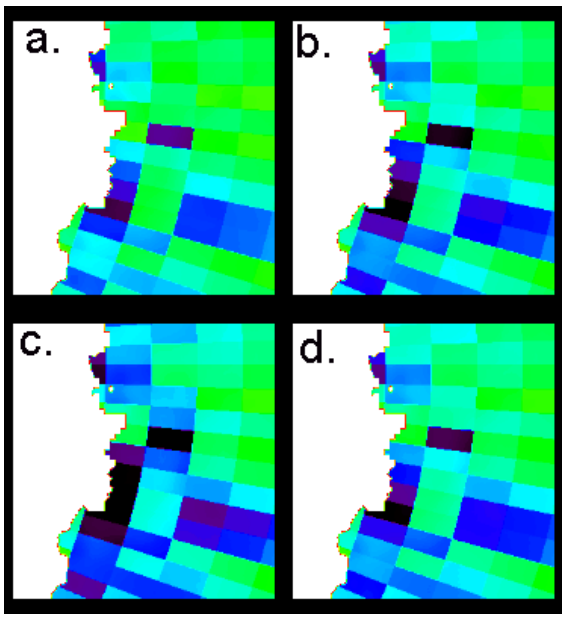

Figure 9.25: Sample plot of erythemal UV (mW m^{-2}) for Shackleton region for Nov 2000 at a. top of ice beneath snow of thickness Z_s (0.404, 39.777); b. under snow and half way through ice of thickness Z_i (0.182, 33.522); c. under snow and at bottom of ice (0.082, 28.251); and d. under snow and at fixed depth of ice, i.e. 20 cm (0.281, 28.251) [300].

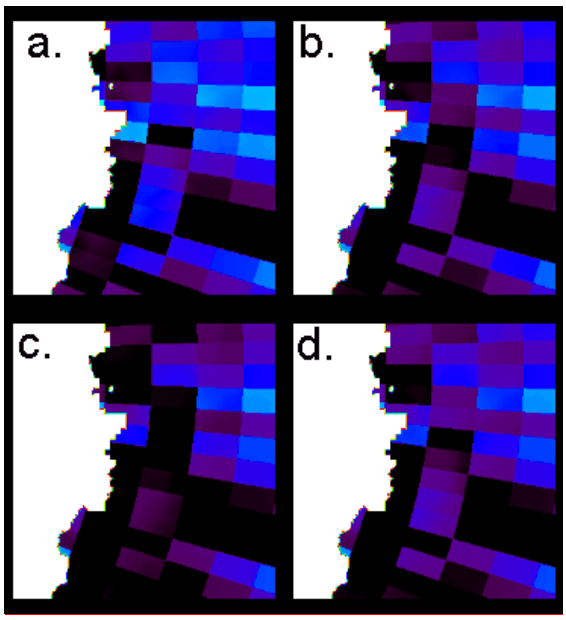

Figure 9.26: Sample plot of DNA dose rate (mW m^{-2}) for Shackleton region for Nov 2000 at a. top of ice beneath snow of thickness Z_s (0.032, 9.642); b. under snow and half way through ice of thickness Z_i (0.014, 7.330); c. under snow and at bottom of ice (0.006, 5.613); and d. under snow and at fixed depth of ice, i.e. 20 cm (0.022, 5.613) [400].

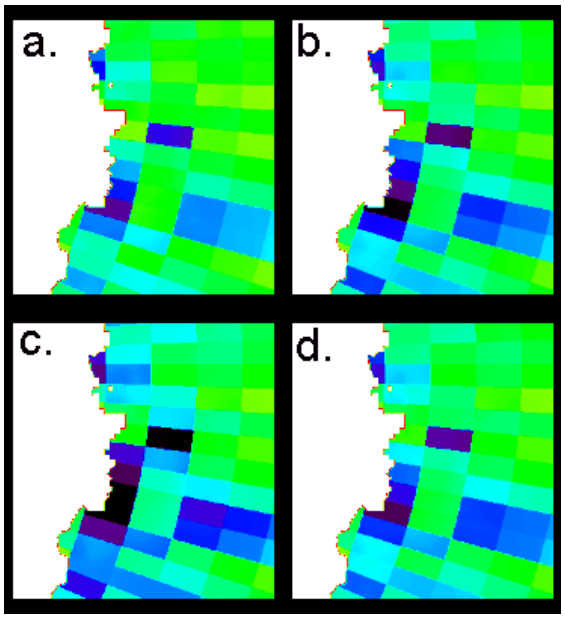

Figure 9.27: Sample plot of BEH dose rate (mW m^{-2}) for Shackleton region for Nov 2000 a. at top of ice under snow of thickness Z_s (1.332, 108.930); b. under snow and half way through ice of thickness Z_i (0.616, 92.483); c. under snow and at bottom of ice (0.285, 78.519); and d. under snow and at fixed depth of ice, i.e. 20 cm (0.938, 78.519) [600].

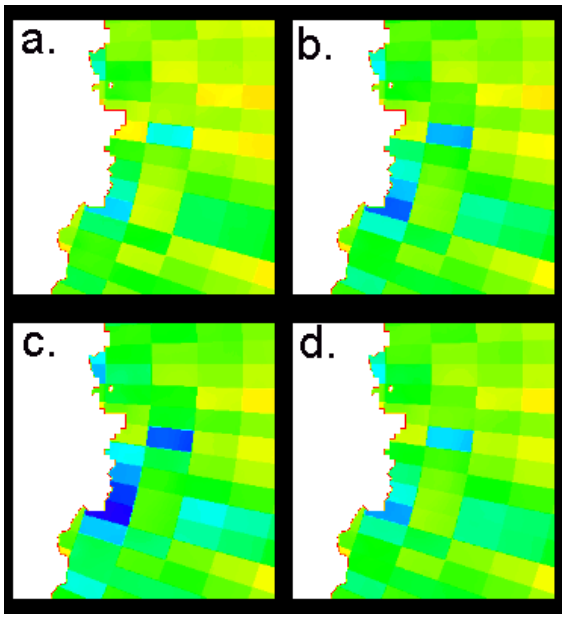

Figure 9.28: Sample plot of PHO dose rate (mW m^{-2}) for Shackleton region for Nov 2000 a. at top of ice under snow of thickness Z_s (1.403, 33.314); b. under snow and half way through ice of thickness Z_i (0.801, 29.585); c. under snow and at bottom of ice (0.457, 27.235); and d. under snow and at fixed depth of ice, i.e. 20 cm (1.087, 27.235) [100].

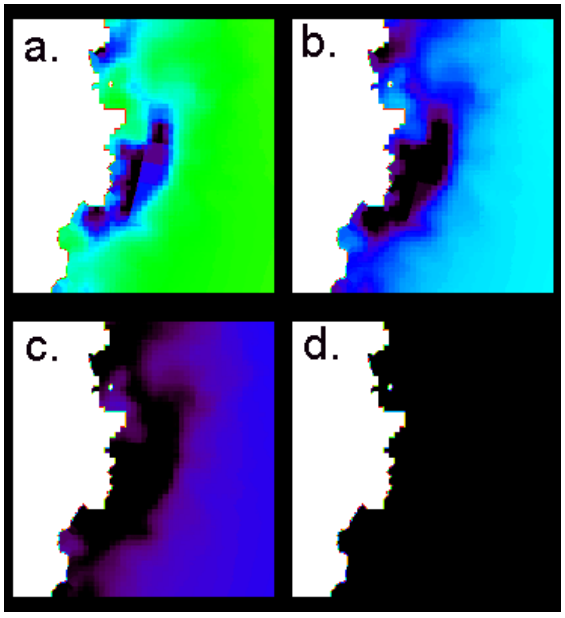

Figure 9.29: Sample plot of pixel-averaged erythemal UV (mW m^{-2}) for Shackleton region for Nov 2000 beneath snow and ice at a. Z1 (0.025, 26.737); b. at Z2 (0.006, 5.966); c. at Z3 (0.001, 1.331); and d. at Z4 (0.0003, 0.297) (where Z1, Z2, Z3 and Z4 are detailed in Table 9.4) [300].

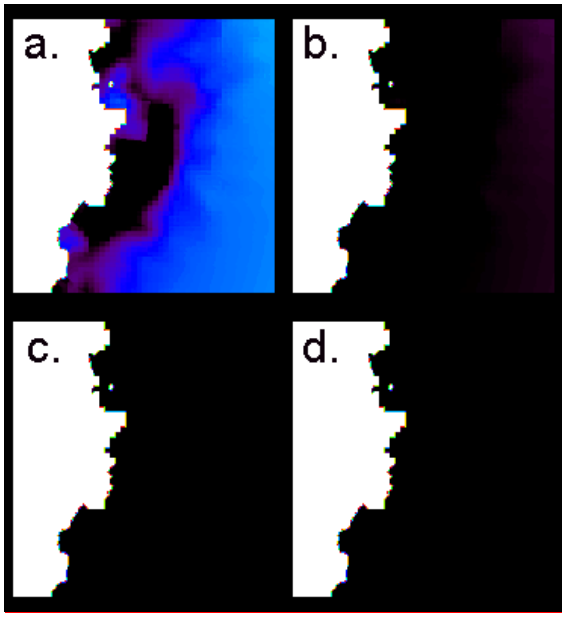

Figure 9.30: Sample plot of pixel-averaged DNA dose rate (mW m^{-2}) for Shackleton region for Nov 2000 beneath snow and ice at a. Z1 (0.002, 4.801); b. at Z2 (0.0004, 0.596); c. at Z3 (9.566e-05, 0.109); and d. at Z4 (2.134e-05, 0.023) (where Z1, Z2, Z3 and Z4 are detailed in Table 9.4) [400].

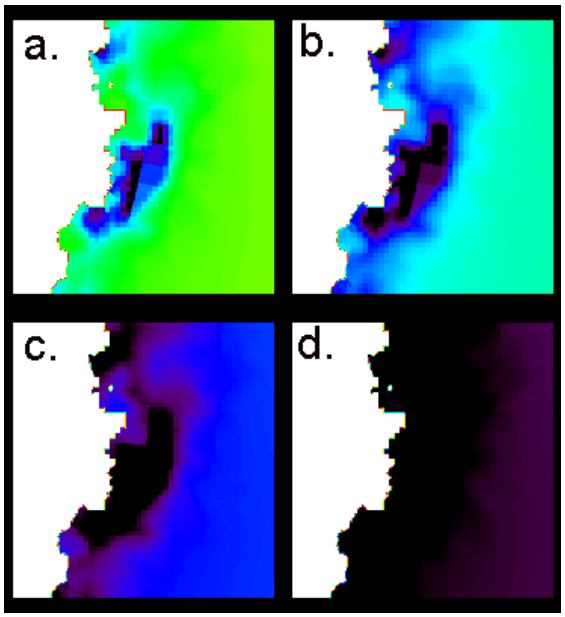

Figure 9.31: Sample plot of pixel-averaged BEH dose rate (mW m^{-2}) for Shackleton region for Nov 2000 beneath snow and ice at a. Z1 (0.092, 76.096); b. at Z2 (0.022, 17.888); c. at Z3 (0.005, 4.205); and d. at Z4 (0.001, 0.989) (where Z1, Z2, Z3 and Z4 are detailed in Table 9.4) [600].

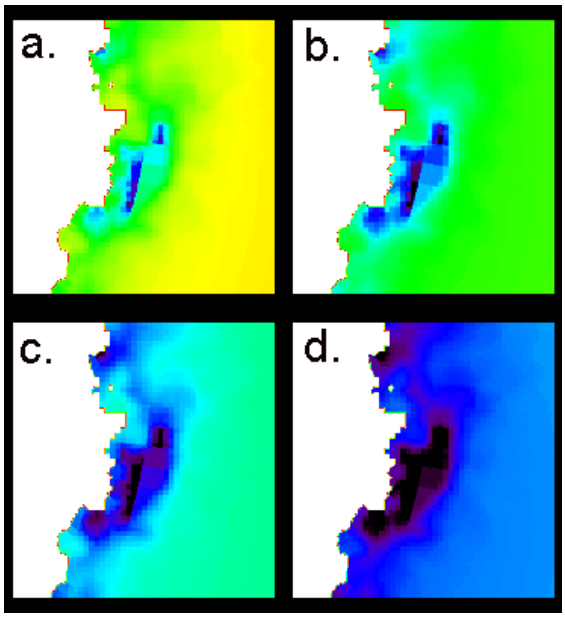

Figure 9.32: Sample plot of pixel-averaged PHO dose rate (mW m^{-2}) for Shackleton region for Nov 2000 beneath snow and ice at a. Z1 (0.202, 27.054); b. at Z2 (0.070, 9.305); c. at Z3 (0.025, 3.246); and d. at Z4 (0.009, 1.133) (where Z1, Z2, Z3 and Z4 are detailed in Table 9.4) [100].

9.2.3 Temporal variation of biological dose rates

Another IDL routine, *uwts.pro* was developed to enable the user to enter the coordinates of a sub-area in a region (A, S, D or M) (as in Figures 8.15-8.18), for which time series plots on both normal and logarithmic axes were produced. Tables 9.7 and 9.8 are to be used in conjunction with the plots in this section to assess the temporal variation in the biological dose rates for each month across a year.

Table 9.7: Colour code for time series plots in following Figures 9.33-9.35 and Figure 9.38.

Plot colour	Biological dose rate
Purple	Surface value
Dark blue	Pixel-averaged value at 5 metres
Light blue	Pixel-averaged value at 10 metres
Green	Pixel-averaged value at 15 metres
Red	Pixel-averaged value at 20 metres

Table 9.8: Normalisation value for plot b. in the following Figures 9.33-9.35 and Figure 9.38.

Biological dose rate	Normalisation value
Erythemal	300 mW m^{-2}
DNA	400 mW m^{-2}
BEH	600 mW m^{-2}
PHO	100 mW m^{-2}

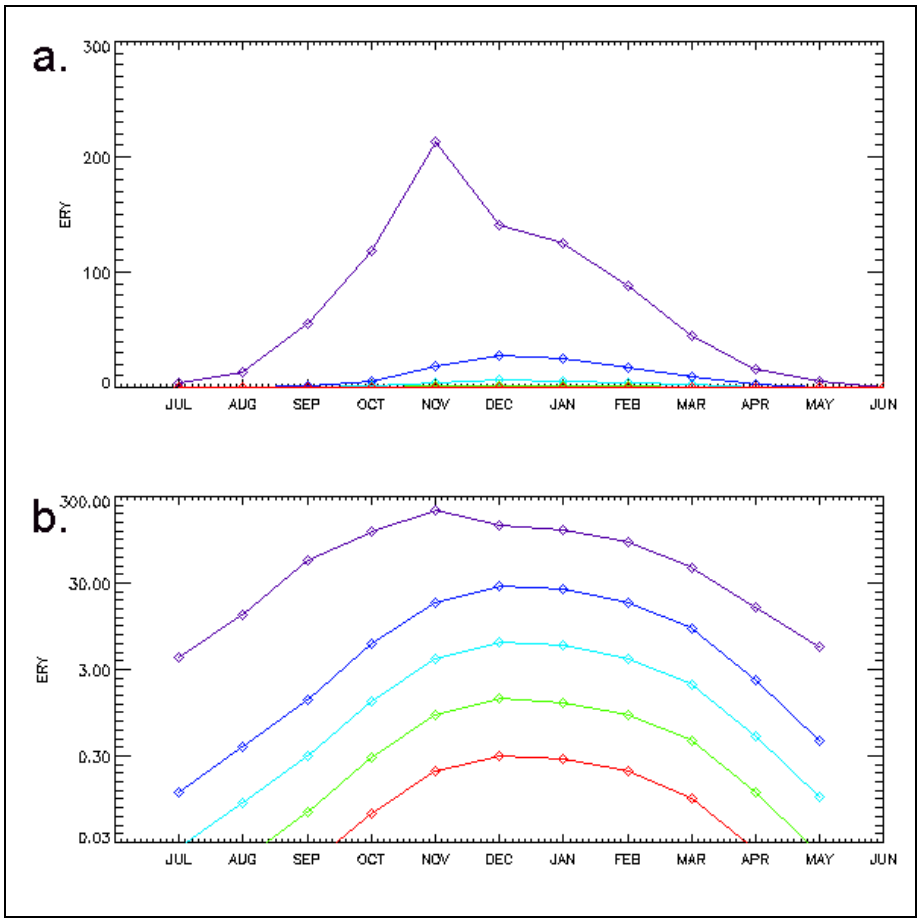

Figure 9.33: For sub-area no. 1 in Amery region for 2001 a. sample plot of erythemal UV and b. sample plot of erythemal UV using logarithmic scale.

Figure 9.33 demonstrates the following:

1. The peak in surface erythemal UV occurred in November 2001 (as shown also in Figure 8.26), which was explained by low values of TOC (Figure 8.24) and high sea ice concentration (Figure 8.25) in sub-area no. 1 in Amery region at that time.
2. The peak in the pixel-averaged values of erythemal UV at positions under the surface (as designated in Table 9.5), occurred in December 2001. This is explained by the lower sea ice concentration (~2% as per Figure 8.25) at that time.
3. Minimum sub-surface erythemal UV values occurred May-July 2001, with the largest decrease in the first 5 metres occurring in July-November (due to the attenuation of higher concentrations of sea ice for this period). Erythemal UV doses did not penetrate to 10 metres until after July, 15 metres after August and at 20 metres, between September and October (based on achieving 0.03 mW m^{-2}).

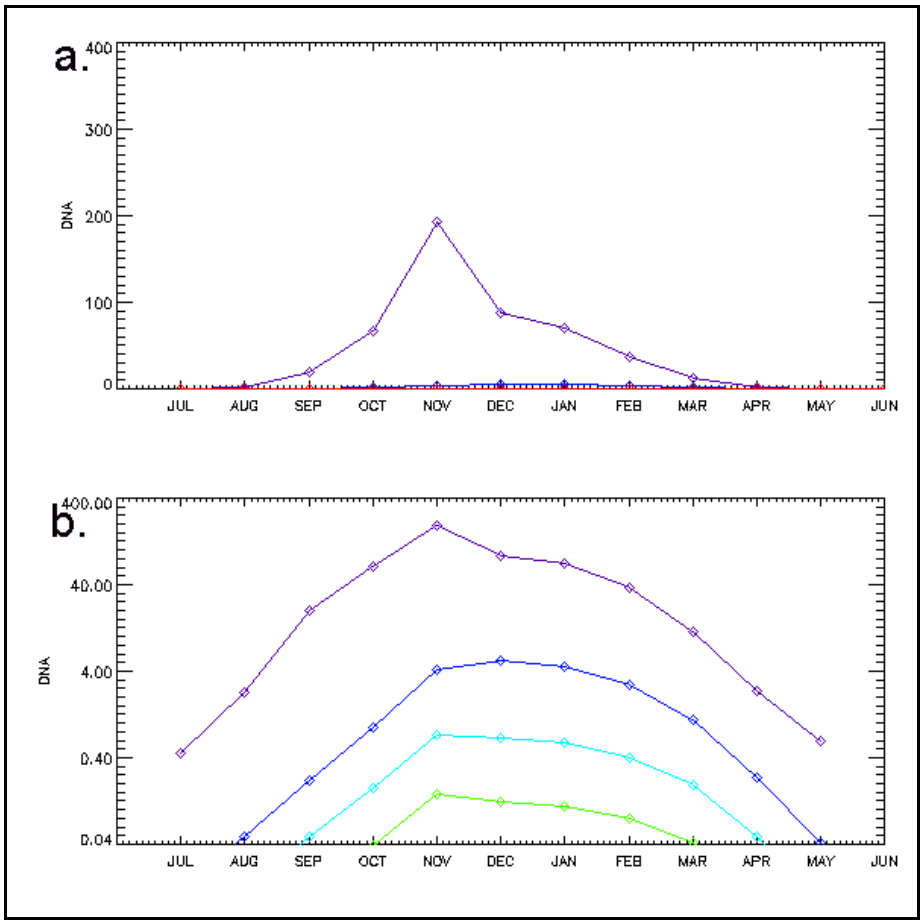

Figure 9.34: For sub-area no. 1 in Amery regions for 2001 a. sample plot of DNA dose rate and b. sample plot of DNA dose rate using logarithmic scale.

Figure 9.34 demonstrates the following:

1. The peak in the surface DNA dose rate occurred in November 2001 in sub-area no. 1 in the Amery region.
2. The peak in the pixel-averaged values of DNA dose rate at positions under the surface (as explained in Table 9.5) did not occur until December. The sea ice concentration for December was ~2% (as per Figure 8.25), which meant less attenuation, causing the higher doses for this month. As mentioned in Section 9.2.2, the DNA dose rate is strongly attenuated in water and ice.
3. The DNA biological dose rate does not penetrate to 5 metres depth (based on achieving 0.04 mW m^{-2}) until August and ceases in May; and the DNA biological dose rate penetrates to 10 metres from September until April. At 15 metres, sub-surface DNA dose rate values were minimal between October and March, and during this time there was no penetration of DNA doses to depths of 20 metres.

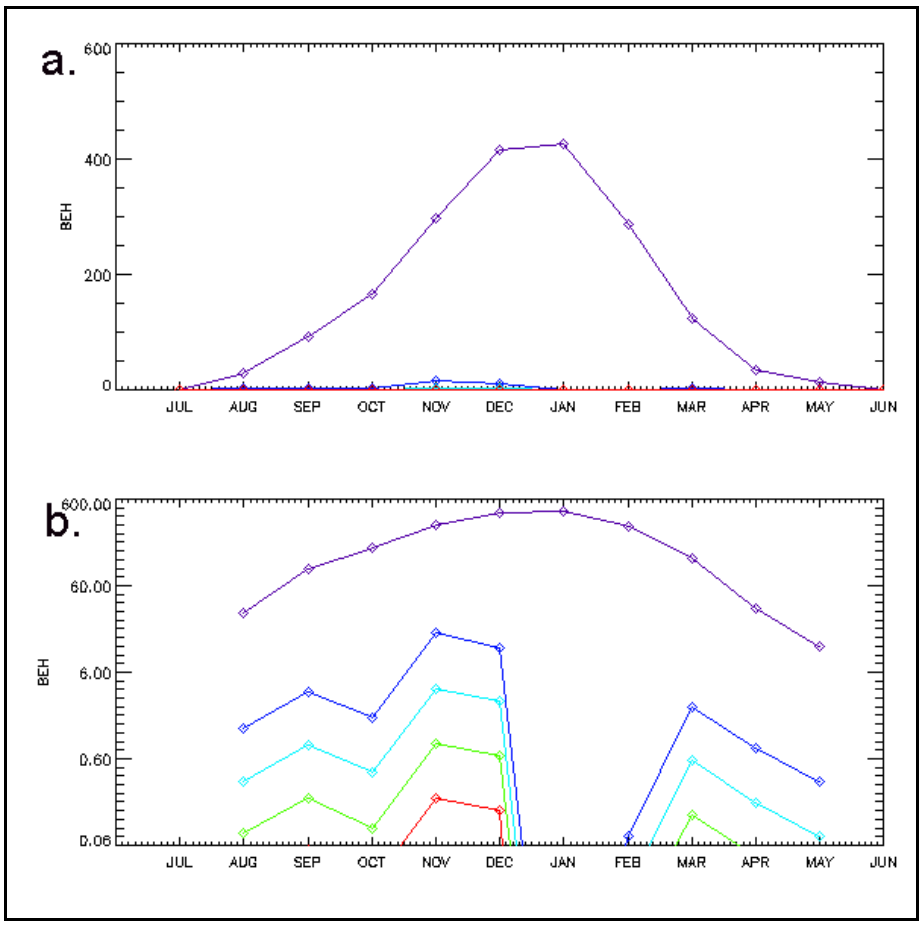

Figure 9.35: For sub-area no. 1 in Mertz regions for 2000 a. sample plot of BEH dose rate and b. sample plot of BEH dose rate using logarithmic scale.

Figure 9.35 demonstrates the following:

1. The peak in the surface BEH dose rate occurred in Mertz sub-area no. 1 in January 2000.
2. TOC was at its maximum in October (Figure 9.36), and gradually decreased to its minimum values in December to March, before it started increasing again. This explains the trend in the surface values of BEH dose rate. It also explains the sub-surface BEH dose rate values, i.e. decreasing in October and then beginning to increase again before the sea ice concentration countered the TOC effect (see point 3. below).
3. The peak in the pixel-averaged values of BEH dose rate at positions under the surface (as explained in Table 9.5) occurred in November, decreasing to nil for all sub-surface positions in January to February. The sea ice concentration for this period was 100% (see Figure 9.37), and Figure 8.17 gives the position of Mertz no. 1 sub-area in an area of ~7 m thick ice (Figure 9.8) and ~0.75 thick snow (Figure 9.9) ensuring maximum attenuation.

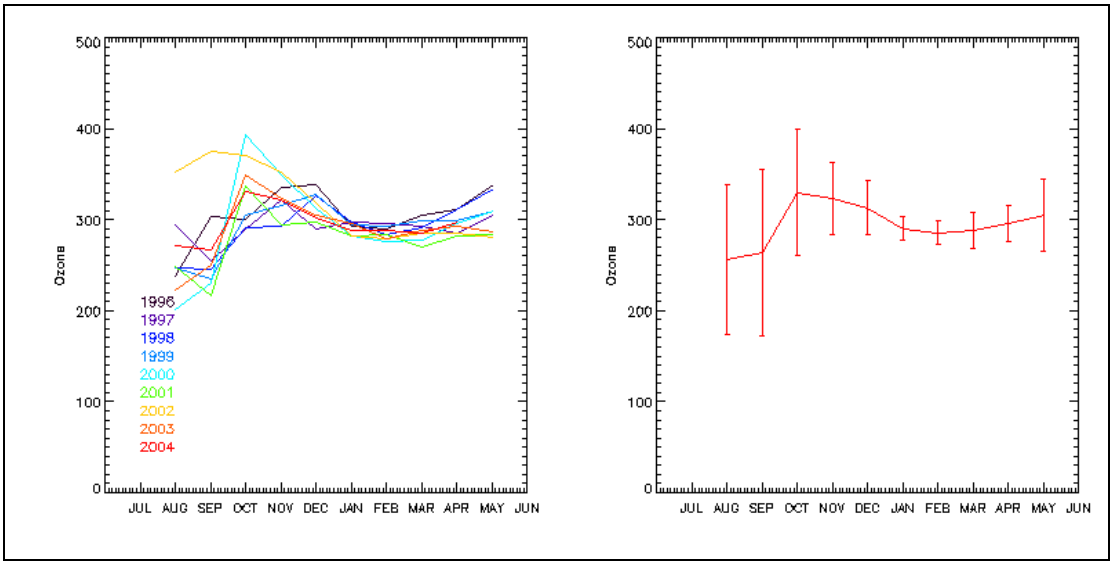

Figure 9.36: Plots of TOC for Mertz no. 1(Left panel – all nine years, Right panel – 9-year average plus error bars – 2 s.d.).

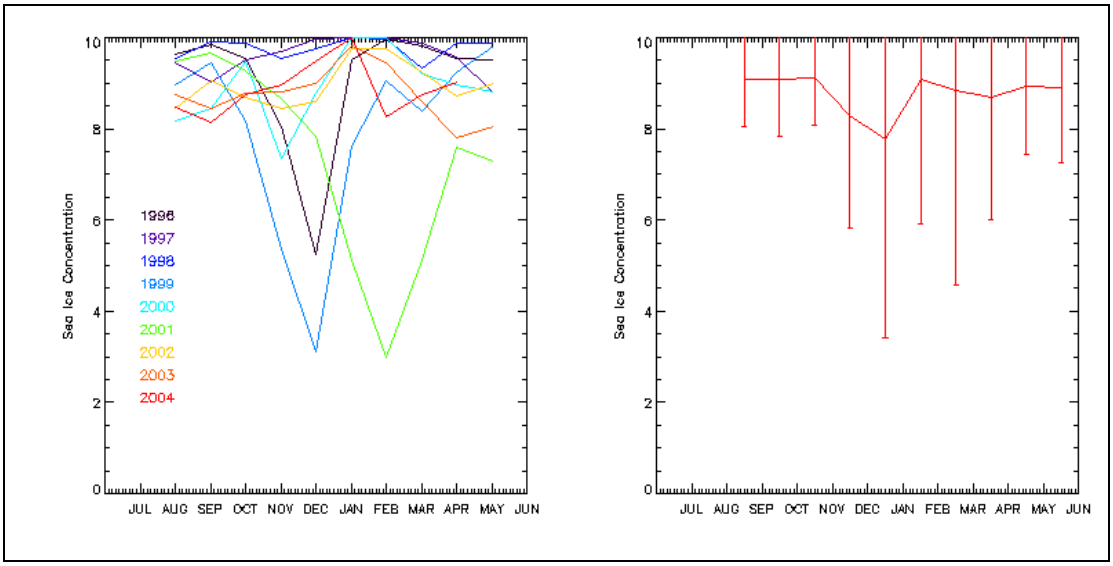

Figure 9.37: Plots of sea ice concentration for Mertz no. 1 (Left panel – all nine years, Right panel – 9-year average plus error bars – 2 s.d.).

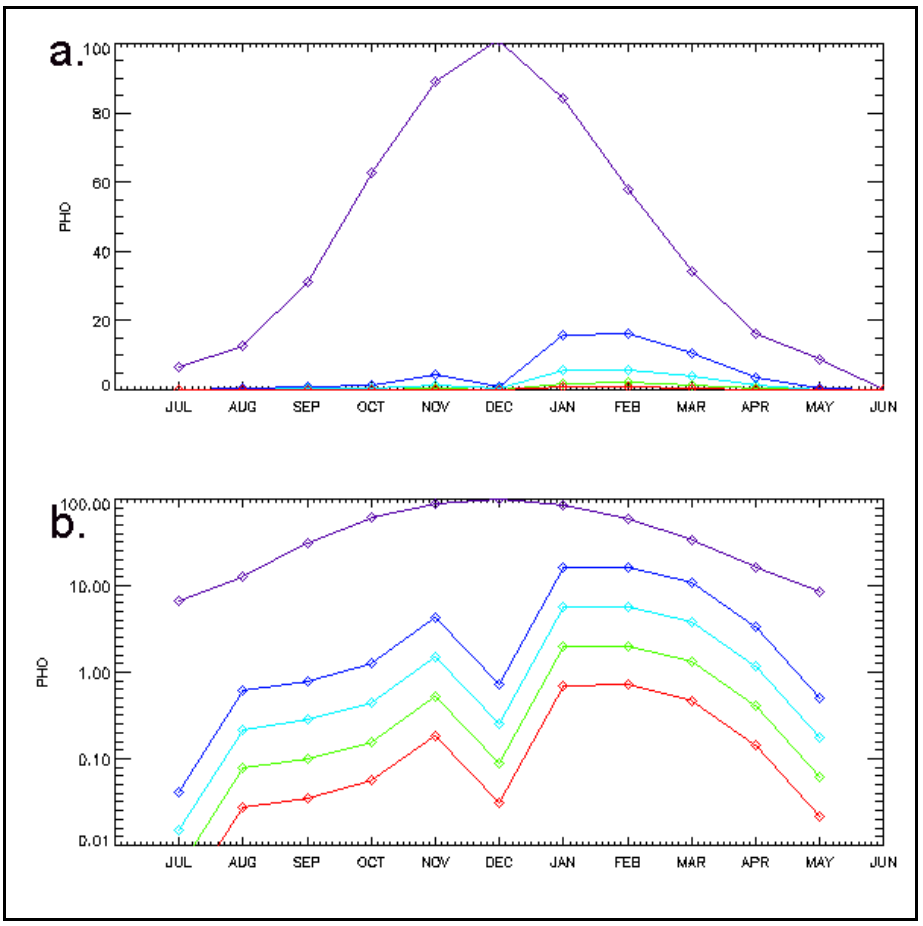

Figure 9.38: For sub-area no. 1 in Dalton region for 1998 a. sample plot of PHO dose rate and b. sample plot of PHO dose rate using logarithmic scale.

Figure 9.38 demonstrates the following:

1. The peak in the surface PHO dose rate occurred in Dalton sub-area no. 1 in December 1998.
2. Despite TOC having its maximum values in December 1998 (Figure 9.39), the sea ice concentration was at its maximum of 100% in this month (Figure 9.40), which pushed the erythemal UV to its maximum, the conversion of which resulted in the maximum photoinhibition dose in December.
3. The sea ice concentration decreased from 100% in July to 90% in November, and at the same time, TOC was increasing towards its maximum. For the relationship between D_{ERY} and D_{PHO}, an increase in ozone values is accompanied by a shift of the relation towards higher values of D_{PHO}. These factors would explain the upward trend in the D_{PHO} for July to November. The pixel-averaged PHO dose rate decreased for all four sub-surface values (as explained in Table 9.5) in December, due to the attenuation by the sea ice. Sub-surface D_{PHO} was maximum in January-February 1998, when sea ice concentration had decreased to between 20-60% and ozone was ~300 DU.

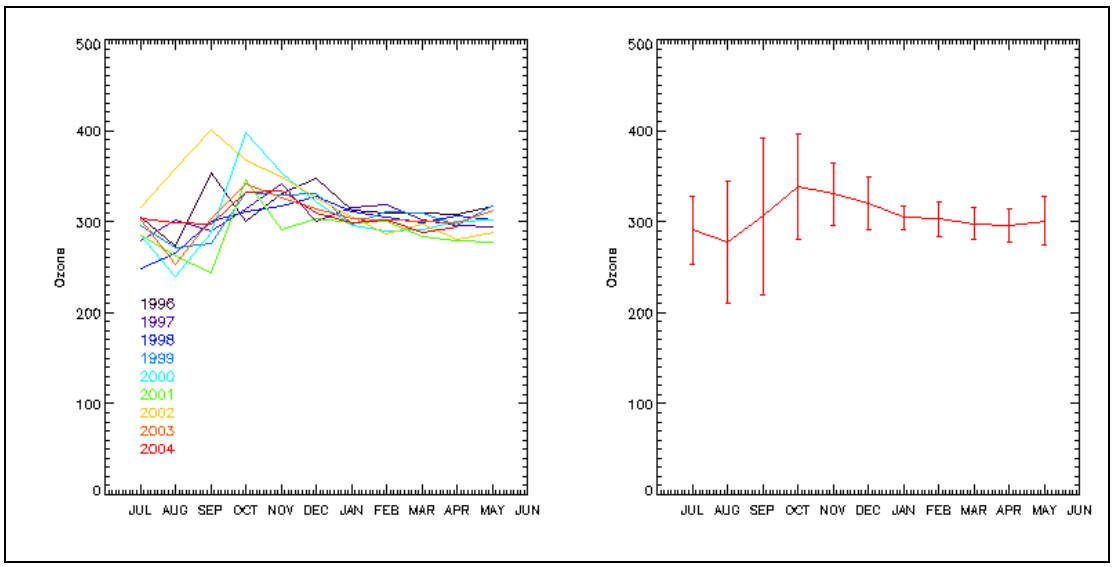

Figure 9.39: Plots of TOC for Dalton no. 1 (Left panel – all nine years, Right panel – 9-year average plus error bars – 2 s.d.).

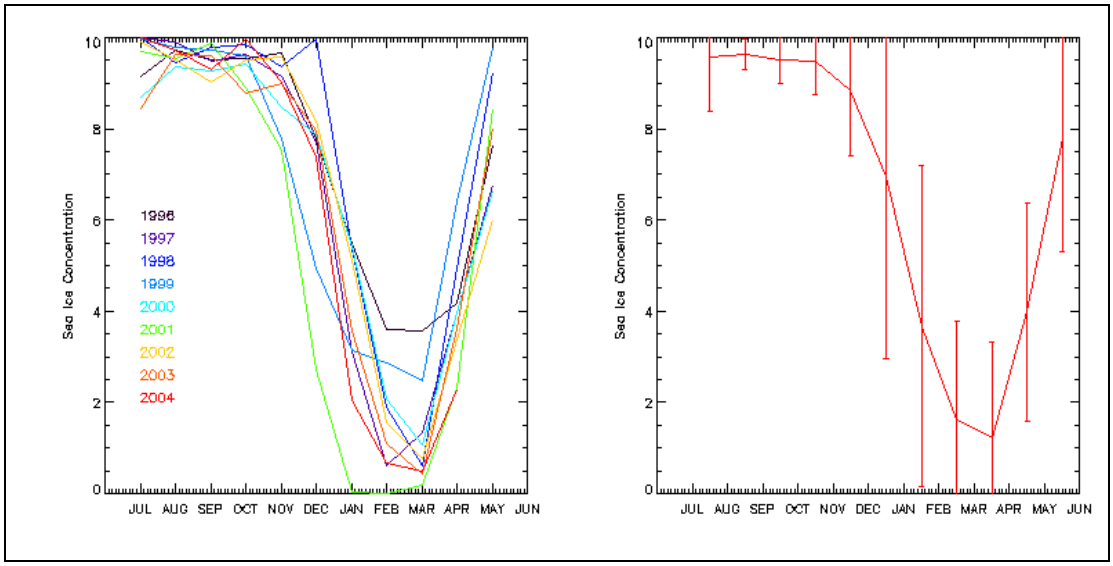

Figure 9.40: Plots of sea ice concentration for Dalton no. 1 (Left panel – all nine years, Right panel – 9-year average plus error bars – 2 s.d.).

9.2.4 Summary of the results of mapping biological dose rates

The lower levels of TOC have a significant effect on the surface values of the four biological doses discussed in this section. Whereas higher sea ice concentrations can increase the surface levels of the biological doses, it has a negative effect on the sub-surface values of the biological dose rates, with the DNA dose rate affected the most. Higher sea ice concentrations therefore protect the marine organisms living at depths within the water column but expose those living at or near the surface to more damaging levels.

Assessment of the time-series plots indicates the dramatic effects that 'out-of-season' variations in sea ice concentration can have on the biological doses. For example, it would be expected that sea ice concentration would decrease for the summer months of January and February, thus allowing higher levels of biological dose rates to penetrate the water column, whereas in January and February in Mertz sub-area no. 1, the sea ice concentration increased to 100%, blocking sub-surface penetration. The higher values of sea ice concentration would cause higher within-ice values for algae living within that medium.

This study provides a broad overview, and more work is necessary to examine and map biological dose rates specific to polynyas and the MIZ.

10. CONCLUSION AND FUTURE RESEARCH

10.1 Conclusions

The primary objective of this research was to develop maps of surface levels of erythemal UV for the East Antarctic marginal ice zone from satellite data, for the period mid-1996 to mid-2005. The second objective was to include the attenuation of snow, ice and water in the calculations, and map sub-surface levels of erythemal UV. The third objective was to use spectral biological weighting functions to develop a set of non-linear conversions between the erythemal and more biologically relevant dose rates. Because the other BWFs have a different action spectrum to the erythemal BWF, then the depletion of the derived doses with distance in water, snow or ice is different from the erythemal dose. Therefore, it was extremely important to present maps of the DNA dose rate (Setlow 1974) and two different photoinhibition dose rates (Jones and Kok (1966) and Behrenfeld (1993)), both at and below the surface for the benefit of scientists studying biological systems for which the DNA and the two different photoinhibition doses are relevant. These products will provide biologists with new information to aid their studies of the effects of enhanced UV radiation on organisms and ecosystems in the Antarctic sea ice zone. AVHRR PPF data, TOMS ozone data, and ASPeCt sea ice and snow thickness data provided the basic information with which to create the maps. The radiative transfer model, UVSPEC and sundry purpose-coded software modules (see Appendix A) provided the tools with which to manipulate the above datasets and create the maps.

For ease of presentation of the results for this project and to highlight and examine regional variability, the East Antarctic sea ice zone was sub-divided into four regions; Amery, Shackleton, Dalton and Mertz. The radiative transfer model UVSPEC was used to develop a look-up table of erythemal UV values for various combinations of ozone, SZA and albedo (Section 7.3). AVHRR PPF satellite images of the regions were processed using software that extracted an estimated value of surface, cloudy-sky, erythemal UV from the LUT for each pixel/day. This method was more efficient than calculating an erythemal UV estimate for every pixel of every image, with the possibility of repeating the same calculations for reoccurring combinations of the parameters, SZA, surface albedo and TOC (obtained from the TOMS ozone data for that pixel/day). These estimated daily erythemal UV values were validated using data collected at the three Australian Antarctic stations, Davis, Casey and Mawson, as well as data collected onboard the RSV *Aurora Australia* during voyages on its way to, and from, the above-mentioned stations (Section 8.2). For each of the regions and for each day (when data was available), a data file was created that contained the following parameters for each pixel of the region – noon-time, cloudy-sky erythemal UV; cloudy-sky daily dose of erythemal UV; TOC; sea ice concentration; cloud modification factor; surface UV albedo; and the count of the number of days for which data existed. Monthly averages of these data were calculated and plotted. The monthly-averaged

data files and associated plots were saved to disk, and are contained in Appendix A to this thesis.

These monthly-averaged data demonstrated the interannual variability in the parameters: ozone, cloud modification factor, sea ice concentration, snow thickness distribution, surface UV albedo and noon-time cloud-affected erythemal UV. The values of the parameters ozone, sea ice concentration and noon-time, cloud-affected erythemal UV generally followed an annual cycle, although some years had unusually high/low values for some months in some regions, e.g. low values of ozone, high values of sea ice concentration and high values of noon-time erythemal UV for spring and summer 2001 in the Amery and Shackleton regions. It should be noted that, despite the ozone hole developing in early spring, the highest levels of erythemal UV tended to occur in the study regions between November and January, when the polar vortex had disintegrated and allowed the lower TOC values to spread towards the coast and sea ice zone. This exposed marine organisms to elevated levels of erythemal UV without the shading effect of the sea ice that is normally present in early spring. It was noted that the areas of high erythemal UV and low ozone did not always match spatially, although analyses of various sub-areas (Section 8.3.4) showed that the peaks/dips in ozone for the various sub-areas often did display the same cycles of dips/peaks in erythemal UV. The lack of complete anti-correlation between erythemal UV and TOC is driven by changes in other factors (for example, cloud amount and varying albedo due to changes in sea ice concentration) affecting erythemal UV. The amount of cloud can have a significant effect on levels of erythemal UV at the surface, but lack of detail in the cloud data made it difficult to have confidence in attributing any changes in levels of erythemal UV to this parameter. The plots of ozone showed that the Dalton and Mertz regions are not affected to the same extent by low TOC values during the study period (as compared to the Amery and Shackleton regions), and even when the ozone hole was present, its effect was more continental rather than over the sea ice zone.

Massom *et al.* (2004, 2006) described exceptional sea ice conditions from September 2001 to February 2002 in East Antarctica, resulting from a strongly positive atmospheric pressure anomaly in the South Atlantic coupled with strong negative anomalies in the Bellingshausen-Amundsen and southwest Weddell Seas (see Figure 2.3) plus persistent blocking high activity in the south Tasman Sea. The abnormal erythemal UV conditions noted in 2001 of this study may be attributable in part to the same sea ice anomalies and corresponding albedo-related feedback.

Trend analysis for ozone and sea ice concentration demonstrated negative slopes for all seasons over the nine years for most sub-areas (see exceptions for both parameters in Section 8.3.6). The regression statistics for erythemal UV for all seasons and sub-areas were divergent – six of the trend lines for noon-time erythemal UV demonstrated significant trends – four negative trends in spring and two positive trends in summer (see Section 8.3.6 for details of sub-areas).

The second objective was achieved using IDL software, *uw1.pro*, that determined the attenuation values for specified scenarios (i.e. at depths of 5, 10, 15 and 20 metres in the water column and averages for the upper 5, 10, 15 and 20 metres of water) using 0.3 m^{-1} as the attenuation coefficient of water and 0.1 as a reflection coefficient (Booth and Morrow 1997; Rasmus *et al.* 2004). Visual assessment of the plots of erythemal UV dose rates in the water column demonstrated that the same pattern of erythemal UV at the surface is transferred down through the water column, but with reduced amplitudes. The average erythemal UV value over the upper 5, 10, 15 and 20 metres of water was included for the purpose of estimating the effect of UVB on marine organisms that inhabit these niches of the upper mixed layer (UML). The degree of UVR exposure within a mixed layer is dependent on the depth of the mixing, and for a fixed mixing depth the average attenuated dose was greater than that at the same depth in an unmixed water column. In particular, the plots indicate that the levels of erythemal UV in the 0-20 metre mixed layer are approximately equivalent to the levels of erythemal UV at the 5 metre level.

Participation in the SIPEX voyage in 2007 (Chapter 6) facilitated research to determine the attenuation coefficients for snow and ice. The IDL software, *uw1.pro,* applied attenuation coefficients for snow (11.3 m^{-1}), and ice (2.0 m^{-1}) and a reflection coefficient for snow (0.67) to determine the attenuation values for the specified scenarios where pixels were covered by sea ice (i.e. below the layer of snow at the top of the ice, half-way through the ice, at the bottom of the ice and also at 20 cm depth in the ice cover). The erythemal UV estimates at the surface were multiplied by the attenuation values, as described above, and the erythemal UV estimates within and at the bottom of the ice and associated plots were saved to disk (see Appendix A). The erythemal UV estimates at the bottom of the ice were then included in calculations to determine estimates that would penetrate further into the water column below the cover of snow and ice. These data were saved to disk along with the associated plots (Appendix A).

The plots of the ASPeCt data demonstrated that as ice thickness increases, so does snow thickness. Penetration of UVR into and through sea ice is strongly dependent on the thickness of sea ice and its snow cover. Snow has a much higher attenuation and reflection coefficient than water and ice, and this was borne out by the map of sub-surface erythemal UV for which the greatest reduction was at the snow/ice interface. Surface-dwelling organisms without a cover of sea ice are at greater risk from increased UV than those living within or under sea ice. Only low levels of erythemal UV will reach organisms living in the water column beneath a cover of ice and snow – a gradual reduction occurred with depth, resulting in very little effect at the 20 metre level. To examine the situation where a pixel is only partially covered by sea ice, the sea ice concentration was included in the calculations in the software, *uw1.pro* to arrive at pixel-averaged erythemal UV at the specified depths of 5, 10, 15 and 20 metres below the ocean or ice surface. Plots of these sub-surface values are included in Appendix A.

Discussions with expert biologists from the Australian Antarctic Division and the Antarctic Climate and Ecosystem Cooperative Research Centre revealed that monthly climatologies of relevant biologically-effective dose rates would aid research to determine whether increased radiation as a result of the ozone hole is having a deleterious effect on Antarctic organisms. This third objective was achieved using the best-fit functions for the relations between each of the three calculated doses (D_{DNA}, D_{BEH}, D_{PHO}) and the erythemal dose (D_{ERY}), as initially determined by Ali (2001) for fixed values of TOC. The coefficients in each set of equations (equations (9.2), (9.3) and (9.4) in Section 9.2.5) were separately plotted against a scaled ozone column to derive relationships which allowed conversion of D_{ERY} into the other dose values, D_{DNA}, D_{BEH}, and D_{PHO}, for any value of ozone. These equations were included in the software module, *uw1.pro* which produced the same series of maps (surface, in the water column, in the ice, in the water column under ice and the pixel-averaged values) as already produced for erythemal UV, but for the three other doses mentioned above.

The lower levels of TOC have a significant effect on the surface values of the four biological doses. Whereas higher levels of sea ice concentration can increase the surface levels of the biological doses, they have a negative effect on the sub-surface values of the biological dose rates, with the DNA dose rate affected the most. Higher sea ice concentration therefore protects the marine organisms living at depths within the water column, but expose those living at or near the surface to more damaging levels. There are sometimes anomalous variations in sea ice concentration which have dramatic effects on biological doses. For example, instead of the sea ice concentration decreasing for the summer months of January and February in 2000 in Mertz sub-area no. 1, it increased to 100%, to effectively block sub-surface penetration of radiation. While organisms living beneath the ice would be afforded the protection of the ice, the organisms occupying the surface and within-ice niches would be exposed to increased radiation in this time period due to the higher surface albedo. This anomalous change in the regional sea ice regime in the vicinity of the Mertz Glacier Polynya was attributed to a major late-season shift in atmospheric circulation over the East Antarctic sea ice zone that occurred in October 1999 (Massom *et al.* 2003). The mean wind direction at 65º S, 145º E changed from south-south-easterly to west-south-westerly, resulting in almost a complete reversal of the climatological East Wind Drift pattern in large scale sea ice advection over the Southern Ocean sector 135º-170º E. By comparison with National Centers for Environmental Prediction/National Center for Atmospheric Research Reanalysis time series from 1980 to 2000, this shift was shown to be unusual in terms of both its persistence and impact. This had a profound impact on sea ice concentration and extent over a vast area. This physical shift had a flow-on, first-order effect on the structure of ecosystems at high latitudes (Nicol *et al.* 2000b).

10.2 Future research

The following points (1.–8.) encapsulate some of the possibilities for research to extend the results of this study. The data files and maps created by this project (as summarised in a. and b. below) will be stored at, and accessible through the Australian Antarctic Data Centre for sharing with the scientific community. The products include the monthly averages of the following (when basic data available) for the years, 1996-2005 for each region (Amery, Shackleton, Dalton and Mertz):

a. Total ozone column, sea ice concentration, count of days when data are available, surface mask, noon-time erythemal UV, daily dose of erythemal UV and surface albedo. The erythemal UV data were the basis for the production of maps and data files of the other three biological dose rates (in b. below).

b. For each of the dose rates, erythemal UV (McKinlay and Diffey 1987), DNA (Setlow 1974 - from Smith and Baker 1980) , photoinhibition (Behrenfeld *et al.* 1993) and photoinhibition (Jones and Kok 1966 - from Smith and Baker 1980), the following products were produced:

- Surface maps;
- Maps at depths of 5, 10, 15 and 20 metres in the water column;
- Maps of averages in the upper 5, 10, 15 and 20 metres of the water column;
- Maps at the snow/ice interface, midway through the ice, at the bottom of the ice, and at a depth of 20 cm in the ice;
- Maps at 5, 10, 15 and 20 metres in the water column beneath snow and ice (taking the ice draft into account where draft = $0.9*Z_i$ and Z_i = thickness of the ice);
- Maps of the pixel-averaged dose rate taking into account that in general, a pixel will not be totally covered by sea ice. The sea ice concentration was included in the calculations to determine the estimates at the specified depths of 5, 10, 15 and 20 metres below the ocean or ice surface.

1. Phytoplankton provide a link between two of the issues regarding anthropogenic modification of the Earth's environment, i.e. global warming and ozone depletion. Ozone-induced changes in UVB impacting on phytoplankton abundance could, in turn, reduce the amount of atmospheric carbon dioxide sequestered by phytoplankton in the ocean, thus accelerating the process of global warming. The maps and data files produced by this project will be valuable for researchers investigating the first part of this problem (i.e. the effect of ozone depletion on levels of UVB radiation). Some preliminary work by Cadman (2001) used TOMS ozone data as an indicator of levels of UVB, and ocean colour satellite data as a proxy for phytoplankton, to investigate relationships between these two

parameters over the spring and summer of four years (1997-2000). Cadman's investigations demonstrated that as ozone increased in December, phytoplankton also increased, but the relationships were not statistically robust. The increases/decreases in the ozone values do not necessarily indicate decreases/increases in erythemal UV levels because of the effect of the other parameters (cloud amount and albedo of the surface), as demonstrated in this study. The methods developed by Cadman (2001) could be reapplied, based on the maps of levels of erythemal UV (or other biological dose rates) developed in this project instead of the TOMS ozone data. For smaller areas, where *in situ* biomass data (e.g. phytoplankton, krill, sea ice algae etc.) have been collected, the data files can be queried to obtain the biological dose rates for the same area by entering the coordinates of the bottom left and top right corners of the area (Section 8.3.2).

2. The methods in this study could be used to develop a LUT of PAR (photosynthetically active radiation) for combinations of SZA and surface reflectance (ozone is not necessary in this case, as it has no effect on PAR). The PAR estimates in the LUT could be input to the Vertical Generalized Production Model (VGPM) (Behrenfield and Falkowski 1997), which describes the relationship between surface chlorophyll and depth-integrated primary production. The core equation explaining the VGPM can be found at http://marine.rutgers.edu/opp/programs/VGPM.html (Behrenfeld 2000). Importantly, the VGPM approach would need to be modified to account for a temporally and spatially variable sea ice cover and an appropriate mixed layer depth.

3. The methods used in this project could be adapted and extended to determine biological doses for other key components of the microbial loop (e.g. viruses, bacterioplankton).

4. The methods developed for this project could be applied to more recent data, e.g. from 2005 onwards. The data used for this project was the 'best available' (and sometimes the only data available) for that temporal coverage. The NSIDC Polar Pathfinder project was not funded to produce data past 30th June 2005. The output from future efforts to model erythemal UV levels in Antarctica would benefit from improvements in the accuracy, and spatio-temporal resolution and coverage of all the basic data sets. This is particularly relevant for the sea ice and snow thickness data.

    a. Negotiating sea ice to collect *in situ* measurements to improve the spatio-temporal coverage and resolution of snow and sea ice thickness data is not generally practicable, especially not for large scale investigations. Satellite remote sensing can fill some of the voids in data availability, but *in situ* data remains invaluable for the calibration and validation of satellite-derived geophysical parameters. Other techniques are available to collect sea ice thickness data (see summary pages 509-510 in Lubin and Massom (2006)) and while they provide important information, they are logistically expensive, variable in accuracy, temporally and spatially limited in coverage, and are not carried out in a systematic repetitive fashion. The

Geoscience Laser Altimeter System (GLAS) instrument on NASA's Ice, Cloud, and land Elevation satellite (ICESat) was launched on 12th January 2003, and up until 2009, provided multi-year elevation data needed to determine ice sheet balance as well as cloud property information, especially for stratospheric clouds common over polar areas. Detailed information on ICESat data is given by Zwally *et al*. (2002). The second generation of ICESat (i.e. ICESat-2) is scheduled for launch in late 2015.

b. Another key source of sea ice thickness in the future will be CryoSat-2. European Space Agency's first CryoSat mission (Drinkwater *et al.* 2005; Wingham 2005) suffered a launch failure in October 2005 and was succeeded by CryoSat-2, launched on 8th April 2010. CryoSat-2 is in a highly inclined polar orbit, reaching latitudes of 88° north and south, to maximise its coverage of the poles. Its main payload is an instrument called Synthetic Aperture Interferometric Radar Altimeter (SIRAL) (Lubin and Massom 2006). Previous radar altimeters have been optimised for operations over the ocean and land, but SIRAL is the first sensor of its kind designed for ice. Scientists will be able to deduce sea ice thickness from the data collected by CryoSat-2 (Lubin and Massom 2006).

c. Snow cover thickness plays an important role in modulating the exchange of energy and mass across the polar atmosphere-ice-ocean interaction system, and also in the ecology of ice-covered oceans (Lubin and Massom 2006). It was obvious from this study that snow cover is particularly effective at reducing the transmission of UV (and the other biological dose rates) through to the ice. Perovich (1993) determined that UVB is reduced by about 2 orders of magnitude by a 0.1 m-thick snow cover. Snow cover also has a major impact on the amount of PAR entering the ice and upper ocean (Perovich 1996), although sea ice covered with snow reduces the transmission of harmful irradiance more than it does the biologically-beneficial PAR (Perovich 1993). While snow properties and layer characteristics are important, the snow depth distribution is probably the single most frequently used measurement of the snow cover. Despite this, there is surprisingly limited understanding of the global thickness distribution of snow on the sea ice because of:

- the vast extent of the ice;
- the seasonal, year-to-year, and spatial variability of the snow (making it difficult to obtain comparable measurements); and.
- the fact that remote sensing of snow depth remains problematic (Sturm and Massom 2010).

A promising recent development has been an algorithm to derive global estimates of snow depth over sea ice from time series of satellite passive-microwave

brightness temperature data, specifically from the NASA Aqua Advanced Microwave Scanning Radiometer-Earth Observing System (AMSR-E), details of which can be found in Comiso *et al.* (2003). The US National Snow and Ice Data Centre (http://nsidc.org) has made AMSR-E snow depth products available from 2002, mapped at 12.5 km resolution. Recent validation campaigns suggest however, that this product underestimates actual snow depth by as much as a factor of 2-3 (Worby *et al.* 2008b), due primarily to ice surface roughness effects (Stroeve *et al.* 2006). Work is underway to improve the accuracy, possibly by incorporating ice surface roughness information acquired on a similar scale by satellite radar scatterometers (Sturm and Massom 2010).

5. Despite being a convenient 'package' of appropriate data for this project, the AVHRR Polar Pathfinder data does not extend beyond 2005. As one of the new generation of sensors, the MODerate-resolution Imaging Spectroradiometer (MODIS) signifies substantial improvements in spatial resolution, number of spectral channels, radiometric calibration, and geometric quality (Kaufman *et al.* 1998). This state-of-the-art instrument carried onboard the Terra and Aqua Earth Observing System satellites provides an enhanced set of derived atmospheric, terrestrial and oceanic products (Houborg *et al.* 2007), including surface temperature and reflectance. Together with AMSE-R, these two sensors provide the equivalent data to the AVHRR Polar Pathfinder dataset.

6. The lack of accurate cloud information is a crucial factor. The only information on clouds available for determining cloudy-sky erythemal UV at the surface for this project, was the presence/absence of cloud in a 5 x 5 km pixel – there were no associated data on cloud base height, cloud type, cloud thickness or how the cloud changed throughout the day. Such limited cloud information compromised the accuracy of the estimates of cloudy-sky erythemal UV, and there was also not enough spatial detail in the cloud data to be able to attribute any of the changes in the levels of erythemal UV to changes in cloud conditions. A way to improve this aspect of the modelling is to incorporate satellite data of finer spatial resolution (e.g. 1 km), with better cloud detection and better estimates of cloud at the surface (Ackerman *et al.* 1998). For example, evaluation of the MODIS cloud detection algorithm by Liu *et al.* (2004b) determined that it performs well in polar regions during the day. Two new cloud tests improved the night-time mis-identification of cloud as clear (from 19.8% to 2.7%), when tested against collocated radar/lidar observations from the Antarctic station at the South Pole. In 2006, NASA also launched CloudSat and the d-Aerosol Lidar and Infrared Pathfinder Satellite Observation (CALIPSO) spacecraft to study the role that clouds and aerosols play in regulating Earth's weather, climate and air quality. CloudSat measures vertical profiles of clouds at a vertical resolution of 500 metres and a horizontal cross-track resolution of 1.2 km.

7. The measurements taken on the SIPEX voyage in 2007 were simplistic, in that no spatio-temporal variation was taken into account. The data will benefit from further direct measurements of attenuation of fast ice and pack ice because the mode of growth (mainly thermodynamic *vs* dynamic-thermodynamic) for each type influences its optical properties (Perovich 1996).

8. *In situ* measurements of the UV attenuation of Antarctic waters allowing the resolution of spatio-temporal variations would provide a better estimate of the amounts of sub-surface radiation. The amount of dissolved, organic carbon or chromophoric dissolved organic matter determines the UV attenuation (Laurion *et al.* 1997; Laurion *et al.* 2000), therefore attenuation coefficients for water during seasons of increased biological activity (e.g. algal blooms in spring, swarms of krill, etc.) would improve accuracy of the estimates of the sub-surface levels of the biological doses at these times.

This research has demonstrated that low ozone values can increase erythemal UV values. It has also shown that low sea ice concentrations can counter the positive effect that low ozone values have on erythemal UV. The analyses also indicated that even with high ozone values, areas with high sea ice concentration can still be affected by high erythemal UV as a result of the multiple reflections of incoming irradiance by the high albedo sea ice. The sub-surface maps of the biologically effective dose rates illustrated the attenuation caused initially by the snow cover on the sea ice, and secondly by the sea ice itself. This implies that phytoplankton in the water column are afforded shading from excessive biological dose rates by snow and sea ice, whereas sea ice algae are exposed to these high biological dose rates. Further research with improved data, as suggested above, will enable scientists to research how extensive the effects of increased levels of biologically effective dose rates are on Antarctic marine organisms.